Kinematic properties of b-quark pairs in boosted $Z + b\bar{b}$ events and the search for $V(H \to b\bar{b})$

Chloe Gray

Submitted in fulfilment of the requirements for the
Degree of Doctor of Philosophy

School of Physics and Astronomy
College of Science and Engineering
University of Glasgow

November 2019

Abstract

The study of b-quarks is very important as they play an important role in many Higgs and beyond-the-Standard-Model searches, and their treatment using perturbative quantum chromodynamics (QCD) is not completely understood. This thesis presents a measurement of cross-sections for the production of a boosted Z-boson in association with a large-radius jet, differential in kinematic variables of the jet and its b-tagged sub-jets. This measurement provides an important test of perturbative QCD with emphasis on the production rates and kinematics of the bottom quarks. The phase space probed in the measurement is particularly relevant for beyond-the-Standard-Model searches. The differential and total cross-sections are presented at particle-level, where the fully Bayesian unfolding method was used to correct the data. The $Z + b\bar{b}$ process is a significant background to several important Higgs-boson searches; a particular example being the search for a Higgs boson decaying to b-quarks, produced in association with a vector boson, $V(H \to b\bar{b})$. A study of the signal-modelling uncertainties in the 2017 search for $V(H \to b\bar{b})$, where the first evidence for the $H \to b\bar{b}$ decay was observed, is presented in this thesis. These analyses would not be possible without b-tagging algorithms to identify the b-quarks in the final state. It is important that the performance of b-tagging algorithms in data is well modelled by Monte Carlo simulation. A calibration of the b-tagging efficiency of the MV2c10 algorithm in small-radius track-jets is therefore also presented.

Contents

List of Tables

List of Figures

Acknowledgements

The work carried out in this thesis would not have been possible without the advice, support, and encouragement from a number of people. First and foremost, I would like to thank my supervisor, Andy Buckley, who has been an invaluable source of knowledge, advice, and guidance throughout my PhD. I would also like to thank Chris Pollard, who has always been patient with my numerous and often silly questions.

I would like to extend a thank you to everyone else at Glasgow, staff and students, past and present, for providing a friendly and supportive working environment. I am grateful for all of the fun times both in the department, and at the pub after work on Fridays. I would like to thank the University and STFC for allowing me the opportunity to carry out this PhD, and for funding my research. Glasgow is a city I now happily call home, and without this opportunity that would not have been the case.

I would like to thank the SB's: Bethany, Emily, Lauren and Kiran for their friendship. You are simply always there to welcome me home in Newcastle with open arms, and just generally be great friends. I would like to thank Emily Graham who has shared this testing journey with me from undergraduate to Dr. Thank you in particular the whistle-stop tour of Switzerland that we managed to cram into our remaining months of LTA – it was great. For the friends I made at CERN whilst on LTA, thank you for the numerous and excellent fun times.

Thank you to my family. Without your constant and unconditional support I would not be where I am today. You have always enthusiastically encouraged me with my studies, and pushed me when I needed it.

Finally despite not wanting to be "cheesy", it would be remiss not to thank Pete, who has been an invaluable support throughout. Thank you for providing me with chocolate at times when thesis-writing got too much, for constantly encouraging me when my confidence wavered, and for going above and beyond to cheer me up after a bad day. Quite simply, thank you for being there, always.

Declaration

Chapters 2 and 3 are introductory chapters describing the theoretical framework on which the work in this thesis is built and giving an overview of the experimental apparatus used to collect data for this thesis – the LHC and the ATLAS detector. The tireless efforts that went into building the Standard Model, the ATLAS detector and LHC are a result of many years of hard work by many notable scientists – none of which are the author.

The calibration described in Chapter 4 was carried out by the author under the supervision of the ATLAS flavour-tagging calibration sub-group. The software used to perform the calibration was adapted from software written by Dr Mark Cooke.

The boosted $Z \to b\bar{b}$ cross section measurement presented in Chapter 5 was performed by the author under the supervision of Dr Andy Buckley and Dr Chris Pollard. The framework used to carry out the fully Bayesian unfolding was written by Dr Chris Pollard. The reweighting required for the data-driven closure test described in Section 5.5.4 was carried out by Dr Andy Buckley. Everything else in this chapter was done by the author.

The signal modelling studies for the $V(H \to b\bar{b})$ search described in Chapter 6 were carried out by the author under the supervision of Dr Valerio Dao, Dr Carlo Pandini and Dr Andy Buckley.

Chapter 1

Introduction

A particle consistent with the Standard Model Higgs boson was observed by the ATLAS and CMS experiments at the Large Hadron Collider (LHC) in 2012 via its $H \to \gamma\gamma$ and $H \to VV$ decay modes [1, 2]. Following this discovery, exploring the properties of the Higgs and its coupling with other particles is very important. In 2017, evidence for the $H \to b\bar{b}$ decay was found in a search where the Higgs boson was produced in association with a vector boson, $V(H \to b\bar{b})$. In this thesis, the study of the signal-modelling uncertainties in this analysis is presented.

A dominant background for many Higgs searches, including $V(H \to b\bar{b})$, is a vector boson produced in association with b-tagged jets ($V + b\bar{b}$). The mis-modelling of this background was a dominant systematic error in the $V(H \to b\bar{b})$ search, therefore improving our understanding of it is a key part of improving the $V(H \to b\bar{b})$ search in the future. It is also a very important process in its own right. It is sensitive to prediction-uncertainties from perturbative QCD, so measurements can help to constrain some of the main associated theory and modelling uncertainties relating to the treatment of the kinematics and amplitude of b-quarks in the initial and final state.

Identifying b-quarks is a crucial aspect of the $V(H \to b\bar{b})$ search and $Z + b\bar{b}$ cross-section measurement presented in this thesis, which is done using b-tagging algorithms. It is very important that the performance of these algorithms is well-understood and correctly modelled by Monte Carlo simulation, therefore calibrations are performed to derive any necessary correction scale-factors. A measurement and subsequent calibration of the b-tagging efficiency in Run-2 data was made using the tag-and-probe method in $t\bar{t}$ events.

Chapter 2 gives a brief overview of the Standard Model of particle physics and how it is used for making cross-section predictions at the LHC. A description of the LHC and the ATLAS detector is given in Chapter 3, as well as how the information from the detector is used to reconstruct physics objects for use in analysis. The calibration of the b-tagging efficiency using the MV2c10 algorithm

for track-jets is presented in Chapter 4. In Chapter 5 the measurement of differential fiducial cross-sections in events where a Z-boson is produced in association with two b-quarks is described. Finally, a description of the signal-modelling studies performed for the $V(H \to b\bar{b})$ search is given in Chapter 6 before closing the thesis with some concluding remarks in Chapter 7.

Chapter 2

Theoretical framework

Over a century of experiments by physicists working to gain insight into the fundamental nature of the world around us has culminated into one of the most precise physical theories: the Standard Model. The Standard Model encapsulates our understanding of the interactions between three of the four fundamental forces of the universe and the currently known particles within it. It is a robust theory which has been tried and tested and yet still holds up to scrutiny.

Despite its resilience, the Standard Model has some flaws. To start off, it does not include gravity; one of the four fundamental forces. This is not a problem for particle physics as gravity's effect can be considered negligible at the subatomic scale, but it does throw into question whether the Standard Model really is the "final say". It also leaves some pertinent questions unanswered. The majority of the matter in the universe is hypothesised to be dark matter, a type of matter inferred from its gravitational effect on the rotation of galaxies [3] and the harmonic structure of the cosmic microwave background, and yet the Standard Model does not offer any clues as to what this is. In the Big Bang an equal amount of matter and antimatter should have been created, yet the universe is made primarily of matter. An explanation for this is CP-violation: a violation of charge-conjugation parity-(CP) symmetry which states that the laws of physics should be invariant under the exchange of a particle and antiparticle, and under a mirror inversion of the physical system [4]. The result of this violation is that particles and antiparticles behave differently. The Standard Model contains sources of CP violation [5], but not enough to explain the remaining matter-antimatter imbalance. These are just a few examples of such questions. Whilst the Standard Model describes what we know very well, it isn't giving us the answers to the unknown.

The work carried out in this thesis focuses on Standard Model processes. In this chapter, the Lagrangian formalism of the Standard Model is presented, before going on to describe how this is used to calculate cross-sections for physics processes at the LHC. To test Standard Model predic-

tions against data, simulations are used which are provided by Monte Carlo event generators. An overview of how these generators work is given in the final section.

2.1 The Standard Model

The Standard Model describes the properties of the known fundamental particles and their interactions with three of the four fundamental forces. The known cohort of particles can be split into two categories according to their spin: fermions, which have half-integer spin, and bosons which have integer spin. Fermions are the fundamental constituents of matter and are comprised of quarks and leptons, the properties of which are summarised in Tables 2.1 and 2.2 respectively. Quarks interact with both the strong force and the electroweak force by virtue of their colour charge and electric charge. Charged leptons interact via the electromagnetic and the weak force, whilst neutrinos which are neutral particles, interact via the weak force only. For each fermion, there exists a corresponding anti-particle. Fermions interact via the fundamental forces through the exchange of force-mediating bosons; the electromagnetic force is mediated by the photon, the strong force is mediated by the gluon, and the weak force is mediated by the vector bosons W and Z. The properties of these bosons are summarised in Table 2.3. Also included is the Higgs boson which is a scalar boson which arises via the Higgs mechanism, described in Section 2.1.3.

The Standard Model is formulated as a quantum field theory. It is a composite gauge theory which is locally invariant under transformations of the $SU(3)_{\mathrm{C}} \times SU(2)_{\mathrm{L}} \times U(1)_{\mathrm{Y}}$ symmetry group. In this formalism, the interactions of the fundamental forces are described using gauge fields and particles are described using quantum fields. An overview of the different components of the Standard Model Lagrangian is given in the following sections and is based on the following References [6, 7, 8, 9, 10], where further details of the material presented can be found.

2.1.1 Quantum electrodynamics

Quantum electrodynamics (QED) describes the interactions between electrically charged fermions and photons via the electromagnetic force. The Lagrangian density describing the interaction is derived by requiring that the Lagrangian density for freely propagating fermion fields, ψ, is locally invariant under gauge transformations of the $U(1)$ symmetry group. This is ensured by defining a gauge-invariant derivative,

$$D_\mu = \partial_\mu + ieA_\mu, \tag{2.1}$$

	Quarks		
Generation	Particle	Mass [MeV]	Charge(Q)
1st	u	2.4	2/3
	d	4.8	-1/3
2nd	c	1.27×10^3	2/3
	s	104	-1/3
3rd	t	171×10^3	2/3
	b	4.2×10^3	-1/3

Table 2.1: A summary of the mass and charge of quarks [11].

	Leptons		
Generation	Particle	Mass [MeV]	Charge(Q)
1st	e	0.511	-1
	ν_e	$< 1.1 \times 10^{-6}$ [12]	0
2nd	μ	105.7	-1
	ν_μ	< 0.17	0
3rd	τ	1.77×10^3	-1
	ν_τ	< 15.5	0

Table 2.2: A summary of the mass and charge of leptons [11].

	Bosons		
Interaction	Particle	Mass [GeV]	Charge(Q)
EM	Photon γ	0	0
Weak	W-boson $W^\pm$	80.39	± 1
	Z-boson Z	91.19	0
Strong	gluon g	0	0

Table 2.3: A summary of the properties of the vector-boson mediators of the fundamental forces included in the Standard Model [11].

where A_μ is the electromagnetic gauge field, the manifestation of which is the photon. This couples to the fermion field with a strength defined by the coupling constant, e. With the addition of a kinetic term describing the interaction between the fermion field and the electromagnetic field, the resulting QED Lagrangian density is

$$\mathcal{L}_{\text{QED}} = -\frac{1}{4}F^{\mu\nu}F_{\mu\nu} + \overline{\psi}\left(i\gamma^\mu D_\mu - m\right)\psi, \tag{2.2}$$

where $F^{\mu\nu}$ is the electromagnetic field strength tensor defined as,

$$F_{\mu\nu} = \partial_\mu A_\nu - \partial_\nu A_\mu. \tag{2.3}$$

There is no photon self interaction term here which reflects the fact that photons are not self-coupling. Such a term would have an analogous form as the gluon-interaction term shown in the next section.

2.1.2 Quantum chromodynamics

Quantum chromodynamics (QCD) describes the interaction of quarks and gluons via the strong force [13, 14]. It is invariant under the $SU(3)_c$ symmetry group, which gives rise to the conserved quantity color charge, c. The Lagrangian density of QCD is derived analogously to QED; the Lagrangian density for free quark fields, ψ_j^f, where f denotes the quark flavour and j denotes its colour charge which can be red, green, or blue, is required to be invariant under an $SU(3)_c$ transformation of colour space. To ensure this, a gauge-invariant derivative, D_{ij}^μ, is defined

$$D_{ij}^\mu = \partial^\mu \delta_{ij} + ig_S t_{ij}^a \mathcal{A}_a^\mu, \tag{2.4}$$

where t_{ij}^a are the Gell-Mann matrices which are generators of the $SU(3)$ group. There are eight generators corresponding to eight gluon fields, $\mathcal{A}_a^\mu$, whose coupling strength with the quark fields is governed by g_S, the strong coupling constant (where $g_s^2 = 4\pi\alpha_s$). The resulting QCD Lagrangian density is defined as

$$\mathcal{L}_{\text{QCD}} = -\frac{1}{4}F_{\mu\nu}^a F_a^{\mu\nu} + \sum_f \overline{\psi}_i^f \left(i\gamma_\mu D_{ij}^\mu - m_f \delta_{ij}\right)\psi_j^f, \tag{2.5}$$

where m_f is the quark mass. The gluon field strength tensor, $F_{\mu\nu}^a$, is defined as

$$F_{\mu\nu}^a = \partial_\mu \mathcal{A}_\nu^a - \partial_\nu \mathcal{A}_\mu^a - g_s f_{abc} \mathcal{A}_\mu^b A_\nu^c, \tag{2.6}$$

where a, b, c denote the colour indices of the gluon fields which can run over their eight degrees of freedom, and f_{abc} are the structure constants of the $SU(3)$ group. The third component of Equation 2.6 represents gluon self-coupling, which is a distinguishing feature of QCD with respect to QED and reflects that $SU(3)$ is non-abelian.

2.1.3 Electroweak theory and the Higgs mechanism

The weak nuclear force and the electrodynamic force can be unified into a single electroweak force which has a $SU(2)_L \times U(1)_Y$ gauge symmetry [15, 16, 17]. The L subscript represents the fact that the weak force couples to left-handed fermions fields only (or right-handed anti-fermion fields), where "left-handed" refers to the particle's chirality. The Y subscript corresponds to the hypercharge quantum number which is the resulting conserved quantity of the $U(1)_Y$ symmetry group.

Using a similar approach to that used for QED and QCD, the Lagrangian density is derived by requiring that the fermion fields are invariant under $SU(2)_L$ and $U(1)_Y$ gauge transformations. The resulting Lagrangian density is defined as

$$\mathcal{L}_{\mathrm{EW}} = \sum_{l=e,\mu,\tau} \mathcal{L}(l) + \mathcal{L}_W + \mathcal{L}_B + \mathcal{L}(q). \tag{2.7}$$

The first term, $\mathcal{L}(l)$, represents the interactions between massless W/Z gauge bosons and leptons. The second and third terms are kinetic terms for the interactions of the vector fields, B_μ and W^i_μ, defined as

$$\mathcal{L}_B = -\frac{1}{4} B_{\mu\nu} B^{\mu\nu}, \quad \mathcal{L}_W = -\frac{1}{4} \sum_i \left(W_{\mu\nu}\right)^i \left(W^{\mu\nu}\right)^i. \tag{2.8}$$

Each physical field representing a vector-boson can be written as a superposition of these fields, the mixture of which depends on the coupling strength of the fields and the weak mixing angle, θ_{w}, as follows

$$\begin{aligned} W^{\pm}_\mu &= \tfrac{1}{\sqrt{2}} \left(W^1_\mu \mp i W^2_\mu \right), \\ Z_\mu &= W^3_\mu \cos\theta_W - B_\mu \sin\theta_W, \\ A_\mu &= W^3_\mu \sin\theta_W + B_\mu \cos\theta_W. \end{aligned} \tag{2.9}$$

So far, the electroweak Lagrangian does not contain mass terms. This is not a problem for photons, as experimental evidence tells us that they are massless. Simply adding these terms by hand to the Lagrangian does not work as this would break $SU(2)_L \times U(1)_Y$ invariance. These terms are generated via the Brout-Englert-Higgs mechanism [18, 19] where an $SU(2)_L$ doublet of a complex scalar field, the Higgs field, ϕ, is introduced. This field is described by the following

Lagrangian density,

$$\mathcal{L}_{\text{Higgs}} = \left(D_\mu \phi\right)^\dagger \left(D^\mu \phi\right) - V(\phi), \tag{2.10}$$

where

$$V(\phi) = \lambda \left(\phi^\dagger \phi\right)^2 - \mu^2 \phi^\dagger \phi, \tag{2.11}$$

is the $SU(2)_L$-invariant scalar potential and μ and λ are scalar constants. When $\mu^2 > 0$, the potential has a minimum centred on the origin. When $\mu^2 < 0$, the potential has degenerate minima given by $\phi_{\text{min}} = \pm\sqrt{-\mu^2/\lambda}$, which are referred to as the vacuum expectation values, v. The shape of this potential is depicted in Figure 2.1. Choosing one of these non-zero minima, a process referred to as spontaneous symmetry breaking, and performing a perturbative expansion of ϕ around it gives $\phi_{\text{min}} = v + H$. This leads to a new Higgs Lagrangian with mass terms,

$$\begin{aligned}\mathcal{L}_{\text{Higgs}} = &\frac{1}{2}\partial_\mu H \partial^\mu H + \frac{1}{4}g^2\left(H^2 + 2vH + v^2\right) W_\mu^+ W^{-\mu} \\ &+ \frac{1}{8}\left(g^2 + g'^2\right)\left(H^2 + 2vH + v^2\right) Z_\mu Z^\mu \\ &+ \mu^2 H^2 + \frac{\lambda}{4}\left(H^4 + 4vH^3\right).\end{aligned} \tag{2.12}$$

Mass terms have only been generated for the vector bosons and there is no photon term, reflecting the fact that the photon is massless. A mass term also arises for the field H introduced by the spontaneous symmetry breaking mechanism, which corresponds to the mass of the Higgs boson. There are no mass terms generated for the fermion sector therefore additional terms must be added to the Lagrangian which are called Yukawa coupling terms. The Yukawa coupling terms in the Lagrangian for each fermion f have the form

$$\mathcal{L}_{\text{Yukawa}} = -G_f \left(\bar{\Psi}_L \phi \Psi_R + \bar{\Psi}_R \phi^\dagger \Psi_L + hc\right), \tag{2.13}$$

where G_f is the Yukawa coupling term, Ψ_L is an isospin doublet of left-handed fermions, Ψ_R is an isospin singlet of right-handed fermions, ϕ is the complex scalar Higgs field, and hc is the hermitian conjugate.

The final term of Equation 2.7 describes the interaction between quarks and the W/Z gauge bosons. In the interaction between W-bosons and quarks (the charged-current interaction), the Cabibbo-Kobayashi-Maskawa (CKM) matrix is introduced which controls the mixing between quark flavours [20, 21]. When a quark propagates "freely" it is said to be in a mass eigenstate whilst when it interacts with the weak force, it is in a weak eigenstate. The CKM matrix describes the transition between these states and specifies the amplitudes of the interactions between quark

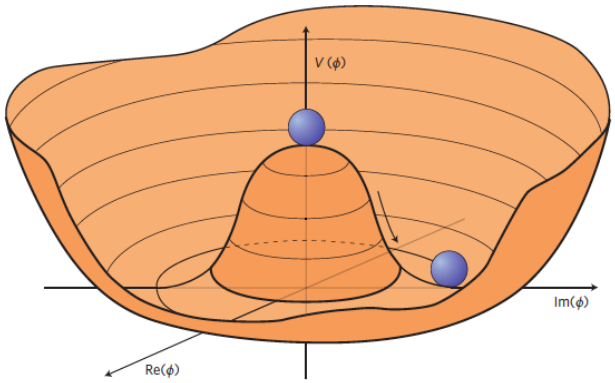

Figure 2.1: A diagram showing the shape of the scalar Higgs potential, $V(\phi)$, for the case when $\mu^2 < 0$. The minima of the potential are $\phi_{\text{min}} = \pm\sqrt{-\mu^2/\lambda}$ and correspond to the points around the lower circle of the "Mexican hat". This diagram was taken from Reference [22].

flavours. These amplitudes have been measured by experiments [11] and their values are

$$V_{\text{CKM}} = \begin{pmatrix} |V_{ud}| & |V_{us}| & |V_{ub}| \\ |V_{cd}| & |V_{cs}| & |V_{cb}| \\ |V_{td}| & |V_{ts}| & |V_{tb}| \end{pmatrix} \approx \begin{pmatrix} 0.974 & 0.224 & 0.004 \\ 0.218 & 0.997 & 0.042 \\ 0.008 & 0.039 & 1.019 \end{pmatrix}. \tag{2.14}$$

This shows that quarks of the same generation have the highest interaction amplitudes, demonstrated by the diagonal elements of the matrix. In particular, the top quark decays almost exclusively to a W-boson and a bottom quark. It is also notable that $|V_{cb}|$ and $|V_{ub}|$ are very small. In practice this means that b-hadrons are long lived as the quark transitions involved in their decay are highly CKM-suppressed.

The CKM matrix can be parametrised in terms of three mixing angles, θ_{ij}, which control the mixing between quarks in generations i and j, and a complex phase, δ,

$$V_{\text{CKM}} = \begin{pmatrix} c_{12}c_{13} & s_{12}c_{13} & s_{13}e^{-i\delta} \\ -s_{12}c_{23} - c_{12}s_{23}s_{13}e^{i\delta} & c_{12}c_{23} - s_{12}s_{23}s_{13}e^{i\delta} & s_{23}c_{13} \\ s_{12}s_{23} - c_{12}c_{23}s_{13}e^{i\delta} & -c_{12}s_{23} - s_{12}c_{23}s_{13}e^{i\delta} & c_{23}c_{13} \end{pmatrix}, \tag{2.15}$$

where $s_{ij} = \sin\theta_{ij}$ and $c_{ij} = \cos\theta_{ij}$. The presence of the complex phase in this matrix is the source of CP violation in flavour-changing weak interactions in the Standard Model [11].

2.2 Proton interactions

Generally in particle physics, and indeed for the analysis presented in Section 5, we are interested in testing the predicted cross-section for a particular physics process. Cross-sections are calculated from scattering amplitudes which represent the transition rate from an initial state to a final state. These scattering amplitudes can be interpreted from a perturbative expansion of the Standard Model Lagrangian density using Feynman diagrams and Feynman rules [23].

The formalism presented so far has dealt with the interactions of fundamental particles however protons are not fundamental particles; they are composite particles made up of quarks and gluons (collectively called partons). As a result, the calculation of the cross-section must take into account the structure of the proton as well as the hard interaction of its partons, which is described in this section. The discussion presented is based on References [8, 24, 9], from which further details can be found.

2.2.1 The running coupling

Divergences due to the inclusion of loop corrections in a calculation can be absorbed via the process of renormalisation, where the parameters of the Lagrangian are redefined such that the divergences are subtracted. This leads to a dependence of the α_s on the scale at which these subtractions take place, the renormalisation scale, μ_R. As a result, the strong coupling exhibits what is referred to as "running" behaviour–its value depends on the scale at which it is being probed. This behaviour is governed by the beta function, which can be expanded as

$$\beta(\alpha_s) = -\alpha_s^2(b_0 + b_1\alpha_s + b_2\alpha_s^2 + \ldots), \tag{2.16}$$

where b_0 is the leading order (one-loop) coefficient and b_1 is the next-to-leading order (two-loop) coefficient. At leading order, the strong coupling coupling constant can be defined as

$$\alpha_s\left(Q^2\right) = \frac{\alpha_s\left(\mu_R^2\right)}{1 + \alpha_s\left(\mu_R^2\right) b_0 \ln\left(\frac{Q^2}{\mu_R^2}\right)}. \tag{2.17}$$

From this equation we see that as $Q^2 \to \infty$, α_s tends to zero; a behaviour which is called asymptotic freedom. In this regime the partons can be approximated as being free, i.e. non-interacting, and perturbation theory is used to make calculations (referred to as perturbative QCD, pQCD). Conversely, as Q^2 decreases towards ~ 200 MeV, the coupling becomes increasingly large. This effect

is called confinement and is the reason quarks are only observed in bound states (hadrons). The exception to this is the top-quark, which decays before confinement takes hold and hence top quarks are also never "seen".

2.2.2 Factorisation theorem

The factorisation theorem can be used to apply our knowledge of quark/gluon interactions to proton interactions. In this formalism, the structure of the proton can be considered as being independent to the hard interaction process. This factorization of these different regimes into less than μ_F and greater than μ_F, where μ_F is the factorization scale, allows us to write the cross-section for a generic collision of protons carrying momentum $P_{1,2}$ as

$$\sigma\left(P_1, P_2\right) = \int_0^1 dx_1 dx_2 \sum_{i,j=q,\bar{q},g} f_i\left(x_1, \mu_F^2\right) f_j\left(x_2, \mu_F^2\right) \hat{\sigma}_{ij} \left(x_1 P_1, x_2 P_2, \alpha_s\left(\mu_R^2\right), \frac{Q^2}{\mu_R^2}, \frac{Q^2}{\mu_F^2} \right). \tag{2.18}$$

where the hard-interaction cross-section between partons i and j carrying momentum $p_{1,2} = x_{1,2} P_{1,2}$ is denoted as $\hat{\sigma}_{ij}$, and $f_{i,j}\left(x_{1,2}, \mu_F^2\right)$ are parton distribution functions (PDFs). These describe the probability that a given parton carries a fraction $x_{1,2}$ of the proton's total momentum. The introduction of the factorisation scale, which defines the boundary between what is considered part of the PDF and what is considered part of the partonic cross-section, means that both the partonic cross-section and the PDF depend on this scale.

As a result of asymptotic freedom, the partonic cross-section can be expressed as a perturbative series in α_s,

$$\hat{\sigma}_{ij} = \alpha_s^k \sum_{m=0}^{n} c^m \alpha_s^m, \tag{2.19}$$

where the c^m coefficients are functions of $x_{1,2}$, and the index m denotes the incremental increase in the series, with each additional term describing real quark/gluon emissions and loop corrections. The index k denotes the leading order at which a specific process contributes. For example, for Z + jets, the minimum order is $k = 1$. In practice this series is often truncated at a fixed order, n, where $n = 0$ is referred to as a leading order (LO) prediction, $n = 1$ a next to leading order prediction (NLO), and so on. There is also a distinction to be made between full NLO, where virtual-loops are accounted for in the calculation, and tree NLO where only real-emission corrections are accounted for. The truncation of the series at a fixed order means that the cross-sections are dependent on μ_R and μ_F, whereas a calculation to all orders would not have this dependence. It is therefore recommended that the effect of varying these scales is taken into account in measurements, and in

theory comparisons with data.

2.2.3 Parton distribution functions

PDFs are not directly calculable from first principles and are therefore derived from fits to experimental data. The PDFs are parametrised as a function of x at a starting scale, Q_0, using a specific ansaetz, and are then evolved to other scales using the DGLAP evolution equations [25, 26, 27], which give the Q^2 dependence of the PDFs. The DGLAP equations are coupled such that the evolutions takes into account the momentum modification resulting from emissions and splitting of the quarks and gluons, where different splitting kernels exist for the different possible splittings of the quarks and gluons.

There is some ambiguity when it comes to the b-quark PDF and indeed heavy-flavour quarks in general, but the b-quark is of particular relevance to the work presented in this thesis. To address this, there are generally two different schemes which are used for calculations. The first is the four flavour number scheme (4FNS) where the b-quark is massive and its PDF is zero. In this scheme b-quarks can only participate in the hard scatter via matrix-element (ME) gluon splitting and they do not enter in the PDF evolution. Conversely, the b-quark may be considered as being massless. In this case the b-quark PDF is not zero meaning there can be b-quarks in the initial state as well as the final state [28]. In general it is not clear which of these schemes is "most correct", therefore calculations are made using both schemes and are compared with the data.

There are a number of different collaborations which perform global PDF fits, such as `NNPDF`, `CTEQ`, and `MSTW`. These groups use different starting ansaetz for the initial parametrisation of the PDF, different data in their fits, and different fitting techniques. This means that the results can differ and it is therefore recommended that the effect of using different PDF sets on a measurement is assessed and an uncertainty assigned for any observed differences.

2.3 Monte Carlo simulation

Monte Carlo (MC) event generators encompass our understanding of the Standard Model and are used to model physical processes, allowing us to compare data to predictions made from theory. This allows us to both check our understanding of the Standard Model and to test beyond-the-Standard-Model (BSM) theories.

Modelling proton-proton interactions typical at the LHC is a challenging task due to the complex nature of the interactions, which is illustrated by Figure 2.2, which shows a schematic diagram of

a proton-proton collision. The colliding protons are shown by the horizontal green lines. The hard partonic interaction occurring between two partons shown in blue is depicted by the central dark red circle. The particles resulting from the hard interaction, depicted in red, undergo showering until they succumb to QCD confinement and hadronise, which is represented by the green ovals. The decay of these hadrons is shown by the green arrows. In parallel to the hard interaction, an additional partonic interaction occurs as shown by the purple oval and purple shower.

The simulation is tasked with providing accurate simulations for these various components of the interaction. It can therefore be broken down into the following steps:

- Calculation of the primary hard interaction using matrix elements,
- Modelling of the parton shower which arises due to QCD radiation from quarks and gluons,
- Hadronisation of the partons into hadrons,
- Describing the additional interactions occurring simultaneously with the hard interaction, referred to collectively as the underlying event,
- Simulation of the detector response to particles interacting with it.

A summary of the matrix element calculation, parton shower model and hadronisation is given below in addition to a description of how these are combined to provide a full prediction. The last two steps are not discussed here and the reader is referred to References [29, 30] for further details.

Matrix elements

Matrix element event generators simulate the central part of the event based on the partonic interaction cross-section described in Section 2.2.2. The partonic cross-section can be expressed in terms of the matrix element, $\mathcal{M}$, which can be interpreted as the sum of all participating Feynman diagrams contributing to the process,

$$\mathcal{M}_{ab\to n} = \sum_i \mathcal{F}^{(i)}_{ab\to n}. \tag{2.20}$$

The matrix element generator performs an integration over the phase space defined by the allowed configurations of the momenta of participating partons, and samples the partons' helicity and colour configurations in order to calculate the cross-section. Monte Carlo integration techniques are particularly well suited to the high-dimensions typical for these phase-space integrations due to their quicker convergence rate with respect to other integration techniques. These calculations can become complex and time consuming at higher orders where virtual and real emissions are included.

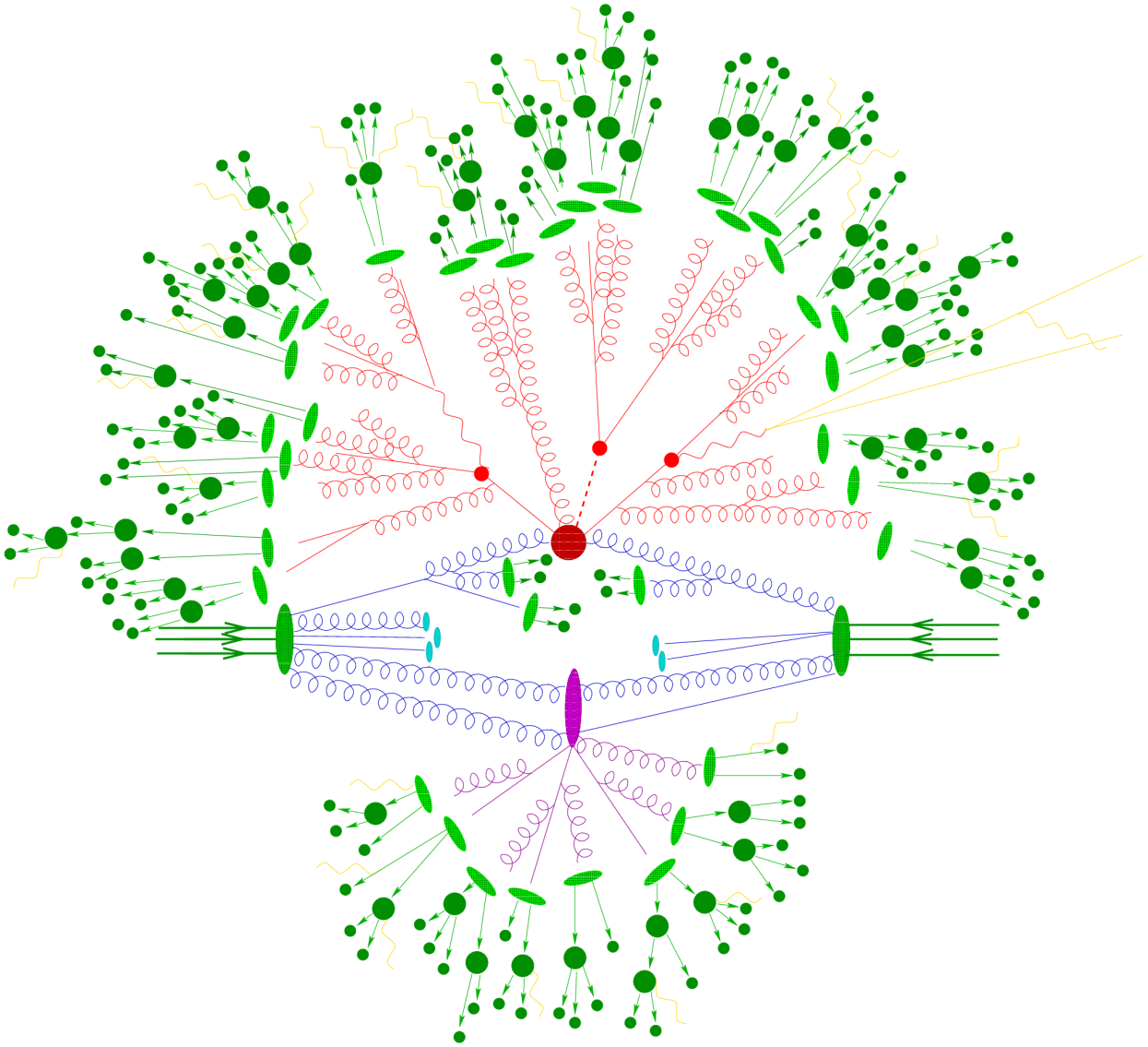

Figure 2.2: A schematic overview of the different interactions happening as a result of a proton-proton collision which are simulated using Monte Carlo generators. This image was sourced from Reference [31].

This is because there can be numerous extra Feynman diagrams contributing to a process and divergences in the calculation arise which must be taken into account. The divergences can also cause sharp peaks in the probability density, which can make sampling of the phase-space inefficient.

Parton showers

A parton shower generator models the soft and collinear branching of quarks and gluons in both the initial state and the final state. The modelling involves the iterative calculation of the probability for a parton a to split to partons b and c, which is described by the DGLAP evolution equations and a set of splitting functions ($P_{a\to bc}(z)$). In order to restrict the branching probability to be ≤ 1, the probability that the parton does not split in a particular iteration of the evolution (i.e between scales Q^2 and Q_0^2) must also be accounted for. This is done via the Sudakov form factor [32] which is added to the DGLAP evolution equations and is defined as

$$\Delta_i\left(Q^2, Q_0^2\right) = \exp\left\{-\int_{Q_0^2}^{Q^2} \frac{\mathrm{d}k^2}{k^2}\frac{\alpha_\mathrm{s}}{2\pi}\int_{Q_0^2/k^2}^{1-Q_0^2/k^2} \mathrm{d}z P_{a\to bc}(z)\right\}, \tag{2.21}$$

where z is the fraction of parton a's momentum carried by the outgoing partons b or c. The DGLAP equations govern the splitting and evolution in the momentum transfer from the momentum scale of the hard process to the scale where QCD confinement takes hold and hadronisation occurs.

Of particular importance for the analysis presented in Chapter 5 is the $g \to b\bar{b}$ splitting function. The general splitting function for a $g \to q\bar{q}$ splitting is defined as

$$P_{g\to q\bar{q}}(z) = T_R\left(z^2 + (1-z)^2\right) \tag{2.22}$$

where $T_R = 1/2$ is a colour factor fixed by convention, and z is the fraction of the gluons momentum carried by the outgoing quarks. This is defined under the assumption of massless quarks however, therefore alterations must be made to take into account the quark masses in the case of $g \to b\bar{b}$ splitting. It is not a priori clear what is the correct way to do this. One option which some generators employ is the so-called quasi-collinear limit [33] which results in an additional term in the $g \to q\bar{q}$ splitting function. It is also not clear what scale should be used for α_s in the splitting. Generally the relative p_T of the quarks is used, but an alternative option could be their mass, or a combination of the two [34]. Measurements of $g \to b\bar{b}$ splitting can help inform the choice of scale.

Hadronisation

When the momentum transfer of the partons reaches the scale of QCD confinement, pQCD ceases

to be a good basis and hadronisation occurs. The hadronisation models which govern this transition of coloured particles to hadrons can be split into two categories: string models [35] and cluster models [36]. In the string models, as two quarks are pulled apart, their potential energy increases due to QCD confinement until it is high enough that a new pair of quarks is created from the vacuum. In the cluster model, clusters are formed from colour-connected pairs of quarks which are formed from $g \to q\bar{q}$ splitting. The string model is the nominal model utilised by the PYTHIA MC generator, whilst cluster models are nominally used by SHERPA and HERWIG. After hadronisation, there can be unstable hadrons remaining which are decayed to stable, final-state hadrons.

Matching/Merging

The matrix element generator and parton shower generators have complimentary strengths: the matrix element is better at modelling hard, well-separated parton topologies whilst parton showers model soft, collinear emissions well. To get a full prediction, we usually combine the results of these generators, taking care not to double count any of the emissions. In practice this a complex and non-trivial procedure therefore a very simplified description is given here, with further details available in Reference [29]. There are two methods used to combine matrix element predictions with parton shower predictions, called matching and merging. A matching method is used by POWHEG, where the hardest emission in the parton shower prediction is corrected to reproduce the matrix element. In the merging procedure, the phase space is sliced such that one region is described mainly by the matrix element and the other is described by the parton shower, where the boundary is defined by a choice of scale. Merging algorithms are used by SHERPA, HERWIG and MADGRAPH.

Chapter 3

Reconstruction of physics objects using the ATLAS detector at the LHC

When a particle passes through a detector it leaves a unique signature based on the components of the detector that it interacts with, which allows it to be identified. The work presented in this thesis was carried out using data collected by the ATLAS detector from proton-proton collisions at the LHC. In this section, an overview of the LHC, the ATLAS detector and its components are given. Following this, the identification and reconstruction of particles using the ATLAS detector is detailed.

3.1 The LHC

The Large Hadron Collider (LHC) [37], situated at the European Organisation for Nuclear Research (CERN), is the world's largest particle accelerator. In a tunnel with a circumference of 27 km, which was previously occupied by the Large Electron Positron collider [38], it accelerates two beams of protons in opposite directions using a series of radio-frequency cavities. Superconducting magnets are used to bend the beams and stabilise their trajectory. The protons collide at several defined interaction points at a centre of mass energy of 13 TeV. It is also capable of colliding lead ions but for the purposes of this thesis, its function as a proton-proton (pp) collider is described.

Protons produced from ionised hydrogen first enter the LINAC2 which is a linear accelerator. Here the protons are accelerated to 50 MeV before being delivered to the Proton Synchrotron Booster (PSB). The PSB splits proton bunches into stacks of circular synchrotron rings and accelerates them to an energy of 1.4 GeV. The bunch structure required for the LHC is a maximum of 2800 proton bunches separated by 25 ns. The protons from the PSB are directed to the Proton

Synchrotron (PS) which arranges them to match the LHC bunch structure and accelerates the protons to 25 GeV. At this point they are brought to the injection energy of 450 GeV at the Super Proton Synchrotron (SPS) before being injected into the LHC beam pipes. This process is shown schematically in Figure 3.1.

At the interaction points situated around the LHC ring are the four main experiments: ATLAS , CMS, LHCb, and ALICE [40, 41, 42, 43]. The ATLAS detector is the largest of the two general-purpose detectors, the other being CMS. The work for this thesis was carried out using data collected from the ATLAS detector, which is described in Section 3.2.

3.1.1 Luminosity

It is important to know the integrated luminosity of the dataset used in analyses. The instantaneous luminosity, defined as the ratio between the rate of a process and its cross section, is expressed as

$$\mathcal{L} = f_r n_b \frac{N_1 N_2}{4\pi\sigma_x\sigma_y}, \tag{3.1}$$

where f_r is the beam revolution frequency, n_b is the number of bunches, $N_{1,2}$ are the respective number of protons in each beam, and $\sigma_{x,y}$ define the transverse profile of the beam. The beam profile is calibrated using Van-der-Meer scans, where the beams are scanned across each other in the transverse plane and the interaction rate as a function of the beams' transverse separation is measured [44, 45]. From this, the total integrated luminosity, L, can be calculated as

$$L = \int \mathcal{L} \mathrm{d}t. \tag{3.2}$$

Figure 3.2 shows the accumulation of integrated luminosity during 2015 and 2016 of the LHC Run-2 [46], the dataset used by analyses presented in this thesis. The plot shows a comparison of the luminosity delivered by the LHC and the luminosity recorded by the ATLAS detector. The recorded data undergoes further processing to ensure that the reconstructed physics objects are of good quality for physics analysis. Following this, the total integrated luminosity available for analysis from this period was $36.1 \pm 1.2\ \mathrm{fb}^{-1}$.

3.1.2 Pile-up

For a given bunch-crossing there is typically one hard interaction of interest. Since there are around 100 billion protons per bunch, multiple soft pp interactions can happen simultaneously with the

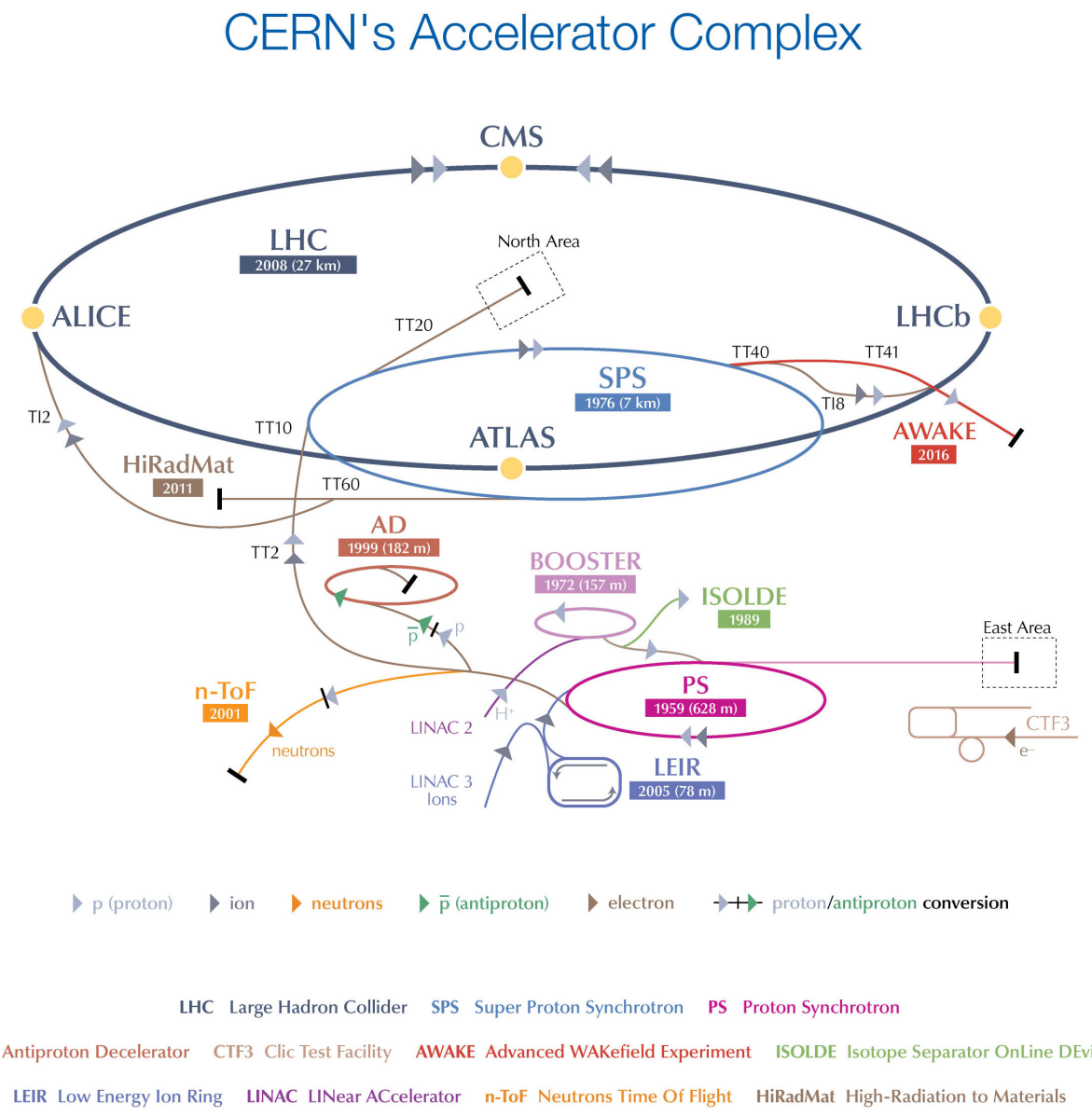

Figure 3.1: A diagram showing the LHC accelerator and injection chain at the CERN accelerator complex taken from Reference [39].

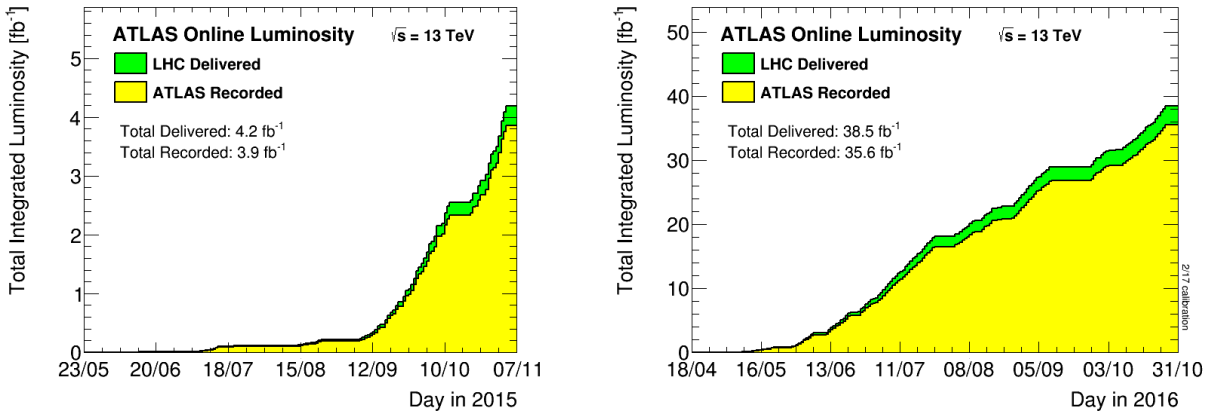

Figure 3.2: The integrated luminosity accumulated during each day of the 2015 and 2016 data taking periods of Run-2 at the LHC. The green plot shows the luminosity delivered by the LHC and the yellow plot shows the luminosity recorded by the ATLAS detector, which differs due to data-taking inefficiencies in the detector [46].

hard interaction, which is referred to as pile-up. These additional interactions make it difficult for analyses to identify the hard interaction of interest. The average number of pile-up interactions, μ, is defined as

$$\mu = \frac{\mathcal{L}\sigma}{n_b f_r}. \tag{3.3}$$

The average number of pile-up interactions per bunch crossing was calculated for data collected in 2015 and 2016 of Run-2 of the LHC and is shown in Figure 3.3 [46]. Simulated samples used in analysis are reweighted such that their simulated pile-up profile matches the profile measured in data.

3.2 The ATLAS detector

The ATLAS (A Toroidal LHC ApparatuS) detector is the largest experiment at the LHC and in fact is the largest particle detector ever built, with a length of 46 m and a width of 25 m. It is a general purpose detector designed to investigate a wide range of physics from precision measurements of SM processes, to searches for new physics. This section provides a brief overview of the detector, with a complete description available in Ref [40].

ATLAS has a cylindrical geometry around the beam pipe and forward-backward symmetry with respect to the collision point at its center. Its main subsystems are arranged in concentric cylindrical layers around the beam pipe and can generally be split into two regions: the central barrel

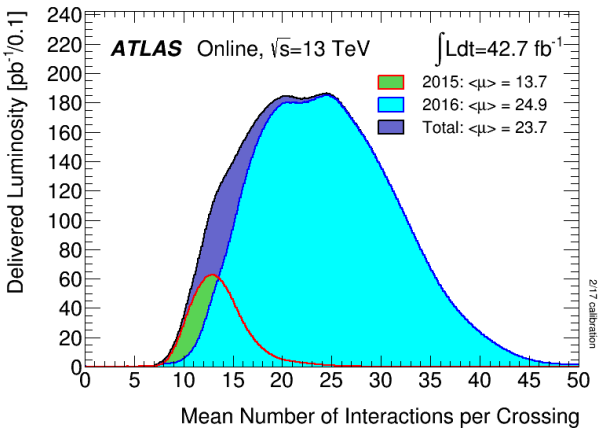

Figure 3.3: The luminosity delivered as a function of the average number of pile-up interactions per bunch crossing for data collected during the 2015 and 2016 data taking periods of Run-2 at the LHC [46].

region which is parallel to the beam-line and the end-caps which are perpendicular to the beam-line. The subsystems used for particle detection are the inner detector, the calorimeters, and the muon spectrometer, with their respective layout depicted in Figure 3.4.

Each subsystem has an important role to play in the reconstruction of physics objects. Figure 3.5 shows examples of the subsystems involved in the detection of different particles. An overview of these systems is given in the following sections, followed by further details of how they are used to reconstruct particles in Sections 3.3 to 3.6.

3.2.1 Coordinate system

ATLAS uses a right-handed coordinate system where the origin is situated at the nominal interaction point in the centre of the detector, the z-axis is aligned along the beam line, the y-axis points vertically (upwards) and the x-axis points horizontally to the centre of the ring. Being transverse to the beam-line, the x-y plane is defined as the transverse plane. Cylindrical coordinates are used to reflect the geometry of the detector: the azimuthal angle around the z-axis is described by ϕ; the polar angle with respect to the beam-line is described by θ; the radial distance from the centre of the detector in the transverse plane is described by r.

The momentum of a physics object is $\vec{p} = (p_x, p_y, p_z)$, where p_x, p_y, p_z are the components of the momentum in the x, y, and z direction. The transverse momentum of an object, p_{T}, will be used most often in this thesis and is the projection of the momentum in the transverse plane, $p_{\mathrm{T}} = p \sin\theta$.

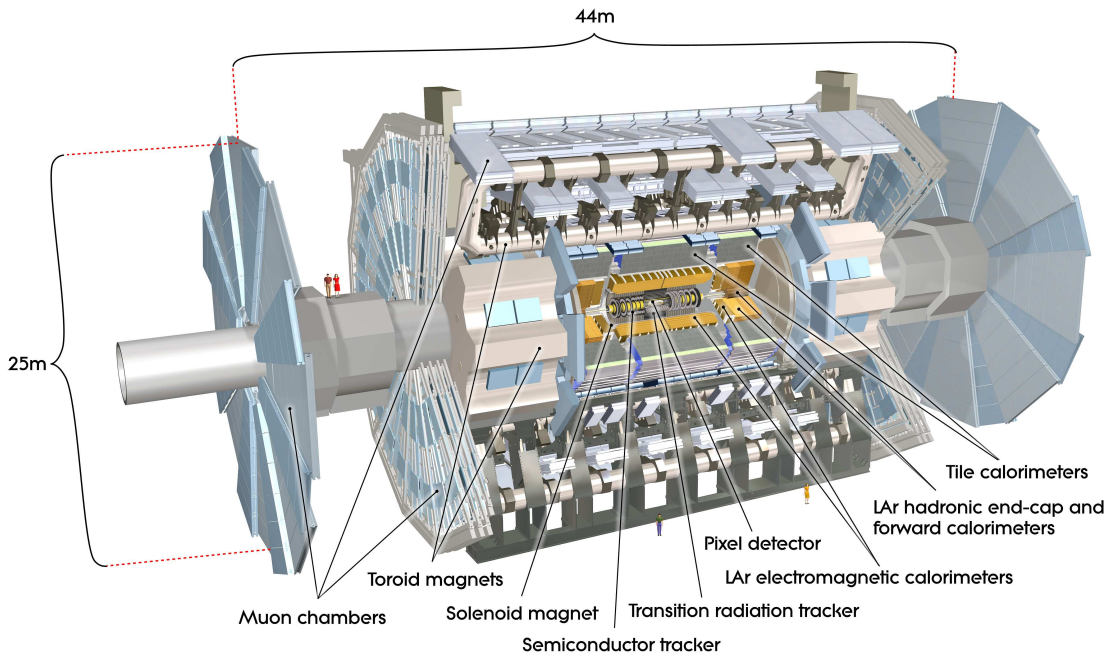

Figure 3.4: A diagram of the ATLAS detector labelling its main components, the majority of which are described in more detail later in the chapter [40].

A transformation of the polar angle, pseudorapidity, η, is defined as

$$\eta = \log\left(\tan\left(\frac{\theta}{2}\right)\right). \tag{3.4}$$

In the case of a massless particle, the pseudorapidity becomes equivalent to rapidity, y. Differences in rapidity are Lorentz invariant under boosts along the z-axis. This is especially important at hadron colliders because since hadrons are composite particles, the momentum of their interacting constituents is unknown. If one of these constituents has significantly more momentum than the other, the decay products will be boosted with respect to the lab frame. It is convenient to shift to the centre-of-mass frame of the constituent collision, hence it is important to use variables which transform well under this shift. The rapidity is defined as

$$y = \frac{1}{2}\log\frac{E + p_z}{E - p_z}. \tag{3.5}$$

A particle travelling perpendicular to the beam-line has $\eta = 0$, whilst a particle travelling parallel to the beam-line has $\eta = \infty$. The spatial separation between particles, ΔR, is defined as $\Delta R = \sqrt{\Delta\eta^2 + \Delta\phi^2}$.

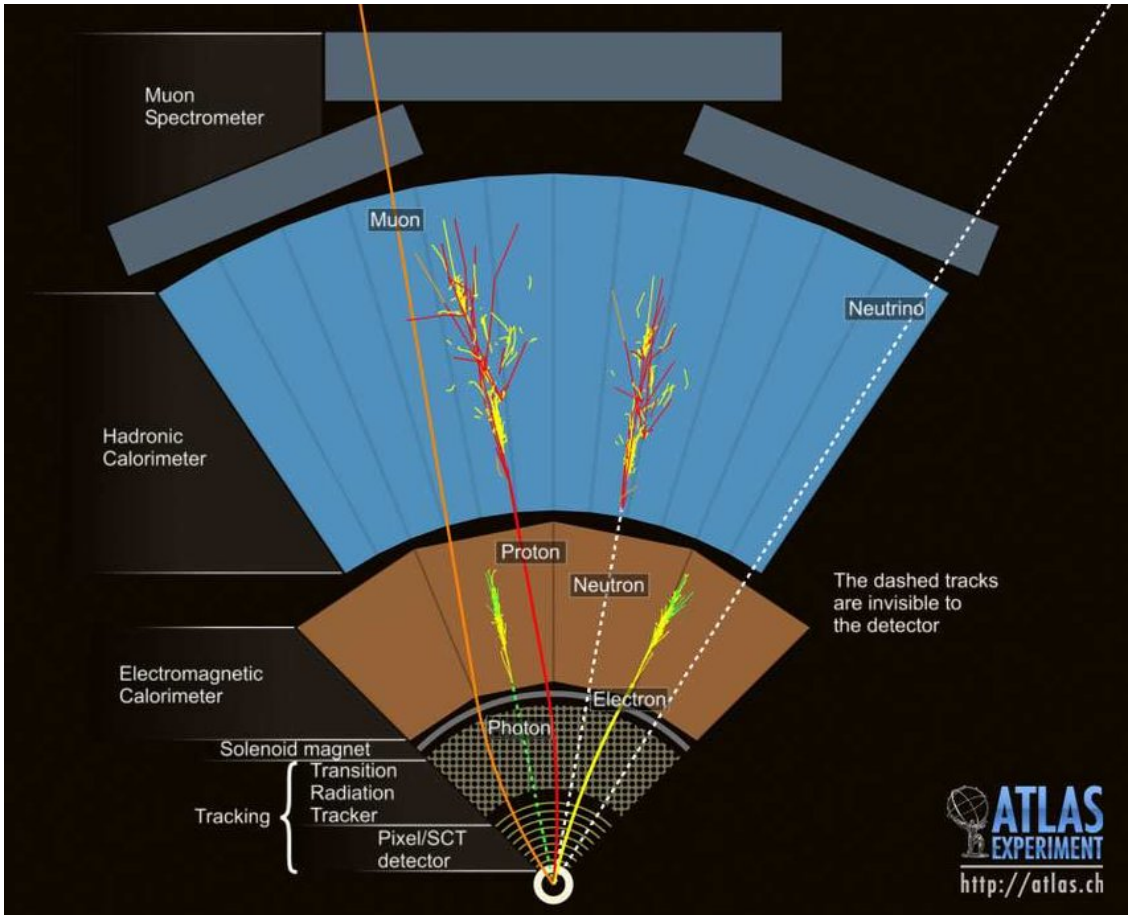

Figure 3.5: A diagram of the components of the ATLAS detector involved in the detection and reconstruction of different particles taken from the ATLAS public web page (http://atlas.ch). The muon passes through each layer of the detector before reaching the muon spectrometer, which is the outermost layer of the detector. The photon and electron are both stopped by the electromagnetic calorimeter, but the electron has a curved trajectory due to its charge and the magnetic field created by the solenoid magnet. Similarly the proton and neutron are both stopped in the hadronic calorimeter but can be distinguished by the fact that the proton has a curved trajectory.

3.2.2 Inner detector

The inner detector (ID) is the innermost sub-detector and is used to reconstruct the tracks of charged-particles and vertices in an event [47]. It is situated between the beam pipe and the calorimeters at a radius of up to 1.1 m and covers the range $|\eta| < 2.5$. A surrounding solenoid magnet immerses the ID in a 2 T magnetic field which bends the trajectory of a charged particle as it traverses the detector. The points at which each particle interacts with the detector material, referred to as hits, are fitted to reconstruct the particle's trajectory. The curvature of the track is used to estimate the charge-to-momentum ratio of the particle. The ID is made up of four independent sub-systems: the insertable B-layer (IBL), the pixel detector, the semi-conductor tracker (SCT), and the transition radiation tracker (TRT), with their layout shown in Figures 3.6 and 3.7.

The innermost layer is the IBL which is situated between the inner layer of the pixel detector (the B-layer) and the beam pipe at a radius of 33 mm [48]. It is a pixel layer which was added during the long shut down of the LHC before Run-2 to preserve the lifetime of the B-layer, which is highly susceptible to radiation damage. This preserved the b-tagging and tracking performance of the ATLAS detector, whilst also improving the precision of vertex-finding (vertexing) and tagging by providing an additional measurement closer to the interaction point.

The next layer of the ID is the pixel detector which covers radii between $40 < r < 140$ mm. It is a high-precision detector composed of three layers of silicon pixels in both the barrel and the end-cap regions. Together with the IBL, it is designed to provide measurements as close to the interaction point as possible and hence determines the impact-parameter resolution of a particle, making it a vital component for the identification of b-hadrons. As an example, the expected transverse impact-parameter resolution for a pion with $p_{\mathrm{T}} = 200$ GeV is approximately 10 µm. The pixel and IBL together provide four precision measurements of a particle's track.

The SCT is situated in the intermediate radial range of the ID, covering radii between $300 < r < 520$ mm. It is a silicon strip detector with four layers in the barrel region and nine in the end-cap. The SCT provides a further four complementary precision-measurements of the track and thus contributes towards the measurement of momentum, impact parameter & vertex position, and pattern recognition.

The outermost layer of the ID is the TRT which is both a straw-tube tracker and transition-radiation detector. The TRT extends between radii of $560 < r < 1080$ mm. The straw tubes are filled with xenon gas, which is ionised by charged particles in the detector. The gaps between the straws are filled with a mixture of gases which have a varying refractive index, causing particles to radiate photons. Electrons radiate more photons than hadrons which aids in their identification. The TRT is designed to allow continuous tracking of particles with up to 36 measurements of a

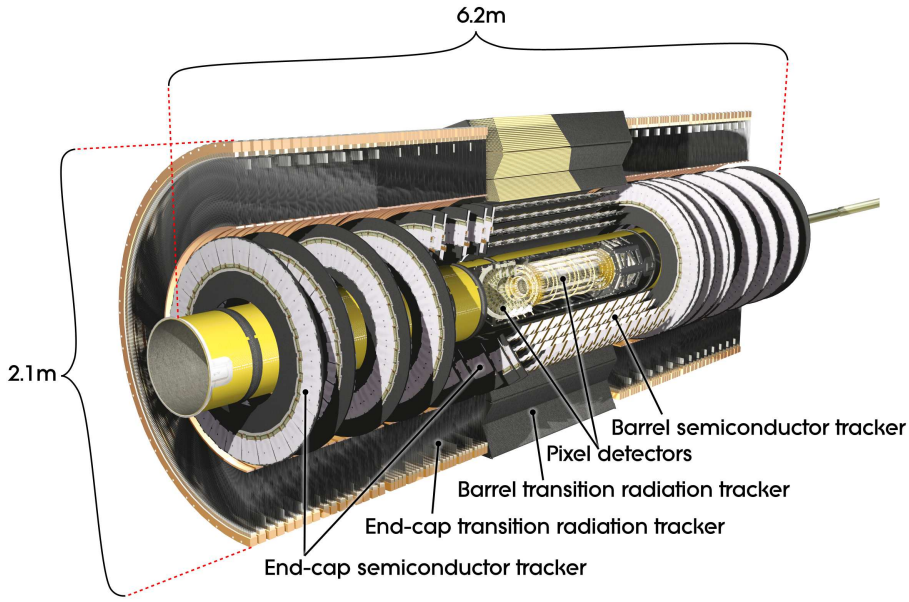

Figure 3.6: Diagram of the ATLAS inner detector labelling its main components [40].

track. The large number of measurements compensates for their reduced precision and aids track pattern-recognition.

3.2.3 Calorimeters

The calorimeters are situated outside of the ID and their purpose is to measure the energy of particles by entirely stopping them, whilst the ID is designed to absorb as little energy as possible. There are two categories of calorimeter: the electromagnetic calorimeter (ECAL) which is designed to measure the energy of electrons and photons, and the hadronic calorimeter (HCAL) which is designed to measure the energy of hadrons [40]. Their layout is depicted in Figure 3.8.

The ECAL is a high-granularity liquid argon (LAr) sampling calorimeter which covers the pseudorapidity range $|\eta| < 3.2$. The ECAL uses liquid argon as the active material for particle detection and lead as the particle absorber. It has an accordion geometry which ensures complete symmetric coverage in ϕ, as shown in Figure 3.9. Electromagnetic (EM) particles undergo bremsstrahlung after interacting with the lead, initiating an EM shower. The evolution of this shower is characterised by the calorimeter's radiation length, X_0, which is defined as the distance over which the EM particle loses all but $1/e$[1] of its energy. An important design requirement for the calorimeter was that it must provide adequate containment of the shower, therefore the length of the ECAL is

[1] This is the exponential e, not the electron charge

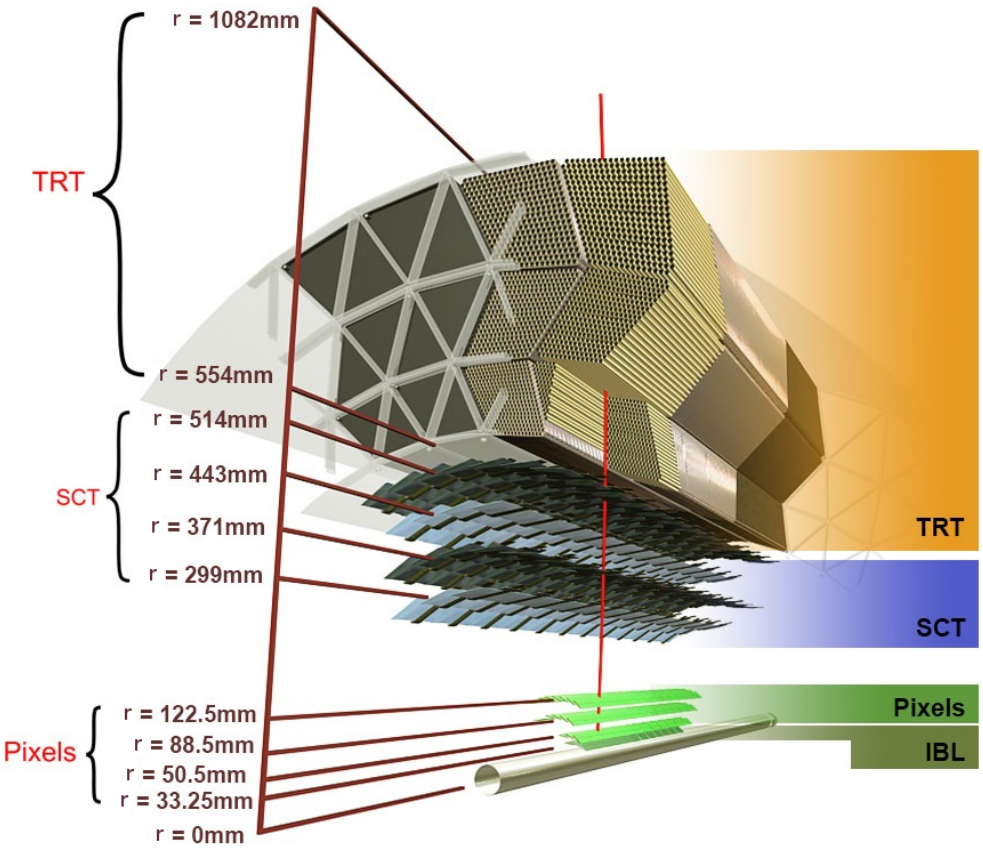

Figure 3.7: Additional diagram of the ATLAS inner detector showing the radii of its various components in the barrel region [49].

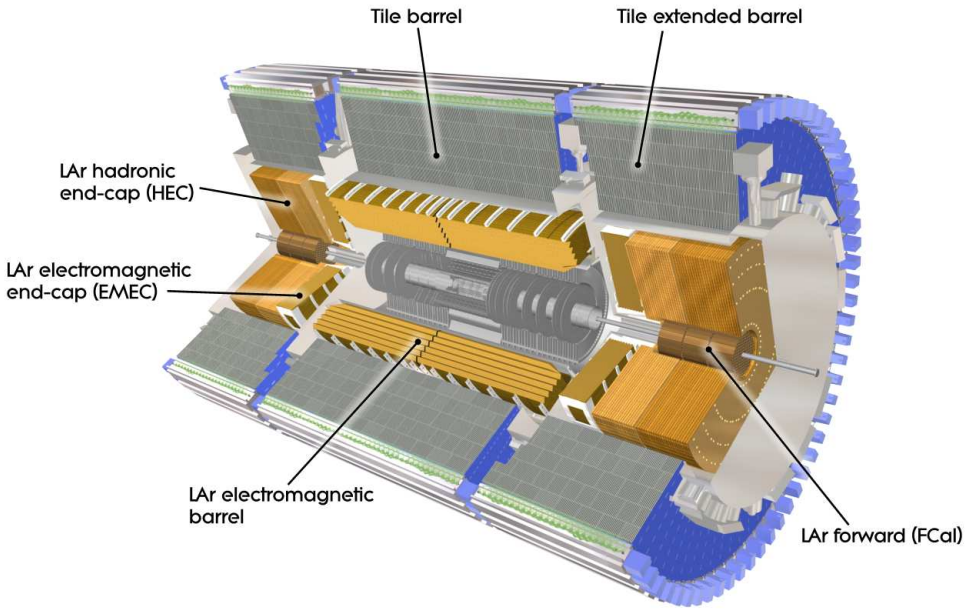

Figure 3.8: Diagram of the ATLAS calorimeters labelling their main components [40].

at least $22X_0$ in the barrel region and $24X_0$ in the end-caps.

The HCAL is comprised of a scintillator-tile calorimeter covering $|\eta| < 1.7$ in the barrel region, LAr calorimeters in the end-caps covering $|\eta| > 1.5$, and additional LAr calorimeters in the end-caps providing coverage in the forward region up to $|\eta| < 4.9$. In the tile calorimeters, the active material is the scintillating tiles and steel is used as the absorber. Hadrons interact with the calorimeter via the strong force as well as the electromagnetic force. They interact with the steel initiating a hadronic shower. This is characterised by the nuclear interaction length of the material, λ, defined as the distance over which the hadronic particle loses all but $1/e$ of its energy. In addition to measuring the energy of hadrons and containing the hadronic shower, the HCAL has the additional task of limiting the "punch-through" of non-muon particles into the muon system. The HCAL has a depth of approximately 7.5λ in the barrel region. Together with the ECAL, the calorimeter system has a total depth of approximately 9.7λ, which both limits punch-through and provides adequate energy resolution for jet measurements.

3.2.4 Muon spectrometer

The muon spectrometer is the outermost layer of the detector. It is made up of different components designed for measuring the muon tracks and for triggering, which are shown in Figure 3.10. Muons

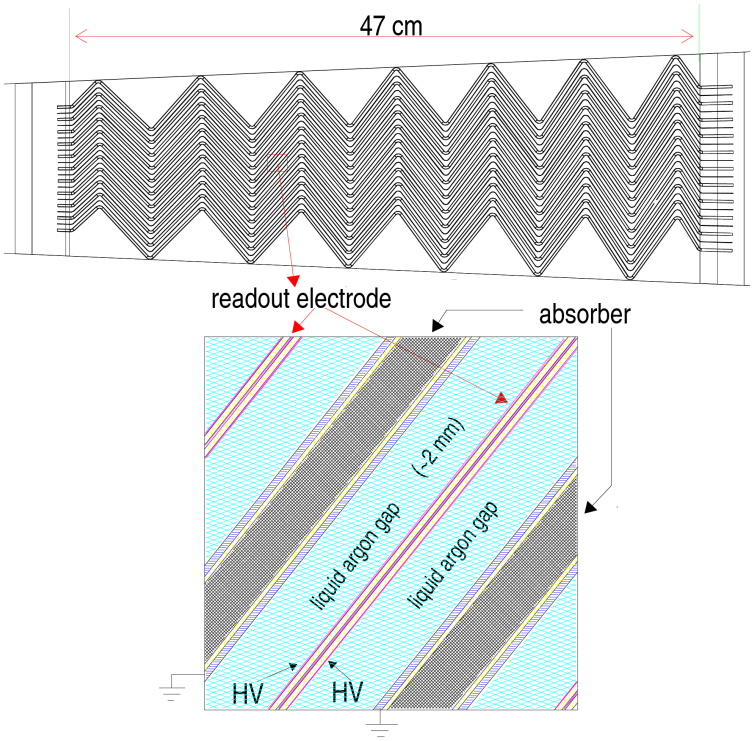

Figure 3.9: Diagram showing the accordion geometry of the ECAL, where the layers of lead absorber and liquid argon are labelled. This diagram is an adaptation of a similar diagram taken from Reference [50].

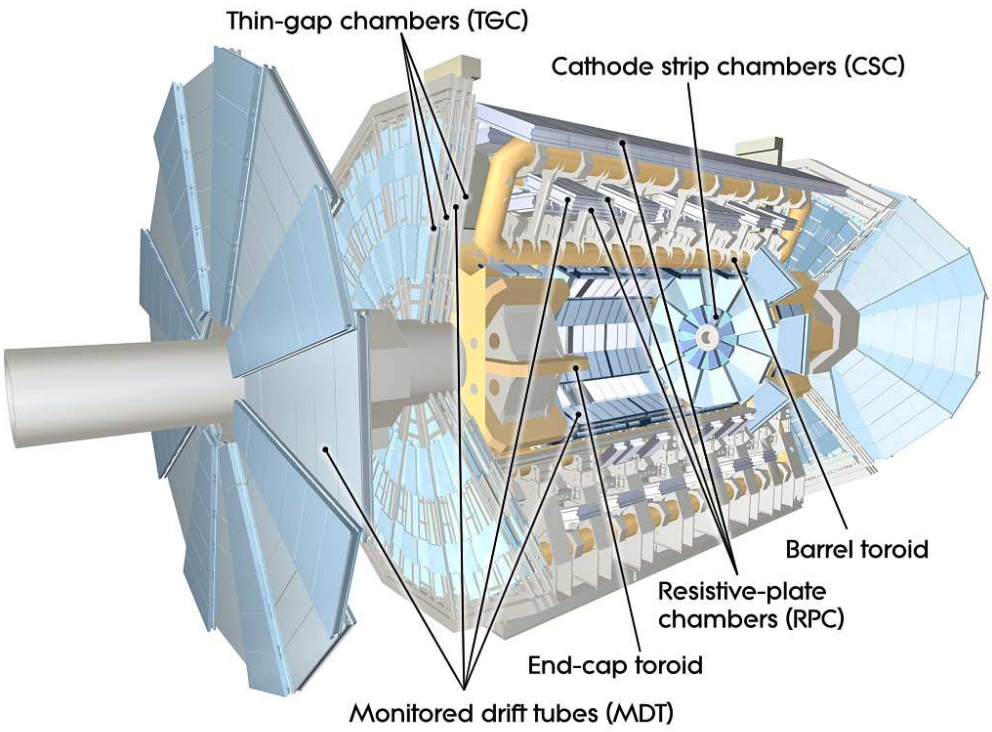

Figure 3.10: Diagram of the ATLAS muon system labelling its main components [40].

have a higher mass with respect to electrons meaning they lose less energy to bremsstrahlung radiation as they pass through the detector. As a result they are expected to be the only detectable particle which can make it through the calorimeter. The spectrometer can provide a momentum measurement with a minimum relative resolution of 10% for muons with $p_{\mathrm{T}} = 1$ TeV going down to 3% for muons with $p_{\mathrm{T}} = 100$ GeV.

Toroidal magnets surround the muon spectrometers, deflecting the muon's trajectory and allowing its charge and momentum to be measured. The components used for the momentum measurement are the monitored drift tube (MDT) chambers and the cathode strip chambers (CSC). These chambers cover the pseudorapidity range $|\eta| < 2.7$, where the MDT chambers cover most of this range and the innermost region (high η) is covered by the CSCs since they have higher granularity and can withstand the higher muon flux and backgrounds [51].

The muon trigger system is made up of resistive plate chamber's (RPC) in the barrel region which cover $|\eta| < 1.05$ and thin gap chamber's (TGC) in the end-cap region which cover $1.05 < |\eta| < 2.4$. Together they provide good spatial and time resolution for fast particle-triggering.

3.2.5 Trigger

There are approximately 40 million events per second occurring in the ATLAS detector; a rate which is far too high to record every event. As such, a trigger system which identifies events of interest for storage is essential. The system is tasked with ensuring that events of interest are recorded with a high efficiency whilst maintaining an appropriate level of background rejection. The system has two levels: the hardware-based level 1 (L1) trigger and the high level trigger (HLT), which is software based. Together these systems reduce the event rate to 1 kHz, the maximum rate for storage.

The L1 trigger is the first stage and reduces the event rate from 40 MHz to 100 kHz with a decision time (latency) of 2.5 μs [40, 52]. The L1 uses information from the calorimeters and muon spectrometers to find interesting features such as high p_{T} particles or large missing/total transverse energy deposits. The L1 identifies regions of interest (ROI) which contain these interesting features, defined by their location in η-ϕ. As well as the coordinate position, the ROI contains information on the type of feature found and the particular pre-defined threshold it passed. These ROIs are passed to the HLT for processing.

The HLT uses a farm of computers to reconstruct events using designated reconstruction algorithms. In the ROI, the HLT uses supplementary detector data at full granularity and full precision to implement selections. The processing is split into two steps; the first being a fast first-pass to reject events and the second being a slow precision reconstruction step [53]. The HLT reduces the event rate from 100 kHz to 1 kHz .

The list of L1 and HLT triggers used in ATLAS constitute the trigger menu. The composition of the trigger menu and the trigger thresholds can be altered to ensure that the HLT output rate does not exceed the 1 kHz limit. To maintain optimal performance of the triggers, the trigger thresholds are modified to account for changes in the instantaneous luminosity. For example, pre-scales can be applied to set a limit on the fraction of events that are accepted by the triggers. The events that are accepted by the trigger system are saved into streams. The "Main" stream is where events used by physics analyses are saved.

3.3 Tracks and vertices

Tracks

A "hit" is the interaction of a particle with a layer of the inner detector. These hits are clustered (clusters) to form space-points which are three-dimensional measurements representing the point at which the particle traversed the ID. A track seed is formed from sets of three space-points orig-

inating from the SCT, the pixel system, or from both. Track candidates are built by combining additional space-points compatible with the track trajectory with the track-seed [49].

A single track-seed can result in multiple track-candidates, therefore it is necessary to resolve any ambiguities by ranking tracks using a score system. The track score is based on the number of clusters it has, the number of holes (an expected cluster which is missing), the χ^2 of the track fit, and its p_{T}. A cluster can be shared by no more than two track candidates, therefore tracks with the highest score are given precedence for keeping the shared cluster. Track candidates are rejected if they have $p_{\mathrm{T}} < 400$ MeV, $|\eta| > 2.5$, and < 7 clusters.

At this point the TRT hits are considered. The track seeded from pixel and SCT hits is extrapolated outwards to find compatible TRT hits. If compatible hits are found and their addition to the track improves its score, the TRT information is added to the track [54].

The track reconstruction efficiency measured in MC simulation as a function of the initial particle's p_{T} is shown in Figure 3.11 which is taken from Reference [49]. At low p_{T}, the track reconstruction efficiency reaches a maximum of around 95% which degrades to between 70% and 90% depending on the number of charged particles in the vicinity of the measured track. Figure 3.11 also shows the track reconstruction efficiency of tracks inside jets as a function of the separation between the track and the jet, $\Delta R(\text{jet}, \text{particle})$. The maximum reconstruction efficiency for these tracks is around 95%. For high-p_{T} jets and low separations corresponding to the centre of the jet where the density of charged particles is high, the efficiency drops to as low as 80%.

Vertices

A vertex seed is found by extrapolating tracks which pass quality criteria back to the beam line to look for an intersection. The vertex seed and the tracks are iteratively fitted and tracks found not to be compatible based on an assigned weight are removed [55]. To find other vertices in the event, this process is repeated for the remaining tracks until there are no more vertices left to be found or no more tracks. The primary hard-scatter vertex is defined as the vertex with the highest sum of its associated tracks' p_{T}^2.

3.4 Electrons

3.4.1 Reconstruction

Electron reconstruction uses information from both the ECAL and the ID. Localised energy clusters in the ECAL are used to measure the energy of the electron, and charged particle tracks measured in the ID are used to define the direction of the electron at the interaction point. The first step

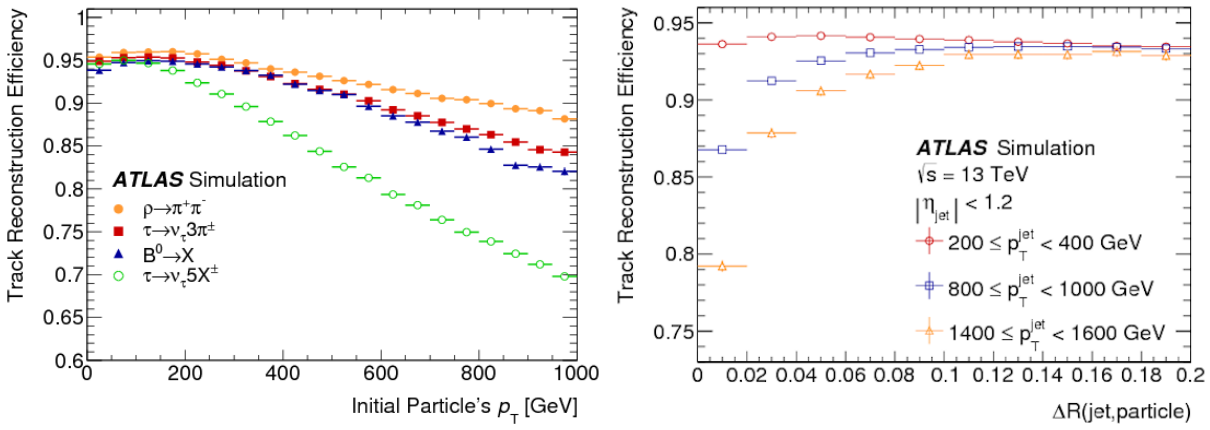

(a) Efficiency vs initial particle p_{T}

(b) Efficiency vs ΔR(jet, particle)

Figure 3.11: The track reconstruction efficiency as a function of a) the initial parent particle p_{T}, where the particular parent particle and decays considered are shown in the legend, and b) the separation between the track and a jet, ΔR(jet, particle), for tracks reconstructed within a jet, where the p_{T} of the jet considered is shown in the legend. These plots were taken from Reference [49].

in the reconstruction is finding the EM clusters, known as seed-cluster reconstruction [56]. The ECAL is divided into a grid of towers, each of size $\Delta\eta \times \Delta\phi = 0.025 \times 0.025$ which matches the granularity of the middle layer of the calorimeter. A sliding-window algorithm is used to find EM cluster candidates [57]. A cluster is formed when the window of size 3×5 towers contains energy deposits with a total transverse energy above 2.5 GeV. The next step is ID track-reconstruction, starting with a pattern recognition algorithm. A pion or electron hypothesis is used to model the energy loss due to bremsstrahlung by default. If a track seed with $p_{\mathrm{T}} > 1$ GeV cannot be extended to a full track with at least seven silicon hits, and it forms within a loosely defined EM cluster ROI, then the electron hypothesis is used allowing up to 30% energy loss per intersection. The track candidates are fit using a χ^2-fitter [58] which resolves any ambiguities relating to tracks sharing hits. A final fitting procedure, an optimised Gaussian-sum filter [59], is applied to better account for bremsstrahlung effects. The final step is applying a matching procedure to the cluster and track. The tracks are considered matched to EM clusters if they are within $\Delta\eta < 0.05$ and $\Delta\phi < 0.05$ of the cluster.

3.4.2 Identification

The signature of prompt electrons can be mimicked by background processes which include electrons from photon conversions, electrons from heavy-flavour hadron decays, and jets which mimic electrons. A likelihood-based identification procedure is used to distinguish the signal electrons

from backgrounds [56]. The probability density functions (pdfs) of discriminating variables in both the signal and background are used to construct likelihoods. The signal and background likelihoods, L_{S} and L_{B}, are defined as

$$L_{\mathrm{C}}(x) = \prod_{i=1}^{n} P_{\mathrm{C},i}(x_i), \tag{3.6}$$

where $\vec{x}$ is the vector of the discriminating variables, and $P_{\mathrm{C},i}(x_i)$ ($\mathrm{C} \in \mathrm{S}, \mathrm{B}$) are the signal/background pdfs for the i'th discriminating variable. Some examples of discriminating variables used in this procedure are track quality, TRT radiation and track-cluster matching. For each electron candidate, these likelihoods are used to form the discriminant, d_{L}, defined as:

$$d_{\mathrm{L}} = \frac{L_{\mathrm{S}}}{L_{\mathrm{S}} + L_{\mathrm{B}}}. \tag{3.7}$$

Working points are defined based on this discriminant. These working points are *Loose*, *Medium*, and *Tight*, where the cut on d_{L} increases between *Loose* and *Tight*. The *Tight* working point gives the highest background rejection at the expense of decreased signal acceptance, whilst the converse is true for the *Loose* working point. The efficiencies of these working points are measured in data using a tag-and-probe method in $J/\psi \to ee$ and $Z \to ee$ events, where one electron is tagged and the efficiency of selecting the other electron/positron is probed. As an example, for an electron with $80 < p_T < 150$ GeV the *Tight*, *Medium*, and *Loose* working points have identification efficiencies of 90%, 94%, and 96% respectively.

3.4.3 Isolation

Electrons from background processes such as heavy hadron decays tend to be surrounded by the other particles from the decay, therefore isolation requirements are enforced on electrons to help distinguish the signal from background [56]. The isolation variables used are:

- $E_{\mathrm{T}}^{\mathrm{cone}}$, which is a calorimeter-based variable and is defined as the sum of the transverse energy of topological clusters (which are defined in Section 3.6.1) found within a cone of radius $\Delta R = 0.2$ around the electron candidate,

- $p_{\mathrm{T}}^{\mathrm{varcone}}$, which is a track-based variable and is defined as the sum of the transverse momentum of tracks passing quality requirements found within a variable radius cone around the electron track. The cone radius is defined by $\Delta R = \min(10/p_{\mathrm{T}}[\mathrm{GeV}], R_{\mathrm{max}})$ and it decreases as the electron p_{T} increases.

Isolation selection criteria, referred to as working points, are defined based on the ratio of these variables with the electron p_{T}. The working points relevant for analyses in this thesis are *Loose*, which is defined such that the efficiency is fixed for uniform electron p_{T} and η , and *Gradient*, which is defined such that the efficiency is fixed for uniform p_{T} but not η. There is an additional working point, *LooseTrackOnly*, which has the same definition as *Loose* but only the track-based isolation variable is used. The isolation efficiencies for the *Loose* and *LooseTrackOnly* working points are 98% and 99% across the whole electron p_{T} range. For the *Gradient* working point, the efficiency is 90% for an electron with $p_{\mathrm{T}} = 25$ GeV, rising to 99% for $p_{\mathrm{T}} = 60$ GeV.

3.4.4 Systematic uncertainties

Electron calorimeter energies are calibrated to the true electron energy in simulation, the details of which can be found in Reference [60]. Any discrepancies between the energy scale and resolution in the simulation with respect to the data are corrected using scale-factors which are used to re-scale the measured energies. There are systematic uncertainties associated with the calibration procedure arising largely from uncertainties in the measurement of the electron energy by the calorimeter. In addition to the calibration, the efficiency of selecting leptons in MC simulation, including reconstruction and application of the isolation and identification working points, is corrected using scale-factors derived from data using the tag-and-probe method in $J/\psi \rightarrow ee$ and $Z \rightarrow ee$ events [56]. In this method, an electron selected using strict identification requirements is considered as the "tag", and the other electron in the event is considered as the probe; efficiency measurements are made on the probe electron. These scale factors also have associated statistical uncertainties and systematic uncertainties arising from the procedure, which are encoded as alternative scale-factors.

3.5 Muons

3.5.1 Reconstruction

Muons are identified in the ATLAS detector using information from the muon spectrometer, the inner detector, and the calorimeters. Muon track reconstruction is performed independently in the inner detector and muon spectrometer. In the muon spectrometer, a candidate track is formed from the combination of track-segments in its different layers. This combination occurs by performing a χ^2 fit to the hits in the segments [61].

Muons can be categorised into four types based on the particular sub-detectors used for its reconstruction:

- *Combined muon (CB)* tracks are formed from a combined fit to the hits from the independent tracks reconstructed in the inner detector and the muon spectrometer.
- *Segment-tagged muon (ST)* tracks are formed from the combination of an ID track and at least one matching track-segment in the MDT or CSC chambers.
- *Calorimeter-tagged muon (CT)* tracks are reconstructed from an ID track which has a matching energy deposit in the calorimeter compatible with a muon.
- *Extrapolated muon (ME)* tracks are reconstructed from only a MS track which is compatible with originating from the interaction point.

The CB muon takes precedence over the other types if there are any overlaps. Other muon types are designed to recover muons which would not have been detected due to their low p_{T} or because they fell in a region of reduced acceptance in the MS, or to extend the reconstruction acceptance past the η limits of the ID.

3.5.2 Identification

A prompt muon is produced at an interaction point and may come from the decay of a W or Z boson, to name a few examples. Muons from other sources are non-prompt and are considered as backgrounds. Sources of these non-prompt muons include the in-flight decays of pions and kaons, a charged hadron punching through the calorimeters and being detected in the muon system, and semi-leptonic decays of heavy-flavour hadrons. A set of identification criteria can be applied to distinguish prompt muons from these backgrounds [61]. The main background comes from the muons originating from in-flight hadron decays, which are characterised by having a bend in their reconstructed track resulting from the displaced decay vertex of the hadron. This bend tends to result in poor fit quality and incompatible momenta measurements made in the MS and ID. Variables which encompass these differentiating features are:

- the q/p significance, which is defined as the absolute difference between the charge (q) to momentum (p) ratio of muons measured in the ID and in the MS, divided by the quadrature-sum of the corresponding uncertainties;
- ρ', defined as the absolute value of the difference between the transverse momentum measurements in the ID and MC divided by the p_{T} of the combined track;

- normalised χ^2 of the combined track fit.

There are also requirements on the number of hits in the ID and MS for a given track. Identification working points are defined based on these variables. These working points are *Loose*, *Medium*, and *Tight*. The *Tight* working point gives the highest background rejection at the expense of decreased signal acceptance, whilst the converse is true for the *Loose* working point. For a muon with a p_{T} between 20 and 100 GeV, the identification efficiencies of the *Loose*, *Medium*, and *Tight* working points are 98.1%, 96.1%, and 91.8% respectively.

3.5.3 Isolation

Prompt muons are mostly produced isolated from other particles in the event which means that measuring the detector activity around a muon candidate can help to distinguish it from background muons [61]. Two variables are defined to serve this purpose:

- A track-based isolation variable, $p_{\mathrm{T}}^{\mathrm{varcone30}}$, which is the scalar sum of the transverse momenta of tracks within a cone of size $\Delta R = \min(10\ \mathrm{GeV}/p_{\mathrm{T}}^{\mu}, 0.3)$ surrounding the muon candidate, where p_{T}^{μ} is the muon's momentum.
- A calorimeter-based isolation variable, $E_{\mathrm{T}}^{\mathrm{topocone20}}$, which is the sum of the transverse energy of topological clusters in a cone of size $\Delta R = 0.2$ around the muon.

Isolation working points are defined using the ratio of these isolation variables to the transverse momentum of the muon itself. The working points relevant to the work presented in this thesis are: *LooseTrackOnly* which is defined by a cut on $p_{\mathrm{T}}^{\mathrm{varcone30}}/p_{\mathrm{T}}^{\mu}$ and is 99% efficient for all η and p_{T}; and *Gradient* which is defined by cuts on $p_{\mathrm{T}}^{\mathrm{varcone30}}/p_{\mathrm{T}}^{\mu}$ and $E_{\mathrm{T}}^{\mathrm{topocone20}}/p_{\mathrm{T}}^{\mu}$ and is 90% efficient at $p_{\mathrm{T}}^{\mu} = 25$ GeV rising to 99% for $p_{\mathrm{T}}^{\mu} \geq 60$ GeV.

3.5.4 Systematic uncertainties

The muon momentum scale and resolution are calibrated such that the MC simulation describes the data correctly. This calibration is carried out in $J/\psi \to \mu\mu$ and $Z \to \mu\mu$ events where a fit is used to extract correction scale-factors, as described in Reference [61]. Systematic uncertainties arise from this procedure which come from varying the parameters of the fit. Similarly, measurements of the reconstruction, isolation, identification and trigger efficiencies are made in data and MC using the tag-and-probe method in $J/\psi \to \mu\mu$ and $Z \to \mu\mu$ events [61]. Any discrepancies found between data and MC are corrected for using scale factors, where systematic uncertainties are introduced by these corrections.

3.6 Jets

3.6.1 Reconstruction

Proton-proton collisions produce a large number of quarks and gluons which immediately hadronise into a collimated shower of particles. These are reconstructed and referred to as "jets". Jets are a very useful tool for approximating the kinematics of the hadronic final states which are typical at the LHC. Jets can be categorised based on their constituents: calorimeter jets are built from energy deposits in the calorimeter and track-jets are built from ID tracks. Truth-jets can also be defined which are built from stable, final-state particles in MC generators.

Specifically, the building blocks of calorimeter jets are topological clusters (topo-clusters) of energy deposits in the calorimeters [62]. The topo-clusters are formed by collecting calorimeter cell signals according to their energy significance, defined as

$$S_{\text{cell}} = \frac{E_{\text{cell}}}{\sigma_{\text{noise, cell}}}, \tag{3.8}$$

where E_{cell} is the energy deposited in the cell and $\sigma_{\text{noise, cell}}$ is the cell's average expected background noise arising from pile-up or electronic noise sources. These components are measured on the EM scale meaning that the energy deposits from electrons and photons are reconstructed correctly but the hadron energy deposits are not.

The algorithm to build the topo-clusters begins by collecting all calorimeter cells with a signal significance passing $S_{\text{cell}} > 4$, which are the seeds. Cells neighbouring a seed which have $S_{\text{cell}} > 2$ are iteratively added until the final neighbours have $S_{\text{cell}} > 0$. Finally, the clusters are corrected to the hadronic scale using a local hadronic cell weighting scheme (LCW) [62]. This is a calibration derived from MC which corrects for: the "non-compensating" nature of ATLAS calorimeters, where the signal for a hadron is lower than that of an electromagnetic particle despite depositing the same energy, and signal losses due to noise-suppression in topo-cluster formation & inactive calorimeter material.

The final topo-clusters are clustered using the anti-k_t jet-algorithm [63] to reconstruct the jets. This is an iterative algorithm which is based on two distance measures defined as

$$d_{ij} = \min\left(k_{ti}^{2p}, k_{tj}^{2p}\right) \frac{\Delta_{ij}^2}{R^2}, \tag{3.9}$$

which is the distance between two clusters, and

$$d_{iB} = k_{ti}^{2p}, \tag{3.10}$$

which is the distance between a cluster and the beam. In these equations, Δ_{ij}^2 is defined as

$$\Delta_{ij}^2 = (y_i - y_j)^2 + (\phi_i - \phi_j)^2, \tag{3.11}$$

where k_{ti} is the transverse momentum of cluster i, y_i is the cluster's rapidity, ϕ_i is its azimuthal angle and R is the radius parameter of the jet. The variable p is a parameter of the algorithm which governs its behaviour. For $p = -1$, the equation represents the anti-k_t algorithm, $p = 1$ corresponds to the inclusive k_t algorithm, and $p = 0$ corresponds to the Cambridge-Aachen algorithm.

The algorithm begins by calculating d_{ij} and d_{iB} for all of the clusters. Cluster i and cluster j are combined if the smallest distance found was d_{ij}. The distances are then recalculated using this new cluster. On the other hand, if the smallest distance was d_{iB}, then cluster i is considered to be a complete jet and is removed from the procedure. This process is continued until all of the clusters have been clustered into jets. The behaviour of the algorithm is such that soft particles tend to cluster with hard particles before they cluster together. This suppresses soft-particles from influencing the shape of the jet, whilst hard particles dominate. In practice this means that jets built using the anti-k_t algorithm are circular, whilst jets built using the k_t-algorithm can have irregular boundaries due to the influence of soft particles. This is demonstrated in Figure 3.12. The benefit of circular jets is that they are compatible with ATLAS jet trigger algorithms.

To reconstruct the track-jets, the anti-k_t jet-clustering algorithm is used as described above but the inputs are ID tracks rather than topo-clusters. There are two different jet collections used in analyses presented in this thesis: $R = 1.0$ calorimeter jets (which are referred to as large-R jets), and $R = 0.2$ track-jets. ATLAS also makes use of calorimeter jets clustered with $R = 0.4$ and "reclustered" jets with $R = 1.0$ which are built from calibrated $R = 0.4$ jets.

3.6.2 Large-R jets

Trimming

At high p_{T}, the jets produced from a two- or three-body decay can start to merge, making it difficult to resolve them using standard $R = 0.4$ calorimeter jets. This effect is generically referred to as "boosting". To capture the decay products, a larger radius of $R = 1.0$ is used during jet reconstruction. However the larger radius of the large-R jet means that it is more likely to be contaminated

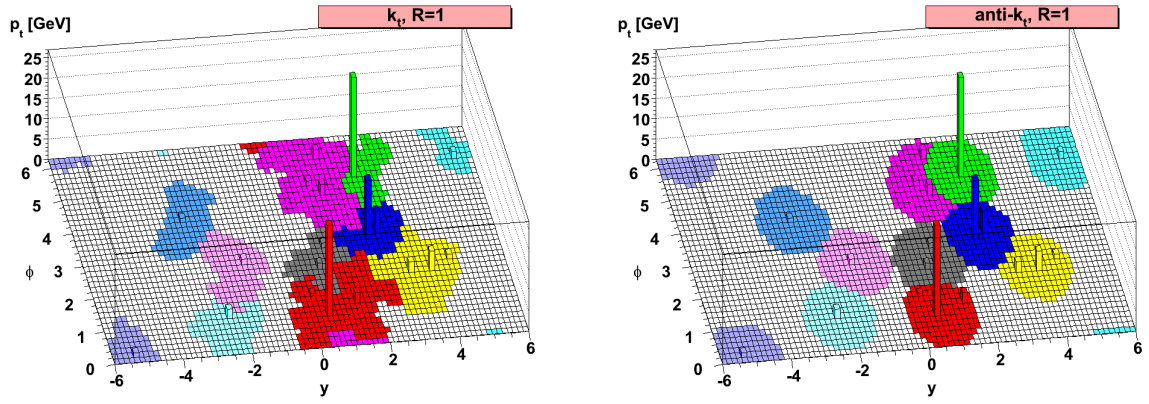

(a) (b)

Figure 3.12: A comparison of jet shapes when built using a) the k_t-algorithm and b) the anti-k_t-algorithm. Jets built using the latter tend to have regular, circular shapes whilst jets built using the k_t-algorithm have irregular boundaries due to the influence of soft-particles [64].

with soft energy clusters originating from multiple partonic interactions within the signal pp collision (the "underlying event"), pile-up interactions, and extra QCD radiation. Since we are primarily interested in the hard-scatter signal process, these soft components must be removed.

The technique used to do this is called "trimming" [65]. The constituents of the large-R jet are re-clustered using the inclusive-k_t algorithm described by Equations 3.9 and 3.10, to build $R = 0.2$ sub-jets. Sub-jets with a p_{T} less than 5% of the p_{T} of the original jet are discarded.

Calibration

A calibration is performed to restore the energy and mass of the jet to the truth jet energy scale. The calibration accounts for effects such as calorimeter non-compensation, where the response of the hadronic calorimeter is lower than the electromagnetic calorimeter, energy deposits which don't pass noise thresholds, and energy deposits which fall outside of the calorimeter acceptance [66].

Firstly, a jet energy scale (JES) calibration derived from MC simulation is applied to the jet which accounts for the calorimeters response to the true jet energy and corrects the jet four-momenta to the particle-level energy scale. Following this, an analogous jet mass scale (JMS) calibration is applied to correct the jet mass to the particle-level mass.

Systematic uncertainties

The large-R jet energy scale (JES) and jet mass scale (JMS) uncertainties are derived by comparing the ratio of kinematic variables (e.g mass or p_{T}) of calorimeter jets to track jets, in data and MC simulation. The ratio

$$r^{p_{\mathrm{T}}} = \frac{p_{\mathrm{T}}^{\text{calo-jet}}}{p_{\mathrm{T}}^{\text{track-jet}}} \tag{3.12}$$

is constructed for both MC and data. Since the track jets and calorimeter jets are affected by uncorrelated systematic effects, the physics – which *is* correlated – can be separated from the detector systematic effects by comparing variables between the two jet collections. The dependence on the double ratio comparing data to MC,

$$R^{p_{\mathrm{T}}} = \frac{r^{p_{\mathrm{T}},\mathrm{data}}}{r^{p_{\mathrm{T}},\mathrm{MC}}}, \tag{3.13}$$

on the variable p_{T} in this example, is used to determine the uncertainty associated with the calibration [67][68].

The uncertainties are split into four components which account for the difference between data and simulation, the parton shower modelling differences, uncertainties relating to the reference tracks used in the ratios, and the statistical uncertainty on the measurement. The uncertainty in the jet mass resolution (JMR) is estimated by smearing the jet mass such that its resolution is reduced by 20%, and for the jet p_{T} resolution (JER), an absolute uncertainty of 2% was recommended [69].

3.7 *b*-tagging

The ability to identify jets containing b-quarks, referred to generically as b-tagging, is of crucial importance for many analyses; two particular examples being described in Chapters 5 and 6. It is made possible by the fact that b-flavoured hadrons have unique decay properties which help to distinguish them from other hadrons. In ATLAS there are three baseline algorithms which exploit these properties. Their distinguishing power is condensed into a single discriminant using a multivariate algorithm, described in Section 3.7.2.

3.7.1 Baseline algorithms

All of the baseline algorithms described in this section use information about the tracks associated to the jet. Tracks are associated to the jet based on their angular separation, $\Delta R(\text{track}, \text{jet})$, where the limit varies as a function of the jet p_{T} to account for the increased collimation of high p_{T} b-

hadron decay products. A track can only be associated to one jet, so if it satisfies the association requirement for more than one jet then it is associated to the closest jet. Tracks are also required to pass quality requirements which differ depending on the particular algorithm being used [70].

Secondary vertex tagger

The main exploited feature of the b-hadron decay is its long lifetime. With a lifetime of around 1 ps, b-hadrons tend to travel distances of order 1 mm before decaying which means it is possible to resolve a second decay vertex displaced from the primary interaction vertex using inner detector tracks. The baseline algorithm which exploits this property is the inclusive secondary vertex (SV) algorithm. The algorithm uses tracks associated to a jet to construct two-track vertices. After discarding vertices consistent with light-hadron decays, these two-track vertices are combined to construct a single vertex. An iterative χ^2 fit is applied to this vertex, which removes incompatible tracks until the vertex passes defined quality criteria. The properties of this secondary vertex can be used to distinguish b-jets from other jets.

Jet fitter

b-hadrons most commonly decay to c-hadrons since the CKM matrix element $|V_{cb}|^2 \gg |V_{ub}|^2$, which means a third decay vertex coming from the c-hadron decay can also be resolved in addition to the secondary vertex. A multi-vertex reconstruction algorithm called jet fitter (JF) reconstructs the full b-hadron decay chain using these vertices and their properties. Properties of the reconstructed decay chain are the resulting discriminating variables from this algorithm.

Impact parameter taggers

Additional features used to distinguish b-jets are the signed impact parameter significances of the tracks in the jets. The impact parameter of a track is defined as its point of closest approach to the primary vertex. There are two components: the transverse impact parameter, d_0, which is measured in the r-ϕ plane, and the longitudinal impact parameter, z_0, which is measured in the z-direction. The impact parameters are signed such that they are positive if the track crosses the jet-axis in front of the primary vertex, and negative if they do not [71]. Their significances are defined as d_0/σ_{d_0} and z_0/σ_{z_0}, where σ_{d_0} is the uncertainty on d_0 and σ_{z_0} is the uncertainty on z_0. Tracks originating from b/c-hadrons tend to have positively signed impact parameters and tracks originating from a b-hadron tend to have a higher average decay length significance compared to those originating

from c-hadrons and light particles. Probability density functions (pdfs[2]) of the signed significances are used to construct likelihood ratios for different jet-flavour combinations. The tagger named IP2D uses only the transverse significances in the pdfs whilst the tagger named IP3D uses both the transverse and longitudinal significances in the pdfs. The output of each likelihood ratio is the resulting discriminating variable from these taggers.

3.7.2 MV2c10 algorithm

Each of the individual baseline algorithms provide a degree of separation between the different flavoured jets, however they are more powerful when they are combined into a single discriminant using a multivariate algorithm. The algorithm and resulting discriminant used for analyses presented in this thesis is MV2c10 [70].

The MV2c10 algorithm uses a boosted decision tree (BDT) trained to discriminate b-jets from c/light- jets using simulated $t\bar{t}$ events. The discriminating variables from the individual baseline taggers are the input parameters to the BDT. In the training sample, b-jets are assigned as the signal and c- and light- jets as the background. The background is composed of 7% c-jets and 93% light-jets [72]. The composition of c- and light-jets in the background can be changed to alter their respective rejection rates. This configuration was chosen as it was found to give sufficient c-jet rejection whilst maintaining high light-jet rejection. At the 70% b-tagging efficiency working point for track-jets, the measured c-jet rejection rate, defined as the inverse of the c-jet tagging efficiency, is 7.09 and the light-jet rejection rate is 119 [73].

A cut on the MV2c10 discriminant corresponds to a particular b-tagging efficiency working point. The BDT is trained separately for each jet collection meaning the values of MV2c10 corresponding to a particular working point differ between jet collections.

3.7.3 Truth-flavour labelling

To check that a jet identified as a b-jet according to the MV2c10 algorithm really was a b-initiated jet, a flavour-labelling scheme where a truth-level hadron is matched to a jet can be used. A final-state, weakly-decaying hadron with $p_{\mathrm{T}} > 5$ GeV is matched to a jet if it is within $\Delta R < 0.2$ of the jet. A hadron may be matched to one jet only therefore the hadron is matched to its closest jet if there is more than one candidate. The jet can therefore be identified as b-initiated if a b-hadron is matched, c-initiated if a c-hadron and no b-hadron is matched, and light if there is no c or b hadron

[2]Note that the lower-case version of this acronym as presented here refers to a generic probability distribution function, whilst the upper-case version of the acronym PDF refers to a parton distribution function

matched to the jet.

3.7.4 Systematic uncertainties

The b-tagging efficiency in simulation is calibrated to the data using scale-factors. For jets which are not b-tagged, an inefficiency scale factor is also applied.The systematic uncertainties associated with the calibration arise due to detector effects and uncertainties from $t\bar{t}$ modelling. Details of the calibration and associated uncertainties are given in Chapter 4.

Chapter 4

Calibration of the *b*-tagging efficiency in track-jets

Many important physics analyses rely on *b*-tagging algorithms to identify *b*-quarks in the final state. These algorithms exploit the unique properties of *b*-hadron decays to identify them within a jet, as described in Chapter 3.7. Their performance is evaluated by measuring the efficiency of the algorithm to select *b*-flavoured jets – referred to as the *b*-tagging efficiency. Since the algorithms are developed and trained using MC simulated events, they may perform differently in the data. To compensate for these potential discrepancies, a calibration is performed to derive per-jet scale-factors which correct the *b*-tagging efficiency in MC, ε_{MC}, to that in data, $\varepsilon_{\text{data}}$. For a tagged jet, the scale factor is defined as

$$s^b = \frac{\varepsilon^b_{\text{data}}}{\varepsilon^b_{\text{MC}}}. \tag{4.1}$$

Scale-factors also exist for un-tagged jets. These are known as inefficiency scale-factors and are defined as

$$s = \frac{1 - s^b \varepsilon_{\text{MC}}}{1 - \varepsilon_{\text{MC}}}. \tag{4.2}$$

The total scale factor for a given MC event is the product of the individual jet scale-factors for each jet in the event.

There are two main methods used to carry out a calibration: the combinatorial likelihood method and the tag-and-probe method. The combinatorial likelihood method uses a likelihood formalism to extract the *b*-tagging efficiency [72]. This leads to a more precise measurement of the efficiency as it retains event-level jet correlations. The tag-and-probe method uses a sample of probe jets to measure the *b*-tagging efficiency. This chapter focuses on the details of the tag-and-

probe method and how it was used to calibrate the b-tagging efficiency of the MV2c10 algorithm in track-jets. The event selection and details of the data and samples used to perform the measurement are given in Sections 4.1 and 4.2. Following this, the use of the the tag and probe method to measure the efficiency is described in Section 4.3. Comparisons between the data and MC predictions and an outline of the systematics uncertainties considered in the analysis are then given, before presenting the results in Section 4.6.

4.1 Event selection

The semi-leptonic decay mode of the top-quark to a b-quark, $t \to Wb$, has a branching fraction of 99.9%. The calibration analysis was therefore performed using $t\bar{t}$ events as they provide an abundant source of b-jets to study. To select these di-leptonic $t\bar{t}$ events, exactly one electron and exactly one muon with opposite charge were required. The opposite-charge and different-flavour requirements reduced contamination from background processes. Similarly the ee and $\mu\mu$ decay modes were not targeted as these suffer from additional backgrounds from $Z+$jets. To target the two b-jets from the $t\bar{t}$ decay, exactly two track-jets were required. At least one of these was required to be b-tagged. Whilst it was initially thought that requiring exactly two track-jets would be a rather strict requirement, it was found that there was roughly a 1:1 correspondence between the number of track-jets in an event and the number of small-radius calorimeter jets. The kinematic requirements on the objects used in the selection are detailed below.

Leptons: The electron was required to be in the fiducial region of the EM calorimeter ($|\eta| < 1.37$, $1.52 < |\eta| < 2.5$) and have $p_{\mathrm{T}} > 28$ GeV. The muon was required to have $p_{\mathrm{T}} > 28$ GeV and $|\eta| < 2.5$. Both the electron and the muon were required to pass the *Medium* identification criteria. They were also both required to be isolated according to the *Gradient* isolation working point. The leptons were required to be identified by single-lepton triggers.

Track-jets: The track-jets were required to have $p_{\mathrm{T}} > 10$ GeV and $|\eta| < 2.5$. For the remainder of this chapter, the track-jets will be referred to generically as "jets".

***b*-tagging:** The b-tagging was performed using the Mv2c10 algorithm, described in Section 3.7.2. The requirement was that the jet must have MV2c10 > 0.6455, corresponding to the 70% b-tagging efficiency working point.

4.2 Data and MC samples

Data collected during Run-2 at the LHC in 2015 and 2016 at centre of mass energy $\sqrt{s} = 13$ TeV were used to perform this calibration. Only events recorded when all components of the detector were fully functioning were used. The data sample corresponds to an integrated luminosity of 36.1 fb^{-1}.

MC samples were used to simulate the signal and background processes. The sources of background considered were single top production in association with a W boson (Wt), which is the dominant non-$t\bar{t}$ process, $Z+$ jets where the Z decays via $Z \rightarrow \tau\tau$, where one tau lepton decays to an electron and two neutrinos and the other tau lepton decays to a muon and two neutrinos, and finally diboson production (WW, ZZ, WZ) where both bosons decay leptonically. The matrix element generators, parton shower generators, and PDFs used to provide simulations for each of these processes are summarised in Table 4.1. In each case, the samples were normalised to the highest cross section available for the given process. In the samples interfaced with PYTHIA8 and HERWIG, the program EVTGEN was used to simulate the decays of bottom and charm hadrons [74]. Each sample was processed using GEANT4 which simulates the ATLAS detector [75]. The $t\bar{t}$ samples listed as "alternative" in Table 4.1 were used to asses systematic uncertainties related to the modelling of the signal, as described in Section 4.5.

4.3 The tag-and-probe method

The tag-and-probe method relies on the expectation that there are at least two b-jets in the event coming from the top-quark decays, as shown in Figure 4.1. As described in Section 4.1, only events with exactly two jets where one of them was b-tagged were selected. The b-tagged jet was defined as the "tag-jet" and the second jet in the event was considered to be the "probe-jet". The b-tagging efficiency measurement was performed only on the probe-jets to avoid any bias from enforcing a tag, but the presence of the tag-jet increased the probability that the probe-jet would also be a b-jet, which helped to achieve high b-flavour purity in the probe-jet sample.

In events where only one jet was b-tagged, the probe-jet was defined as the non b-tagged jet. When both jets passed the b-tagging requirements, they were each considered as probe-jets. It was investigated whether including events with three jets would benefit the analysis, however this resulted in a reduced purity of the probe-jet sample as the extra jets tended to have light or c-flavour, therefore it was decided that the gain in statistics was not worth the reduction in purity. Figure 4.2 shows a comparison of the predicted probe-jet flavour fractions as a function of the jet p_{T} in two-jet

Process	Matrix element	Parton shower	PDF set	Other packages / additional details
		Nominal		
$t\bar{t}$	POWHEG	PYTHIA6	CT10	Perugia 2012 tune $h_{\text{damp}} = m_{\text{top}}$
Wt	POWHEG	PYTHIA6	CT10	Perugia 2012 tune
Diboson	SHERPA 2.1.1	SHERPA 2.1.1	CT10	
Z+jets	POWHEG	PYTHIA8	CT10	
		Alternative		
$t\bar{t}$	MADGRAPH5_AMC@NLO	HERWIG ++	CT10	
$t\bar{t}$	POWHEG	HERWIG ++	CT10	
$t\bar{t}$ (radLo)	POWHEG	PYTHIA6	CT10	Perugia 2012 radLo tune $h_{\text{damp}} = m_{\text{top}}$
$t\bar{t}$ (radHi)	POWHEG	PYTHIA6	CT10	Perugia 2012 radHi tune $h_{\text{damp}} = 2m_{\text{top}}$

Table 4.1: Details of the nominal and alternative samples used to simulate the signal and background processes. The h_{damp} parameter is a variable which controls the cut-off scale for first-gluon emission in the parton shower.

events and three-jet events from different MC samples. This comparison shows that the probe-jet b-purity decreased by around 20% across all of the jet-p_{T} bins. In fact in the three-jet events, the fraction of light-flavour jets even exceeded the fraction of b-flavour jets in the lowest jet-p_{T} bin. In the two-jet events, the b-jet purity reaches a maximum of around 90 %, falling off again at high p_{T}.

4.3.1 Light-jet subtraction and efficiency measurement

The probe-jet sample can be contaminated with light/c-flavour jets due to contributions from background processes, or if the second b-jet from the $t\bar{t}$ decay fell outside of the experimental acceptance. A data/MC comparison of the MV2c10 distribution of probe-jets is shown in Figures 4.3(d) and 4.4, where the contamination of light/c-flavour jets in the data sample can be seen. The probe-jet sample was required to consist only of b-jets for the efficiency measurement, therefore a light-jet subtraction was performed to remove this contamination.

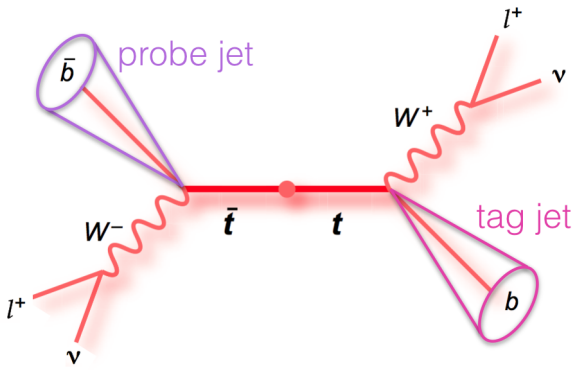

Figure 4.1: A Feynman diagram showing $t\bar{t}$ production and the subsequent decays of the top quarks into b-quarks and W-bosons. The b-quarks are reconstructed as b-jets and selected as either a tag-jet or a probe-jet.

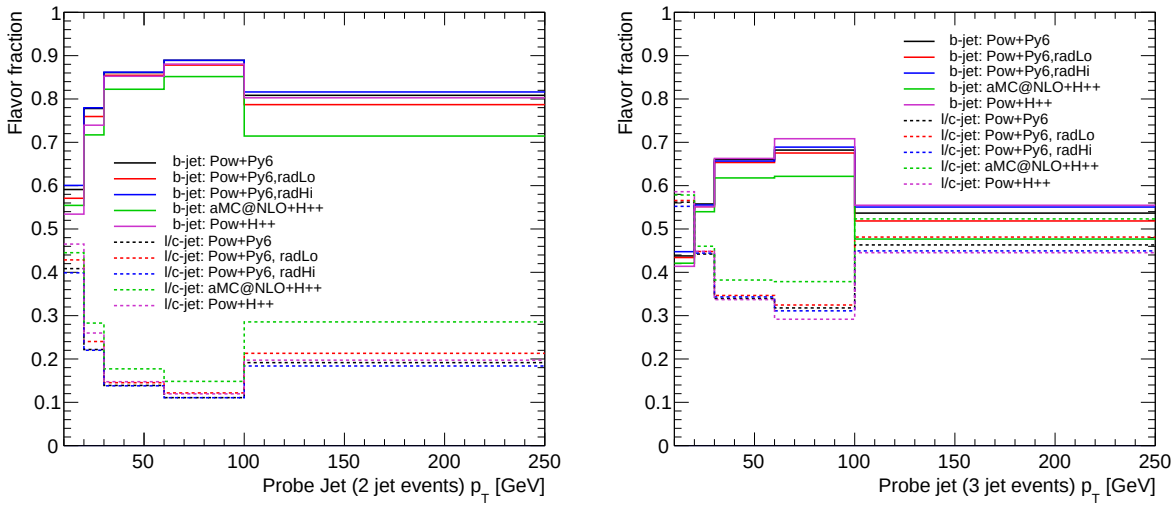

(a) Two-jet

(b) Three-jet

Figure 4.2: The flavour-fractions of the probe-jets as a function of the probe-jet p_{T} in a) two-jet events and b) three-jet events. The probe-jet purity is worse in three-jet events, dropping by approximately 20% in all p_{T} bins. In the two-jet events, the purity increases with jet-p_{T} until around 100 GeV where it flattens and drops off by around 10%.

The light-jets were subtracted from data using the predicted light-jet flavour fraction, $(1 - f_b)$, where f_b is the b-jet purity, measured from the MC as shown in Figure 4.2(a). The subtraction was carried out bin-by-bin in the MV2c10 distribution, where the bin number is denoted by i, according to the following equation:

$$n_i^{\text{corr}} = n_i^{\text{data}} - N_{\text{tot}}^{\text{data}}(1 - f_b)\,\hat{n}_i^{\text{light}}. \tag{4.3}$$

The corrected b-jet yield in data, n_i^{corr}, was obtained by subtracting the light-jet contribution from the original observed number of probe-jets, n_i^{data}. The light-jet prediction was obtained by multiplying together the unit-normalised number of light-flavour jets in MC, $\hat{n}_i^{\text{light}}$, the total number of probe-jets in data across all bins, $N_{\text{tot}}^{\text{data}}$, and the light-jet fraction. The unit-normalised prediction was altered using the total data yield to avoid the results being affected by the absolute MC prediction of the yield.

4.3.2 Measuring the *b*-tagging efficiency

From the corrected sample of probe-jets in data obtained from the light-jet subtraction, the cumulative efficiency as a function of the cut on the MV2c10 discriminant was computed using

$$\epsilon_i = \frac{\sum_{j=i}^{n_{\text{max}}} n_i^{\text{corr}}}{\sum_{j=1}^{n_{\text{max}}} n_j^{\text{corr}}}, \tag{4.4}$$

where $n_{\text{max}} = 50$ is the number of bins in the MV2c10 distribution. The resulting distribution gave the efficiency of selecting a b-jet as a function of the proposed cut on the MV2c10 discriminant. This calculation was carried out for both the data and the MC and any discrepancies between the two were used to derive correction scale-factors to be applied to the MC. The results are presented in Section 4.6.

4.4 Detector-level comparisons

Comparisons between the data and MC prediction for kinematic variables of the physics objects used in the analysis are presented in this section. Figure 4.3 shows the multiplicity of b-tagged jets in each event, and the p_{T}, MV2c10, and η of the probe-jet. From these plots it can be seen that there is good agreement between the data and the MC prediction. The exception to this is the MV2c10 distribution, where disagreement between the data and MC prediction is observed at low values of MV2c10, corresponding to light-flavour jets. This effect was attributed to mis-modelling of the impact-parameter discriminant and its effects were accounted for by the light-jet calibration

scale-factors. Since the mis-modelling occurred for MV2c10 values < -0.4, it had a minor effect on the tag-jet given that the jet was required to have MV2c10 > 0.6455.

The uncertainty bands in these plots correspond to the quadrature sum of the detector modelling uncertainties described in Section 4.5, and the MC statistical uncertainties. Additional lines for the alternative $t\bar{t}$ models are included in the plot. The error bars on the data points are the statistical uncertainties on the data.

4.5 Systematic uncertainties

There were two types of systematic uncertainty considered in the analysis: uncertainties relating to the modelling of the signal, and experimental uncertainties related to the detector performance. The effects of the systematic uncertainties on the scale-factors were assessed via their influence on the predicted light-jet fraction used in the light-jet subtraction procedure described in Section 4.3.1. For each systematic uncertainty, there was a representative varied MC-prediction (either from a different MC sample, or alternative scale-factors applied to the nominal) and hence a varied prediction of the light-jet fraction. The light-jet subtraction procedure was carried out for each of these systematically-varied predictions, and the resulting efficiency was calculated following the procedure described in Section 4.3.2. This resulted in an efficiency for each systematic uncertainty.

For each signal-modelling variation, the absolute difference between the corresponding varied-efficiency and the nominal efficiency was defined as the uncertainty, unless stated otherwise. For the detector-modelling systematics, there were up and down variations for each systematic, corresponding to an increased and decreased effect with respect to the nominal prediction. Varied efficiencies were derived for both the up and down variation, then the maximum difference between the nominal and these variations was taken as the uncertainty. To get the final uncertainty on the scale-factors, each of these components for both detector-uncertainties and modelling uncertainties were added in quadrature. The particular effects considered are described in the following sections.

4.5.1 Signal modelling

Systematic uncertainties relating to the modelling of the $t\bar{t}$ signal were derived using MC-predictions from alternative MC generators. The different aspects of the modelling for which uncertainties were estimated were:

- Parton shower modelling: the uncertainty was estimated using an alternative MC sample

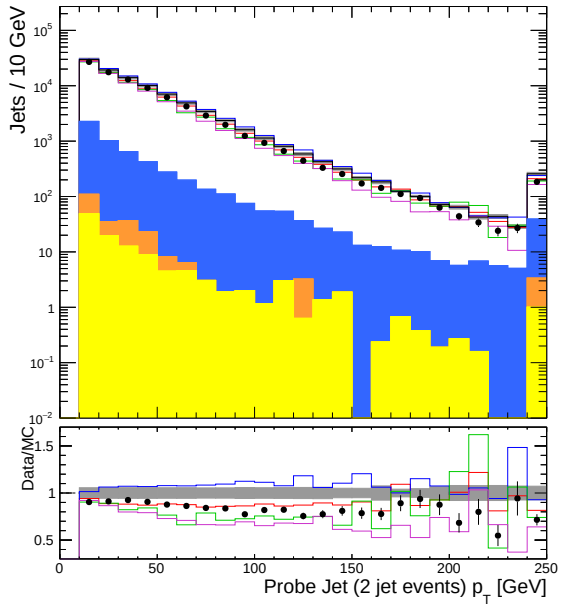

(a) p_T of probe-jets

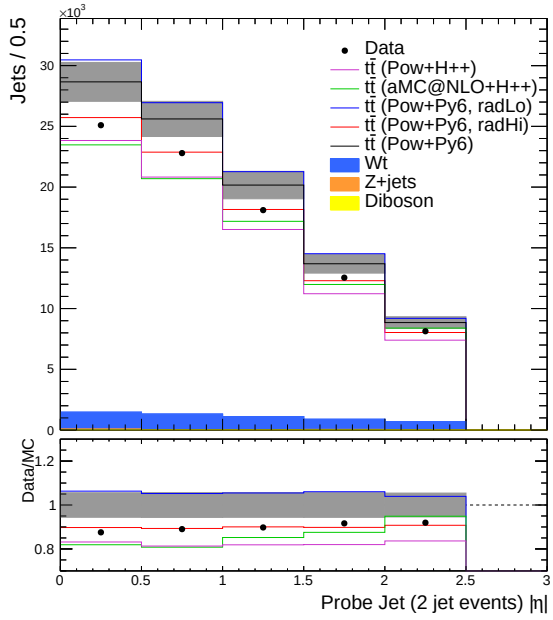

(b) Probe-jet η

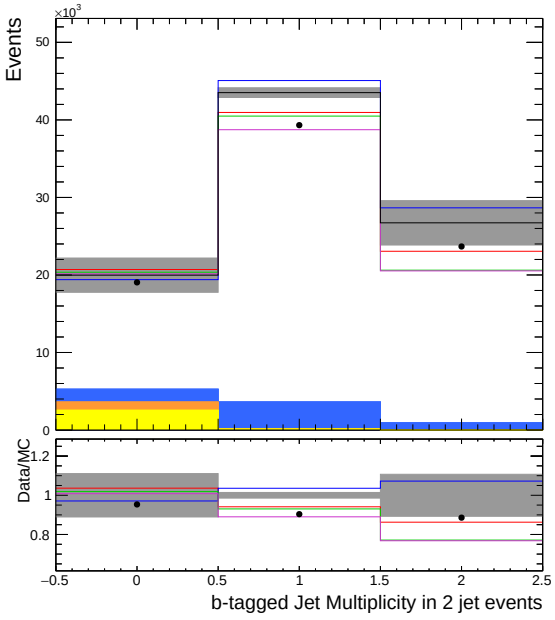

(c) Multiplicity of b-tagged probe-jets

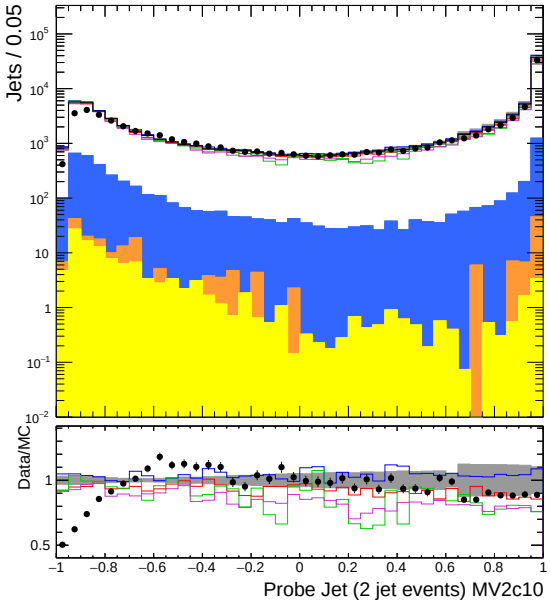

(d) Probe-jet MV2c10

Figure 4.3: Data/MC comparisons of the p_{T}, $|\eta|$, and MV2c10 discriminant of the selected probe jets, as well as the multiplicity of b-tagged jets per event. The grey uncertainty band on the measurement includes systematic uncertainties related to detector effects and MC statistical uncertainties. Alternative $t\bar{t}$ MC predictions are shown by the coloured lines.

with a different parton shower model, POWHEG+HERWIG++.

- Matrix element calculation: the nominal sample used a LO matrix element calculation. To assess the difference when using a NLO matrix element calculation, the POWHEG+HERWIG++ sample was compared to the MADGRAPH5_AMC@NLO+HERWIG++ sample.

- Parton shower radiation: the nominal $t\bar{t}$ sample was compared to similar samples with different tunes which simulated enhanced or suppressed radiation in the parton shower.

4.5.2 Detector uncertainties

Detector uncertainties are considered to reflect our imperfect understanding of the performance of the detector and reconstruction techniques. The aspects of experimental uncertainty considered in this analysis were:

- Light/c-flavour efficiency calibration uncertainties: since the light-jet flavour fraction was a key part of the efficiency measurement, uncertainties relating to the light and c-flavour jet efficiency calibration were assessed.

- Lepton reconstruction effects: uncertainties relating to electron and muon reconstruction were assessed. The specific components considered were uncertainties in the lepton energy/momentum scale and resolution, lepton identification efficiency, lepton isolation efficiency, and the lepton trigger efficiency.

- Luminosity: an uncertainty of 2.1% was assigned for both 2015 and 2016 data, derived by a calibration of the luminosity scale using x–y beam-separation scans, following a methodology similar to that detailed in Reference [76].

- Pile-up: to account for the effects of pile-up, a reweighting was applied to the MC. The uncertainty associated with the pile-up reweighting procedure was evaluated by varying the scale-factors used to perform the reweighting.

4.6 Results

The calibration results were derived as a function of jet-p_{T}. Scale-factors were derived for five jet-p_{T} bins, therefore the MV2c10 distributions were split accordingly into five regions according to

Efficiency working point [%]	MV2c10
60	0.8529
70	0.6455
77	0.3706
85	-0.1416

Table 4.2: The MV2c10 values corresponding to each fixed-cut efficiency working point.

the p_{T} of the probe-jet, as shown in Figure 4.4. The light-jet subtraction described in Section 4.3.1 was then performed in each of these regions to get the "corrected" distributions.

From each of these corrected MV2c10 distributions corresponding to each jet-p_{T} bin, efficiency distributions were derived according the procedure described in Section 4.3.2. From these, the efficiencies at MV2c10 values corresponding to each fixed-cut working point, shown in Table 4.2, were extracted for both the data and MC. These efficiencies were plotted as a function of p_{T} for each working point and are shown in Figure 4.5.

Finally, the scale-factors were derived by taking the data/MC ratio of these efficiencies. The resulting plots are shown in Figure 4.6 and the scale factors along with the breakdown of their uncertainty are given in Tables 4.3 to 4.6. It can be seen that in general all of the scale-factors were consistent with unity across all of the working points, with the exception of the lowest p_{T} bins for the 85% working point. In this case, this is because this working point is most affected by the MV2c10 mis-modelling of light-jets described earlier. For each scale factor derived, the largest contributor to the total systematic uncertainty was the $t\bar{t}$-modelling uncertainty.

These results were an important cross-check for the scale-factors derived using the alternative likelihood calibration method, the results of which are also displayed in Figure 4.6 for comparison. Since it is the more precise method, the likelihood calibration method provides the scale-factors which are used by analyses, however it is important that the results are validated using the tag-and-probe method.

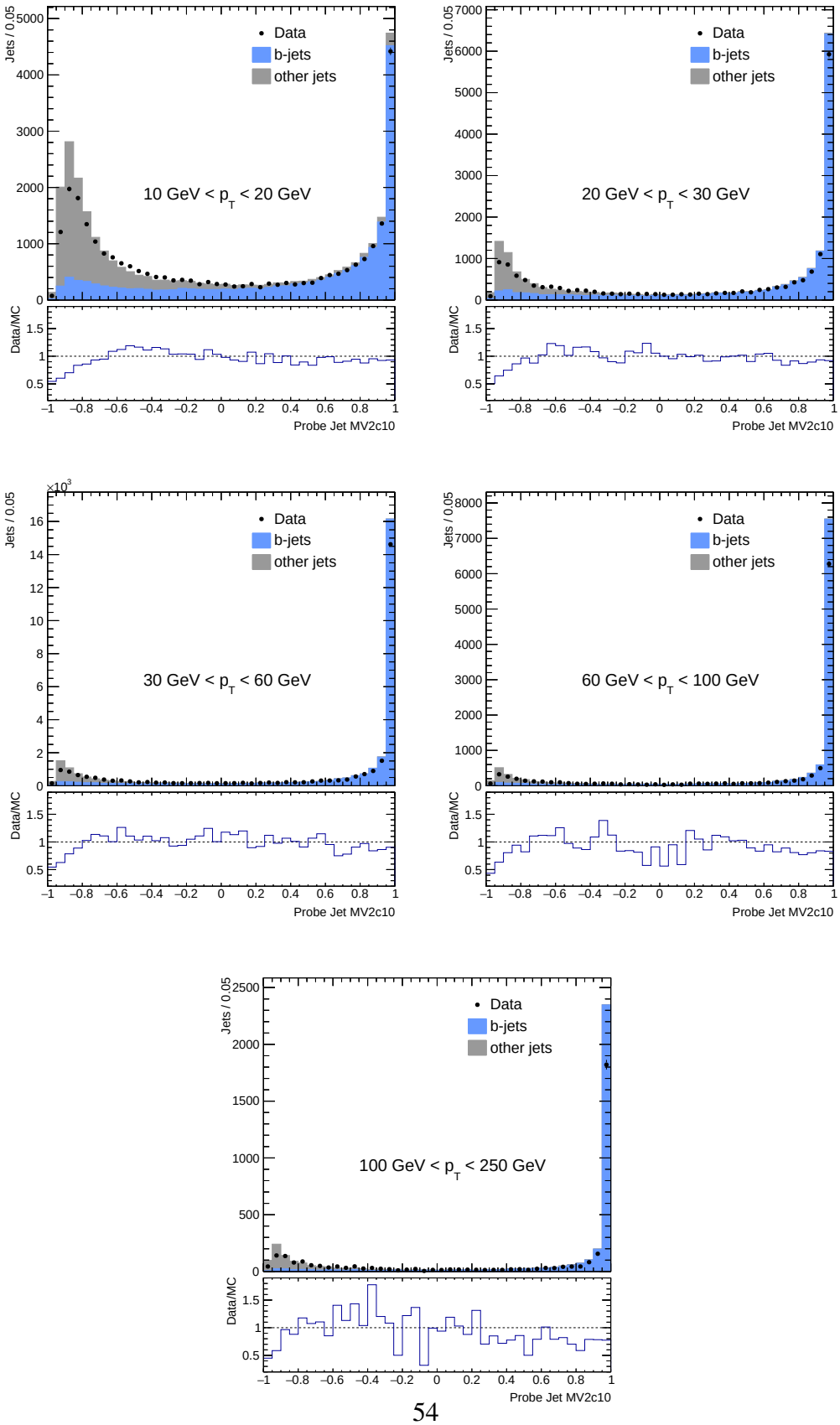

Figure 4.4: Data/MC comparison of the MV2c10 distribution of probe-jets with the p_{T} ranges specified by the labels on the plots. In the MC, the contribution from real *b*-jets is shown in blue and the light-jet contribution is shown in grey.

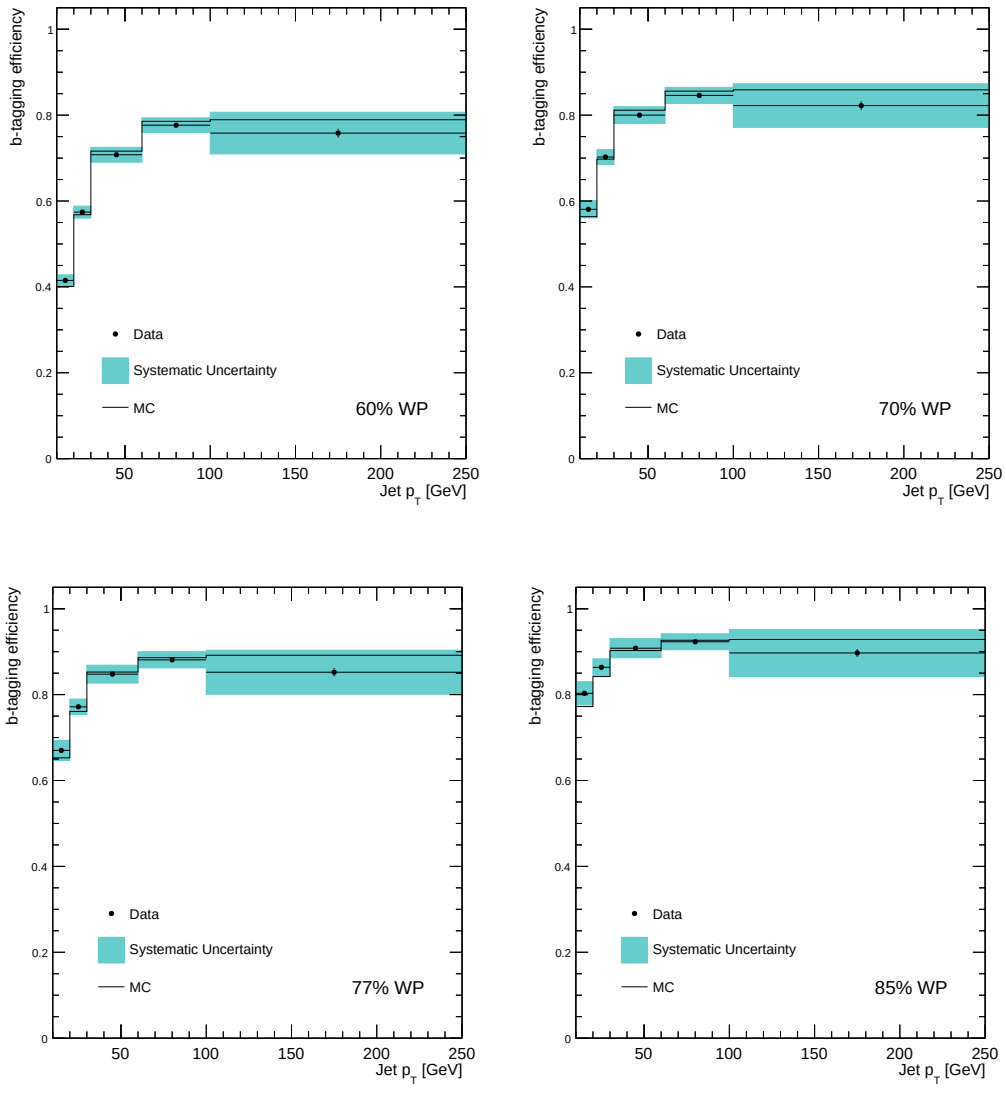

Figure 4.5: The efficiencies as a function of p_T for each fixed-cut working point, for both the MC prediction and the data. The error band in blue shows the size of the systematic uncertainty on the measured efficiency.

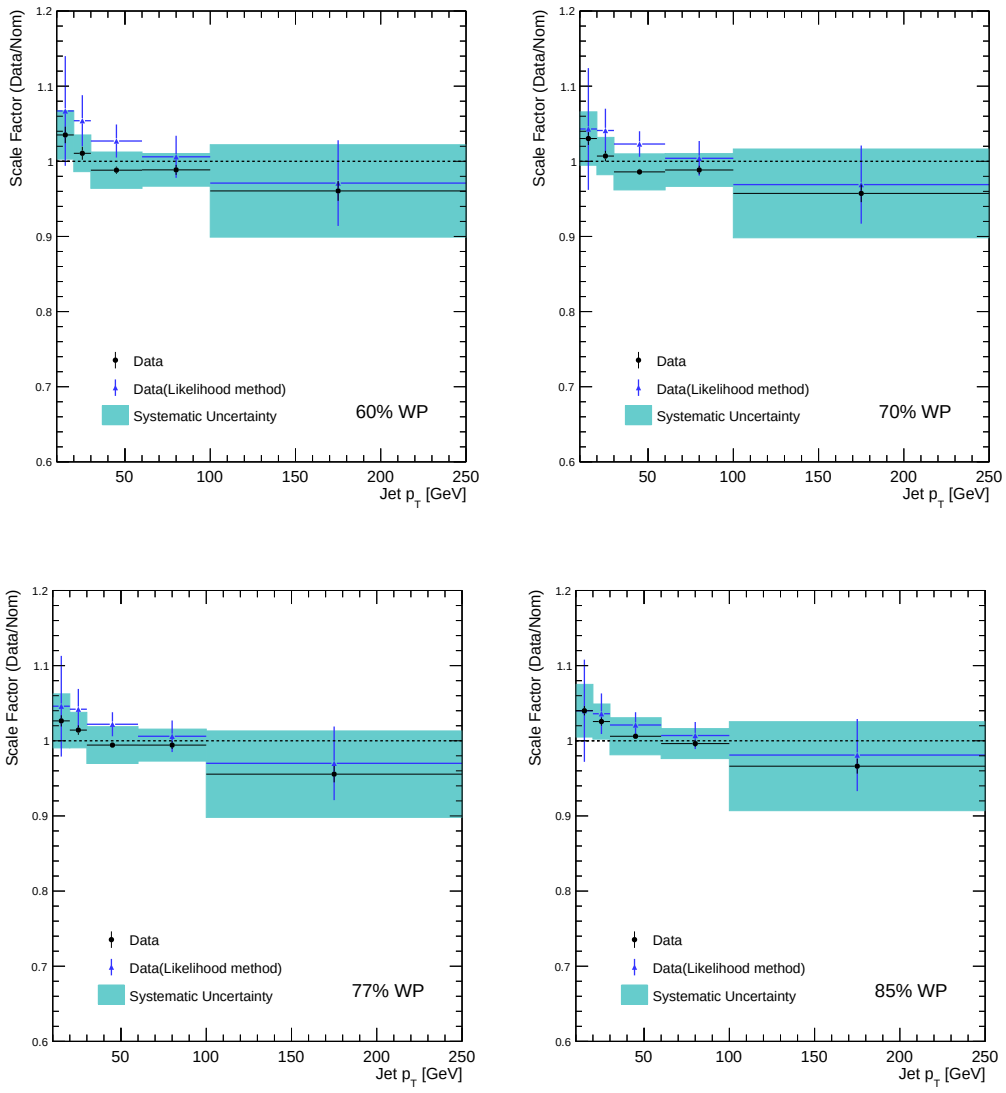

Figure 4.6: The scale-factors as a function of p_T for each fixed-cut working point. The scale-factors are compared to those derived using the likelihood calibration method. The results are consistent between the two methods.

p_T [GeV]	10-20	20-30	30-60	60-100	100-250
Scale factor	1.035	1.011	0.988	0.989	0.960
Total unc	0.035	0.027	0.025	0.024	0.064
Data stat	0.011	0.009	0.005	0.007	0.013
MC stat	0.010	0.007	0.004	0.005	0.009
Detector modelling	0.013	0.004	0.002	0.002	0.003
$t\bar{t}$ modelling	0.030	0.024	0.024	0.022	0.061

Table 4.3: The resulting per-bin scale-factor and associated uncertainties split by category for the 60% fixed-cut efficiency working point.

p_T [GeV]	10-20	20-30	30-60	60-100	100-250
Scale factor	1.030	1.007	0.986	0.988	0.957
Total unc	0.037	0.026	0.025	0.023	0.061
Data stat	0.008	0.007	0.004	0.006	0.012
MC stat	0.007	0.006	0.003	0.004	0.007
Detector modelling	0.016	0.003	0.002	0.002	0.002
$t\bar{t}$ modelling	0.032	0.025	0.024	0.022	0.059

Table 4.4: The resulting per-bin scale-factor and associated uncertainties split by category for the 70% fixed-cut efficiency working point.

4.7 Summary

The results of the *b*-tagging efficiency calibration for the MV2c10 algorithm in track-jets have been presented. Using the tag-and-probe method, the calibration was carried out targeting $t\bar{t}$ events and used the combined 2015+2016 dataset. The scale-factors for each *b*-tagging working point were derived and presented. They were found to be largely consistent with unity. The results were compared to scale-factors derived using the likelihood method, which is the method used to provide the default scale-factors used by analyses [72]. The scale-factors were found to be consistent within the respective uncertainties, therefore providing an important validation of the results.

p_T [GeV]	10-20	20-30	30-60	60-100	100-250
Scale factor	1.026	1.014	0.994	0.994	0.9556
Total unc	0.037	0.025	0.025	0.022	0.059
Data stat	0.007	0.006	0.004	0.005	0.011
MC stat	0.005	0.005	0.003	0.004	0.006
Detector modelling	0.013	0.003	0.002	0.002	0.002
$t\bar{t}$ modelling	0.033	0.023	0.024	0.021	0.057

Table 4.5: The resulting per-bin scale-factor and associated uncertainties split by category for the 77% fixed-cut efficiency working point.

p_T [GeV]	10-20	20-30	30-60	60-100	100-250
Scale factor	1.040	1.026	1.006	0.996	0.966
Total unc	0.036	0.024	0.025	0.021	0.060
Data stat	0.006	0.005	0.003	0.005	0.010
MC stat	0.004	0.003	0.002	0.003	0.005
Detector modelling	0.009	0.003	0.002	0.001	0.002
$t\bar{t}$ modelling	0.033	0.023	0.025	0.020	0.059

Table 4.6: The resulting per-bin scale-factor and associated uncertainties split by category for the 85% fixed-cut efficiency working point.

Chapter 5

Boosted $Z + b\bar{b}$ cross-section measurement

In this chapter I present a measurement of the cross-section for production of a Z-boson in association with a b-tagged large-radius (large-R) jet, differential in kinematic variables of the large-R jet and its associated small-R track-jets. This measurement provides an important test of perturbative QCD, with emphasis on the production rates and kinematics of bottom quarks. This process is also a significant background to several important Higgs boson searches, a particular example being the $V(H \to b\bar{b})$ search presented in Chapter 6.

The chapter begins with an overview of the analysis, which includes the motivation for performing the measurement. After that, the event selection is presented in Section 5.2, followed by details of the dataset and MC samples used in Section 5.3. The detector-level observables are presented in Section 5.4. The procedure used to correct the measurement to particle-level is described in Section 5.5. The systematic uncertainties considered in the analysis and their treatment are described in Section 5.6. Finally, the chapter concludes with the results which are shown in Section 5.7 and remarks on how they can be used in the future in Section 5.8.

5.1 Overview

The production rates and kinematics of bottom quarks produced in both the initial and final state are subject to theory and modelling uncertainties. The source of heavy flavour in the initial state arises perturbatively from gluon splitting to b quarks, which is described via DGLAP evolution [25, 26, 27]. There is an ambiguity in this evolution in the usual factorization scheme regarding whether the emergence of heavy flavour is isolated into the partonic cross-section or if it is also permitted in the evolution of the PDFs.

The former picture is the four-flavour number scheme (4FNS), in which the b-quark density in

the PDF is set to zero. This means that the perturbative generation of initial-state b-quarks comes from gluon splitting to a $b\bar{b}$ pair in the partonic matrix element, where the b-quark is massive. Consequently, in the 4-flavour scheme there are always at least two participating b-quarks, although they may fall outside the region of experimental acceptance. By contrast, in the five-flavour number scheme (5FNS) the PDF evolution can generate initial-state b-quarks (treated as being massless), but in this case it is only possible to resolve one b-quark outside of the proton. Example Feynman diagrams for $Z + b\bar{b}$ production under these two schemes are shown in Figure 5.1.

In a hypothetical all-orders calculation these two schemes would give the same results, but for a truncated perturbation expansion they generally give different predictions. Both of these approaches have relative merits: the 4FNS allows for transverse momentum exchange through the initial-state heavy quarks and hence might be expected to describe event kinematics better, while the 5FNS is able to make use of higher-order calculations not available in matrix elements matched to parton showers. It is therefore important to compare experimental measurements of b-quark production to predictions using both of these schemes.

In addition to these initial-state production uncertainties, theoretical uncertainties are also found in final state production of b-quarks. The usual parton shower formulation for parton splitting is derived in the collinear-emission limit, using the p_{T} of the splitting as the characteristic (renormalization) scale, but this choice is only well motivated for gluon-emission splitting functions [77], and its use in gluon splitting (especially to heavy quarks) is an extrapolation requiring empirical testing. This is important since uncertainties in heavy-flavour production by gluon splitting are a leading systematic limitation on the sensitivity to Higgs boson decays to $b\bar{b}$ in the $t\bar{t}H$, VH and gluon fusion channels – particularly in boosted-Higgs configurations where the two b-quarks are relatively collinear, similar to the dominant gluon-splitting kinematics.

A previous measurement of the $Z+b(\bar{b})$ process was made during Run-1 of the LHC using $\sqrt{s} =$ 7 TeV proton-proton collision data by ATLAS [78] and CMS [79]. Amongst other variables, the differential cross-section as a function of $\Delta R(b, \bar{b})$ (the separation between the b-jets) was measured and was found to be mismodelled by comparing to the MC generators available at the time. These results are shown in Figure 5.2. The mismodelling occurred mostly at low $\Delta R(b, \bar{b})$, which is the region dominated by gluon splitting.

In the measurement presented in this chapter, data recorded during 2015 and 2016 of Run-2 of the LHC were used. The increased centre of mass energy of $\sqrt{s} = 13$ TeV with respect to the Run-1 measurement means that the Z-boson and associated b's are produced with higher transverse momentum, allowing the boosted phase space, where the b's are collimated in the large-R jet, to be explored for the first time for this process. In order to measure smaller separations, typical of

gluon to $b\bar{b}$ splitting and helping to constrain the modelling of this in parton shower generators, small-radius track-jets ghost-associated to the large-R jet were used. Cross sections differential in the following variables were measured:

- Properties of the large-R jet in the inclusive (no tagging requirements) and two-b-tag regions, specifically the jet mass, m_{J}, and transverse momentum, $p_{\mathrm{T}}^{\mathrm{J}}$;
- The separation between the two b-tagged track-jets associated to the large-R jet in the 2-tag region, $\Delta R(b, \bar{b})$.
- Properties of the large-R jet and Z-boson, specifically the transverse momentum, $p_{\mathrm{T}}^{\mathrm{J}+Z}$, of their vector sum and their separation in ϕ, $\Delta\phi(Z, \mathrm{J})$.

The cross sections were measured at detector-level and corrected to particle-level using the fully-Bayesian unfolding method, described in Section 5.5.2. The total fiducial cross sections for both inclusive boosted Z+jets production and boosted $Z + b\bar{b}$ production were also measured using this method.

5.2 Event selection

To select events containing a leptonically-decaying Z-boson candidate produced in association with a large-R jet, exactly two charged leptons of the same flavour (e or μ) and at least one large-R jet were required. The invariant mass of the lepton pair, $m_{\ell\ell}$, was required to be greater than 50 GeV to mirror the same implicit requirement in the MC simulation of V+jets. There was no opposite-sign requirement on the leptons. A large-R jet was considered to be b-tagged if any of the track-jets which were matched to it via the ghost-association method [80] were b-tagged. In this method, the track-jets were provided to the jet clustering algorithm with their p_{T} set to an infinitesimal value to ensure that they don't influence the reconstruction of the jet. The track-jets which lie within the radius of the large-R jet were clustered into it. Events were assigned to two categories depending on how many b-tags were associated to the large-R jet: an inclusive region without b-tag requirements, and an exclusive 2-tag region. In events with more than one large-R jet, the 2-tag jet was considered as the signal jet from which the properties were measured. If there was no 2-tag jet, the highest p_{T} jet was considered as the signal jet. The kinematic requirements on the physics objects used in this selection are defined below.

Leptons: Electrons were required to pass the *Medium* identification criteria. They were required to be detected in the fiducial area of the EM calorimeter ($|\eta| < 1.37$, $1.52 < |\eta| < 2.47$)

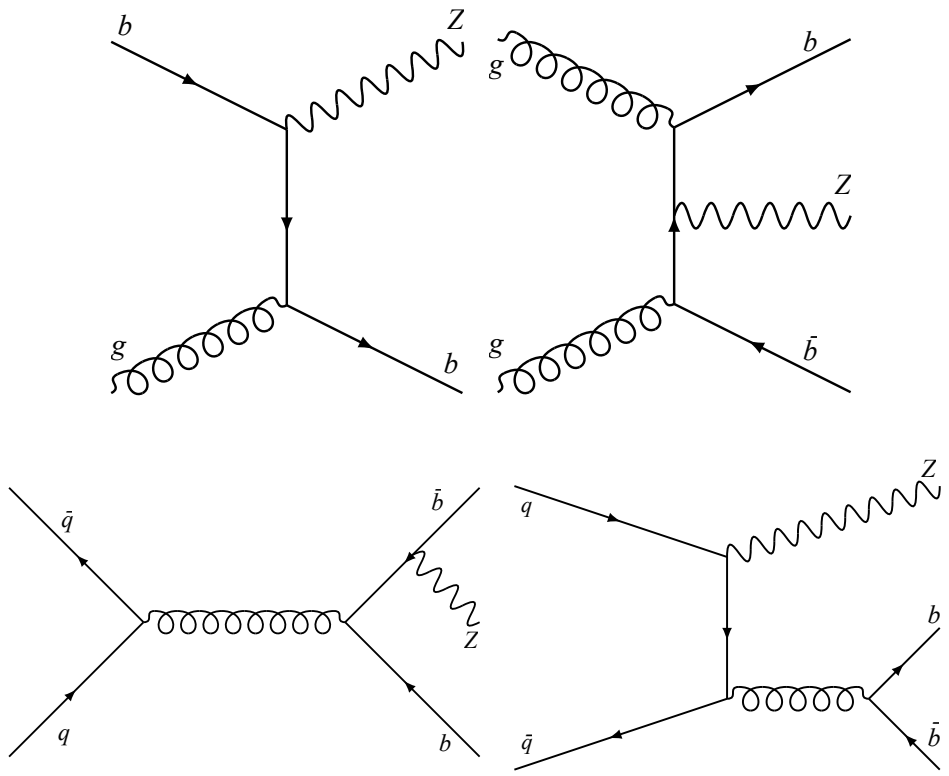

Figure 5.1: Feynman diagrams showing different $Z + b\bar{b}$ production mechanisms. The top left diagram is an example of a 4F diagram, whilst the other three are 5F diagrams.

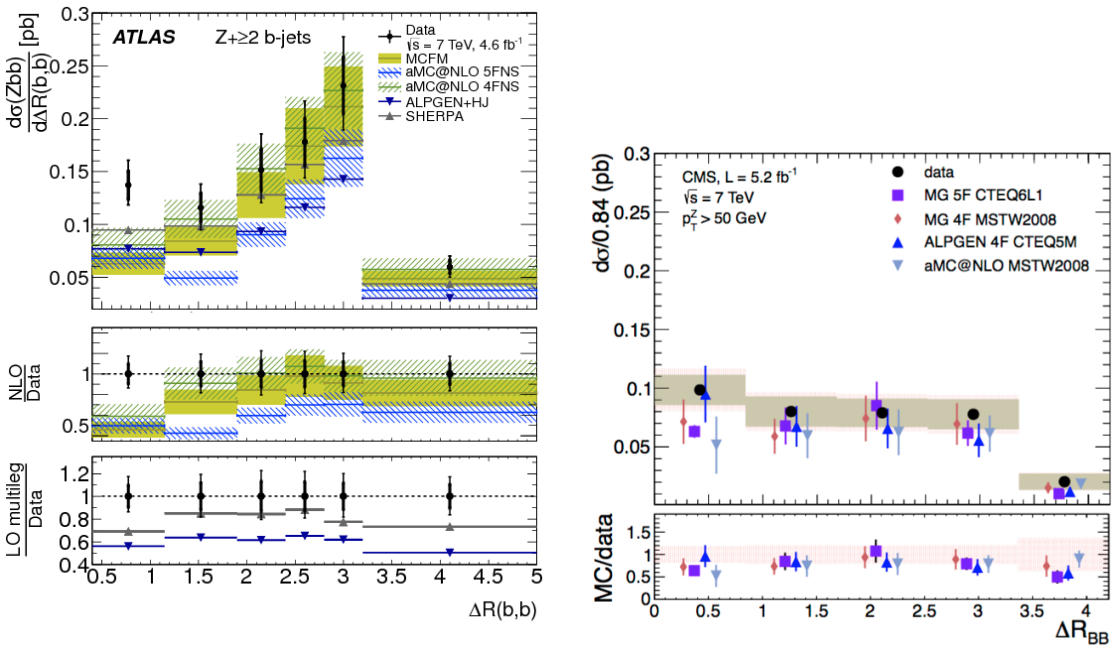

Figure 5.2: An ATLAS measurement (a) and CMS (b) measurement of the differential cross-section of $\Delta R(b,\bar{b})$ in $Z + b\bar{b}$ events using data collected during Run-1 of the LHC at a centre of mass energy of $\sqrt{s} = 7$ TeV [78, 79]. The low $\Delta R(b,\bar{b})$ region typical of gluon-splitting was found to be mismodelled by the predictions compared to at the time.

and have $p_{\mathrm{T}} > 27$ GeV. Muons were required to pass the *Tight* definition in addition to having $|\eta| < 2.5$ and $p_{\mathrm{T}} > 27$ GeV. Both electrons and muons were required to be isolated from significant energy deposits in the calorimeter and from high-momentum tracks; the *LooseTrackOnly* isolation definition was used in both cases. At least one lepton was required to be identified by a single-lepton trigger for each candidate event.

Large-R jets: The large-R jets were required to have $p_{\mathrm{T}} > 200$ GeV and $|\eta| < 2$, to favour a boosted topology and ensure that the majority of the jet lay within the tracker volume. Additionally, the jet calibration was only valid for large-R jets with $p_{\mathrm{T}} > 200$ GeV.

Track-jets and b-tagging: The b-tagging was applied to the matched track-jets which were required to have $p_{\mathrm{T}} > 10$ GeV and $|\eta| < 2.5$. A cut value for the discriminant corresponding to a 70% signal tagging efficiency (in simulation) was used to maintain a low rate of charm- and light-flavour background jets.

Overlap removal: An overlap removal procedure was used to correct for scenarios where a single particle or object leaves multiple signatures in the detector. For example, the calorimeter energy deposit from an electron can be reconstructed as a large-R jet, meaning that the electron would be double-counted. To correct for this, the separation between each lepton and large-R jet in the event was computed. Any large-R jets which were within $\Delta R = 1.0$ of a lepton were discarded. After this procedure, it was required that at least one jet was remaining in the event, otherwise the event was discarded.

In early iterations of the analysis, there were extra kinematic cuts implemented to suppress $t\bar{t}$ background which inclusively appeared to reduce the background at a very small cost. It was later found from studies of the MC events, that these cuts reduced the truth-to-reco efficiency in events with high-p_{T} large-R jets by up to 12%, where truth-to-reco efficiency is the efficiency for a jet produced by the MC generator (a "truth" jet) to pass the detector simulation and be reconstructed. These cuts were: $E_{\mathrm{T}}^{\mathrm{miss}} < 100$ GeV and $71 < m_{\ell\ell} < 111$ GeV, where $E_{\mathrm{T}}^{\mathrm{miss}}$ is the missing transverse energy and $m_{\ell\ell}$ is the dilepton invariant mass. For the $m_{\ell\ell}$ cut, this was understood as being due to the reduced mass resolution at high p_{T}. For the $E_{\mathrm{T}}^{\mathrm{miss}}$-cut, the reason was thought to be that the $E_{\mathrm{T}}^{\mathrm{miss}}$ was reconstructed using $R = 0.4$ calorimeter jets rather than large-R jets. In the boosted topology these jet algorithms cannot always resolve the b-jets so there can be cases where the two b's are reconstructed in one $R = 0.4$ jet which does not properly capture their full p_{T}, leading to an overestimate of the $E_{\mathrm{T}}^{\mathrm{miss}}$. This effect is exacerbated at higher large-R jet p_{T} when the b's become more collimated. Optimisation studies of the $E_{\mathrm{T}}^{\mathrm{miss}}$ cut revealed that there actually was no optimal

Inclusive selection

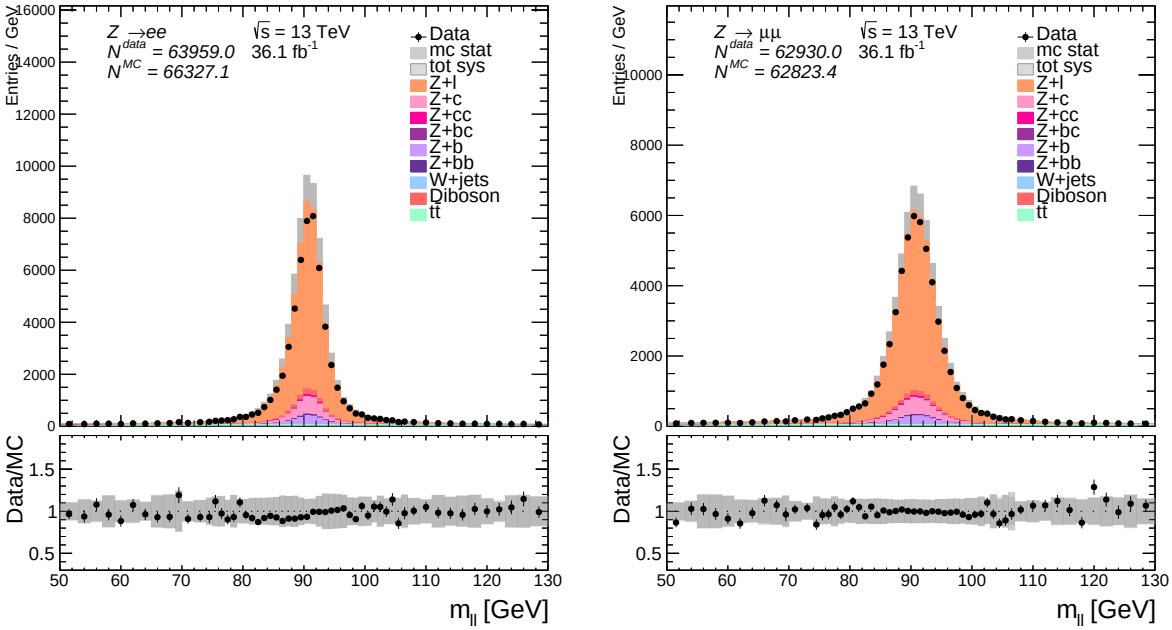

Figure 5.3: INCLUSIVE SELECTION: The dilepton invariant mass in the electron channel (left) and the muon channel (right). The systematic uncertainties are combined and shown by the dark grey band, and the statistical uncertainties are shown by the light grey band. The statistical uncertainty on the data is given by the error bar on the data point.

cut which would maximise the signal to background significance and since the $t\bar{t}$ background was at most 10% of the signal even without the cuts, it was decided to remove them. Figure 5.3 shows the dilepton invariant mass spectrum with these cuts removed in both the electron and muon channel.

There was also a stricter requirement on the number of large-R jets in the event, where previously it had been required that exactly one jet be present in the event. It was found however that this cut also reduced the truth-to-reconstruction efficiency by up to 10%. The efficiency reduction was seen for events where there was exactly one jet at truth-level, but zero or more than one jet at detector-level. This was due to a number of reasons: smearing of the ΔR distance between a jet and a lepton, meaning that a jet failing overlap removal at truth-level "survives" it at detector-level (or vice versa); fake detector-level jets which have no truth-level counterpart; detector-level jets migrating out of detector acceptance; and jet-radius effects where a single jet at truth-level could be reconstructed as two detector-level jets. As a result of this observation, it was decided that this cut should be loosened.

5.3 Data and MC samples

The data used in this measurement were collected during the 2015 and 2016 pp collision runs at $\sqrt{s} = 13$ TeV, corresponding to a total integrated luminosity of 36.1 fb^{-1}. Only collision events where all of the ATLAS sub-detectors were fully operational and the beam conditions were stable were analysed.

Monte Carlo samples were used to simulate the signal events, estimate the contamination from background processes, unfold the data to particle-level, and to make comparisons to the unfolded data. The processes contributing as a background were $W+$jets, $t\bar{t}$, and diboson. The $W+$jets process contributed as a background when a second same-flavour lepton arose through a jet faking the lepton signal in the detector. The $t\bar{t}$ process contributed when each of the W bosons from the top decays decayed to same-flavour leptons. The diboson processes (WW, WZ, ZZ) contributed when one of the bosons decayed hadronically and one decayed leptonically. Single-top had a smaller cross-section and similar acceptance to $W+$jets and therefore was considered negligible.

The matrix element generators, parton shower generators, and PDFs used to provide simulations for each of these processes are summarised in Table 5.1. In each case, the samples were normalised to the highest cross section available for the given process. In the samples interfaced with PYTHIA8 and HERWIG, the program EVTGEN was used to simulate the decays of bottom and charm hadrons [74]. Each sample was processed using GEANT4 which simulates the ATLAS detector [75]. The listed "alternative" samples were used for evaluation of systematic uncertainties relating to signal and background modelling, which are described in Section 5.6. Both the SHERPA samples and the MADGRAPH5_AMC@NLO+PYTHIA8 samples were generated using a 5-flavour number scheme calculation.

Process	Matrix element	PDF set	Parton Shower
	Nominal		
$Z+$jets	SHERPA v2.2	NNPDF30nnlo	SHERPA v2.2
$t\bar{t}$	POWHEGBOX	NNPDF30nnlo	PYTHIA8
$W+$jets	SHERPA v2.2	NNPDF30nnlo	SHERPA v2.2
Diboson	SHERPA v2.1	CT10nlo	SHERPA v2.1
	Alternative		
$Z+$jets	MADGRAPH5_AMC@NLO	NNPDF30nlo	PYTHIA8
$t\bar{t}$	MADGRAPH5_AMC@NLO	NNPDF30nnlo	PYTHIA8
$t\bar{t}$	POWHEG	NNPDF30nnlo	HERWIG7
$t\bar{t}$ (radLo)	POWHEG	NNPDF30nnlo	PYTHIA8
			$h_{\text{damp}} = m_{\text{top}}$
$t\bar{t}$ (radHi)	POWHEG	NNPDF30nnlo	PYTHIA8
			$h_{\text{damp}} = 2 * m_{\text{top}}$

Table 5.1: Details of the nominal and alternative samples used to simulate the signal and background processes used in the analysis.

5.4 Detector-level observables

Detector-level comparisons between data and the MC prediction for the observables of interest are presented in this section. The plots are split such that the electron and muon decay modes of the Z-boson can be compared for each observable, to verify consistency between the two object types. In addition, the modelling of the observables is assessed in two control regions: a $t\bar{t}$-enriched region and a fakes-enriched region. The details of these control regions and the comparisons between data and the MC prediction for the observables in these regions are given in Sections 5.4.2 and 5.4.3.

The observables from the inclusive event selection, i.e. without any requirement on large-R jet b-tagging, are shown in Figure 5.4 for $p_{\mathrm{T}}^{\mathrm{J}}$ & m_{J}, and Figure 5.5 for $p_{\mathrm{T}}^{\mathrm{J}+Z}$ & $\Delta\phi(Z,\mathrm{J})$. From these comparisons it can be seen that the MC simulation overestimates the p_{T} and $p_{\mathrm{T}}^{\mathrm{J}+Z}$, especially at high values. Similarly, the region where the Z-boson and the large-R jet are produced close together, i.e. $\Delta\phi(Z,\mathrm{J}) < 1.0$, is also overestimated. From the $p_{\mathrm{T}}^{\mathrm{J}+Z}$ and $\Delta\phi(Z,\mathrm{J})$ distributions, it can be seen that there appears to be "extra radiation" in the event: if the Z-boson and large-R jet were the only two objects in the event, $p_{\mathrm{T}}^{\mathrm{J}+Z}$ would peak sharply around zero and $\Delta\phi(Z,\mathrm{J})$ would be sharply peaked at π. Whilst the $\Delta\phi(Z,\mathrm{J})$ distribution does peak at π, the distribution is broad and has a long tail down to zero. Additional studies were carried out to investigate this extra radiation, which are discussed in Section 5.4.1.

The observables in the exclusive 2-tag event selection are shown in Figure 5.6 for m_{J} and $p_{\mathrm{T}}^{\mathrm{J}}$, and $\Delta R(b,\bar{b})$ is shown in Figure 5.7. For each of these observables, there is a relatively flat 20% difference between the data and the MC prediction.

The uncertainty bands shown in the distributions are composed of the statistical uncertainty on the MC sample, the detector-related systematic uncertainty, and modelling uncertainties on the signal and $t\bar{t}$ background. Each of these components, which are described in detail in Section 5.6, were added in quadrature to obtain the full uncertainty band.

Inclusive selection

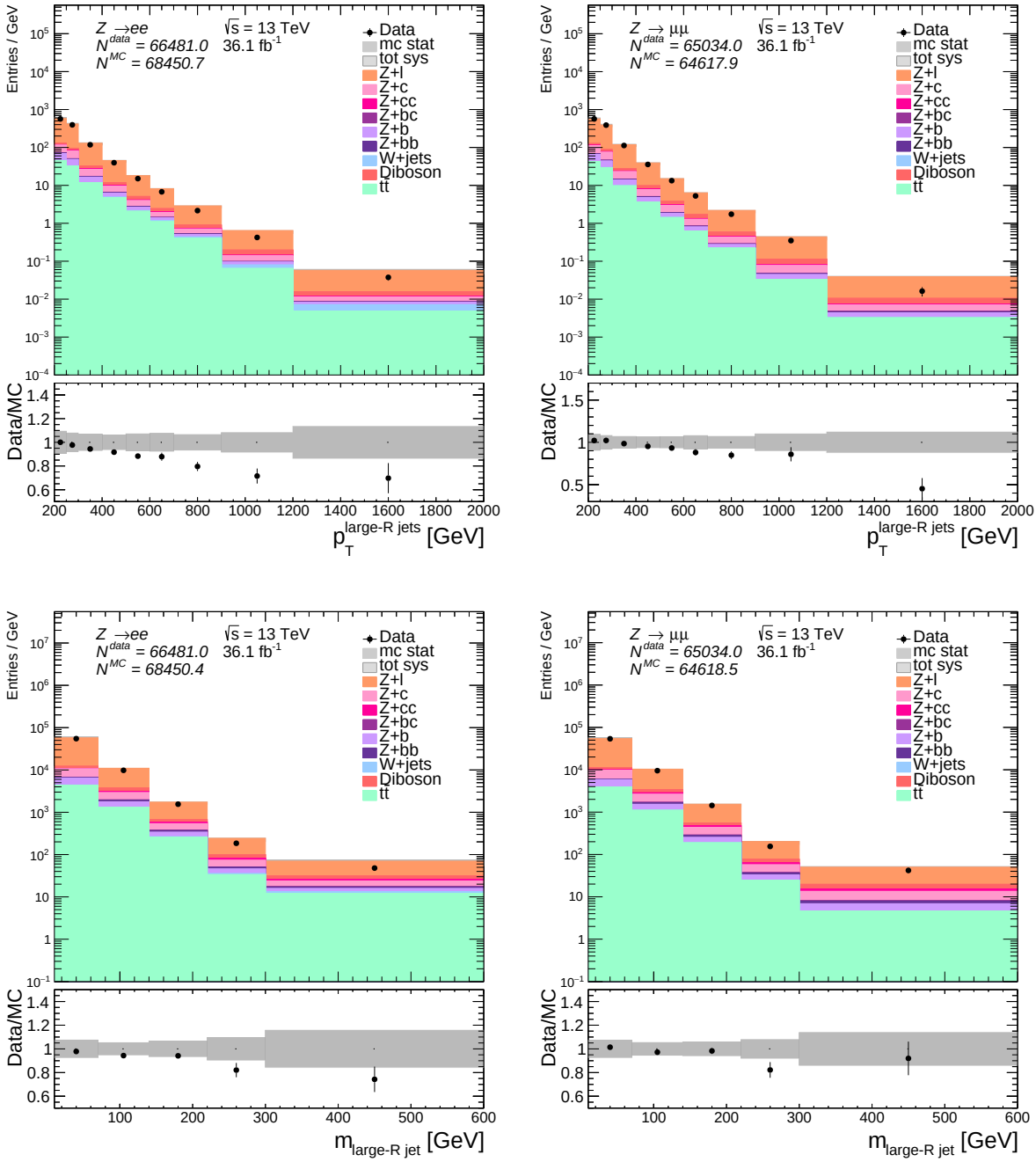

Figure 5.4: INCLUSIVE SELECTION: The transverse momentum (top) and mass (bottom) of the large-R jet, for the electron channel (left) and the muon channel (right). The systematic uncertainties are combined and shown by the dark grey band, and the statistical uncertainties are shown by the light grey band. The statistical uncertainty on the data is given by the error bar on the data point.

Inclusive selection

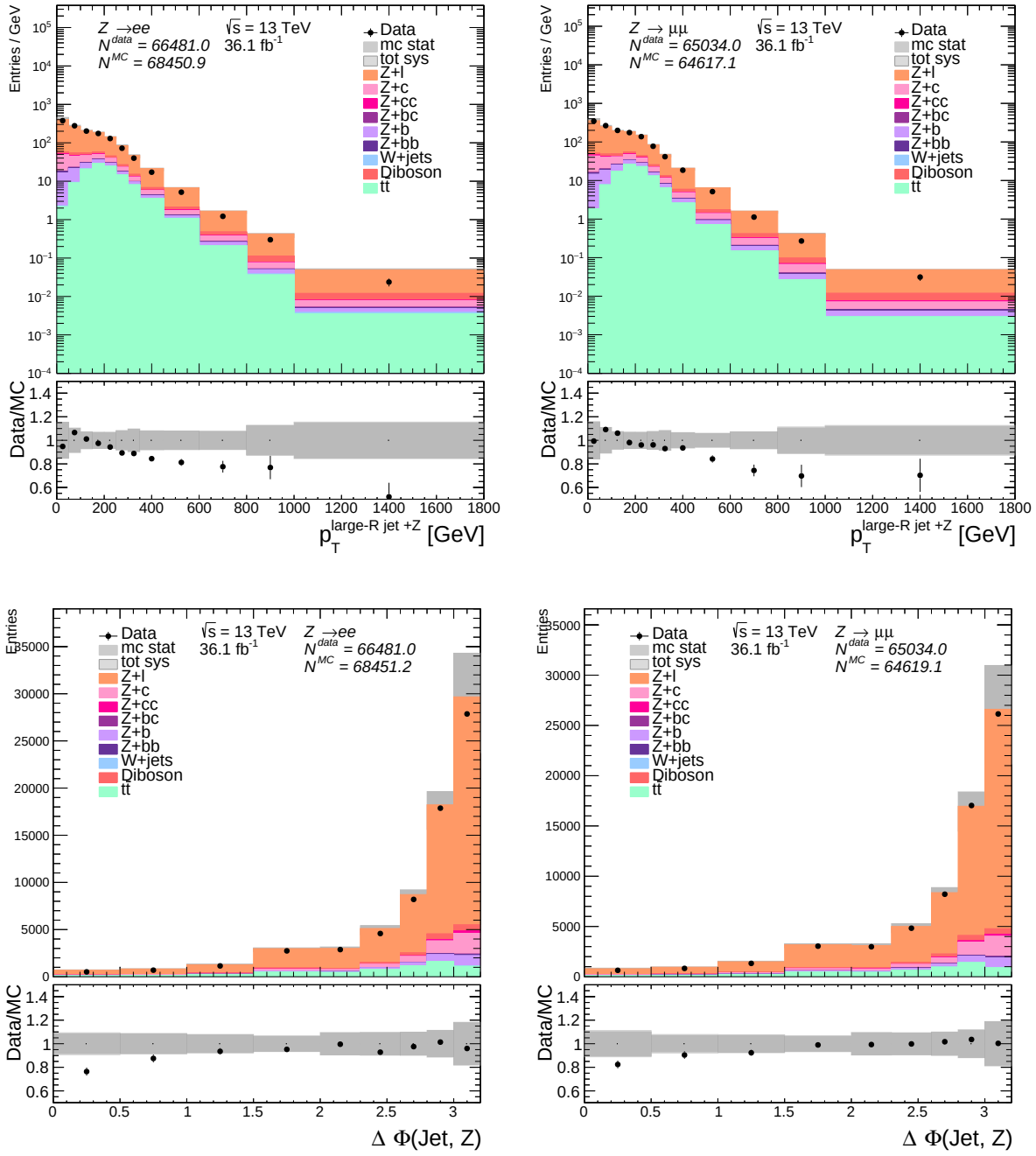

Figure 5.5: INCLUSIVE SELECTION: The p_{T} (top) and separation in ϕ (bottom) of the large-R jet and Z boson, for the electron channel (left) and the muon channel (right). The systematic uncertainties are combined and shown by the dark grey band, and the statistical uncertainties are shown by the light grey band. The statistical uncertainty on the data is given by the error bar on the data point.

2-tag selection

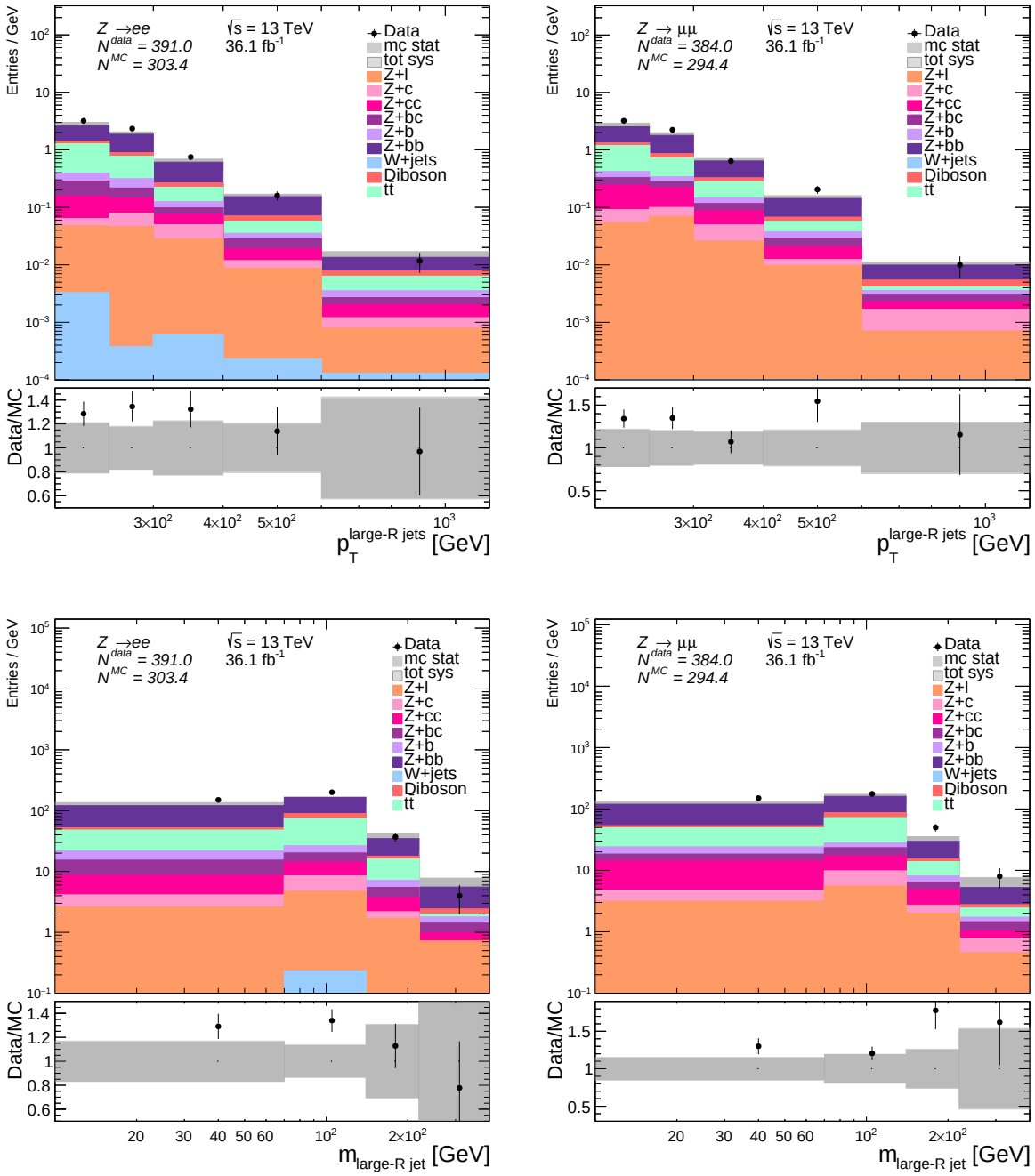

Figure 5.6: 2-TAG SELECTION: The transverse momentum (top) and mass (bottom) of the large-*R* jet, for the electron channel (left) and the muon channel (right). The systematic uncertainties are combined and shown by the dark grey band, and the statistical uncertainties are shown by the light grey band. The statistical uncertainty on the data is given by the error bar on the data point.

2-tag selection

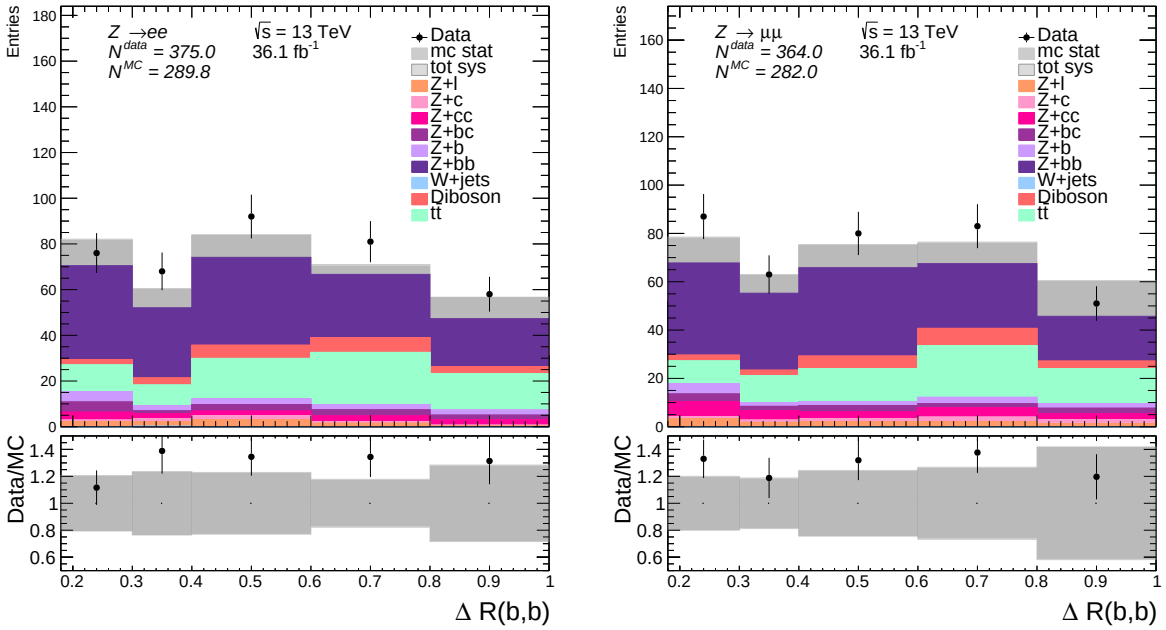

Figure 5.7: 2-TAG SELECTION: The ΔR between the two associated b-tagged track-jets of the large-R jet, for the electron channel (left) and the muon channel (right). The systematic uncertainties are combined and shown by the dark grey band, and the statistical uncertainties are shown by the light grey band. The statistical uncertainty on the data is given by the error bar on the data point.

5.4.1 Studies of extra radiation in the event

It was observed that there were events where the p_{T} of the large-R jet and the Z-boson were not balanced, shown by the broad distribution and long tails to high values in the $p_{\mathrm{T}}^{\mathrm{J}+Z}$ observable. This is to be expected to some extent, given that there was no p_{T}-cut applied to the selected Z-boson whilst the large-R jet was required to have $p_{\mathrm{T}} > 200$ GeV. When investigating the topology of the Z-boson and the large-R jet via their $\Delta\phi$ separation, it was observed that the Z-boson and large-R jet were predominantly produced back-to-back (i.e. $\Delta\phi(Z,\mathrm{J})$ peaks at π), though there were tails down to zero indicating events where this was not the case. This implied that the extra radiation didn't have a strong influence on the topology of the Z-boson and large-R jet, given that $p_{\mathrm{T}}^{\mathrm{J}+Z}$ extends to large values and yet the Z-boson and large-R jet are largely back-to-back.

In an attempt to understand this further, the relationship between $p_{\mathrm{T}}^{\mathrm{J}+Z}$ and $\Delta\phi(Z,\mathrm{J})$, as a function of the large-R jet p_{T} was investigated. Figures 5.8 and 5.9 shows distributions of the average $\Delta\phi(Z,\mathrm{J})$ as a function of $p_{\mathrm{T}}^{\mathrm{J}+Z}$, where the distributions were split according to the large-R jet p_{T}. From Figures 5.8(a) and 5.9(a) it can be seen that for events where the large-R jet p_{T} was between 200 and 400 GeV, as $p_{\mathrm{T}}^{\mathrm{J}+Z}$ increases the $\Delta\phi(Z,\mathrm{J})$ decreases sharply. However for higher large-R jet p_{T} where $p_{\mathrm{T}} > 600$ GeV, the $\Delta\phi(Z,\mathrm{J})$ remains relatively flat as a function of $p_{\mathrm{T}}^{\mathrm{J}+Z}$, as shown in Figures 5.8(c) and 5.9(c). This suggests that in events with a high p_{T} jet, the event is dominated by the high-p_{T} recoiling large-R jet and Z-boson, and the "extra radiation" – at whatever magnitude – is isotropically distributed around either of these objects.

Finally, the scaling of $p_{\mathrm{T}}^{\mathrm{J}+Z}$ as a function of the large-R jet p_{T} and the Z-boson p_{T} was studied. Figures 5.10(a) and 5.10(b) show the average $p_{\mathrm{T}}^{\mathrm{J}+Z}$ as a function of the large-R jet p_{T} in both the electron and muon channel. From these distributions it can be seen that $p_{\mathrm{T}}^{\mathrm{J}+Z}$ scales very strongly with the large-R jet p_{T}. Figures 5.10(c) and 5.10(d) show the average $p_{\mathrm{T}}^{\mathrm{J}+Z}$ as a function of the Z-boson p_{T} in both the electron and muon channel. Here it can be seen that the shape is influenced by the minimum p_{T}-cut on the large-R jet. As the Z-boson approaches $p_{\mathrm{T}} = 200$ GeV, matching the minimum p_{T} of the large-R jet, $p_{\mathrm{T}}^{\mathrm{J}+Z}$ decreases. Beyond this, $p_{\mathrm{T}}^{\mathrm{J}+Z}$ increases before plateauing. The fact that $p_{\mathrm{T}}^{\mathrm{J}+Z}$ was so strongly correlated with the large-R jet p_{T} and less so for the Z-boson p_{T}, led to the conclusion that these were events where the Z-boson was radiated from one of the outgoing quarks.

5.4.2 $t\bar{t}$-enriched region

A selection was defined which closely matched the signal-selection but was enriched in $t\bar{t}$ events, where exactly one electron and exactly one muon were required whilst keeping all other aspects

Inclusive selection - electron channel

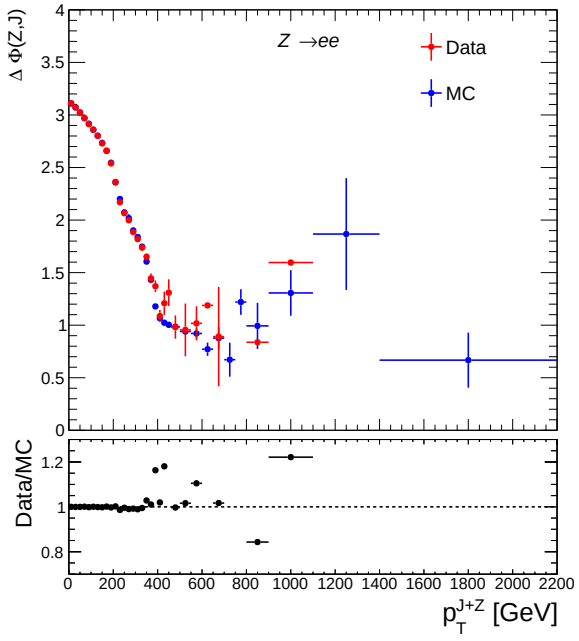

(a) $200 < p_{\mathrm{T}}^{\mathrm{J}} < 400$ GeV

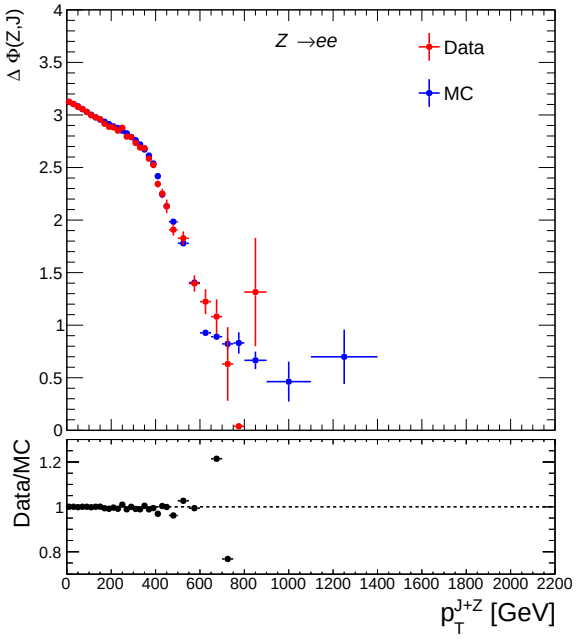

(b) $400 < p_{\mathrm{T}}^{\mathrm{J}} < 600$ GeV

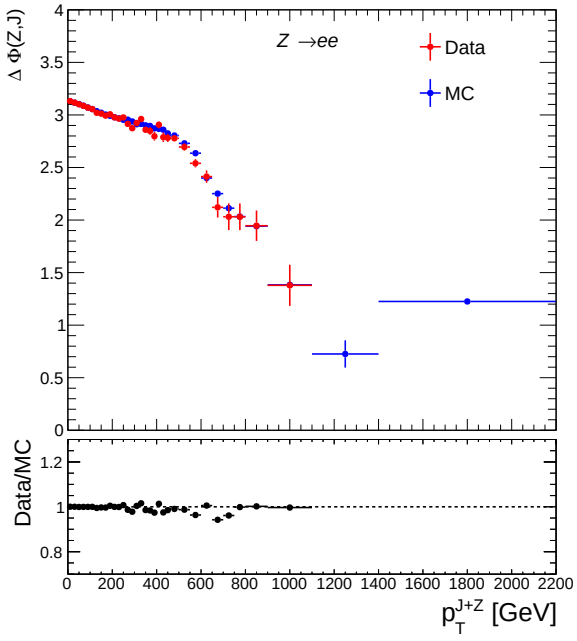

(c) $600 < p_{\mathrm{T}}^{\mathrm{J}} < 1000$ GeV

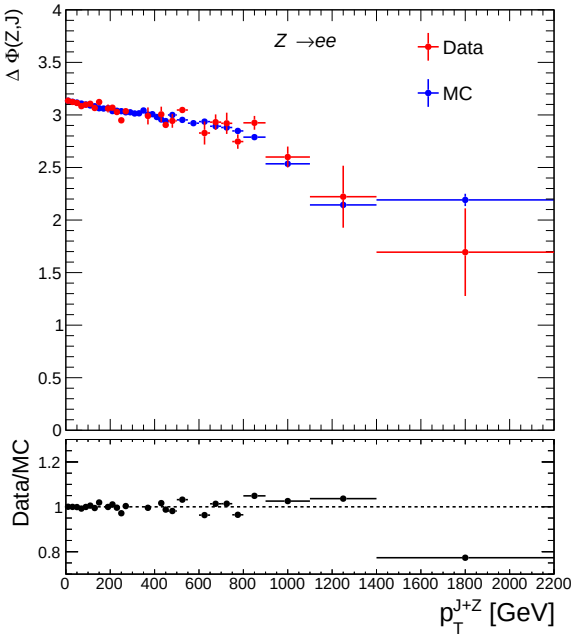

(d) $p_{\mathrm{T}}^{\mathrm{J}} > 1000$ GeV

Figure 5.8: Distributions of the average $\Delta\phi(Z,\mathrm{J})$ as a function of $p_{\mathrm{T}}^{\mathrm{J}+Z}$ in events where the large-R jet p_{T} satisfies the requirement given in the caption of each distribution. The error bar is the standard error on the average.

Inclusive selection - muon channel

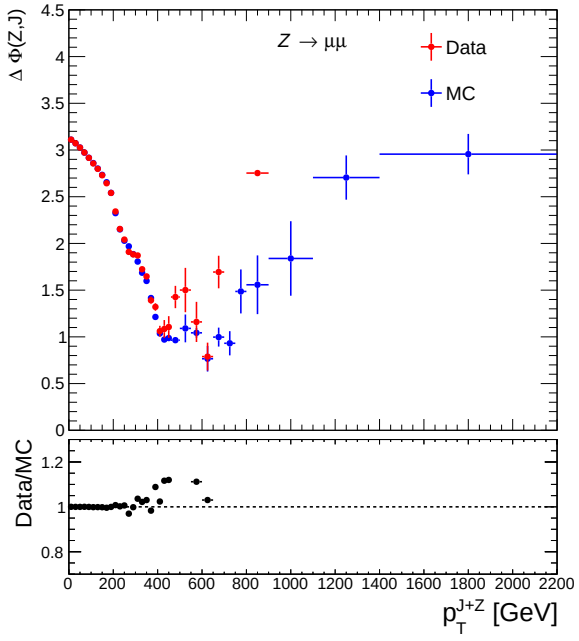

(a) $200 < p_{\mathrm{T}}^{\mathrm{J}} < 400$ GeV

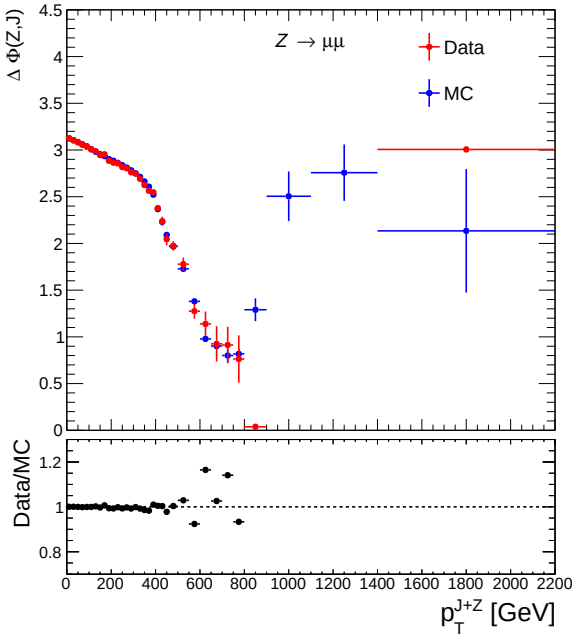

(b) $400 < p_{\mathrm{T}}^{\mathrm{J}} < 600$ GeV

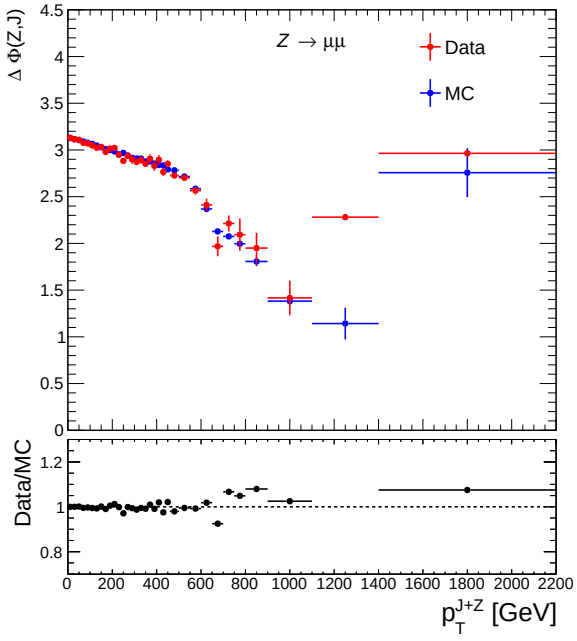

(c) $600 < p_{\mathrm{T}}^{\mathrm{J}} < 1000$ GeV

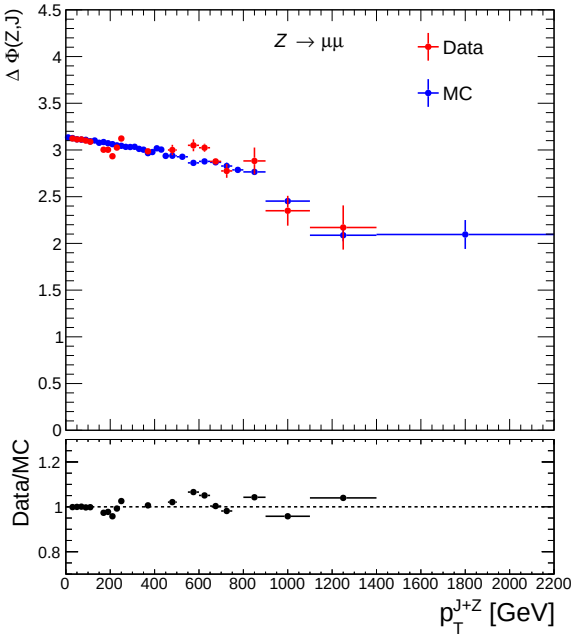

(d) $p_{\mathrm{T}}^{\mathrm{J}} > 1000$ GeV

Figure 5.9: Distributions of the average $\Delta\phi(Z,\mathrm{J})$ as a function of $p_{\mathrm{T}}^{\mathrm{J}+Z}$ in events where the large-R jet p_{T} satisfies the requirement given in the caption of each distribution. The error bar is the standard error on the average.

Inclusive selection

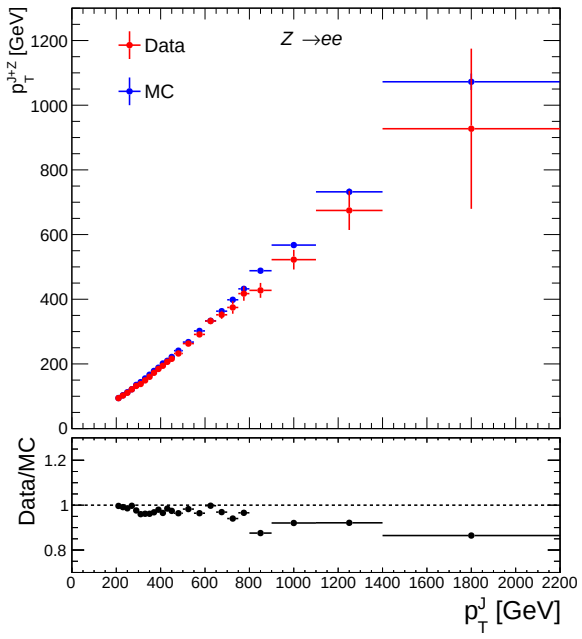

(a) p_T^{J+Z} vs p_T^J- electron channel

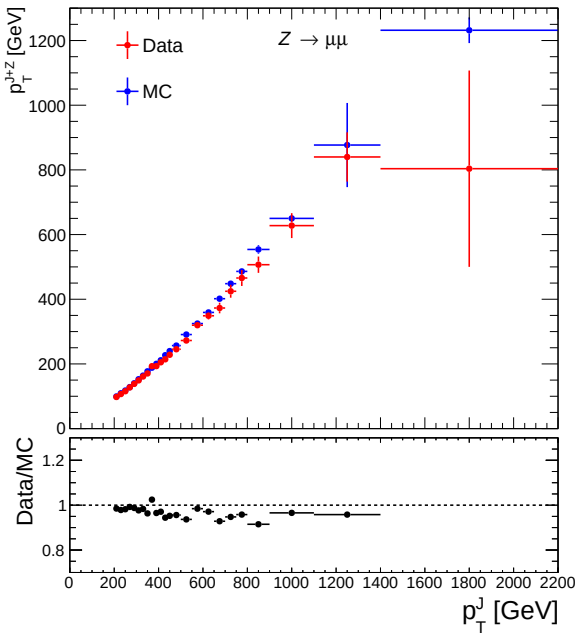

(b) p_T^{J+Z} vs p_T^J- muon channel

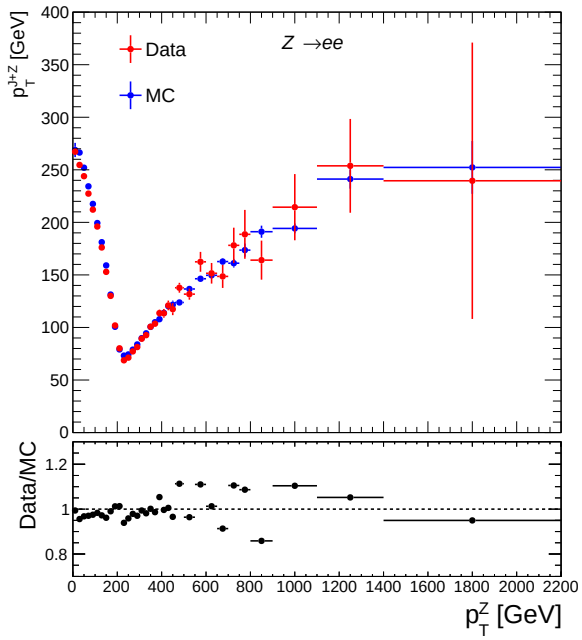

(c) p_T^{J+Z} vs p_T^Z- electron channel

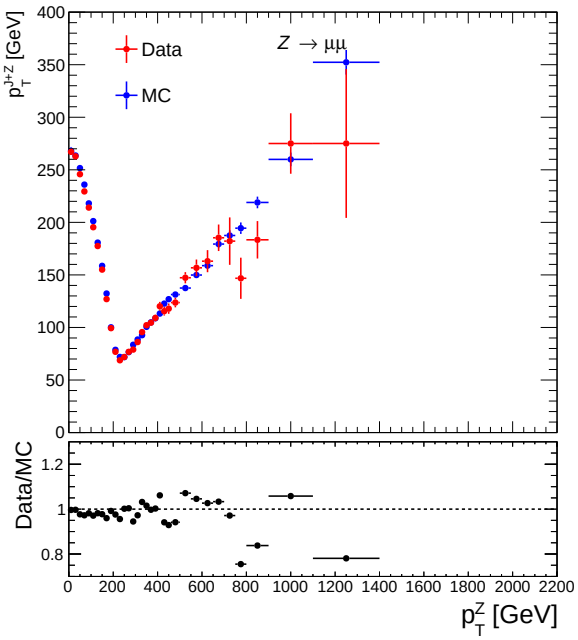

(d) p_T^{J+Z} vs p_T^Z- muon channel

Figure 5.10: Distributions of the average p_T^{J+Z} as a function of a) p_T^J and b) p_T^Z. The error bar is the standard error on the average.

of the selection the same. This $t\bar{t}$-enriched region was created to check that the $t\bar{t}$ background was modelled well.

Comparisons between data and the MC prediction in this region for each observable are shown in Figures 5.11 to 5.12. For the majority of the variables there is no significant mismodelling observed outside of the error band, with the following exceptions: the first two bins of the $p_{\mathrm{T}}^{\mathrm{J}+Z}$ observable, and the first bin of the 2-tag large-R jet p_{T}. To account for these effects, an additional 20% normalisation uncertainty on the $t\bar{t}$ background was assigned for all observables, as well as an additional uncertainty accounting for the $\sim$ 50% discrepancy in the first two bins of the $p_{\mathrm{T}}^{\mathrm{J}+Z}$ observable.

5.4.3 Fakes-enriched region

The background contribution from $W+$ jets largely arises due to jets being mis-reconstructed as a lepton, referred to generically as a "fake". This occurs most commonly for electrons rather than muons given that the jet would have to punch-through the calorimeters and leave a signature in the muon spectrometer to fake a muon, which is uncommon. In the muon channel, $W+$ jets can contribute when a real lepton from a heavy-hadron decay provides the second same-flavour lepton required in the signal selection. To assess the modelling of the $W+$ jets background, a fakes-enriched region was defined where the lepton identification requirements were relaxed to the *Loose* working point, whilst keeping other aspects of the event selection the same. If this background was mismodelled then the modelling of the observables in this fake-enriched region would be worse than in the signal region. There were no significant differences in the modelling observed for any of the variables, despite the increase in the number of fakes, indicating that this process was not mismodelled. As an example, a comparison between the inclusive $p_{\mathrm{T}}^{\mathrm{J}}$ in the signal region and the fakes-enriched region is shown in Figure 5.13. This comparison shows that there is no significant difference in the modelling between these two regions.

Another process which can act as a background is multijet i.e. inclusive QCD. Multijet production has a high cross section and can contribute as a background when at least two jets fake a lepton. To assess whether the analysis was sensitive to contributions from this background, the calorimeter isolation variable, $E_{\mathrm{T}}^{\mathrm{topocone20}}$, was compared in data and MC in the fake-enriched region. If there was multijet-contamination that wasn't being accounted for, then an excess of events in data compared to MC in the tails of the $E_{\mathrm{T}}^{\mathrm{topocone20}}$ variable would be seen, as fake-leptons are less likely to be isolated than real leptons. Figure 5.14 shows the comparison of this variable in the electron and muon channel. It is clear that there is no significant excess of events in data, therefore it was concluded that there was no significant contamination from multijet in this analysis.

Inclusive selection - $t\bar{t}$ CR

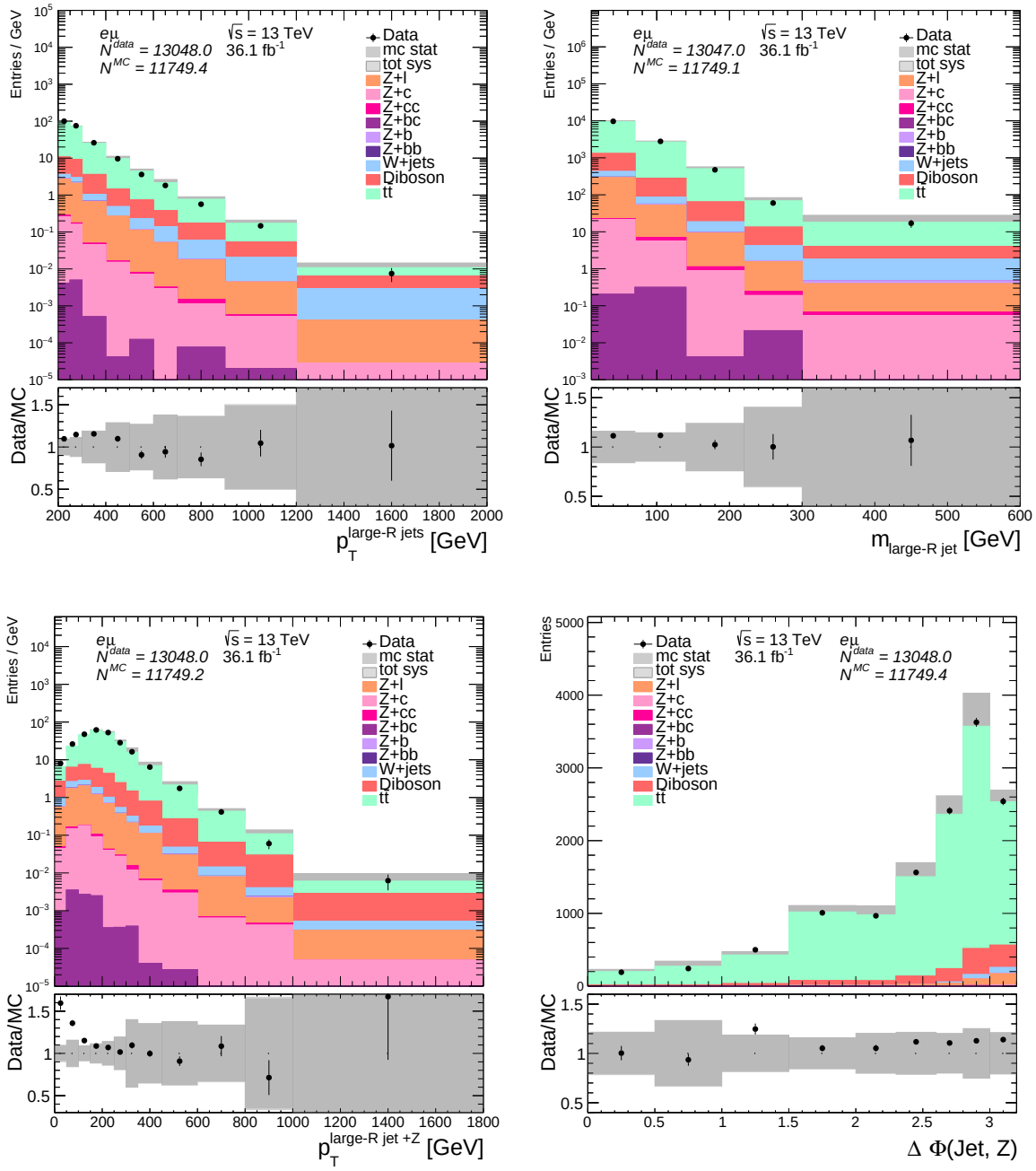

Figure 5.11: INCLUSIVE SELECTION: The transverse momentum (a) and mass (b) of the large-R jet, and the p_{T} (top) and separation in ϕ (bottom) of the large-R jet and Z boson in the top control region. The systematic uncertainties are combined and shown by the dark grey band, and the statistical uncertainties are shown by the light grey band. The statistical uncertainty on the data is given by the error bar on the data point.

2-tag selection - $t\bar{t}$ CR

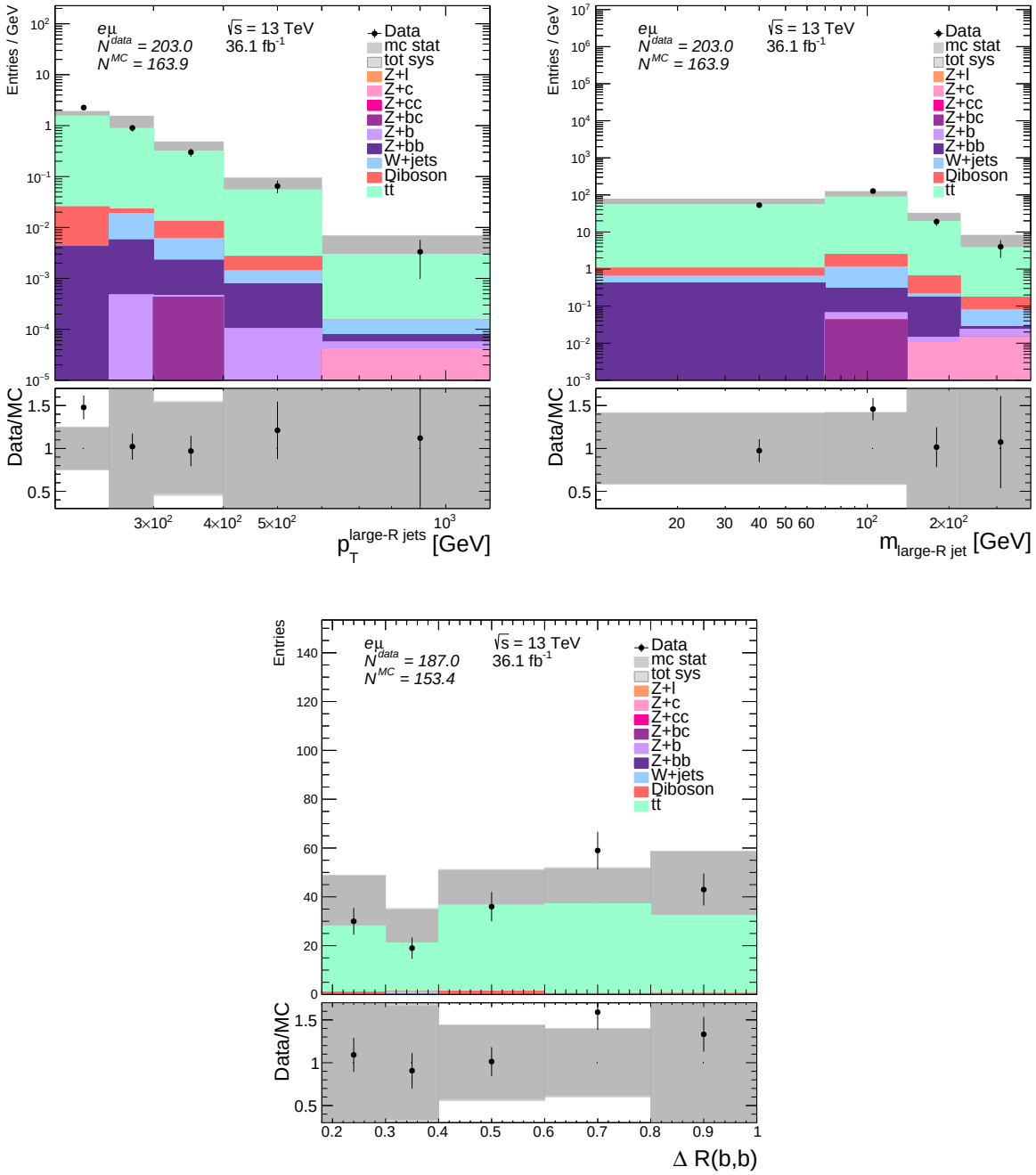

Figure 5.12: 2-TAG SELECTION: The transverse momentum (a) and mass (b) of the large-R jet, and the ΔR between the two associated b-tagged track-jets of the large-R jet (c) in the top control region. The systematic uncertainties are combined and shown by the dark grey band, and the statistical uncertainties are shown by the light grey band. The statistical uncertainty on the data is given by the error bar on the data point.

Inclusive selection - $W+$jets-enriched

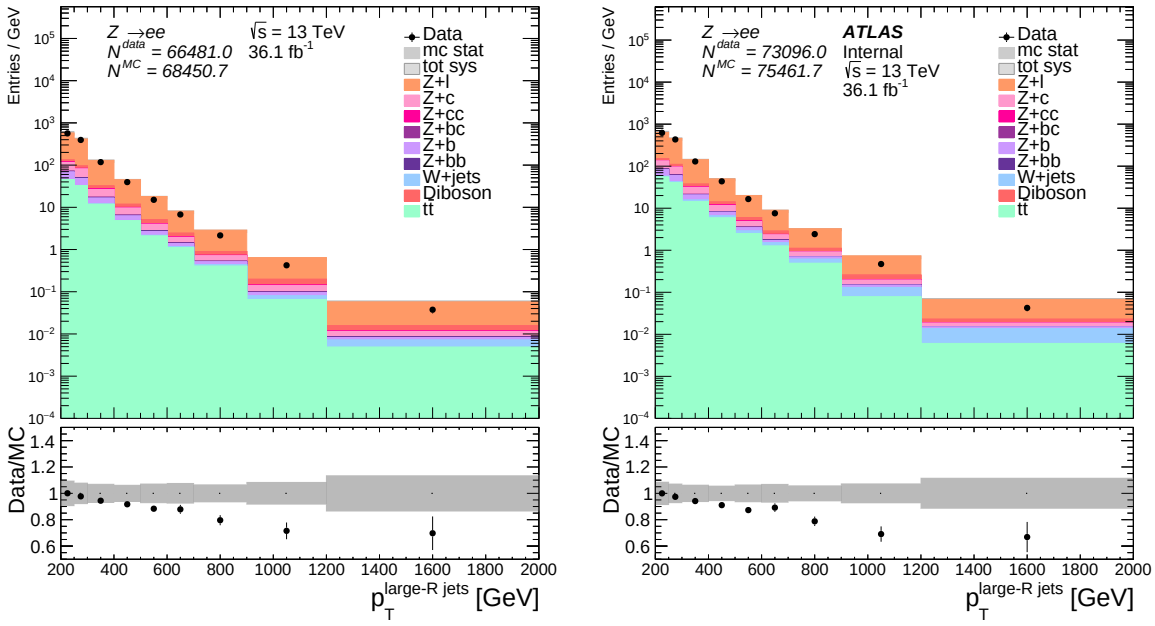

Figure 5.13: A comparison of $p_{\mathrm{T}}^{\mathrm{J}}$ in a) the signal region (also shown in Figure 5.4) and b) the $W+$jets-enriched region. The systematic uncertainties are combined and shown by the dark grey band, and the statistical uncertainties are shown by the light grey band. The statistical uncertainty on the data is given by the error bar on the data point.

Inclusive selection - multijet-enriched

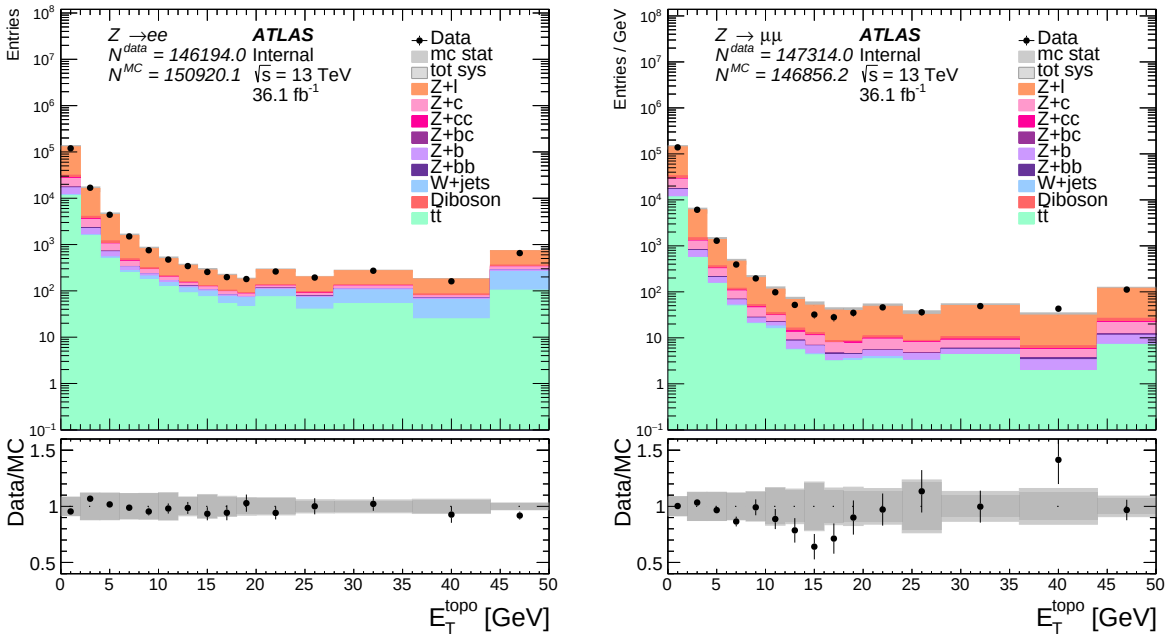

Figure 5.14: INCLUSIVE SELECTION: Data-MC comparison of $E_{\mathrm{T}}^{\mathrm{topocone0.2}}$ in (a) the electron channel and b) the muon channel. The systematic uncertainties are combined and shown by the dark grey band, and the statistical uncertainties are shown by the light grey band. The statistical uncertainty on the data is given by the error bar on the data point.

5.5 Unfolding

The aim of the measurement is to extract particle-level cross-sections differential in the kinematic variables of interest, but so far in this thesis these variables have been measured at detector-level only. To get the particle-level measurement, the data is "unfolded". Unfolding is the term used to describe the procedure of inferring the "true" kinematic distribution from data by removing distortions due to detector resolution effects from the measurement. The primary motivation for unfolding the data is that it allows measurements made using different detectors which perform differently, e.g. ATLAS and CMS, to be directly compared with minimal correction. In addition, it preserves the measurement for comparisons with new predictions in the future, in the case that information about the detector effects becomes unavailable.

The method used to unfold the data in this analysis was the fully Bayesian unfolding technique (FBU) [81], the details of which are presented in Section 5.5.2. The data are unfolded to the particle-level fiducial-selection defined in Section 5.5.1. The response matrices for the observables are presented in Section 5.5.3, followed by the details of tests performed to validate the unfolding method. The final results come from a combined unfolding of the data from both the electron channel and the muon channel. Before doing this, the consistency of the results from each of these channels was checked, as discussed in Section 5.5.4.

5.5.1 Particle-level fiducial selection

The data were corrected to a particle-level fiducial selection which closely matched the detector-level selection, to minimise any model-dependent extrapolation. Exactly two leptons, e or μ, with $p_{\mathrm{T}} > 27$ GeV and $|\eta| < 2.5$ were required to select the Z-boson, where there was no opposite-sign requirement on the leptons. At least one truth-level large-R jet was required, with $p_{\mathrm{T}} > 200$ GeV and $|\eta| < 2.0$. This truth-level large-R jet was built from stable truth-particles. Like in the detector-level selection, overlap removal between the large-R jets and the leptons was applied, where they were required to be separated by $\Delta R > 1.0$.

The events were characterised based on the number of true b-labelled track-jets that were matched to the large-R jet. The truth-level track-jets were built from stable charged particles. The matching was performed by requiring that the track-jets and the large-R jet satisfy the geometric requirement that $\Delta R(\text{track-jet}, \text{large-}R\text{ jet}) < 1.0$. Due to technical limitations, it was not possible to perform ghost-association between the track-jets and the large-R jets which would have been preferred in order to match the detector-level selection more closely. The truth-level track-jets were considered b-labelled if a true b-hadron with $p_{\mathrm{T}} > 5$ GeV was ghost-associated to them. The large-R jet was

considered to have two b-tags if there were exactly two b-labelled track-jets associated to it. In the case that there was more than one large-R jet in the event, if one of the jets was categorised as 2-tag then it was classed as the signal jet, otherwise the highest p_{T} large-R jet was classed as the signal jet.

5.5.2 Fully Bayesian unfolding method

The FBU technique was used to derive the posterior probability of the particle-level differential cross-sections given the observed data [81]. To extract this probability, the likelihood of the data given the MC prediction was constructed, where the parameters of interest were the particle-level signal cross-sections ($\vec{\sigma}^{\mathrm{p}}$). The systematic uncertainties described in Section 5.6 were taken into account using nuisance parameters ($\vec{\rho}$) which allow for additional degrees of freedom in the likelihood.

The first component of the likelihood function was the total predicted number of signal and background events in each bin of the detector-level observables, given a set of $\vec{\sigma}^{\mathrm{p}}$ and $\vec{\rho}$ values. The total predicted event count in bin r of a detector-level observable (x_r) was defined as the product of the luminosity, $\mathscr{L}(\vec{\rho})$, and the predicted cross-sections for background, $b_r(\vec{\rho})$, and signal, $s_r(\vec{\rho})$,

$$x_r(\vec{\sigma}^{\mathrm{p}}, \vec{\rho}) = \mathscr{L}(\vec{\rho}) \left(b_r(\vec{\rho}) + s_r(\vec{\rho}) \right). \tag{5.1}$$

The predicted signal cross section can be defined in terms of the particle-level signal cross-sections via the response matrix, $\mathcal{R}(\vec{\rho})$,

$$s_r(\vec{\rho}) = \sum_t \mathcal{R}_{rt}(\vec{\rho}) \sigma_t^{\mathrm{p}}, \tag{5.2}$$

where t denotes the index of the particle-level bin. The elements of the response matrix represent the conditional probability for a particle-level event in bin t to have a matching detector-level event in bin r. The background predictions, $b_i(\vec{\rho})$, were constructed as linear interpolations between the nominal prediction and the prediction corresponding to each systematic uncertainty. They were defined as

$$b_r(\vec{\rho}) = b_{r,0} + \sum_{k \in \text{ systematics}} \rho_k (b_{r,k} - b_{r,0}). \tag{5.3}$$

where $b_{r,0}$ is the nominal background prediction in bin r, $b_{r,k}$ is the background prediction in bin r from the systematic variation k, and ρ_k is the unit-scaled nuisance parameter corresponding to this

variation. The response matrices are computed in a similar manner

$$\mathcal{R}_{rt}(\vec{\rho}) = \mathcal{R}_{rt,0} + \sum_{k \in \text{systematics}} \rho_k \left(\mathcal{R}_{rt,k} - \mathcal{R}_{rt,0} \right), \tag{5.4}$$

where $\mathcal{R}_{rt,0}$ is the nominal response matrix, and $\mathcal{R}_{rt,k}$ is the response matrix for systematic variation k. Defined in this manner, the background predictions and signal predictions – via the response matrices – were smoothly varied, allowing the space of predictions created by systematic uncertainties to be explored.

Finally, the likelihood was constructed as the product of Poisson probabilities over all detector-level bins r, as a function of the model parameters, $\vec{\sigma}^{\text{p}}$ and $\vec{\rho}$:

$$\mathcal{L}(\vec{d} \mid \vec{\sigma}^{\text{p}}, \vec{\rho}) = \prod_{r \in \text{bins}} \text{Poiss}(d_r, x_r(\vec{\sigma}^{\text{p}}, \vec{\rho})). \tag{5.5}$$

The posterior probability distribution given the observed data was then defined as

$$\mathcal{P}(\vec{\sigma}^{\text{p}}, \vec{\rho} \mid \vec{d}) = \mathcal{L}(\vec{d} | \vec{\sigma}^{\text{p}}, \vec{\rho}) \cdot \prod_{k \in \text{systematics}} \text{Prior}_k(\rho_k). \tag{5.6}$$

The mode of this distribution over all parameters of interest and nuisance parameters was determined using Newton's method of gradient ascent on the log-likelihood [82]. The likelihood distribution was then sampled using a Metropolis-Hastings Markov Chain Monte Carlo, assisted by calculating the Hessian matrix of the likelihood distribution at the maximum-likelihood point. Using this method, the full posterior distribution in the combined space of nuisance parameters and particle-level signal cross-sections was obtained.

A flat prior probability distribution was imposed on the particle-level cross-sections with the requirement that each particle-level cross-section be non-negative. A flat prior was chosen to express "prior ignorance"[1] on the values of the cross sections with the aim of not biasing the results. The prior definitions for nuisance parameters corresponding to systematic variations are discussed in Section 5.6.6.

5.5.3 Response matrices

The effects of the detector were encoded in the response matrix, which is a key ingredient of the unfolding procedure. It is built for each observable from simulated events which fulfil both the

[1] An alternative choice of prior to express "prior ignorance" would be the Jeffreys prior.

detector- and particle-level requirements. Each component of the response matrix, $\mathcal{R}_{rt}$, is the conditional probability for a particle-level object with an observable in bin t to have a matching detector-level object with an observable in bin r. Figures 5.15 to 5.18 show the response matrices for each variable in the inclusive region and 2-tag region for both the electron and muon channel, built using the nominal MC prediction. The matrices are generally diagonal across variables meaning that particle-level events tended to be reconstructed in the same detector-level bin.

Events at particle-level sometimes did not have a detector-level counterpart if the detector-level event lay outside of the experimental acceptance, which lead to a truth-to-reconstruction efficiency, ϵ, which was included in the response matrix. The response matrix can be written in terms of ϵ by introducing the migration matrix $\mathcal{M}_{rt}$,

$$\mathcal{R}_{rt} = \frac{\mathcal{M}_{rt}}{\epsilon_t^{-1} \sum_{i=1}^{n} \mathcal{M}_{it}}, \tag{5.7}$$

where n is the number of particle-level bins. Each element of the migration matrix, $\mathcal{M}_{rt}$, is the joint probability that a particle-level object is produced in observable bin t and reconstructed in observable bin r. The truth-to-reconstruction efficiency for each variable in each channel is shown in Figures 5.19 to 5.22.

Non-fiducial $Z+$jets background

If an event at detector-level did not have a particle-level counterpart, it was considered to be part of a non-fiducial $Z+$jets background. This could happen if the detector-level event migrated into the experimental acceptance whilst its particle-level counterpart was outside of the fiducial-acceptance. This could also happen if the detector-level event was mis-reconstructed. For example in the case of variables in the 2-tag region, a jet which is c- or light-flavour at particle-level may be mis-tagged as a b-jet by the b-tagging algorithms, meaning it passed the detector-level selection but not the fiducial selection. This relies on the assumption that the MC sample was accurately predicting the particle-level properties, which may not have been the case: for this reason, systematic uncertainties on the signal-modelling were taken into account.

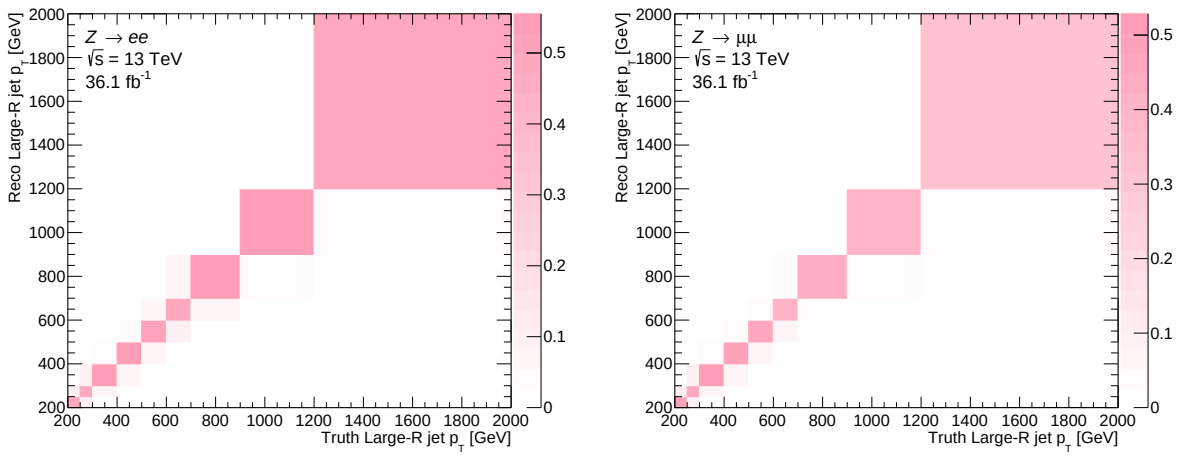

(a)

(b)

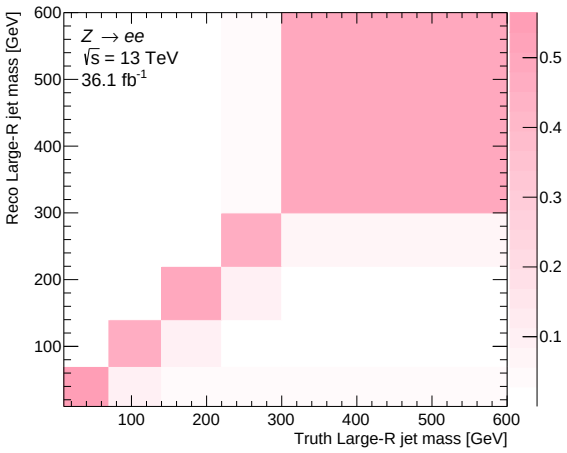

(c)

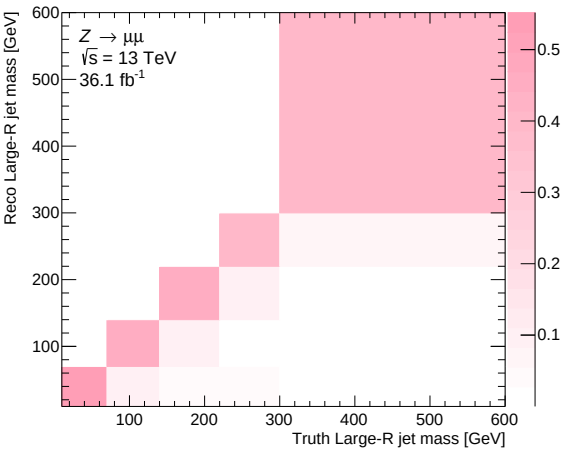

(d)

Figure 5.15: The response matrices for $p_{\mathrm{T}}^{\mathrm{J}}$ (top) and m_{J} (bottom) in the inclusive region for the electron channel on the left, and the muon channel on the right.

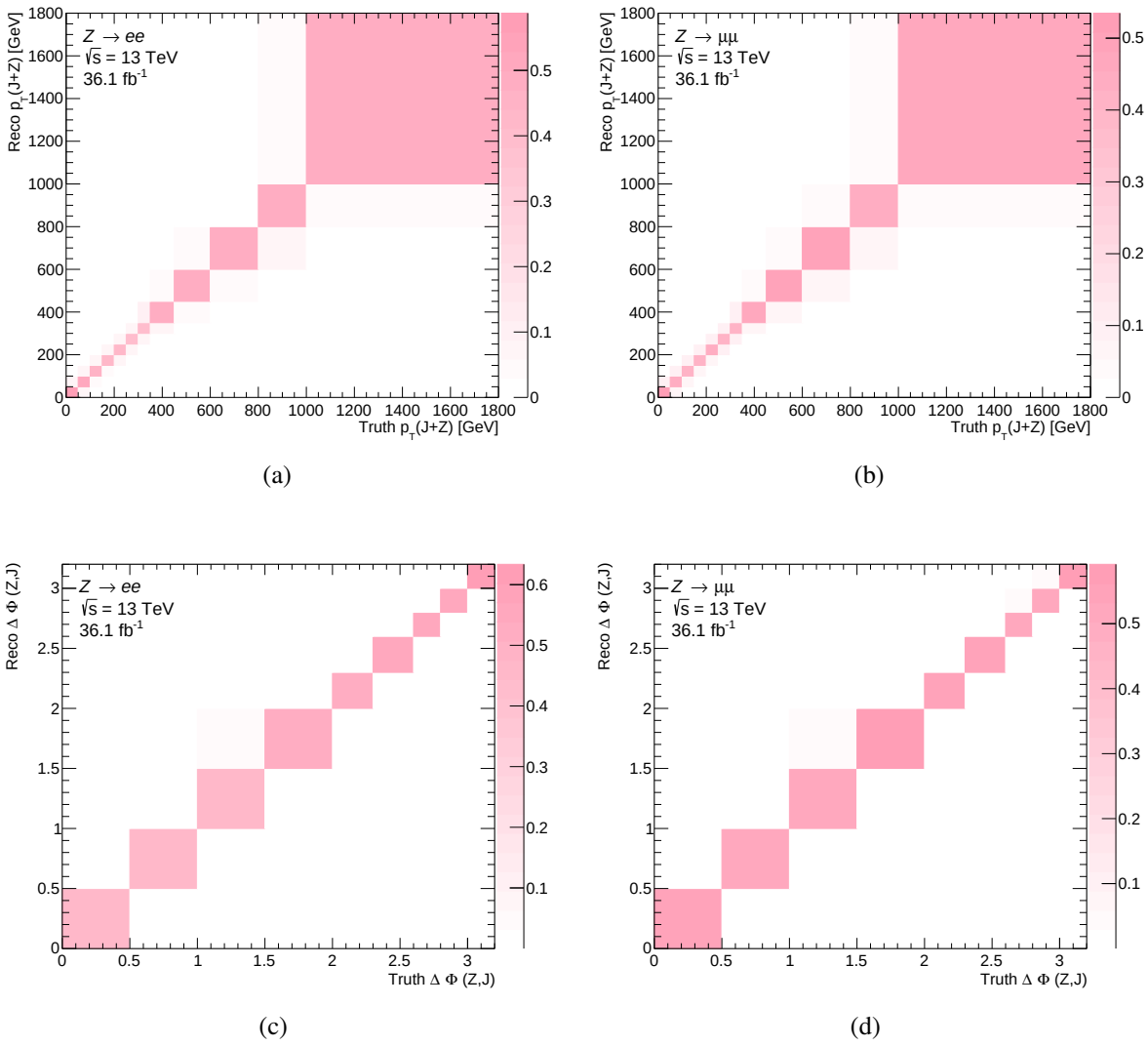

Figure 5.16: The response matrices for $p_{\mathrm{T}}^{\mathrm{J}+Z}$ (top) and $\Delta\phi(Z,\mathrm{J})$ (bottom) in the inclusive region for the electron channel on the left, and the muon channel on the right.

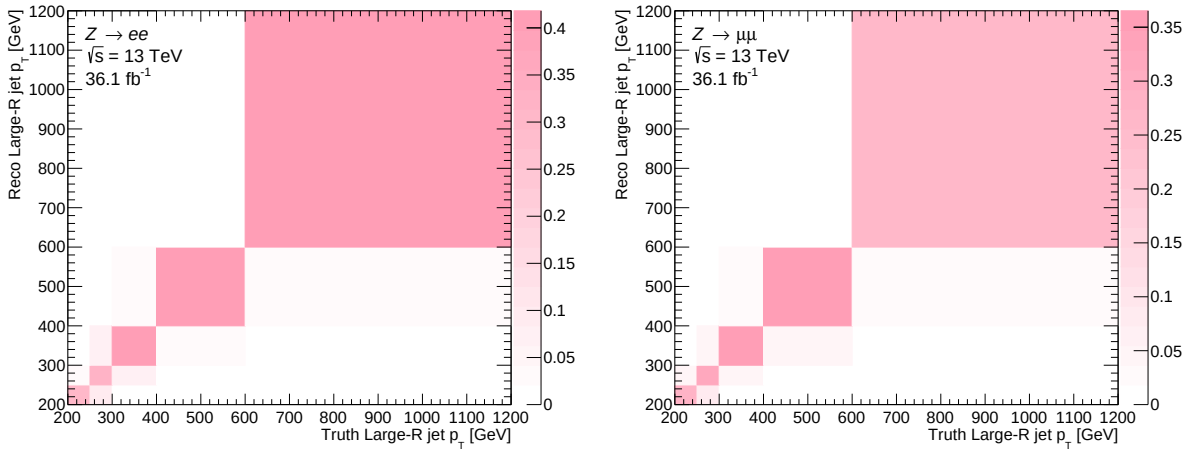

(a)

(b)

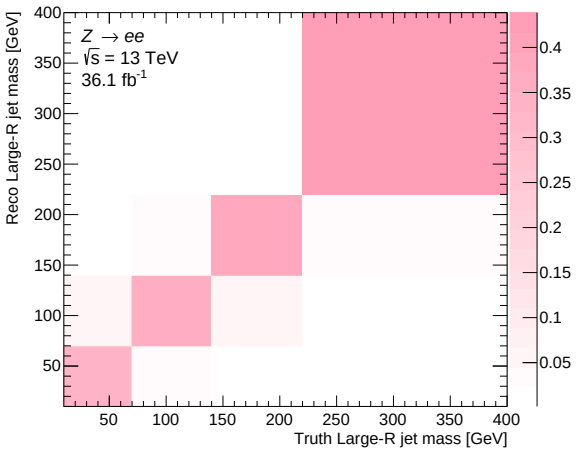

(c)

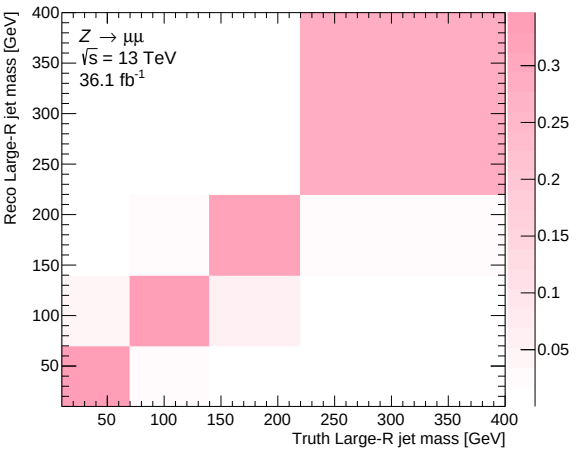

(d)

Figure 5.17: The response matrices for $p_{\mathrm{T}}^{\mathrm{J}}$ (top) and m_{J} (bottom) in the 2-tag region for the electron channel on the left, and the muon channel on the right.

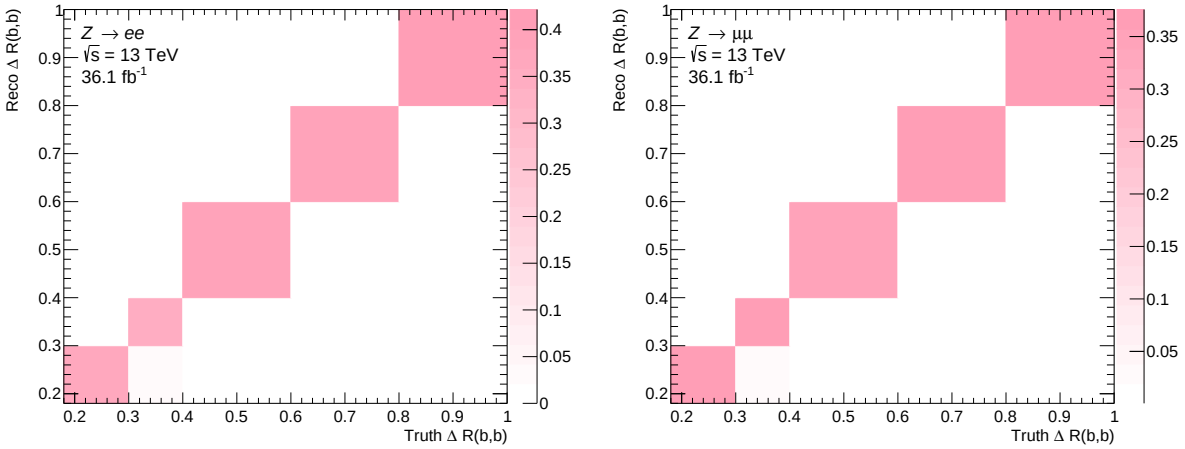

(a) (b)

Figure 5.18: The response matrices for the separation between the b-tagged associated track-jets, $\Delta R(b, \bar{b})$, in the 2-tag region for the electron channel on the left, and the muon channel on the right.

5.5.4 Unfolding tests

To ensure confidence in the unfolding procedure, a series of validation tests were performed. The first was a technical closure test to check that the unfolding framework was able to unfold the nominal detector-level MC prediction to obtain the corresponding truth-level prediction. A so called data-driven closure test was performed to assess the sensitivity of the unfolding method to data/MC shape-differences in the measured observables, the results of which are discussed. Before performing the combined unfolding of the electron and muon channel, the compatibility of the channels was checked. Finally, to assess the sensitivity of the results to the choice of prior on the particle-level cross sections, the unfolding was performed using alternative priors and the results were compared. These tests are now treated in turn. It should be noted that the binning shown in the plots in this section can differ from the binning shown in the final results, as a number of these tests were performed before the binning was finalised.

Technical closure test

The technical closure test was performed to validate the technical implementation of the unfolding procedure. The detector-level MC prediction from the same MC sample that was used to build the nominal response matrix was used as the data. This was then unfolded using the nominal response matrix and the resulting unfolded distribution was expected to match the truth-level prediction from the same MC sample, within the limits of numerical precision. Since the MC events have various scale factors applied, the resulting number of events in a bin can be a non-integer value. The rounding of these non-integer event counts means that the unfolded results may not match exactly with the best prediction from the Poisson distribution. This is especially true in low-population bins where the rounding "error" is a larger fraction of the bin population. Figures 5.23 to 5.26 show the results of this closure test for each variable in both the electron and muon channel and demonstrate that good technical closure was observed.

Data-driven closure test

The data-driven unfolding test was performed to assess whether the unfolded results were sensitive to mismodelling of observables by the MC prediction. This was performed by Dr Andy Buckley by reweighting the MC prediction using a smooth function of truth-level observables, such that the detector-level MC prediction matched the data more closely. The smooth function was obtained by performing a single-value-decomposed pseudo-inversion of the response matrix, which was then applied to the data. The ratio between the resulting truth-prediction from this method and the orig-

inal truth prediction was then fitted with a third-order polynomial. The reweighted detector-level prediction was unfolded using the original, nominal response matrix. If the method was insensitive to data/MC mismodelling, then the unfolded results were expected to be consistent with the reweighted truth prediction.

The procedure was carried out for each variable in each channel and the results are shown in Figures 5.27 to 5.30. It can be seen that for most of the variables, the results were compatible with the reweighted truth-level prediction and therefore the ability to unfold observables was largely unaffected by their data/MC shape differences at detector-level. The exceptions to this were the $p_{\mathrm{T}}^{\mathrm{J}}$ and $p_{\mathrm{T}}^{\mathrm{J}+Z}$ observables, which is not too surprising given that these variables had the worst modelling by the MC predictions at detector level. To account for this effect, the deviations that were observed from this closure test were added in quadrature with the final unfolded uncertainty.

Sensitivity to choice of signal prior

To assess the sensitivity of the unfolded results to the choice of prior on the parameters of interest, the data were unfolded using the following priors:

- A flat prior – the nominal choice of prior,
- A Gaussian centred on the Sherpa-predicted differential cross section in the given bin, denoted as σ^{Sherpa}, with a width of 1.0 in units of the differential cross section,
- A Gaussian centred on σ^{Sherpa}, with a width equal to σ^{Sherpa}.

This was considered to be a stress-test of the procedure, as these priors were not believed to be representative of our prior belief on the particle-level cross section. The unfolded results using these alternative priors were compared to the nominal scenario, where flat priors were used. The results of this test are shown in Figures 5.31 to 5.32. In the bottom panel of these plots, the ratio between the data unfolded with the alternative priors ("Other") and data unfolded with the flat priors are shown. The SHERPA prediction is also included for reference. These results show that the unfolded results obtained using each different priors were largely consistent with one another, with deviations of up to 10% observed for only a handful of bins. Since these priors were not considered to be sensible choices and an uncertainty was already assigned from the results of the data-driven closure-test, there was no additional uncertainty assigned based on this test.

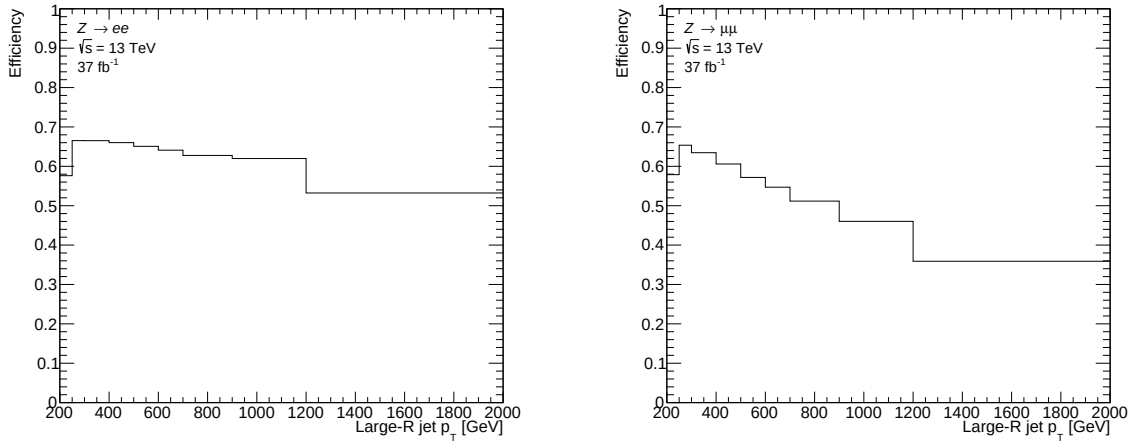

(a)

(b)

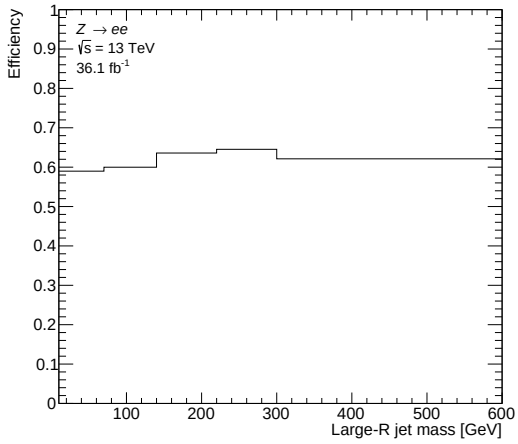

(c)

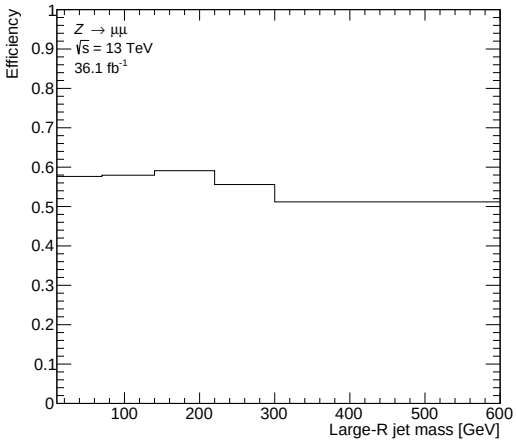

(d)

Figure 5.19: The truth-to-reconstruction efficiency for $p_{\mathrm{T}}^{\mathrm{J}}$ (top) and m_{J} (bottom) in the inclusive region for the electron channel on the left, and the muon channel on the right.

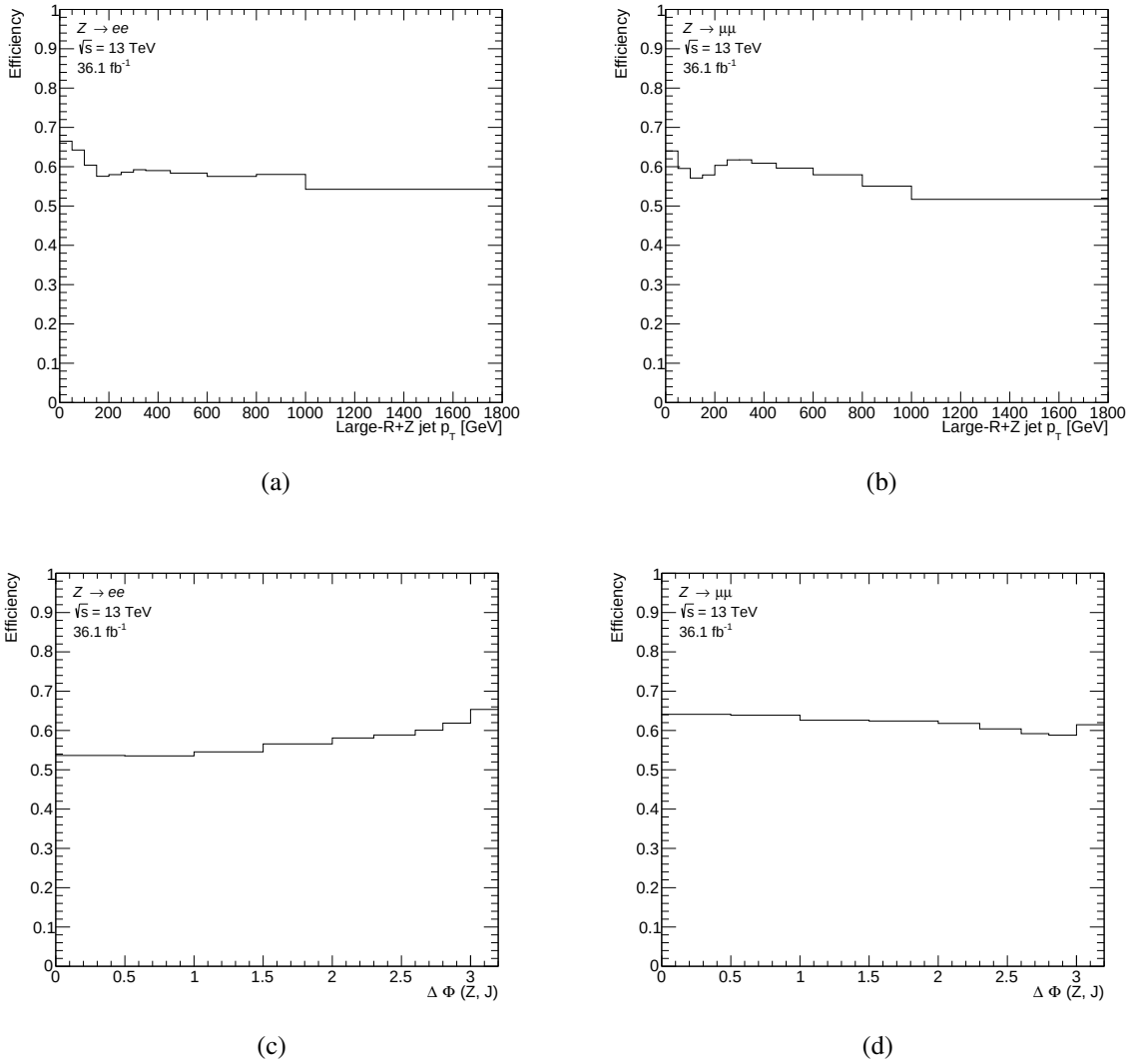

Figure 5.20: The truth-to-reconstruction efficiency for $p_{\mathrm{T}}^{\mathrm{J}+Z}$ (top) and $\Delta\phi(Z,\mathrm{J})$ (bottom) in the inclusive region for the electron channel on the left, and the muon channel on the right.

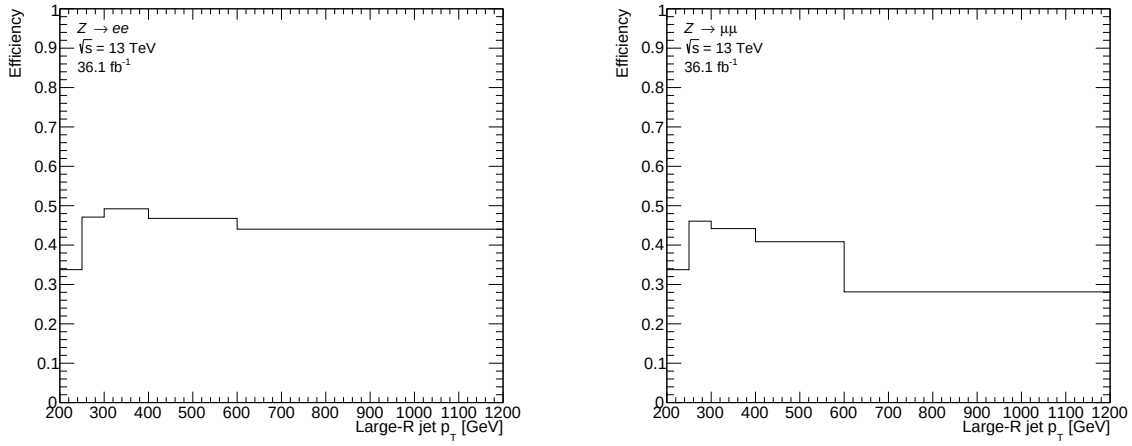

(a)

(b)

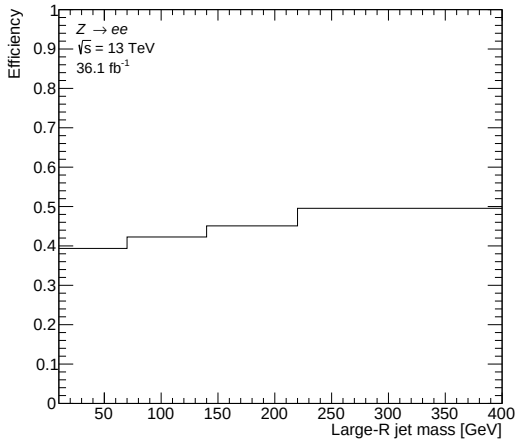

(c)

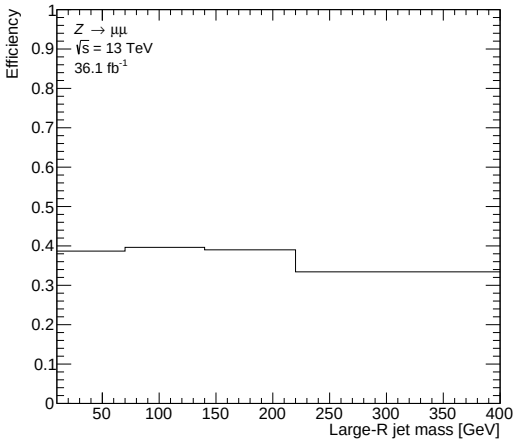

(d)

Figure 5.21: The truth-to-reconstruction efficiency for $p_{\mathrm{T}}^{\mathrm{J}}$ (top) and m_{J} (bottom) in the 2-tag region for the electron channel on the left, and the muon channel on the right.

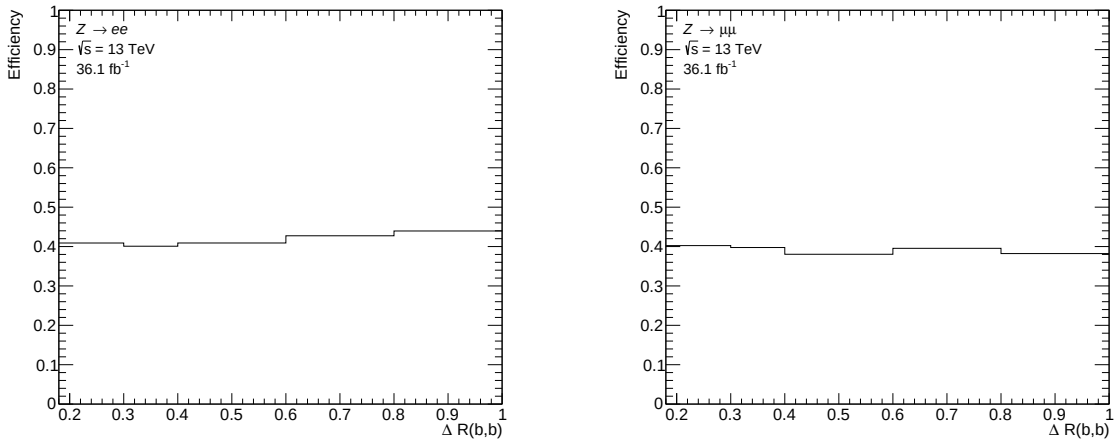

(a) (b)

Figure 5.22: The truth-to-reconstruction efficiency for the separation between the b-tagged associated track-jets, $\Delta R(b,\bar{b})$, in the 2-tag region for the electron channel on the left, and the muon channel on the right.

Inclusive selection: technical closure test

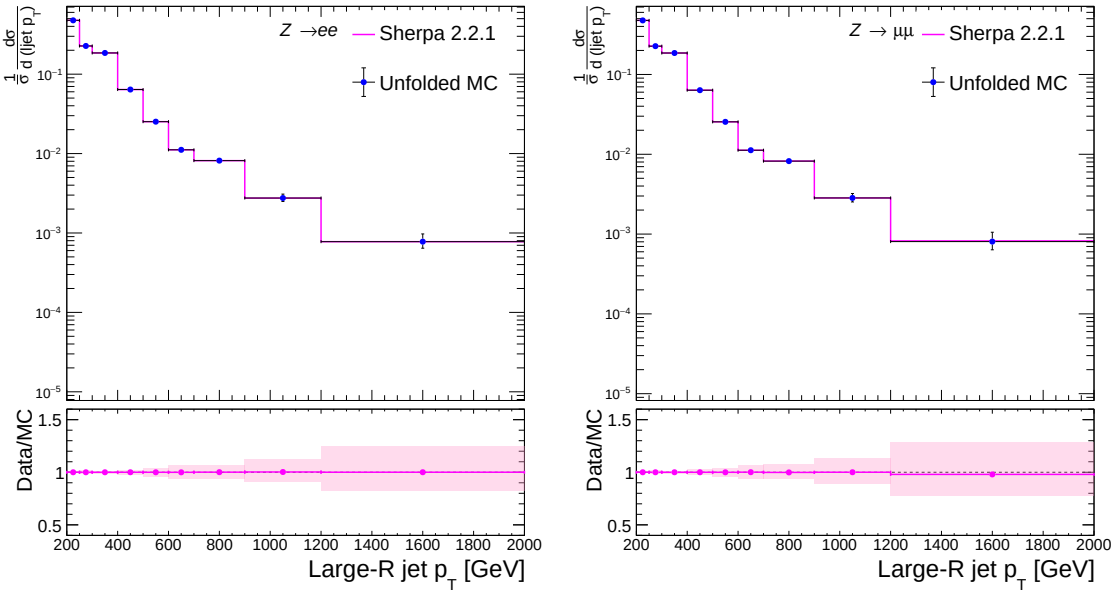

(a)

(b)

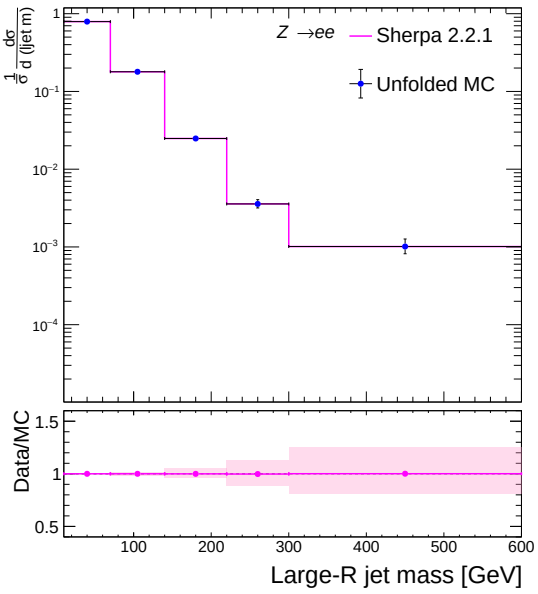

(c)

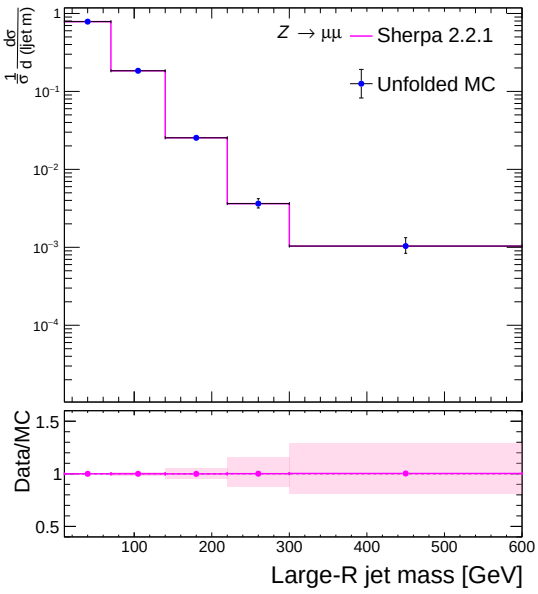

(d)

Figure 5.23: The unfolded SHERPA prediction compared to the truth-level cross section for $p_{\mathrm{T}}^{\mathrm{J}}$ (top) and m_{J} (bottom) in the inclusive region for the electron channel on the left, and the muon channel on the right. The error bars represent the 16–84% quantile range of the posterior distribution of each unfolded bin, and the central value is its the global posterior mode.

Inclusive selection: technical closure test

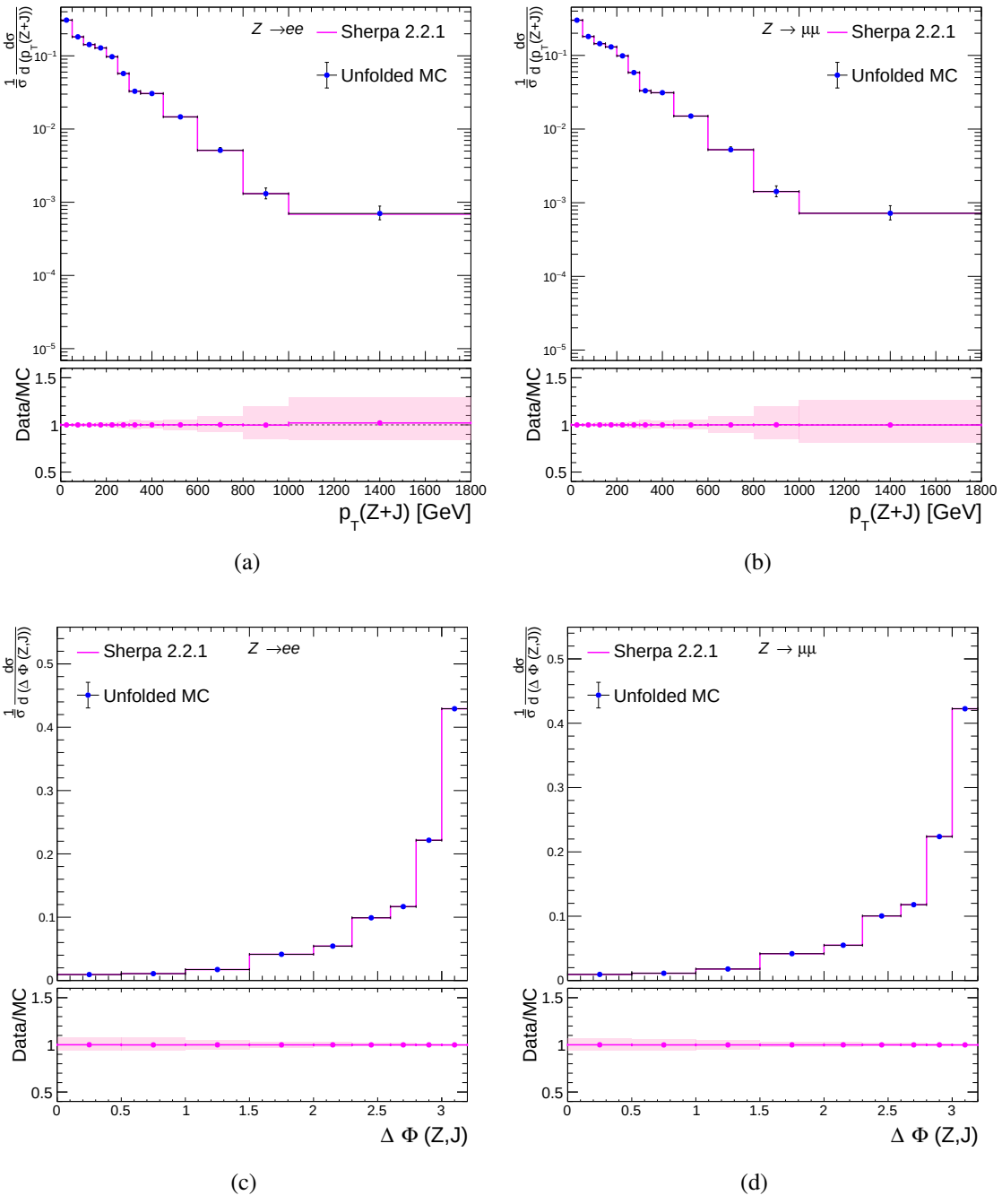

Figure 5.24: The unfolded SHERPA prediction compared to the truth-level cross section for $p_{\mathrm{T}}^{\mathrm{J}+Z}$ (top) and $\Delta\phi(Z,\mathrm{J})$ (bottom) in the inclusive region for the electron channel on the left, and the muon channel on the right. The error bars represent the 16–84% quantile range of the posterior distribution of each unfolded bin, and the central value is its the global posterior mode.

2-tag selection: technical closure test

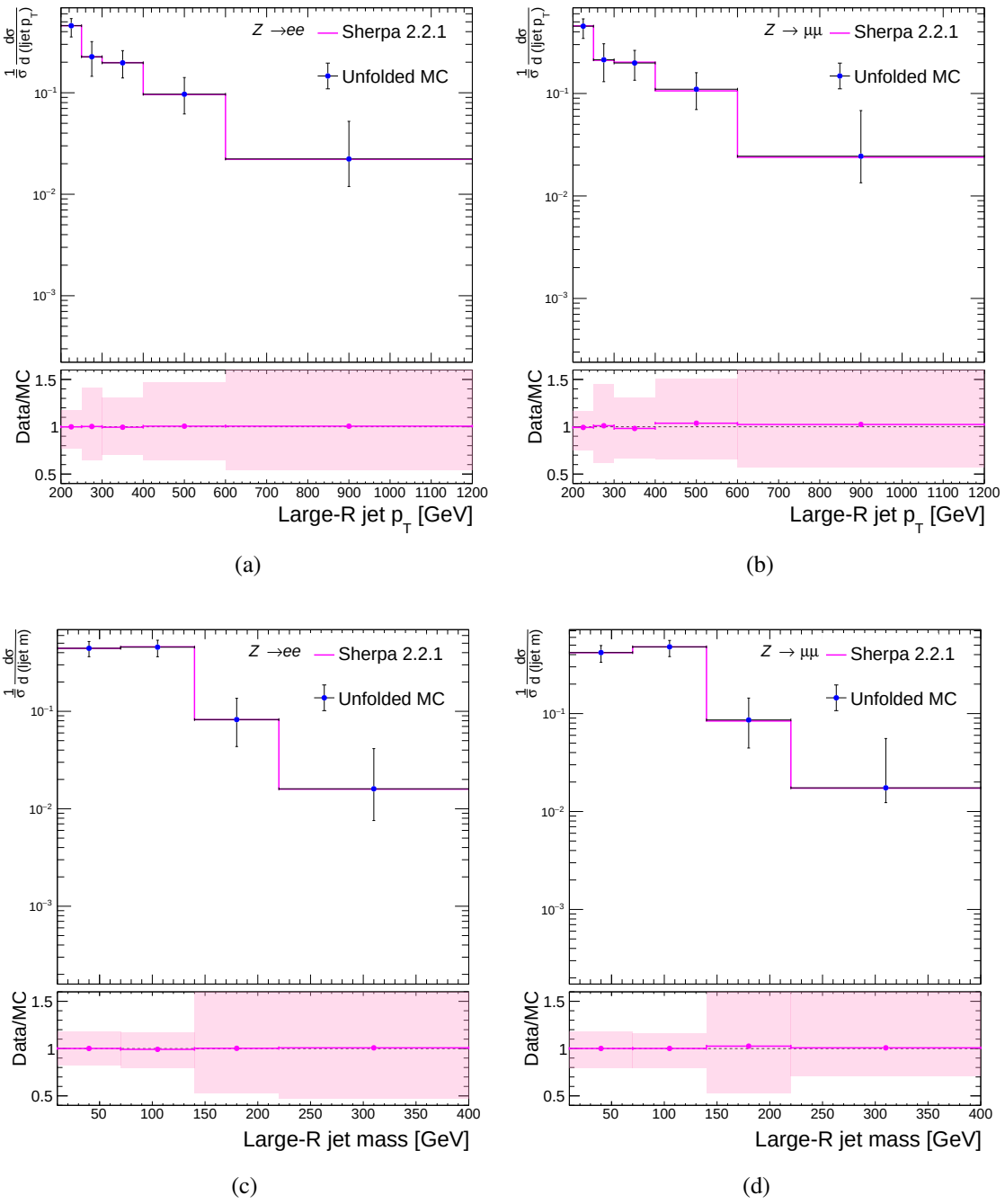

Figure 5.25: The unfolded SHERPA prediction compared to the truth-level cross section for $p_{\mathrm{T}}^{\mathrm{J}}$ (top) and m_{J} (bottom) in the 2-tag selection for the electron channel on the left, and the muon channel on the right. The error bars represent the 16–84% quantile range of the posterior distribution of each unfolded bin, and the central value is its the global posterior mode.

2-tag selection: technical closure test

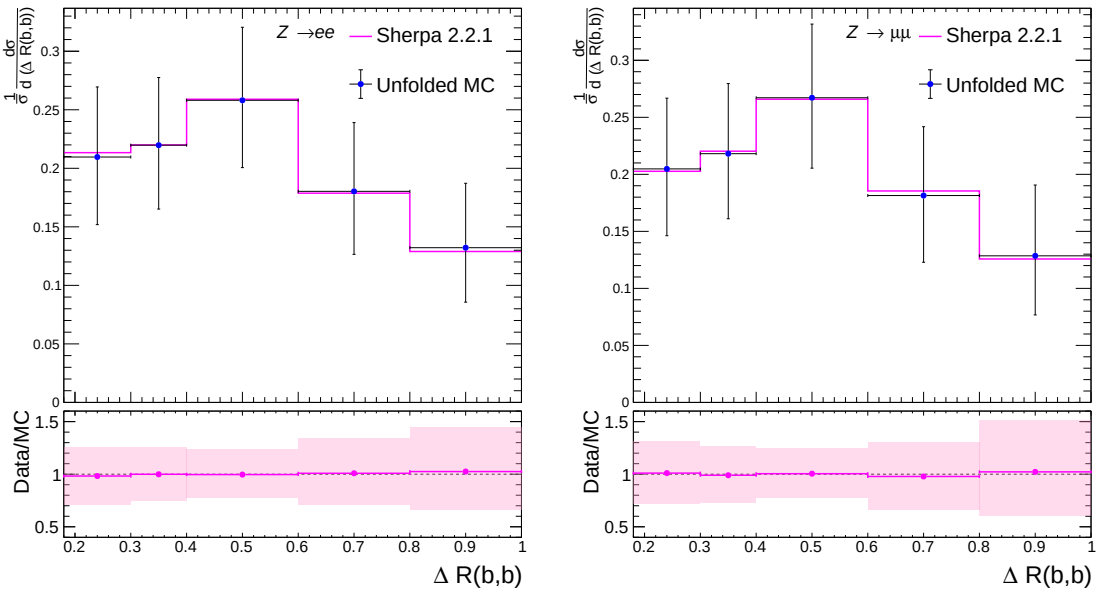

(a) (b)

Figure 5.26: The unfolded SHERPA prediction compared to the truth-level cross section for $\Delta R(b, \bar{b})$ in the 2-tag selection for the electron channel on the left, and the muon channel on the right. The error bars represent the 16–84% quantile range of the posterior distribution of each unfolded bin, and the central value is its the global posterior mode.

Inclusive selection: data-driven closure test

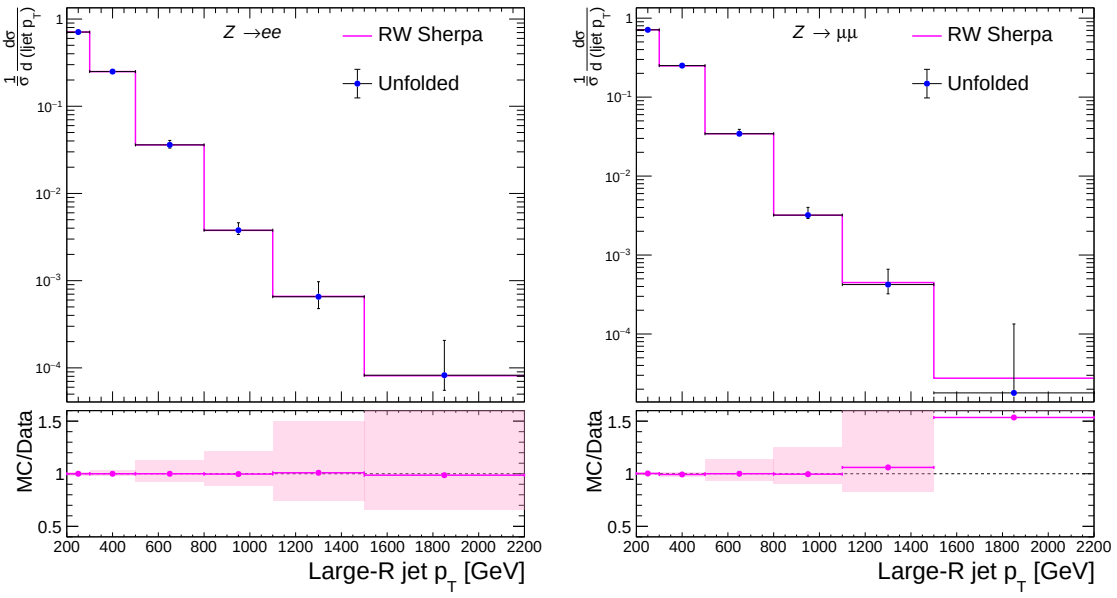

(a)

(b)

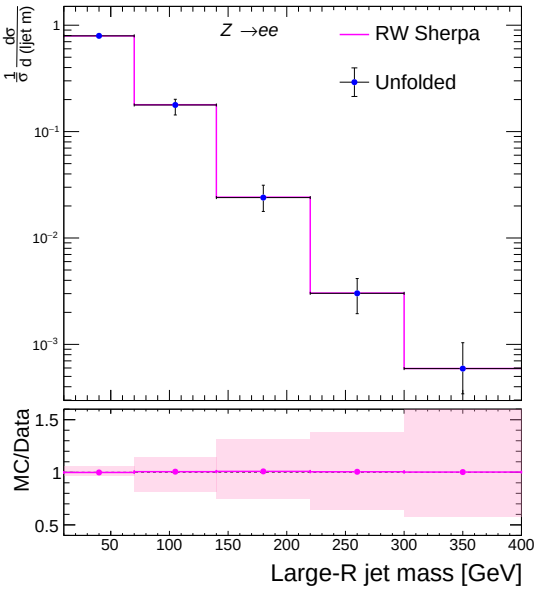

(c)

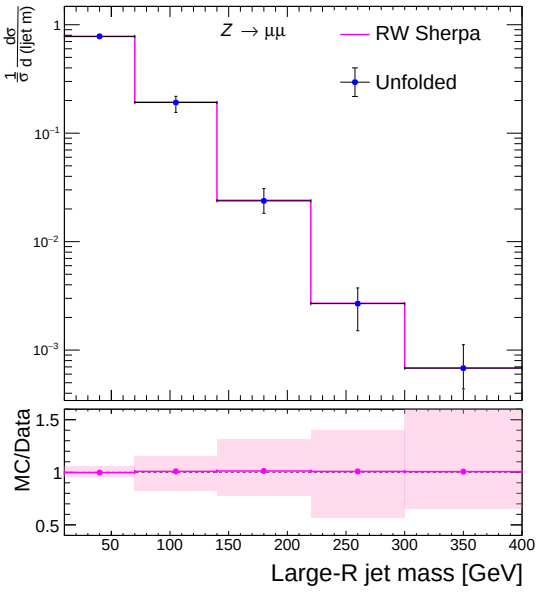

(d)

Figure 5.27: The unfolded pseudo-data compared to the reweighted truth-level cross section for $p_{\mathrm{T}}^{\mathrm{J}}$ (top) in the electron channel (right) and muon channel(left) and m_{J} (bottom) in the electron channel (right) and muon channel(left). The error bars represent the 16–84% quantile range of the posterior distribution of the unfolded pseudo-data in each bin, and the central value is its the global posterior mode.

Inclusive selection: data-driven closure test

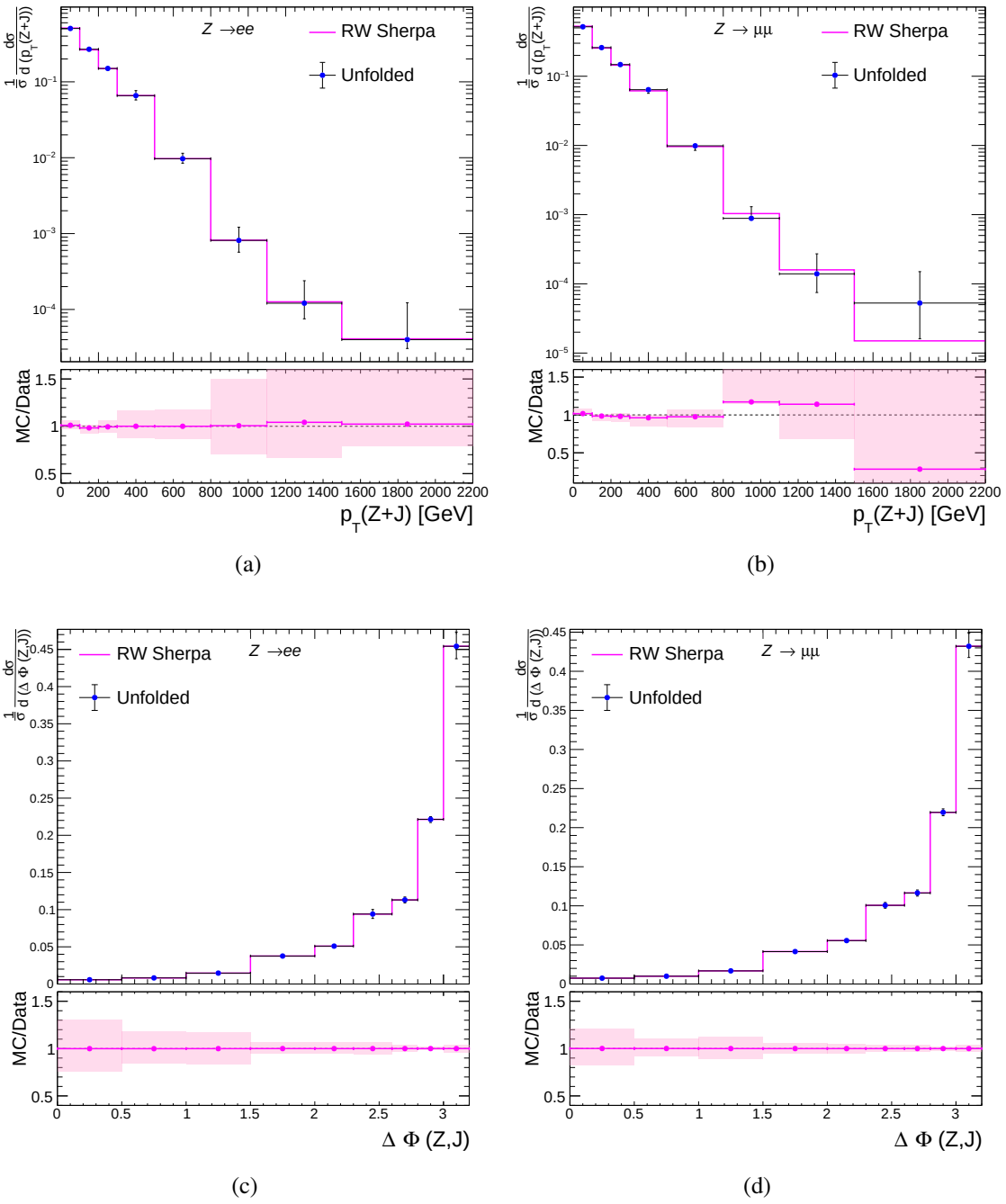

Figure 5.28: The unfolded pseudo-data compared to the reweighted truth-level cross section for $p_{\mathrm{T}}^{\mathrm{J}+Z}$ (top) in the electron channel (right) and muon channel(left) and $\Delta\phi(Z,\mathrm{J})$ (bottom) in the electron channel (right) and muon channel(left). The error bars represent the 16–84% quantile range of the posterior distribution of the unfolded pseudo-data in each bin, and the central value is its the global posterior mode.

2-tag selection: data-driven closure test

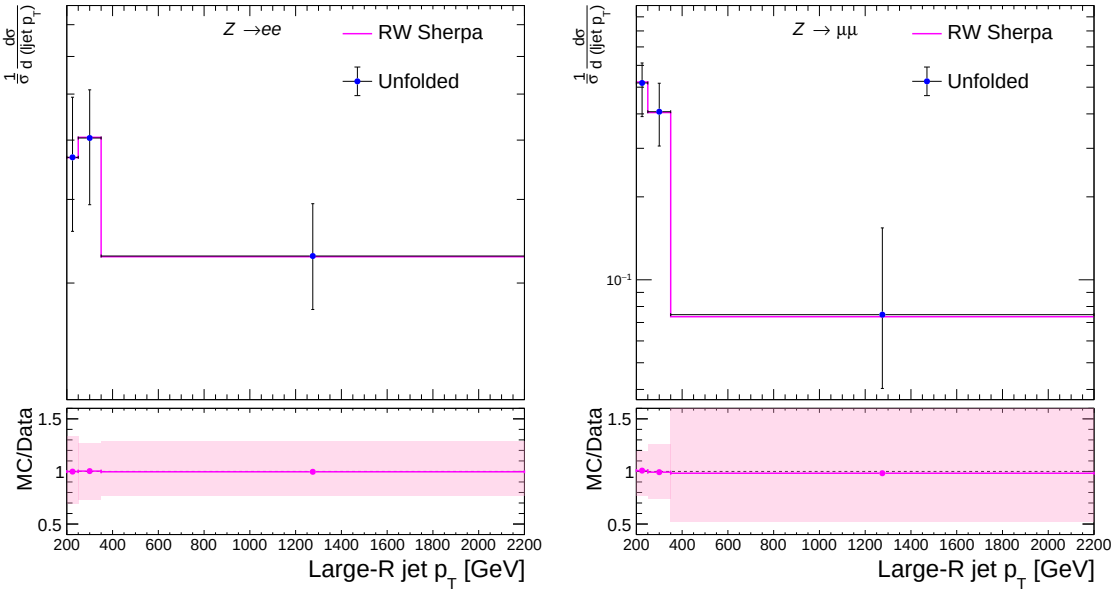

(a)

(b)

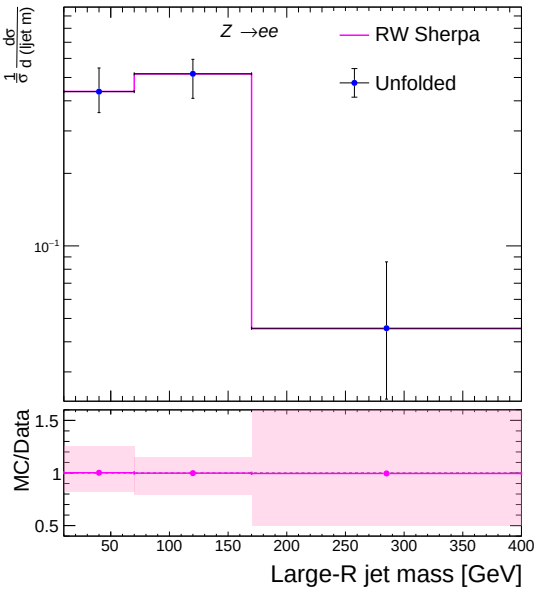

(c)

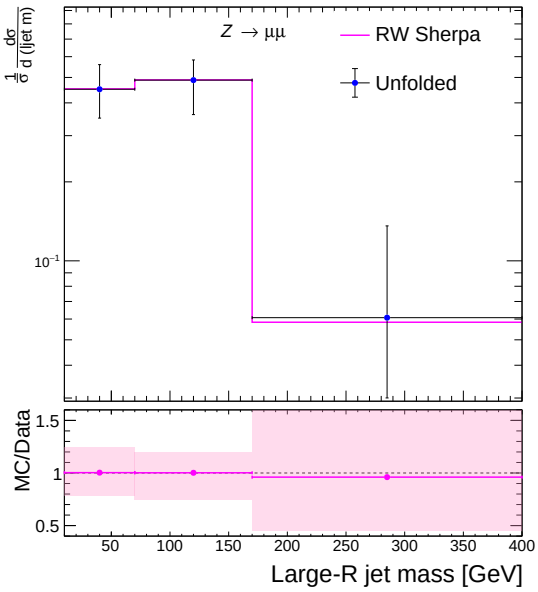

(d)

Figure 5.29: The unfolded pseudo-data compared to the reweighted truth-level cross section for $p_{\mathrm{T}}^{\mathrm{J}}$ (top) in the electron channel (right) and muon channel(left) and m_{J} (bottom) in the electron channel (right) and muon channel(left). The error bars represent the 16–84% quantile range of the posterior distribution of the unfolded pseudo-data in each bin, and the central value is its the global posterior mode.

2-tag selection: data-driven closure test

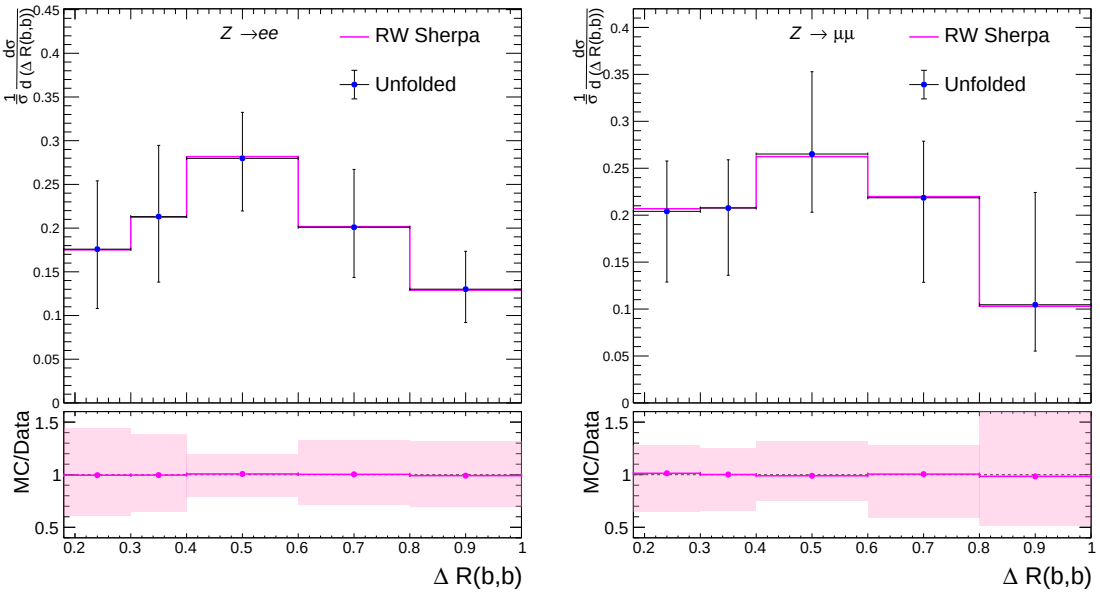

(a) (b)

Figure 5.30: The unfolded pseudo-data compared to the reweighted truth-level cross section for $\Delta R(b, \bar{b})$ in the electron channel (left) and the muon channel (right). The error bars represent the 16–84% quantile range of the posterior distribution of the unfolded pseudo-data in each bin, and the central value is its the global posterior mode.

Inclusive selection: signal-prior comparisons

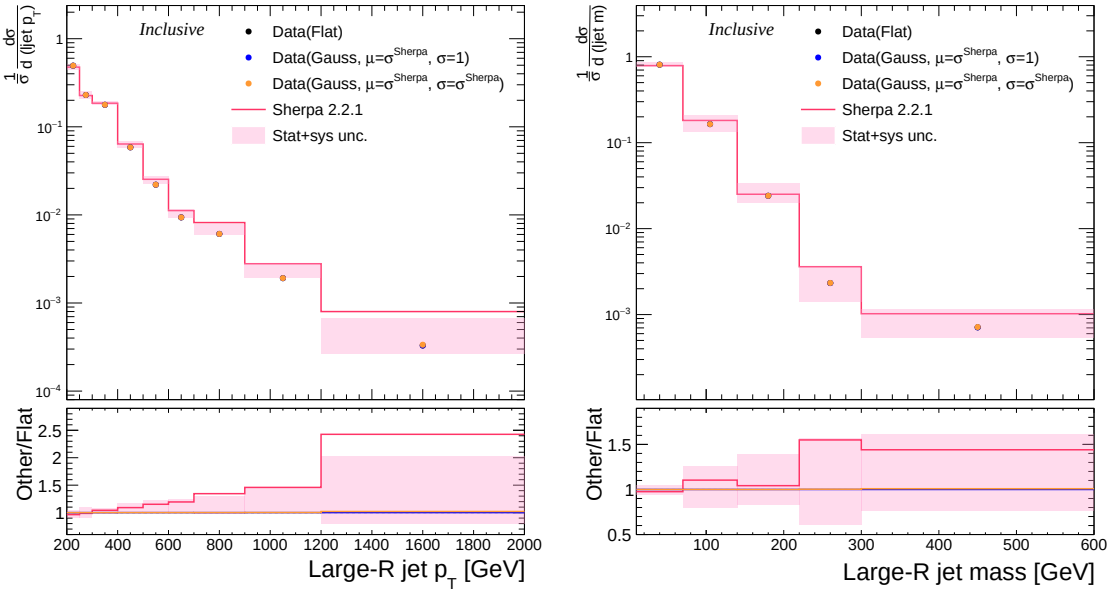

(a) (b)

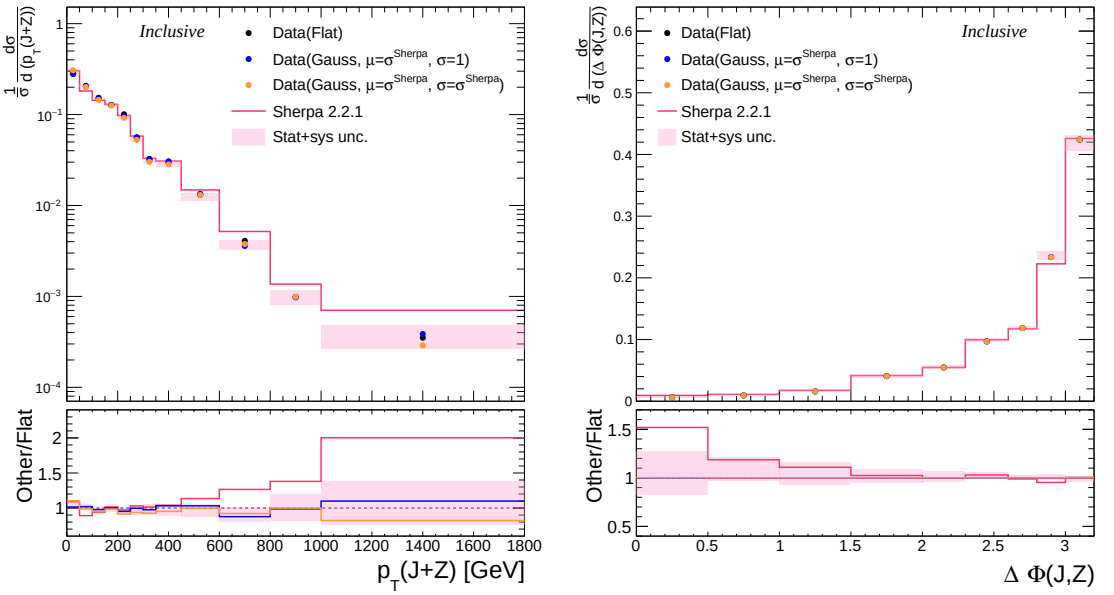

(c) (d)

Figure 5.31: Comparisons of the data unfolded with alternative signal priors to the nominal scenario where the data is unfolded with a flat prior. The inclusive variables a) $p_{\mathrm{T}}^{\mathrm{J}}$, b) m_{J}, c) $p_{\mathrm{T}}^{\mathrm{J+}Z}$ and d) $\Delta\phi(Z,\mathrm{J})$ are shown. The error bars represent the 16–84% quantile range of the posterior distribution of each unfolded bin in the nominal scenario, and the central value is its the global posterior mode.

2-tag region: signal-prior comparisons

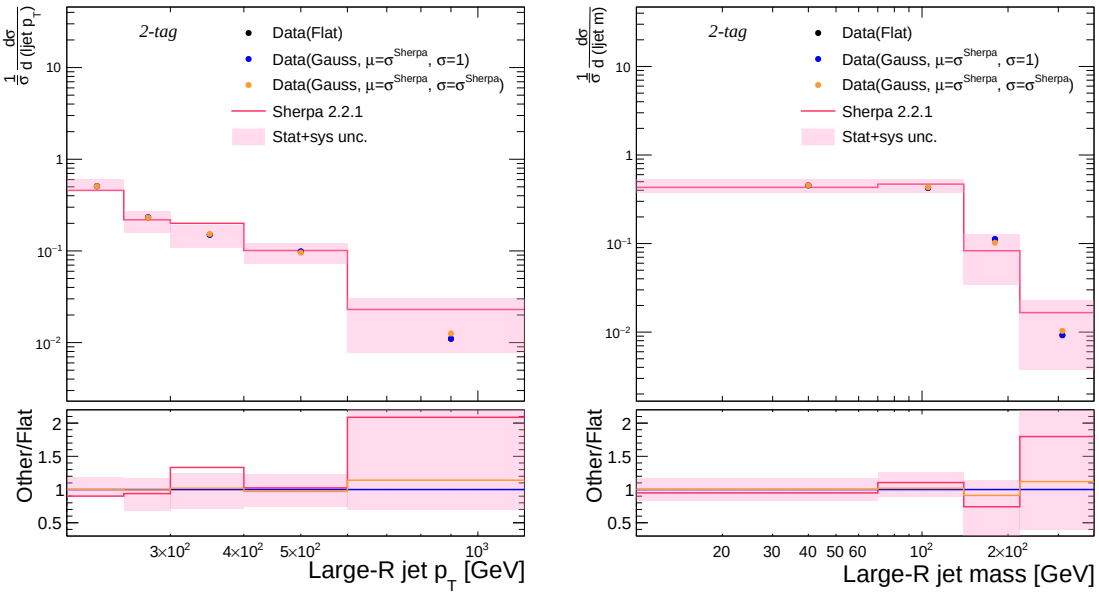

(a) (b)

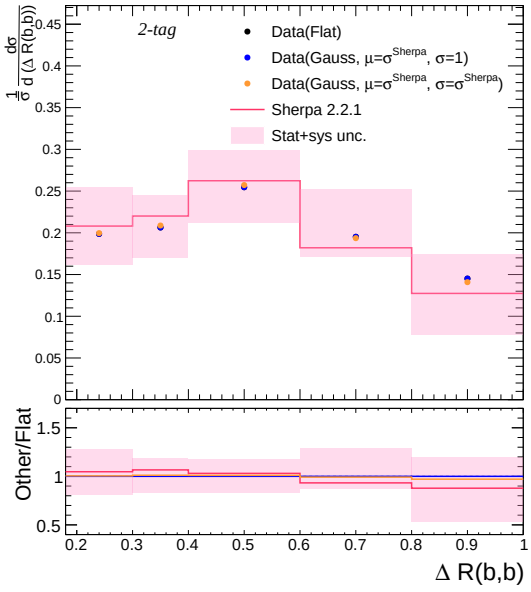

(c)

Figure 5.32: Comparisons of the data unfolded using different signal priors to the nominal scenario where the data is unfolded with a flat prior. The 2-tag variables a) $p_{\mathrm{T}}^{\mathrm{J}}$, b) m_{J} and c) $\Delta R(b,\bar{b})$ are shown. The error bars represent the 16–84% quantile range of the posterior distribution of each unfolded bin in the nominal scenario, and the central value is its the global posterior mode.

Lepton channel compatibility checks

The electron channel and muon channel were unfolded together to the same particle-level fiducial region defined in Section 5.5.1, which is referred to as the "combined" unfolding. To do this, the electron channel and muon channel response matrices are concatenated, as well as the data and background prediction. A diagram of the format of the combined response matrix in shown in Figure 5.33.

Before performing the combined unfolding of the data from the electron and muon channel, the compatibility between the individual results from the channels was assessed. Firstly, the nuisance parameters corresponding to common systematic variations on each variable were checked to ensure that they were compatible between the lepton channels. In particular, it was checked that the common nuisance parameters did not pull in different directions between the channels, which could lead to cancellations when combined. It was found that the nuisance parameter posteriors were compatible between the channels with no significant pulls observed. As an additional check, the unfolded results from the combined unfolding were compared to the results from the individual channels to check the consistency. These comparisons for each variable are shown in Figures 5.34 to 5.35. In some bins there were apparent tensions between the unfolded results from the individual lepton channels; for example the final two bins of the $p_{\mathrm{T}}^{\mathrm{J}+Z}$ distribution and the final bin of the 2-tag $p_{\mathrm{T}}^{\mathrm{J}}$ and m_{J}. To understand if these were significant, the data was unfolded in each lepton channel including only nuisance parameters related to the MC statistical uncertainty and lepton-related systematics. These results for each variable are compared in Figures 5.36 to 5.37. These plots show that in most cases the difference is not significant within the 1σ defined uncertainty.

5.6 Systematic uncertainties

The systematic uncertainties which affected the measurement can be split into two categories: detector-related and modelling-related. The sources of uncertainty from each of these categories are described in the following sections. In the unfolding procedure, the systematics were assessed using nuisance parameters. A nuisance parameter was defined for each systematic uncertainty and was associated with the corresponding "template" of the particular uncertainty, which included the background prediction and response-matrix prediction. In the detector-level comparisons displayed in Section 5.4, each component of uncertainty was added in quadrature to build the total uncertainty band. For systematic uncertainties which had an upward and downward variation, their effect was symmetrized by taking the average of their respective difference to the nominal, since there were not large asymmetries observed. For the other uncertainties, their absolute difference with respect

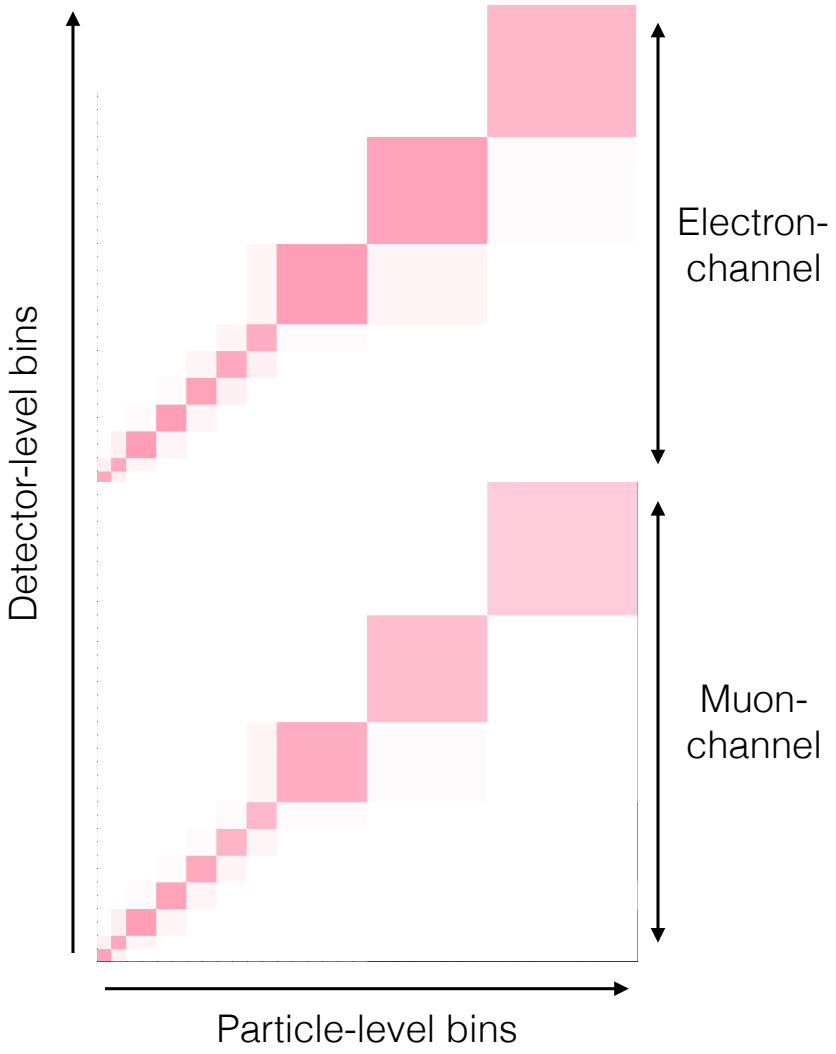

Figure 5.33: An illustration of a combined response matrix used in the unfolding, where the individual response matrices from the electron and muon channel are concatenated.

Inclusive selection

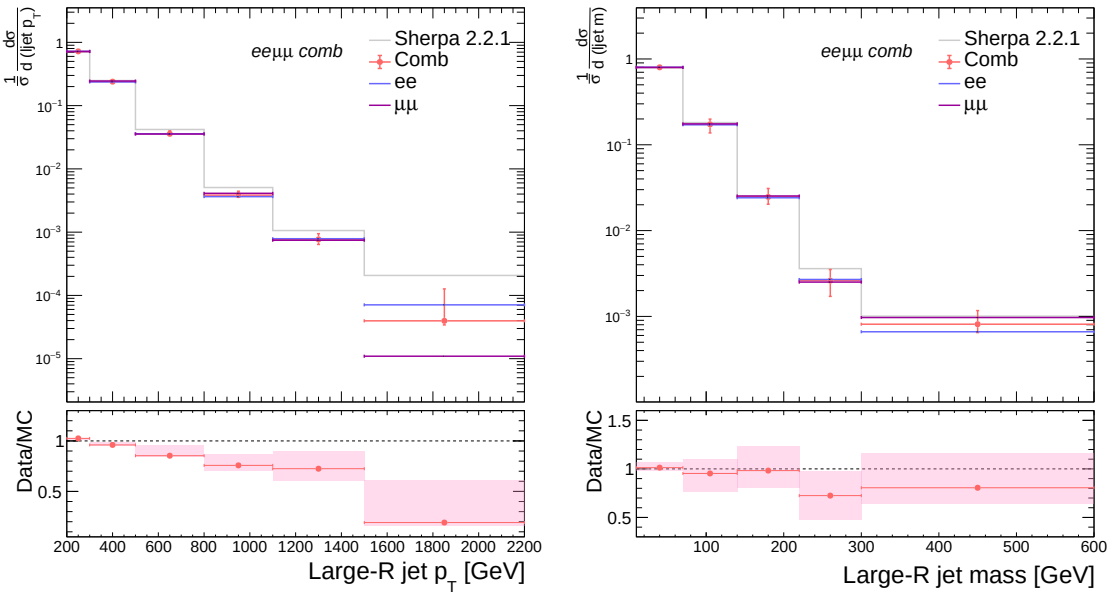

(a)

(b)

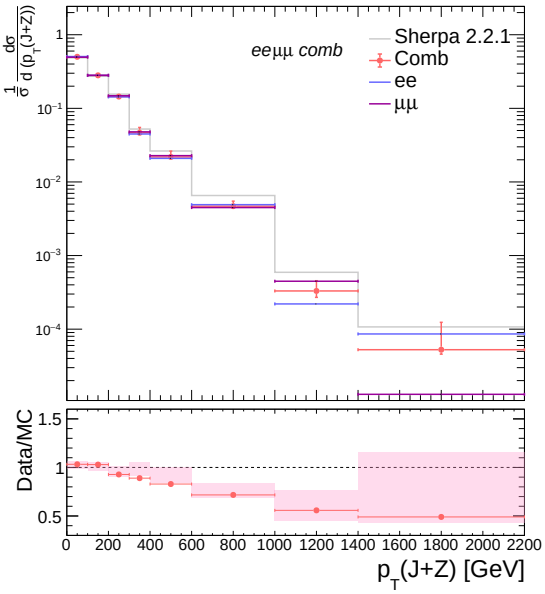

(c)

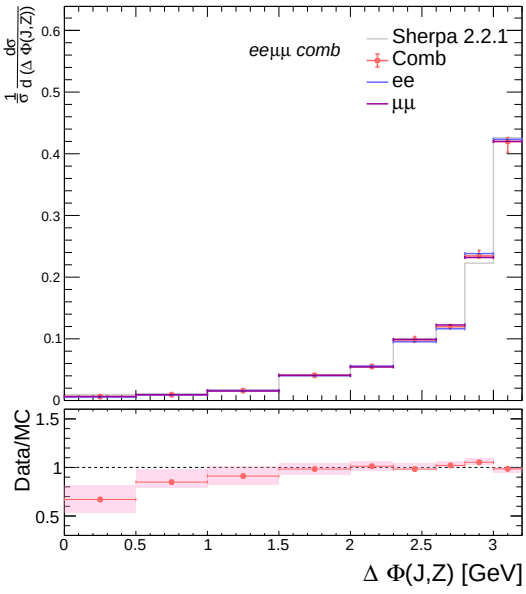

(d)

Figure 5.34: The unfolded data compared to the truth-level cross-sections for the inclusive variables $p_{\mathrm{T}}^{\mathrm{J}}$, m_{J}, $p_{\mathrm{T}}^{\mathrm{J}+Z}$ and $\Delta\phi(Z,\mathrm{J})$. The plots show comparisons between unfolded results when the lepton channels were unfolded separately and when they were unfolded together. The error bars represent the 16–84% quantile range of the posterior distribution of each unfolded bin, and the central value is its the global posterior mode.

2-tag selection

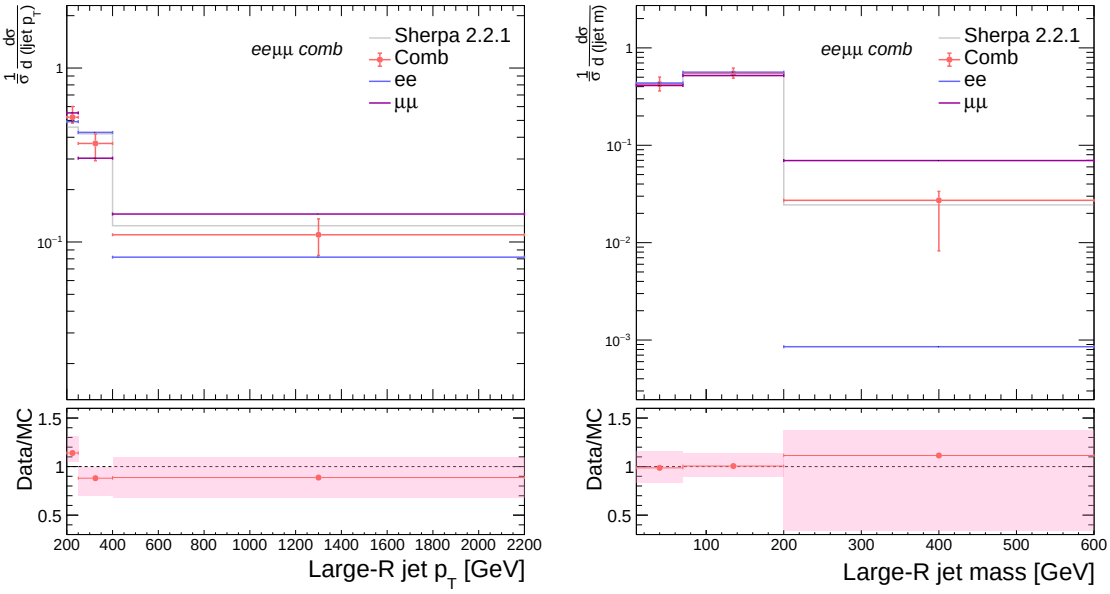

(a) (b)

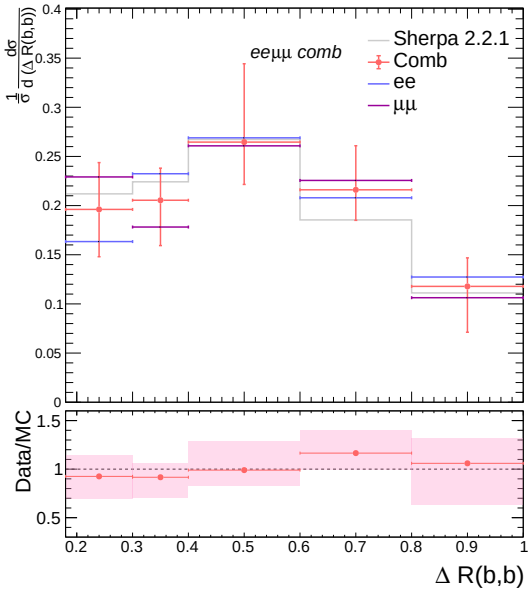

(c)

Figure 5.35: The unfolded data compared to the truth-level cross-sections for the 2-tag variables $p_{\mathrm{T}}^{\mathrm{J}}$, m_{J} and $\Delta R(b,\bar{b})$. The plots show comparisons between unfolded results when the lepton channels were unfolded separately and when they were unfolded together. The error bars represent the 16–84% quantile range of the posterior distribution of each unfolded bin, and the central value is its the global posterior mode.

Inclusive selection

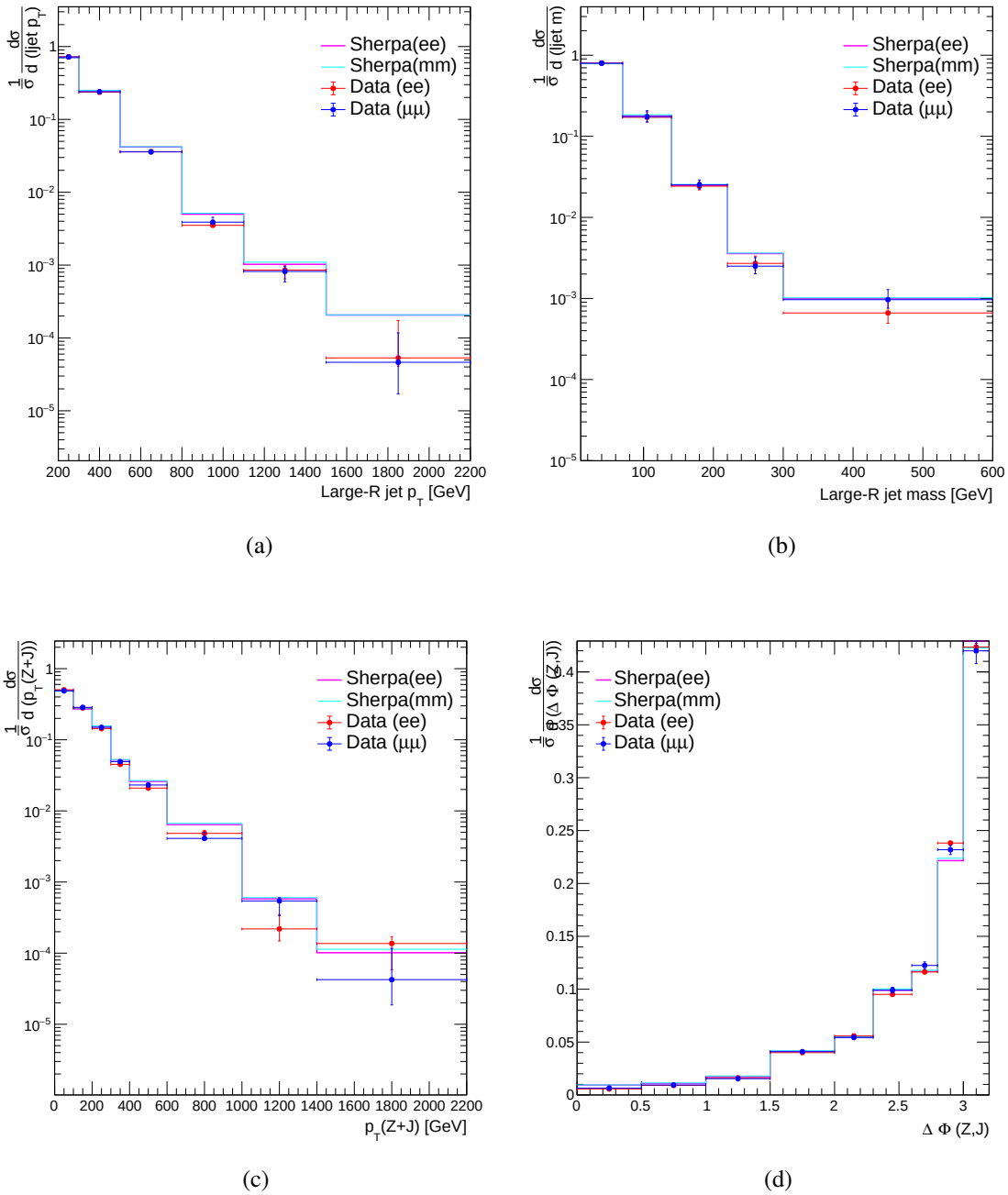

Figure 5.36: Comparison between the unfolded electron-channel data and muon-channel data where only MC-stat nuisance parameters and lepton-systematic nuisance parameters were included in the unfolding model for each inclusive variable: $p_{\mathrm{T}}^{\mathrm{J}}$, m_{J}, $p_{\mathrm{T}}^{\mathrm{J}+Z}$ and $\Delta\phi(Z,\mathrm{J})$. The error bars represent the 16–84% quantile range of the posterior distribution of each unfolded bin, and the central value is its the global posterior mode.

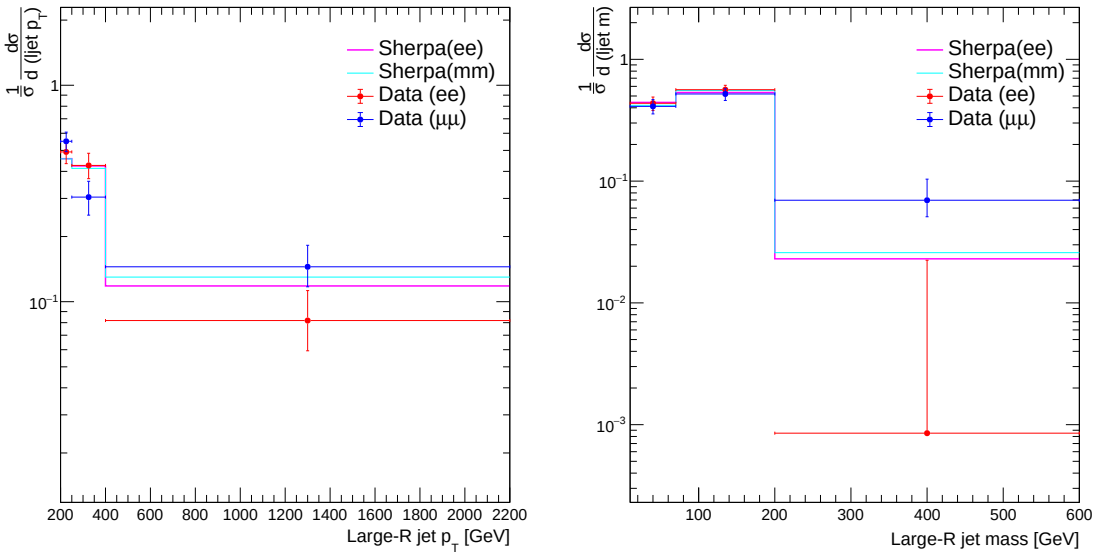

(a) (b)

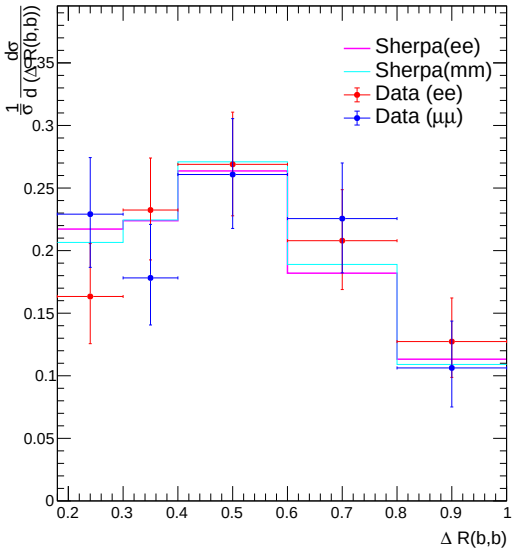

(c)

Figure 5.37: Comparison between the unfolded electron-channel data and muon-channel data where only MC-stat nuisance parameters and lepton-systematic nuisance parameters were included in the unfolding model for each 2-tag variable: $p_{\mathrm{T}}^{\mathrm{J}}$, m_{J} and $\Delta R(b,\bar{b})$. The error bars represent the 16–84% quantile range of the posterior distribution of each unfolded bin, and the central value is its the global posterior mode.

to the nominal prediction was used, unless stated otherwise in the following sections.

5.6.1 Modelling uncertainties

There are aspects of the physics that are not fully understood which are reflected by systematic uncertainties associated with its modelling. In this analysis, uncertainties associated with the modelling of the Z+jets signal were considered as well as uncertainties related to the modelling of the dominant background, $t\bar{t}$.

Signal-modelling

The signal-modelling uncertainties were estimated by applying systematically-varied event weights to the nominal sample to get systematically-varied predictions, or by comparing to an alternative sample. The signal modelling uncertainties considered were:

- Scale variations: the renormalization, μ_R, and factorisation scales, μ_F were varied by a factor of 0.5 or 2 in a correlated and independent manner, leading to a total of six variations. These variations account for the effects of missing higher order terms in the cross section calculation.

- PDF set: alternative PDFs were considered by using the central values of the `CT14nnlo` [83] and `MMHT2014 NNLO` [84] PDF sets.

- $\alpha_s(m_Z)$ value: alternative versions of the nominal PDF set with ± 0.001 shifted variations of $\alpha_s(m_Z) \sim 0.118$ were used to asses the uncertainty.

- Matching scheme: a comparison was made between the SHERPA samples and the MADGRAPH5-_AMC@NLO+PYTHIA8 samples as these generators use different procedures for the matching. This comparison also represents the difference between a LO and an NLO calculation as the SHERPA sample is NLO whilst MADGRAPH5_AMC@NLO+PYTHIA8 is LO.

- $p_{\mathrm{T}}^{\mathrm{J}+Z}$ mismodelling: the samples were reweighted such that the $p_{\mathrm{T}}^{\mathrm{J}+Z}$ distribution in MC matched that in data, giving an alternative prediction to compare to which accounted for the mismodelling of this variable.

In the error bands displayed in detector-level data/MC comparisons, the component of the signal modelling uncertainty arising due to scale uncertainty was computed by taking the envelope of the effect of each individual scale variation. Similarly, the PDF component was computed by taking

the envelope of the effects of the different PDF-set central values. The α_s component was found by symmetrising the effects of each ± 0.001 shifted variation. To get the total signal-modelling uncertainty, each of these components were added in quadrature. The uncertainty derived from the comparison with the MADGRAPH5_AMC@NLO+PYTHIA8 model (referred to as the MG5 uncertainty henceforth) was not included in the error band of the detector-level data/MC comparisons. In the unfolding, each of the variations listed above were included which allowed the full space of predictions to be explored by the unfolding, rather than only using the envelopes.

$t\bar{t}$ background modelling

The uncertainties related to the modelling of the $t\bar{t}$ background were estimated using the alternative MC samples described in Section 5.3. The modelling effects considered were:

- Matrix-element model: an uncertainty related to the choice of model for simulation of the hard-scattering and corresponding matching to the parton shower was assessed by comparing a sample using POWHEG with a sample using MADGRAPH5_AMC@NLO.
- Parton shower model: an uncertainty related to the choice of parton shower model was evaluated by comparing a sample using PYTHIA8 with a sample using HERWIG7.
- Parton shower radiation: uncertainties relating to the modelling of radiation in the shower were assessed by comparing samples with enhanced or suppressed parton shower radiation to the nominal sample.

An additional uncertainty was also added to account for mismodelling of $p_{\mathrm{T}}^{\mathrm{J}+Z}$ in $t\bar{t}$ events, which was discussed in Section 5.4.2.

Background normalisation uncertainties

After assessing the modelling of the backgrounds using control regions as discussed in Section 5.4, additional normalisation uncertainties were added to the analysis to account for any mismodelling of these backgrounds. Specifically, the following uncertainties were added:

- Non-fiducial $Z+$ jets background: a 20% normalisation uncertainty was assigned in the inclusive region, whilst a 50% uncertainty was assigned in the 2-tag region. The uncertainty was increased in the 2-tag region to be conservative about any mismodelling of $Z+$ light/c-flavour jets. Due to limited statistics it was not possible to construct a dedicated control region for this background, although the inclusive region serves as a good proxy.

- $t\bar{t}$, diboson, and $W+$ jets backgrounds: a 20% normalisation uncertainty was assigned for each of these backgrounds in both the inclusive region and 2-tag region.

5.6.2 Detector uncertainties

Detector uncertainties reflect the fact that our understanding of the detector and the performance of the reconstruction algorithms are not perfect. A description of the systematic uncertainties associated with the reconstruction of the various physics objects and how they were derived was given in Section 3. The particular sources of systematic uncertainty considered were:

- Leptons: uncertainties related to the lepton energy scale & resolution, reconstruction efficiency, identification efficiency, isolation efficiency and trigger efficiency were considered.
- Large-R jets: uncertainties on the jet energy scale, jet mass scale, jet energy resolution, and jet mass resolution were considered.
- Flavour tagging: uncertainties related to the calibration of the tagging efficiency for b-flavour jets and the related c-, and light-flavour tagging inefficiencies were considered.
- Pile-up reweighting: the uncertainty associated with the pile-up reweighting procedure was evaluated by varying the scale-factors used to perform the reweighting.
- Luminosity: an uncertainty of 2.1% was assigned for both 2015 and 2016 data, derived by a calibration of the luminosity scale using x–y beam-separation scans, following a methodology similar to that detailed in Ref. [76]. This uncertainty is not included in the error band on the data/MC plots, but it was included in the unfolding.

5.6.3 Pruning of systematic uncertainties

To reduce the time required to perform the unfolding, systematics with a negligible impact on the particle-level observables were pruned. The criteria for pruning were that a systematic uncertainty must change the background prediction by less than 5% relative to the nominal prediction in all detector-level observable bins, and alter the response matrix by less than 0.002 in all bins. The systematic uncertainties which were pruned are:

- large-R jet scale uncertainties: for every variable the scale variations of jet substructure variables were pruned. For the large-R jet p_{T} (inclusive and 2-tag) and $p_{\mathrm{T}}^{\mathrm{J}+Z}$, the mass-scale uncertainties were also pruned.

- large-R jet resolution uncertainties: the jet mass resolution was pruned for every variable excluding the large-R jet mass in the inclusive and 2-tag region.
- b-tagging: all b-tagging uncertainties were pruned for the inclusive variables. For the tagged variables, most of the variations were pruned with the exception of the three largest b-components, an extrapolation component, a c-mis-tag component, and two light-mis-tag components.
- electron uncertainties: most of the calibration uncertainties were pruned. The identification and isolation components of the scale factor uncertainties survived for each variable.
- muon uncertainties: most of the calibration uncertainties were pruned. For the scale factor uncertainties: for each variable all were pruned aside from the identification components, and the isolation components for the inclusive variables.

None of the $t\bar{t}$-modelling, signal-modelling or pile-up uncertainties were pruned for any variable.

5.6.4 Unfolding uncertainty

An additional uncertainty was assigned as a result of the data-driven closure test described in Section 5.5.4. This test showed that the unfolding of the inclusive $p_{\mathrm{T}}^{\mathrm{J}}$ and $p_{\mathrm{T}}^{\mathrm{J}+Z}$ was sensitive to the detector-level mismodelling of these variables by the MC simulation. The difference between the unfolded result and the reweighted prediction in each bin was taken as the uncertainty for each lepton channel, and the envelope of these was used as the final uncertainty in each bin. This was added in quadrature with the final error band on the unfolded results, and was not included as a prior in the unfolding procedure. This resulted in a total increase of $\sim 40\%$ in the uncertainty on the final bin of $p_{\mathrm{T}}^{\mathrm{J}}$ and $\sim 30\%$ in the uncertainty on the final bin of $p_{\mathrm{T}}^{\mathrm{J}+Z}$.

5.6.5 MC statistical uncertainties

Statistical uncertainties in the nominal MC sample were also considered. They are included in the error band of the data/MC comparisons. In the unfolding, a pruning procedure was again applied as it would not have been feasible to add a nuisance parameter for every bin of both the response matrix and the backgrounds. The pruning requirements were:

- For a given background bin, the uncertainty was pruned if its relative effect with respect to the total detector-level prediction in the bin was less than 5%.
- For a given bin in the response matrix, the uncertainty was pruned if it led to a relative effect on the resulting detector-level prediction in the bin of less than 1%.

This procedure was developed to avoid including large statistical uncertainties on very off-diagonal bins in the matrix, which have a small effect on the detector-level prediction.

For all variables, most of the MC statistical uncertainties associated with the off-diagonal bins of the response matrix were pruned. The exception to this was the m_{J} and $p_{\mathrm{T}}^{\mathrm{J}}$ in the 2-tag region, where some of the off-diagonal bin uncertainties survived. For most variables, the MC statistical uncertainties on the background were pruned.

5.6.6 Definitions of the priors on nuisance parameters

The definitions of the nuisance parameters for the different uncertainties were:

- Luminosity uncertainty: no variation templates exist for this uncertainty as it corresponds to a linear scaling of all rates, therefore a log-normal prior was used with $\mu = 0$ and $\sigma = 0.021$, to ensure positive rates and to act as a conservative proxy for the measured luminosity uncertainty

- Background normalisation uncertainties: Gaussian priors with $\mu = 0$ and $\sigma = 0.2$ were used, with the exception of the non-fiducial $Z+$jets background for the 2-tag variables, where a prior with $\mu = 0$ and $\sigma = 0.5$ was used.

- Additional $t\bar{t}$ modelling uncertainty: Gaussian prior with $\mu = 0$ and $\sigma = 0.5$ for the first two bins only.

- All other uncertainties: Gaussian prior with $\mu = 0$ and $\sigma = 1.0$

5.7 Results

The normalised differential cross-sections as a function of the measured observables are presented here compared with the predictions from SHERPA 2.2.1 and MADGRAPH5_AMC@NLO+PYTHIA8 as well as the predicted total fiducial cross-sections for boosted inclusive $Z+$ jets production and $Z + b\bar{b}$ production. Comparisons between the measured normalised differential cross-sections and the predictions allow us to determine whether the MC generators model the shape of these observables well, whilst comparisons between the total fiducial cross-section allow us to determine whether the overall rate of the process is well modelled. A description of how these results were extracted from the multi-dimensional posterior probability distribution is given in Section 5.7.1. The statistical and systematic uncertainties were estimated as described in Section 5.6 and their resulting effect on the unfolded cross-sections was estimated as described in Section 5.7.2.

5.7.1 Extracting the unfolded spectrum

The result of the FBU unfolding technique is the full multi-dimensional posterior probability-distribution over the whole space of nuisance parameters and the parameters of interest. In order to visualise this, the full posterior probability distribution is marginalised into a one-dimensional posterior distribution for each truth-bin. These posterior distributions are then translated into the unfolded spectrum: the central value is the projected global most-likely point and the error bar is defined as the central region containing 68% of the probability. This can lead to asymmetric error bars if the posterior distribution is non-Gaussian, as the most likely point can lie near the edges of this central region. An illustrative example of how the posterior distributions are translated into the unfolded distribution is shown in Figure 5.38. The full posterior can also be marginalised for each nuisance parameter in this manner.

5.7.2 Uncertainties on the final results

The contribution of each individual source of uncertainty – via the nuisance parameters – to the final total error on the measured cross-sections was estimated using the covariances. Specifically, the uncertainty, u, on the parameter of interest σ^{p}, e.g. a particular cross-section bin, due to a nuisance parameter ρ_k is assessed as the covariance between σ^{p} and ρ_k divided by the square-root of the variance of ρ_k,

$$u = \frac{\mathrm{cov}(\sigma^{\mathrm{p}}, \rho_k)}{\sqrt{\mathrm{var}(\rho_k)}}. \tag{5.8}$$

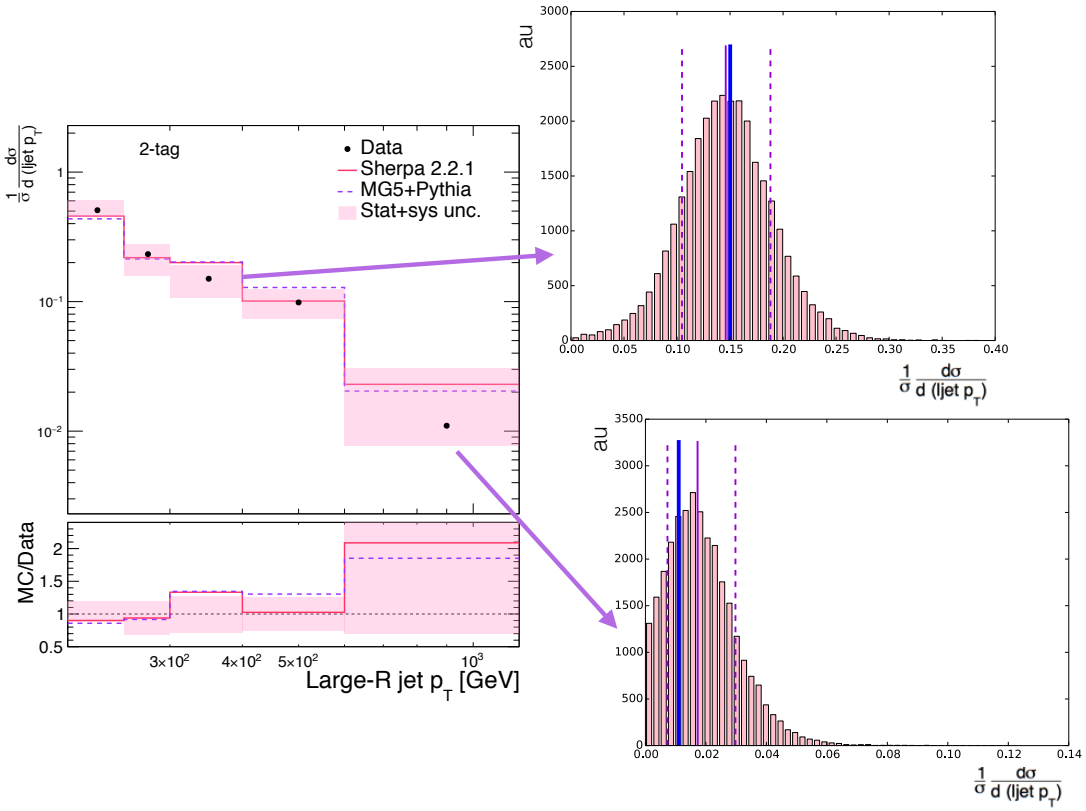

Figure 5.38: An example of how the marginalised posterior distributions of the truth bins are translated into the unfolded spectrum. The posterior distributions are shown on the right hand side. The blue line shows the projected global most-likely point, the purple line shows the median of the marginalised posterior distribution, and the dashed purple lines denote the 16–84% quantile range which defines the error bar.

The covariances are calculated using the n sampled points in the likelihood scan using

$$\mathrm{cov}(\sigma^{\mathrm{p}}, \rho_k) = \frac{1}{n}\sum_{i=1}^{n}(\sigma^{\mathrm{p}} - \bar{\sigma}^{\mathrm{p}})(\rho_k - \bar{\rho}_k), \tag{5.9}$$

where $\bar{\sigma}^{\mathrm{p}}$ and $\bar{\rho}_k$ are the means of the parameter of interest and nuisance parameter, respectively. The relative uncertainty on σ^{p} due to ρ_k is defined as $u/\bar{\sigma}^{\mathrm{p}}$.

This procedure was carried out for each source of nuisance parameter individually, and for groups of nuisance parameters. Figures 5.39 to 5.40 show the estimated relative-uncertainty contributions from the leading sources of systematic uncertainty, for each variable of interest. These are compared with the total uncertainty band, which is the 16–84% quantile range of the posterior distribution of the particular bin. For each variable, the systematic uncertainties associated with the large-R jet, and the modelling of the $t\bar{t}$ background appear as leading sources. In the comparison for $p_{\mathrm{T}}^{\mathrm{J}}$ and m_{J} in the 2-tag region, the error band on the final bin looks very large compared to the contribution from the leading systematic uncertainty. This is because the estimation of the systematic contribution assumes that the posterior distributions are Gaussian, which is not the case for these bins. The estimated contribution to the total uncertainty from nuisance parameter groups is summarised for each variable and each bin in Tables 5.3 to 5.10. Similarly, the quadrature sum of these uncertainty components do not necessarily equal the defined total uncertainty due to anti-correlations of nuisance parameters in the unfolding fit, and the fact that the statistical-error associated with the data is not listed as one of the components. One could approximate this component by unfolding the MC prediction without any systematic nuisance parameters. Since the likelihood is constructed using Poisson statistics, this would give an estimate of the intrinsic Poisson statistical-uncertainty associated with the input data.

Inclusive selection

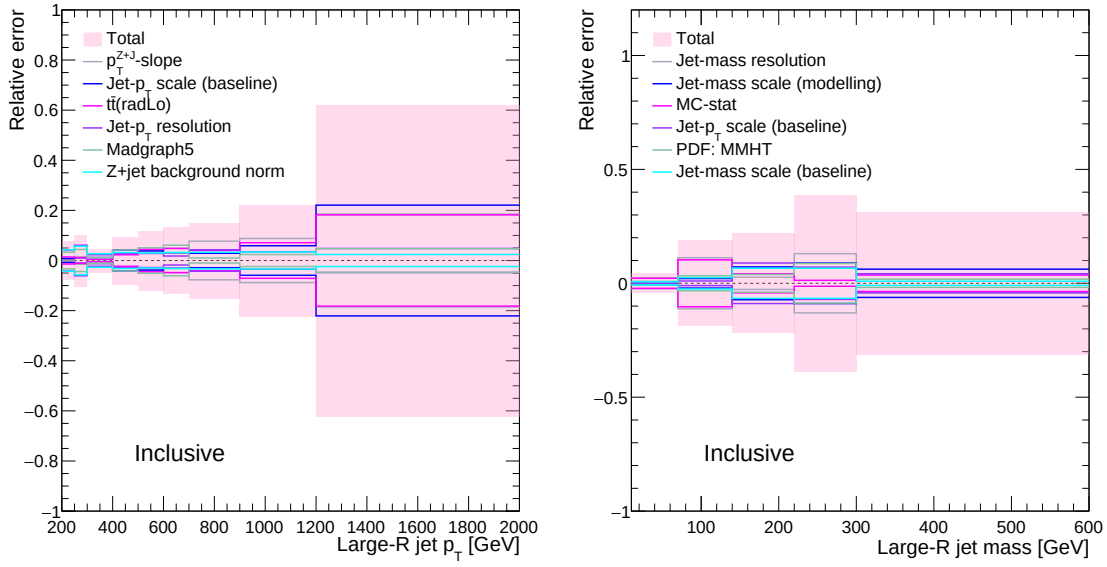

(a) (b)

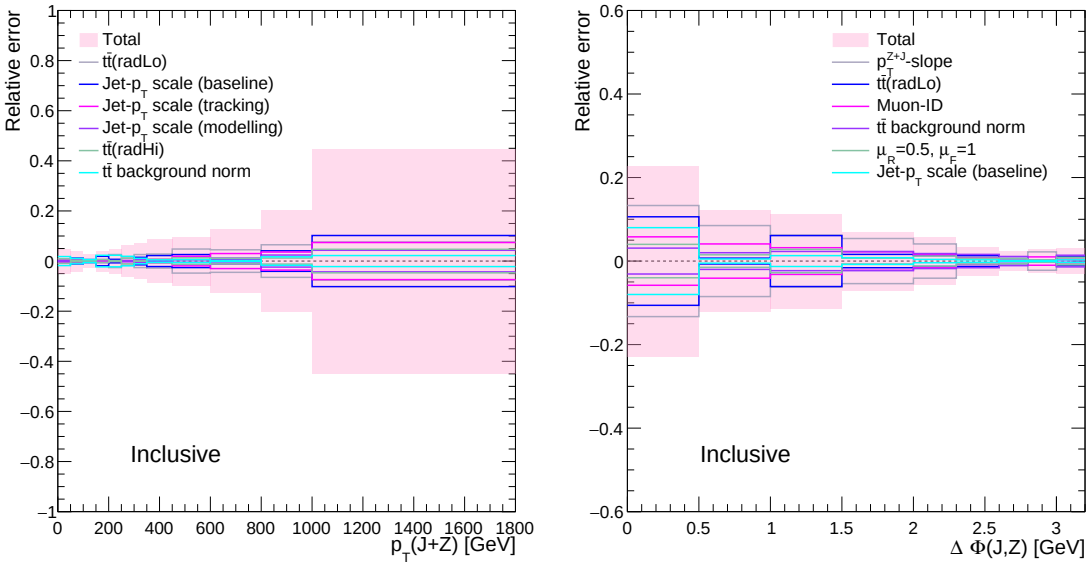

(c) (d)

Figure 5.39: The estimated contribution to the total error from the six leading systematic uncertainties for the inclusive variables a) $p_{\mathrm{T}}^{\mathrm{J}}$, b) m_{J}, c) $p_{\mathrm{T}}^{\mathrm{J}+Z}$ and d) $\Delta\phi(Z,\mathrm{J})$. The error bands represent the 16–84% quantile range of the posterior distribution of each unfolded bin.

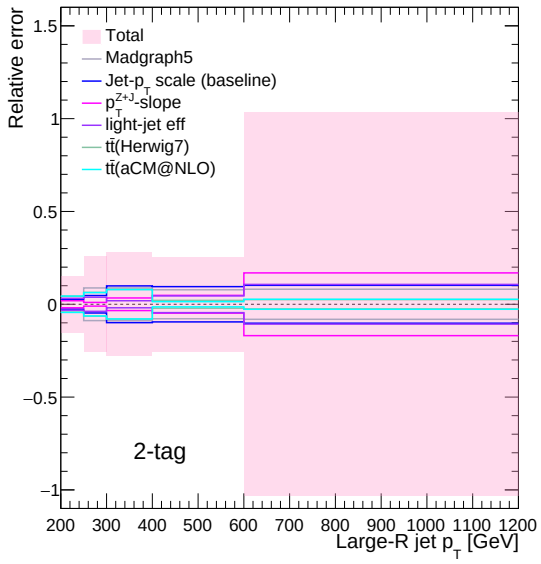

(a)

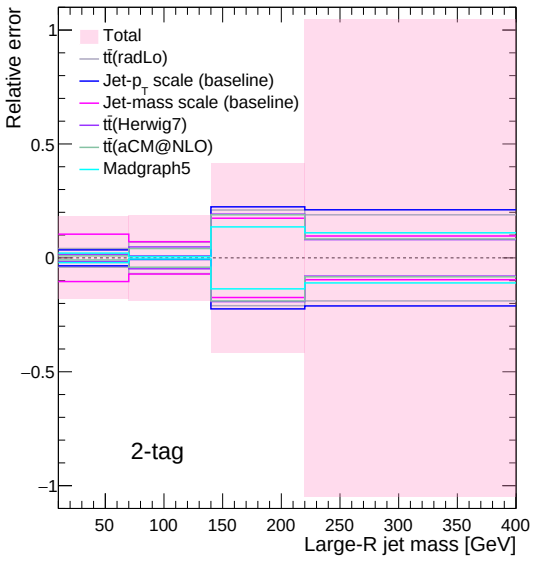

(b)

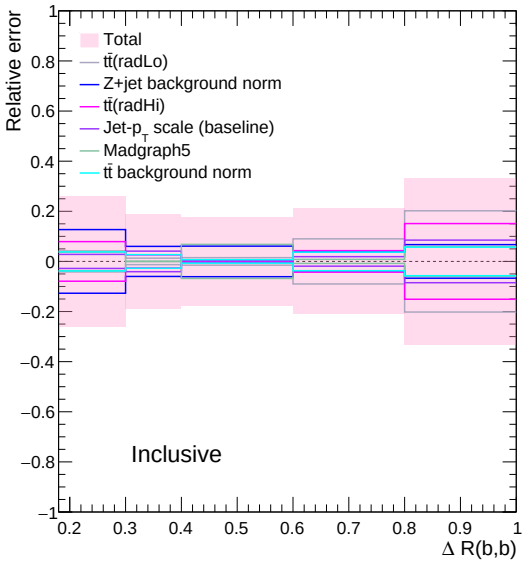

(c)

Figure 5.40: The estimated contribution to the total error from the six leading systematic uncertainties for the 2-tag variables a) $p_{\mathrm{T}}^{\mathrm{J}}$, b) m_{J} and c) $\Delta R(b,\bar{b})$. The error bars represent the 16–84% quantile range of the posterior distribution of each unfolded bin.

Checking the nuisance parameter constraints

Since the systematic uncertainties in this analysis were effectively profiled, it was important to check the constraints of their corresponding nuisance parameters. A full set of nuisance parameter summary plots are shown in Figures 5.41 to 5.44. These plots summarise the posterior probability distributions for each nuisance parameter. In general, it can be seen that there were no strong constraints observed on any of the nuisance parameters, reflected by the fact that the width of their posterior probability distributions was consistent with their prior width. The one exception was the nuisance parameter associated with the MG5 uncertainty, for which strong constraints were observed for each variable. This was not unexpected, as the MG5 model was generally worse at describing the data compared to the nominal Sherpa model.

To assess whether this constraint was resulting in an underestimate of this uncertainty, the nuisance parameter was decomposed into two nuisance parameters: one in which the difference with respect to Sherpa increased as a function of the particular variable in question, and one in which the difference with respect to Sherpa decreased. For example, the contents of a given bin, rt, of the response matrix corresponding to a decomposed nuisance parameter is defined as

$$b^{rt}_{\text{np}} = (\Delta \times f_t) + b^{rt}_{\text{sherpa}}, \tag{5.10}$$

where $\Delta = b^{rt}_{\text{MG5}} - b^{rt}_{\text{sherpa}}$ is the difference between the MG5 prediction (b^{rt}_{MG5}) and the Sherpa prediction (b^{rt}_{sherpa}) in the bin, and f_t is a fraction which varies this difference. For the second nuisance parameter, this fraction would be replaced with $(1-f_t)$. The fraction is varied as a function of the bin number t, such that in one nuisance parameter, Δ increases as a function the variable in question, whilst in the other it decreases. Splitting the nuisance parameter in this manner meant that the resulting decomposed nuisance parameters would have a smaller effect with respect to the original MG5 nuisance parameter, therefore some relaxation of the constraint was expected from this alone.

The nuisance parameter constraints in the single NP scenario and decomposed NP scenario were compared and in general there were no significant reductions in the constraints on the decomposed nuisance parameters with respect to the original. An example comparing the nuisance parameter pulls when unfolding with the single MG5 nuisance parameter and when unfolding with the decomposed MG5 nuisance parameter is shown in Figure 5.45 for $p_{\text{T}}^{\text{J}+Z}$. The size of the resulting error bars from this test were also checked. There was no significant increase in the resulting error bands on the unfolded results in the decomposed-NP scenario, therefore it was concluded that the uncertainty arising from this comparison was not being significantly underestimated.

Inclusive selection

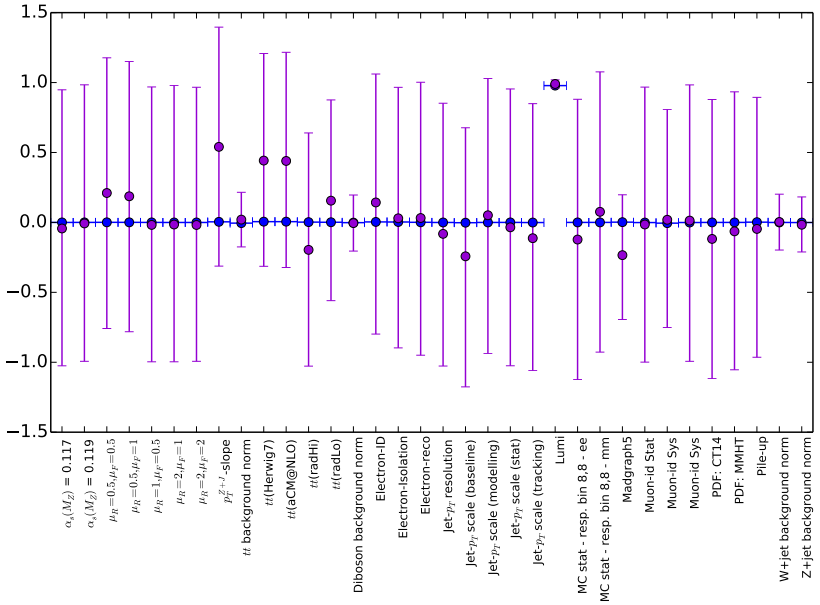

(a) $p_{\mathrm{T}}^{\mathrm{J}}$

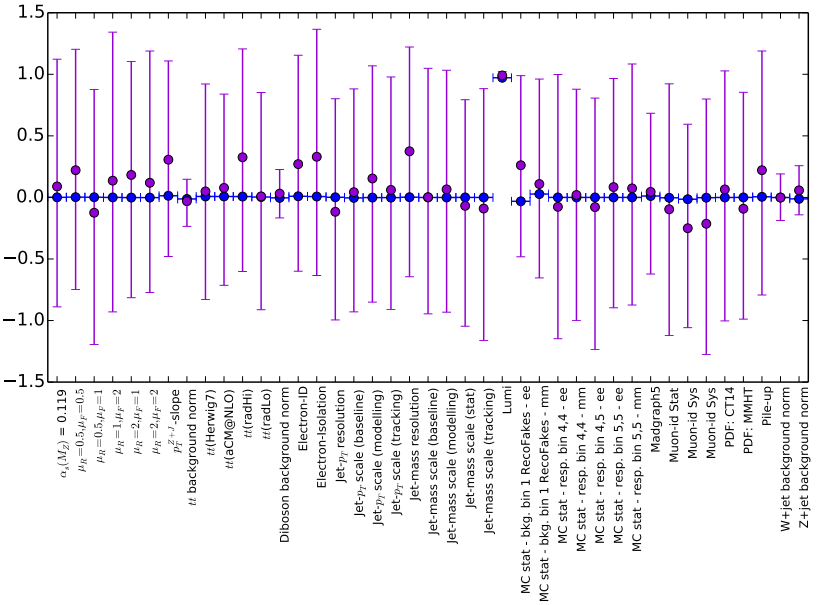

(b) m_{J}

Figure 5.41: Summary plots of the posterior distributions of each nuisance parameter for a) $p_{\mathrm{T}}^{\mathrm{J}}$ and b) m_{J}. The error bands represent the 16–84% quantile range of the posterior distribution of each nuisance parameter, the blue circles represent the global posterior mode, and the purple circles represent the median. Note that the posterior for the luminosity is different as its prior was a log-normal centred on one whilst the others were a Gaussian centred on zero.

Inclusive selection

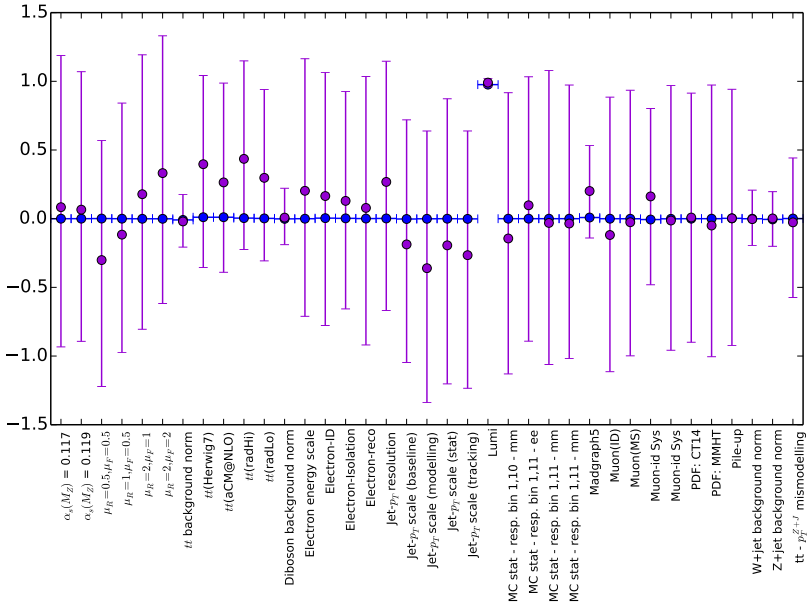

(a) $p_{\mathrm{T}}^{\mathrm{J}+Z}$

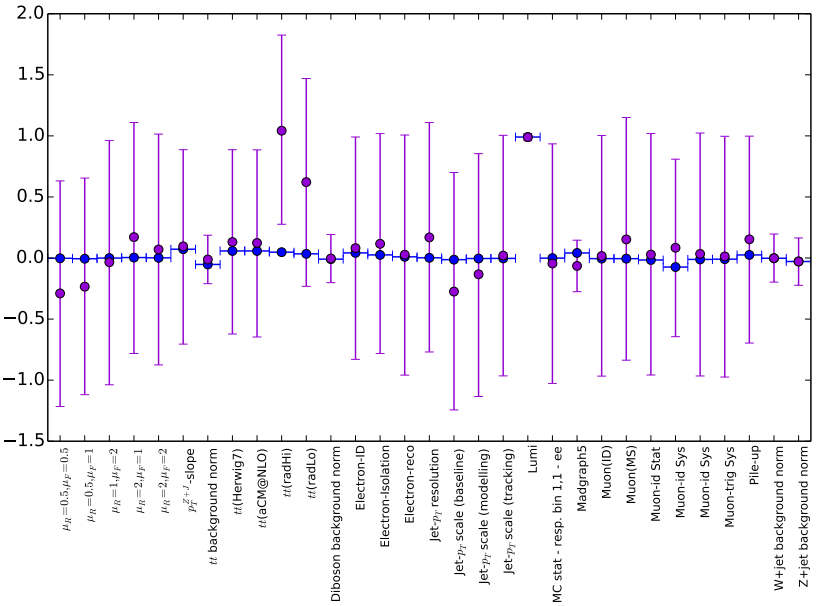

(b) $\Delta\phi(Z,\mathrm{J})$

Figure 5.42: Summary plots of the posterior distributions of each nuisance parameter for a) $p_{\mathrm{T}}^{\mathrm{J}+Z}$ and b) $\Delta\phi(Z,\mathrm{J})$. The error bands represent the 16–84% quantile range of the posterior distribution of each nuisance parameter, the blue circles represent the global posterior mode, and the purple circles represent the median. Note that the posterior for the luminosity is different as its prior was a log-normal centred on one whilst the others were a Gaussian centred on zero.

2-tag selection

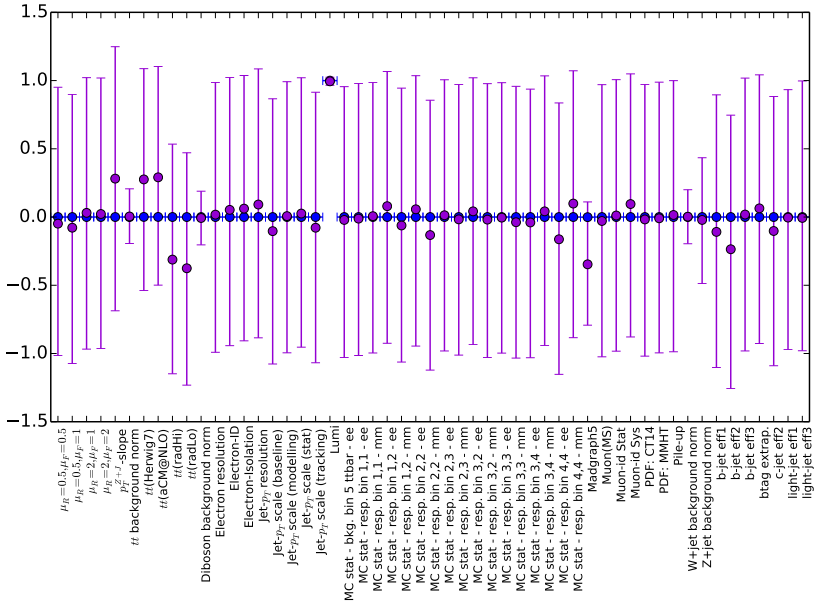

(a) $p_{\mathrm{T}}^{\mathrm{J}}$

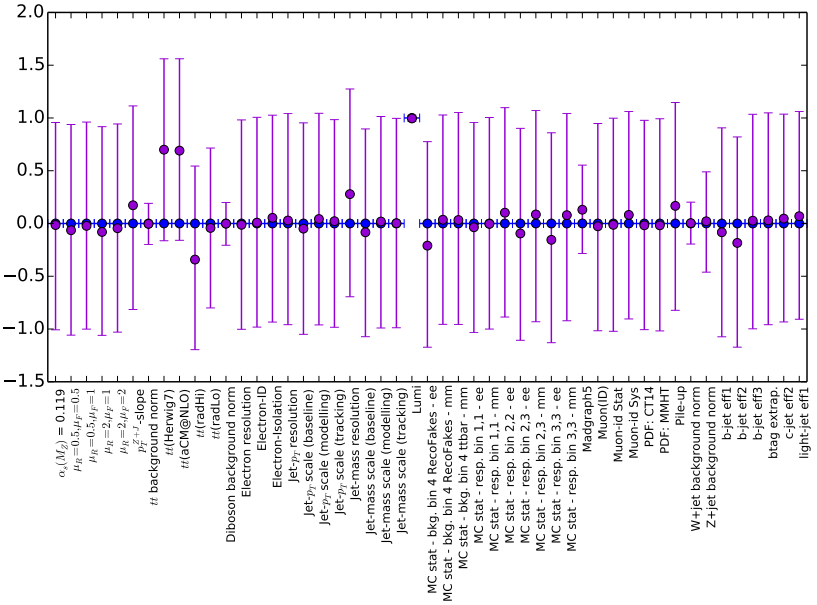

(b) m_{J}

Figure 5.43: Summary plots of the posterior distributions of each nuisance parameter for a) $p_{\mathrm{T}}^{\mathrm{J}}$ and b). The error bands represent the 16–84% quantile range of the posterior distribution of each nuisance parameter, the blue circles represent the global posterior mode, and the purple circles represent the median. Note that the posterior for the luminosity is different as its prior was a log-normal centred on one whilst the others were a Gaussian centred on zero.

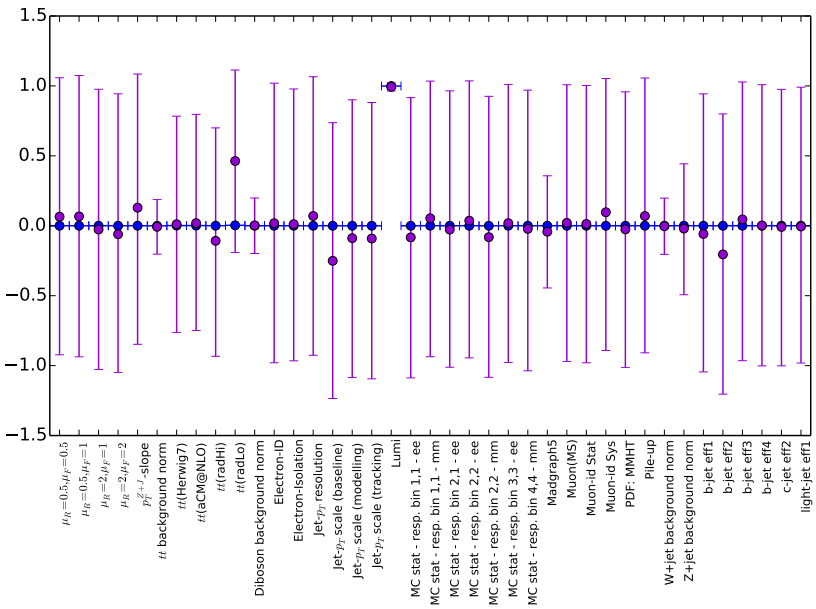

(a) $\Delta R(b, \bar{b})$

Figure 5.44: Summary plots of the posterior distributions of each nuisance parameter for $\Delta R(b, \bar{b})$. The error bands represent the 16–84% quantile range of the posterior distribution of each nuisance parameter, the blue circles represent the global posterior mode, and the purple circles represent the median. Note that the posterior for the luminosity is different as its prior was a log-normal centred on one whilst the others were a Gaussian centred on zero.

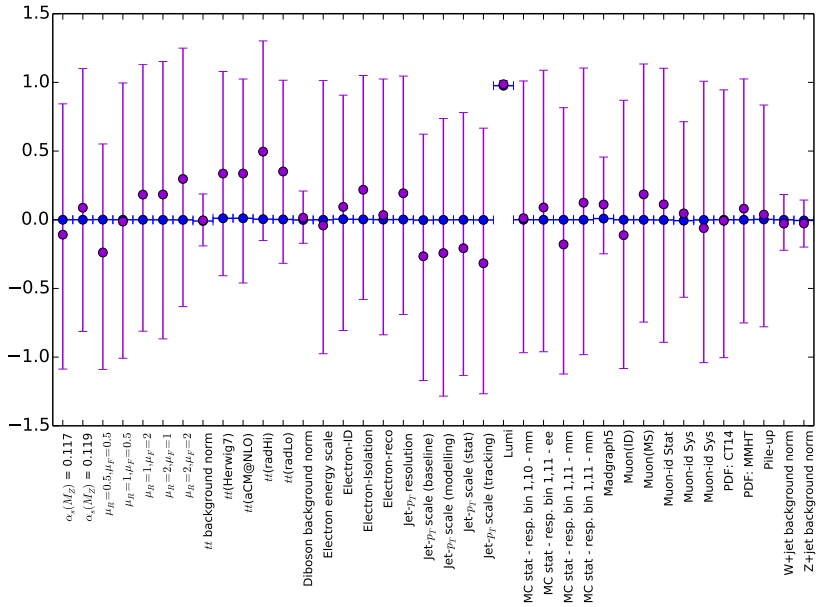

(a) Single MG5 nuisance parameter

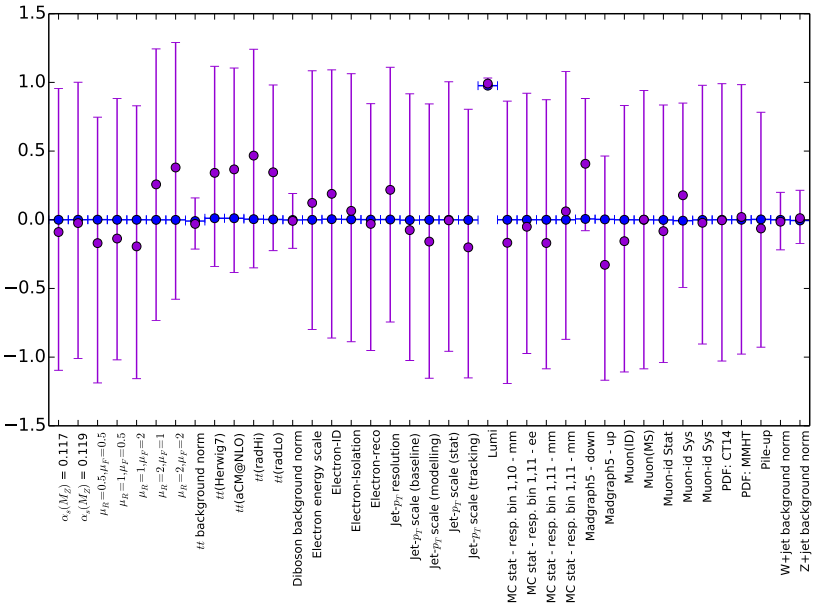

(b) Decomposed MG5 nuisance parameters

Figure 5.45: Nuisance parameter summary when the unfolding was performed with the original MG5 nuisance parameter (a) and when the unfolding was performed with the decomposed MG5 nuisance parameters (b). The error bands represent the 16–84% quantile range of the posterior distribution of each nuisance parameter, the blue circles represent the global posterior mode, and the purple circles represent the median. Note that the posterior for the luminosity is different as its prior was a log-normal centred on one whilst the others were a Gaussian centred on zero.

Sample	$\sigma_{\text{tot}}^{\text{inc}}$ [pb]	$\sigma_{\text{tot}}^{\text{2-tag}}$ [pb]
Data	$2.30^{+0.35}_{-0.21}$	$0.0137^{+0.0058}_{-0.0033}$
SHERPA	2.368 ± 0.006	0.0091 ± 0.0001
MADGRAPH5_AMC@NLO	2.837 ± 0.024	0.0119 ± 0.0014

Table 5.2: The measured total fiducial cross-sections for inclusive Z + jets production, $\sigma_{\text{tot}}^{\text{inc}}$, and $Z + b\bar{b}$ production, $\sigma_{\text{tot}}^{\text{2-tag}}$, compared to the corresponding predictions from MADGRAPH5_AMC@NLO+PYTHIA8 and SHERPA. The errors quoted on the MC predictions are statistical only.

5.7.3 Differential and total fiducial cross-sections

The measured total fiducial cross-sections for both the inclusive and 2-tag region are shown in Table 5.2, and the measured normalised differential cross-sections for each variable of interest are shown in Figures 5.46 and 5.47, where each are compared to the predictions from SHERPA 2.2.1 and MADGRAPH5_AMC@NLO+PYTHIA8 . These final results along with the associated errors and their estimated breakdown into components are also summarised in Tables 5.3 to 5.10.

In the inclusive region, at high $p_{\text{T}}^{\text{J}+Z}$, the data differs from both the SHERPA 2.2.1 and MADGRAPH5_AMC@NLO+PYTHIA8 predictions. A deviation with respect to the predictions is also observed in the lowest bin of the $\Delta\phi(Z, \text{J})$ distribution, whilst the rest of the distribution is described well by the predictions. Similarly, mismodelling is observed at high p_{T}^{J} and high m_{J}. The measured total fiducial cross-section in this region was found to be consistent with the prediction from SHERPA 2.2.1 within 1σ, whilst it differed with the MADGRAPH5_AMC@NLO+PYTHIA8 prediction by more than 1σ.

In the 2-tag region, the measured differential cross-sections are generally consistent with the predictions within the error bar for each variable. The total fiducial cross-section was underestimated by the SHERPA 2.2.1 prediction in this region whilst it was consistent with MADGRAPH5_AMC@NLO+PYTHIA8 within the 1σ uncertainty.

Inclusive selection

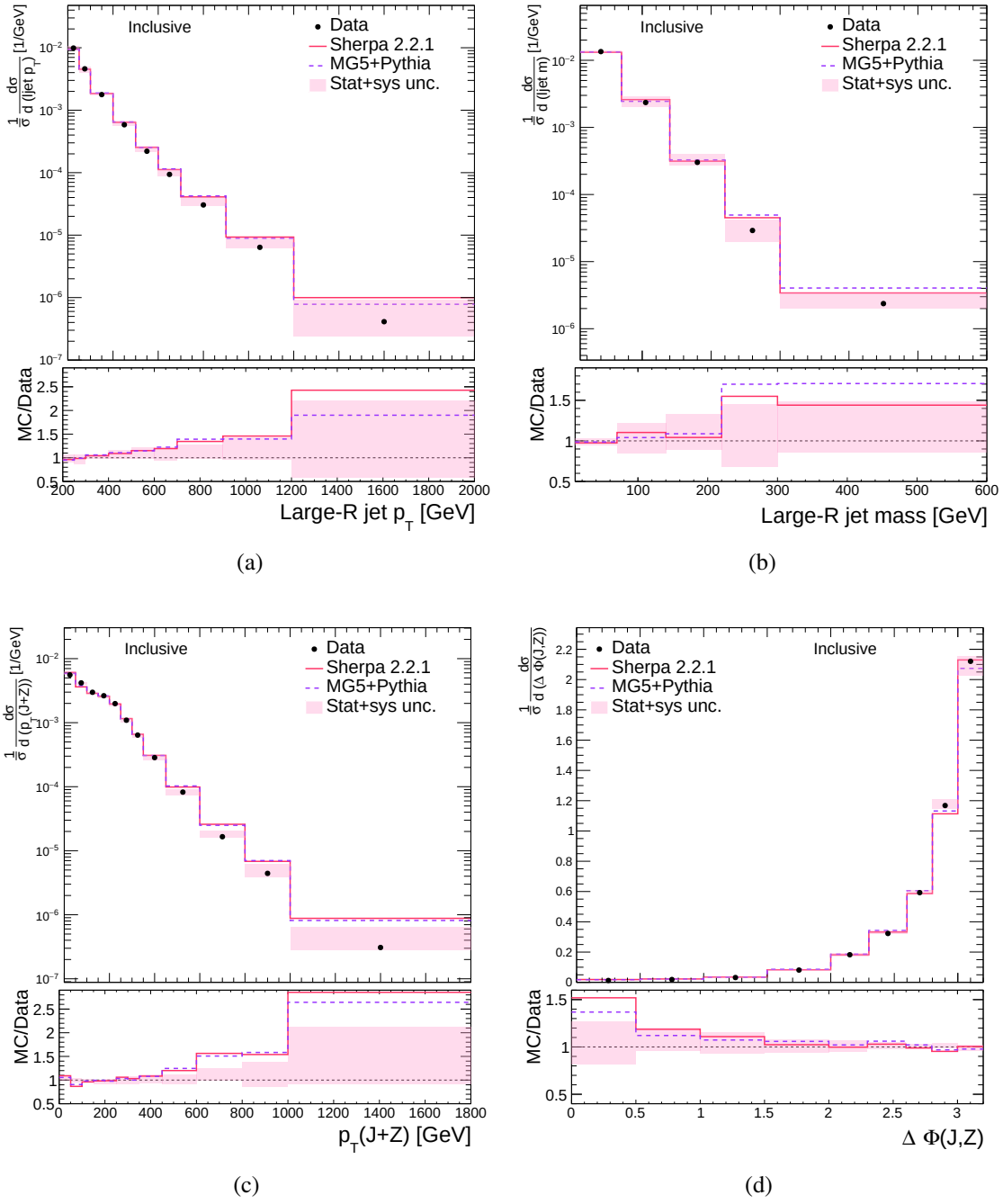

Figure 5.46: The unfolded data compared to the normalised truth-level cross-sections for the inclusive variables a) $p_{\mathrm{T}}^{\mathrm{J}}$, b) m_{J}, c) $p_{\mathrm{T}}^{\mathrm{J}+Z}$ and d) $\Delta\phi(Z,\mathrm{J})$. The error bars represent the 16–84% quantile range of the posterior distribution of each unfolded bin, and the central value is the global posterior mode.

2-tag selection

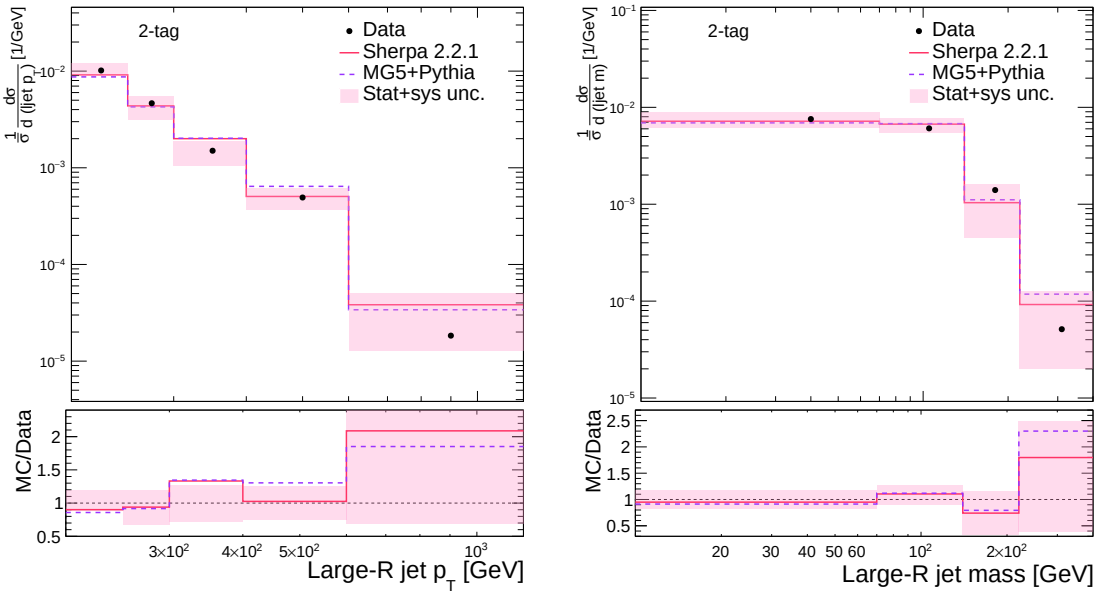

(a)

(b)

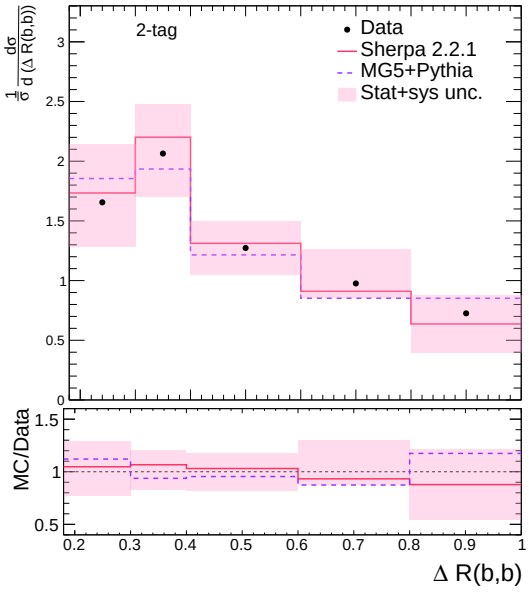

(c)

Figure 5.47: The unfolded data compared to the normalised truth-level cross-sections for the 2-tag variables a) $p_{\mathrm{T}}^{\mathrm{J}}$, b) m_{J} and c) $\Delta R(b,\bar{b})$. The error bars represent the 16–84% quantile range of the posterior distribution of each unfolded bin, and the central value is the global posterior mode.

$p_{\mathrm{T}}^{\mathrm{J}}$ bin (GeV)	200-250	250-300	300-400	400-500	500-600	600-700	700-900	900-1200	1200-2000
					Results				
$\frac{1}{\sigma}\frac{\mathrm{d}\sigma}{\mathrm{d}p_{\mathrm{T}}^{\mathrm{J}}}$ (GeV^{-1})	9.9×10^{-3}	4.6×10^{-3}	1.8×10^{-3}	5.8×10^{-4}	2.2×10^{-4}	9.4×10^{-5}	3.0×10^{-5}	6.4×10^{-6}	4.1×10^{-7}
Total uncertainty (%)	7.7	10.2	4.7	9.5	11.8	13.3	15.1	23.1	81.7
					Uncertainty breakdown (%)				
Scales & PDFs	0.5	0.4	0.0	0.2	0.0	0.1	0.4	1.0	0.7
MC modelling	5.8	2.0	1.3	2.0	3.1	4.2	1.5	0.0	10.5
MC statistics	0.0	0.1	0.1	0.0	0.1	0.1	0.0	1.4	0.1
$t\bar{t}$ modelling	0.7	0.2	0.2	1.6	1.4	2.8	1.1	1.7	4.2
Bkg normalisation	5.3	0.1	1.8	1.6	2.1	2.4	2.9	3.1	5.6
Jet reco	5.4	4.8	5.5	2.8	2.7	3.3	5.9	9.6	25.8
Electron reco	1.9	1.0	1.1	0.4	1.0	1.4	0.4	0.4	0.1
Muon reco	1.1	1.6	1.8	3.3	4.4	5.3	5.2	5.8	9.7
Pile-up	0.7	0.2	0.8	1.6	2.0	1.1	2.1	3.2	9.1
Luminosity	4.3	2.9	3.5	3.4	3.5	3.6	3.6	3.6	4.4

Table 5.3: **Inclusive $p_{\mathrm{T}}^{\mathrm{J}}$**: Summary of the differential fiducial cross-sections as a function of $p_{\mathrm{T}}^{\mathrm{J}}$ and their relative total uncertainty. The breakdown of the uncertainties into defined groups of nuisance parameters are also shown. Note that the quadrature-sum of the individual components may not equal the total uncertainty due to nuisance parameter anti-correlations in the unfolding fit and the fact that the data-statical component is not listed. The total uncertainties displayed here have been symmetrised with respect to the uncertainties displayed in the results plots.

m_{J} bin (GeV)	10-70	70-140	140-220	220-300	300-600
			Results		
$\frac{1}{\sigma}\frac{\mathrm{d}\sigma}{\mathrm{d}m_{\mathrm{J}}}$ (GeV^{-1})	1.3×10^{-2}	2.3×10^{-3}	3.0×10^{-4}	2.9×10^{-5}	2.4×10^{-6}
Total uncertainty (%)	4.3	18.8	21.8	38.8	31.2
			Uncertainty breakdown (%)		
Scales & PDFs	0.3	0.9	1.3	3.2	2.8
MC modelling	2.6	2.0	0.2	11.7	3.6
MC statistics	2.0	1.1	0.8	6.4	1.2
$t\bar{t}$ modelling	1.0	0.9	2.7	3.9	6.2
Bkg normalisation	1.4	3.8	3.2	4.6	6.0
Jet reco	2.1	6.8	6.1	2.1	3.6
Electron reco	1.1	2.8	2.7	7.1	0.5
Muon reco	0.7	1.2	2.3	5.5	0.8
Pile-up	2.6	2.5	0.1	0.3	2.9
Luminosity	2.9	2.1	1.0	0.3	6.7

Table 5.4: **Inclusive m_{J}** : Summary of the differential fiducial cross-sections as a function of m_{J} and their relative total uncertainty. The breakdown of the uncertainties into defined groups of nuisance parameters are also shown. Note that the quadrature-sum of the individual components may not equal the total uncertainty due to nuisance parameter anti-correlations in the unfolding fit and the fact that the data-statical component is not listed. The total uncertainties displayed here have been symmetrised with respect to the uncertainties displayed in the results plots.

$p_{\mathrm{T}}^{\mathrm{J}+Z}$ bin (GeV)	0-50	50-100	100-150	150-200	200-250	250-300
	Results					
$\frac{1}{\sigma}\frac{\mathrm{d}\sigma}{\mathrm{d}p_{\mathrm{T}}^{\mathrm{J}+Z}}$ (GeV^{-1})	5.6×10^{-3}	4.2×10^{-3}	3.0×10^{-3}	2.6×10^{-3}	2.0×10^{-3}	1.1×10^{-3}
Total uncertainty (%)	5.2	4.4	3.1	4.4	5.2	6.5
	Uncertainty breakdown (%)					
Scales & PDFs	0.6	1.4	1.6	3.1	1.3	1.7
MC modelling	5.1	6.4	5.5	2.6	6.1	6.3
MC statistics	0.8	0.0	4.1	0.8	0.1	0.5
$t\bar{t}$ modelling	0.0	0.6	1.1	0.3	0.0	0.3
Bkg normalisation	1.5	2.2	0.9	1.6	3.3	4.3
Jet reco	6.5	4.6	13.9	20.5	5.9	7.4
Electron reco	0.7	1.3	1.7	1.3	0.9	0.8
Muon reco	0.9	0.6	0.2	1.9	0.5	0.2
Pile-up	0.8	0.4	1.9	1.7	0.1	0.1
Luminosity	3.5	3.5	6.7	3.4	4.2	4.8

Table 5.5: **Inclusive $p_{\mathrm{T}}^{\mathrm{J}+Z}$**: Summary of the differential fiducial cross-sections as a function of $p_{\mathrm{T}}^{\mathrm{J}+Z}$ and their relative total uncertainty. The breakdown of the uncertainties into defined groups of nuisance parameters are also shown. Note that the quadrature-sum of the individual components may not equal the total uncertainty due to nuisance parameter anti-correlations in the unfolding fit and the fact that the data-statical component is not listed. The total uncertainties displayed here have been symmetrised with respect to the uncertainties displayed in the results plots.

$p_{\mathrm{T}}^{\mathrm{J}+Z}$ bin (GeV)	300-350	350-450	450-600	600-800	800-1000	1000-1800
	Results					
$\frac{1}{\sigma}\frac{\mathrm{d}\sigma}{\mathrm{d}p_{\mathrm{T}}^{\mathrm{J}+Z}}$ (GeV^{-1})	6.4×10^{-4}	2.4×10^{-4}	8.2×10^{-5}	1.7×10^{-5}	4.4×10^{-6}	3.1×10^{-7}
Total uncertainty (%)	8.0	9.4	10.3	12.9	26.5	60.0
	Uncertainty breakdown (%)					
Scales & PDFs	1.8	1.4	0.6	0.4	0.9	1.0
MC modelling	2.5	2.0	0.7	1.1	1.0	0.6
MC statistics	0.3	0.1	0.1	0.4	0.0	0.0
$t\bar{t}$ modelling	0.9	0.0	0.7	0.7	0.6	1.7
Bkg normalisation	4.2	2.5	2.4	1.7	2.5	1.8
Jet reco	6.5	6.1	5.8	5.8	7.0	8.9
Electron reco	0.1	0.6	0.8	0.5	0.6	0.1
Muon reco	0.6	1.7	1.4	1.8	1.9	0.6
Pile-up	0.2	0.6	1.7	1.8	1.7	1.3
Luminosity	4.9	4.4	4.6	4.8	5.6	4.1

Table 5.6: **Inclusive $p_{\mathrm{T}}^{\mathrm{J}+Z}$ continued**: Summary of the differential fiducial cross-sections as a function of $p_{\mathrm{T}}^{\mathrm{J}+Z}$ and their relative total uncertainty. The breakdown of the uncertainties into defined groups of nuisance parameters are also shown. Note that the quadrature-sum of the individual components may not equal the total uncertainty due to nuisance parameter anti-correlations in the unfolding fit and the fact that the data-statical component is not listed. The total uncertainties displayed here have been symmetrised with respect to the uncertainties displayed in the results plots.

$\Delta\phi(Z,\mathrm{J})$ bin	0.0-0.5	0.5-1.0	1.0-1.5	1.5-2.0	2.0-2.3	2.3-2.6	2.6-2.8	2.8-3.0	3.0-3.2
					Results				
$\frac{1}{\sigma}\frac{\mathrm{d}\sigma}{\mathrm{d}\Delta\phi(Z,\mathrm{J})}$	1.2×10^{-2}	1.9×10^{-2}	3.2×10^{-2}	8.1×10^{-2}	1.8×10^{-2}	0.32	0.59	1.2	2.1
Total uncertainty (%)	22.7	12.1	11.3	7.0	5.7	3.4	2.4	2.8	3.0
					Uncertainty breakdown (%)				
Scales & PDFs	2.7	0.0	0.7	0.0	0.2	0.0	0.2	0.3	0.2
MC modelling	5.7	1.2	2.5	1.5	0.7	0.5	0.5	0.7	0.9
MC statistics	1.0	0.3	0.0	0.3	0.4	0.2	0.2	0.2	0.3
$t\bar{t}$ modelling	9.2	3.7	4.8	3.6	3.2	2.4	1.8	1.2	1.4
Bkg normalisation	6.4	5.0	4.6	4.2	3.8	3.8	3.4	2.8	2.0
Jet reco	9.2	3.7	4.7	4.4	5.0	6.2	6.8	7.4	6.2
Electron reco	1.2	0.1	0.6	0.9	1.1	2.0	2.3	2.8	2.7
Muon reco	5.1	4.2	3.4	2.7	2.2	1.8	1.1	0.5	1.0
Pile-up	1.0	0.2	0.8	0.8	1.2	0.3	0.5	0.5	0.5
Luminosity	5.1	4.8	4.6	4.4	4.2	4.3	4.1	3.9	3.6

Table 5.7: **Inclusive $\Delta\phi(Z,\mathrm{J})$**: Summary of the differential fiducial cross-sections as a function of $\Delta\phi(Z,\mathrm{J})$ and their relative total uncertainty. The breakdown of the uncertainties into defined groups of nuisance parameters are also shown. Note that the quadrature-sum of the individual components may not equal the total uncertainty due to nuisance parameter anti-correlations in the unfolding fit and the fact that the data-statical component is not listed. The total uncertainties displayed here have been symmetrised with respect to the uncertainties displayed in the results plots.

$p_{\mathrm{T}}^{\mathrm{J}}$ bin (GeV)	200-250	250-300	300-400	400-600	600-1200
			Results		
$\frac{1}{\sigma}\frac{\mathrm{d}\sigma}{\mathrm{d}p_{\mathrm{T}}^{\mathrm{J}}}$ (GeV^{-1})	1.0×10^{-2}	4.7×10^{-3}	1.5×10^{-3}	4.9×10^{-4}	1.8×10^{-5}
Total uncertainty (%)	15.3	25.8	27.8	25.4	103.3
			Uncertainty breakdown (%)		
Scales & PDFs	2.4	0.8	1.3	2.7	4.0
MC modelling	0.3	13.8	14.6	2.5	3.9
MC statistics	0.9	2.1	2.1	2.6	3.3
$t\bar{t}$ modelling	0.2	14.9	14.4	2.8	0.4
Bkg normalisation	22.1	9.3	18.7	13.1	36.5
Jet reco	3.0	8.3	8.6	1.7	10.6
Electron reco	3.5	3.5	4.5	4.0	8.2
Muon reco	1.2	0.2	1.2	1.0	2.5
Pile-up	1.4	0.6	1.9	1.4	15.5
Luminosity	6.0	4.9	5.3	4.6	7.4

Table 5.8: **2-tag $p_{\mathrm{T}}^{\mathrm{J}}$** : Summary of the differential fiducial cross-sections as a function of $p_{\mathrm{T}}^{\mathrm{J}}$ and their relative total uncertainty. The breakdown of the uncertainties into defined groups of nuisance parameters are also shown. Note that the quadrature-sum of the individual components may not equal the total uncertainty due to nuisance parameter anti-correlations in the unfolding fit and the fact that the data-statical component is not listed. The total uncertainties displayed here have been symmetrised with respect to the uncertainties displayed in the results plots.

m_{J} bin (GeV)	10-70	70-140	140-220	220-400
	Results			
$\frac{1}{\sigma}\frac{\mathrm{d}\sigma}{\mathrm{d}m_{\mathrm{J}}}$ (GeV^{-1})	7.6×10^{-3}	6.1×10^{-3}	1.4×10^{-3}	5.1×10^{-5}
Total uncertainty (%)	18.0	18.8	41.6	104.7
	Uncertainty breakdown (%)			
Scales & PDFs	0.6	0.1	1.4	3.3
MC modelling	6.2	4.4	5.9	8.9
MC statistics	0.5	1.9	0.9	6.1
$t\bar{t}$ modelling	5.8	12.8	4.0	10.6
Bkg normalisation	20.5	22.7	10.6	12.6
Jet reco	0.9	13.1	3.5	1.9
Electron reco	0.5	0.1	3.5	9.2
Muon reco	3.8	6.7	0.9	0.9
Pile-up	0.0	7.1	2.3	0.8
Luminosity	5.5	6.9	4.3	3.3

Table 5.9: **2-tag m_{J}**: Summary of the differential fiducial cross-sections as a function of m_{J} and their relative total uncertainty. The breakdown of the uncertainties into defined groups of nuisance parameters are also shown. Note that the quadrature-sum of the individual components may not equal the total uncertainty due to nuisance parameter anti-correlations in the unfolding fit and the fact that the data-statical component is not listed. The total uncertainties displayed here have been symmetrised with respect to the uncertainties displayed in the results plots.

$\Delta R(b,\bar{b})$ bin	0.18-0.3	0.3-0.4	0.4-0.6	0.6-0.8	0.8-1.0
			Results		
$\frac{1}{\sigma}\frac{d\sigma}{d\Delta R(b,\bar{b})}$	1.7	2.1	1.3	1.0	0.7
Total uncertainty (%)	26.0	18.8	17.7	21.0	33.3
			Uncertainty breakdown (%)		
Scales & PDFs	0.6	0.0	0.7	0.2	1.5
MC modelling	2.3	2.1	8.7	1.6	5.0
MC statistics	0.8	1.7	0.7	0.3	0.9
$t\bar{t}$ modelling	3.2	1.0	0.8	3.2	2.2
Bkg normalisation	26.3	11.1	11.9	16.8	22.0
Jet reco	4.1	5.5	6.9	7.7	11.4
Electron reco	3.2	1.4	1.4	1.9	3.3
Muon reco	0.2	1.9	2.1	1.9	0.6
Pile-up	1.7	2.6	3.8	3.5	0.8
Luminosity	5.4	4.4	4.6	5.7	6.2

Table 5.10: **2-tag $\Delta R(b,\bar{b})$**: Summary of the differential fiducial cross-sections as a function of $\Delta R(b,\bar{b})$ and their relative total uncertainty. The breakdown of the uncertainties into defined groups of nuisance parameters are also shown. Note that the quadrature-sum of the individual components may not equal the total uncertainty due to nuisance parameter anti-correlations in the unfolding fit and the fact that the data-statical component is not listed. The total uncertainties displayed here have been symmetrised with respect to the uncertainties displayed in the results plots.

5.8 Summary

Cross-sections differential in kinematic variables of the b-tagged large-R jet produced in association with a Z-boson have been measured, as well as total fiducial cross-sections for the inclusive and 2-tag regions. These measurements have been compared to predictions from SHERPA 2.2.1 and MADGRAPH5_AMC@NLO+PYTHIA8 . In the 2-tag region, the shapes of the observables were well modelled by both predictions, whilst the normalisation was better modelled by the MADGRAPH5-_AMC@NLO+PYTHIA8 prediction. This was slightly surprising given that the MADGRAPH5-_AMC@NLO+PYTHIA8 sample was a LO prediction, whilst the SHERPA 2.2.1 prediction was a NLO prediction (for up to two jets, and LO for up to four), hence one might naively expect the SHERPA prediction to do better. In the inclusive region, shape mismodelling was observed for all of the variables by both predictions. Contrary to the 2-tag region, the normalisation was better modelled by the SHERPA prediction.

Systematic uncertainties were largely dominant in the inclusive region, whilst statistical uncertainties became leading in the more extreme regions of phase-space. Despite the fact that the unfolding procedure had the potential to constrain systematic uncertainties, it was not able to do so in this analysis. In future iterations, control regions could be used in the unfolding fit to allow for greater constraint of the uncertainties. In the 2-tag region and in the extreme regions of inclusive phase-space, the measurement was statistically limited. The increase in luminosity from the addition of the remainder of the Run-2 dataset as well as new data from Run-3 of the LHC should help to reduce these limitations in the future.

Due to lack of available samples at time of writing, the results were compared only to samples utilising the 5-flavour number scheme calculation method. It would be interesting to compare the results to a sample utilising the 4-flavour number scheme, to ascertain whether either of these schemes do a better job of modelling the data. In addition, the PYTHIA8 parton shower generator has the functionality to alter the scale choice used in $g \to b\bar{b}$ splitting. It would be interesting to compare the results to some PYTHIA8 samples with different choices of scale, to shine a light on what the most appropriate choice is.

An additional measurement of the $Z+$ jets process was performed in parallel by another ATLAS group of analysers, where a lower momentum phase space was targeted and additional variables were measured. The results from this analysis together with those presented in this chapter will be invaluable for constraining the modelling uncertainties associated with this process and for tuning and developing MC simulations.

Chapter 6

$V(H \to b\bar{b})$ signal modelling studies

A particle with properties consistent with the Standard Model Higgs boson was observed by ATLAS and CMS during Run-1 of the LHC in 2012. With the additional data collected during Run-2, the properties of the Higgs can be measured with increased precision and differential measurements are starting to emerge.

The coupling of the Higgs to fermions was observed via its decay to τ-leptons in Run-1 [85], but its direct coupling to quarks, until very recently, had not been observed. The best candidate for observing Higgs-quark coupling is the b-quark because the $H \to b\bar{b}$ branching ratio is 58%: the largest amongst all of the Higgs decay modes and accounting for over half of the total decay width, as shown in Figure 6.1 [86]. This means $H \to b\bar{b}$ is a very important process for constraining the decay width of the Higgs.

The dominant Higgs boson production mode is gluon-gluon fusion, as shown by the blue line in Figure 6.1, but the $H \to b\bar{b}$ signature is very difficult to disentangle from hadronic activity with the same final state, as its production cross-section is around 10^7 times smaller than that of generic b-jet production [87]. Higgs production in association with a vector boson, VH, offers a cleaner final state owing to the leptonic decay modes of the vector bosons which reduce the background, making this the most sensitive production mode for accessing the $H \to b\bar{b}$ decay.

In 2017, a search for $V(H \to b\bar{b})$ using 36.1 fb^{-1} of data collected during 2015 and 2016 observed an excess of signal events with a significance of 3.5σ, providing the first evidence for $H \to b\bar{b}$ [88]. This chapter details my contribution to this analysis which was evaluating the signal-modelling uncertainties. An overview of the analysis is given in Section 6.1 to contextualise the work followed by details of the study in the subsequent sections. The full details of the analysis can be found in Ref [88].

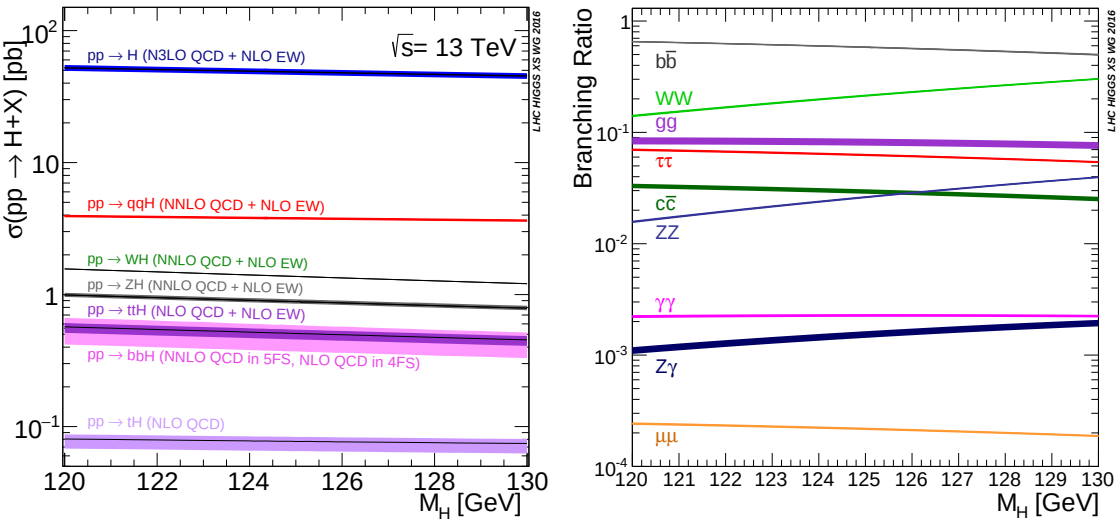

Figure 6.1: The expected production cross-sections for each channel as a function of the Higgs boson mass (a) and the branching ratios for the Higgs boson decay modes as a function of the Higgs boson mass (b), taken from Reference [86].

6.1 Analysis overview

Signal regions were defined to target the different leptonic decay modes of the W or Z boson that is produced in association with the Higgs, with further categorisation based on the number of jets in the event and the p_{T} of the vector boson, p_{T}^{V}. The phase space where the Higgs and the vector boson have high p_{T} was targeted, as this region has the highest signal-to-background ratio. It should be noted that the high p_{T} region referred to here is lower than what is referred to as high p_{T} in the analysis presented in the previous section. The signal and the majority of the backgrounds were estimated using MC simulation. The backgrounds considered were V+jets, $t\bar{t}$, single-top (Wt), and diboson (WW, WZ, ZZ). The multijet background, which arises from jets faking the signature of leptons, was estimated using data-driven techniques in the 1-lepton channel, whilst it was negligible in the 0- and 2-lepton channel as a result of the selection cuts. In the 0-lepton channel, additional cuts on angular variables were implemented, whilst in the 2-lepton channel the requirement of two isolated leptons within a dilepton invariant mass window suppressed the fakes to a negligible level. A W+jets control region was defined in the 1-lepton channel and a top control region was defined in the 2-lepton channel in order to provide constraints on these backgrounds.

A boosted decision tree (BDT) was used to derive the discriminating variable used in the analysis. A BDT is a multivariate statistical analysis technique used to separate signal and background processes; it takes a list of variables shown to give good signal-background discrimination, de-

termines the optimal configuration of these variables for maximal separation, and condenses this information into a single discriminant. A dijet-mass analysis, where the discriminating variable was the invariant mass of the two b-jets, $m_{b\bar{b}}$, was performed in parallel to validate and cross-check the result.

A binned maximum likelihood fit performed simultaneously in each signal region and control region was used to extract the $V(H \to b\bar{b})$ signal strength, μ, along with the probability that the results were consistent with a background only hypothesis, p_0, from the data. Systematic uncertainties associated with detector modelling, limited MC statistics and signal and background modelling were encoded in the fit using nuisance parameters. The likelihood fit relied heavily on MC simulation to model the signal and background, therefore it was important that uncertainties in the modelling were assessed. The modelling uncertainty nuisance parameters were split into two categories: normalisation and shape. The normalisation nuisance parameters controlled the signal and background yields in the different analysis regions and the shape nuisance parameters defined alternative templates for the fitted distributions used in the fit. The work carried out to derive the signal-modelling uncertainties is documented in this chapter.

The extraction of the signal strength using this technique was validated by measuring the SM diboson signal strength, VZ, in parallel. In this cross-check, the BDT was trained to instead extract the $W(Z \to b\bar{b})$ signal. The similar final state with a higher cross-section offered a robust cross check of the methods used. Observing this well understood process with a signal strength consistent with the Standard Model provided reassurance that the framework was working correctly.

Finally, the results using the Run-2 data were combined with the results from the Run-1 analysis. The resulting probability that the observed $V(H \to b\bar{b})$ signal events were a result of background only was $p_0 = 0.018\%$. This corresponds to an observation significance of 3.6 standard deviations, assuming a Higgs mass of $m_H = 125$ GeV. The resulting fitted relative signal strength with respect to the SM for all channels combined was $\mu = 0.90 \pm 0.18(\text{stat.})^{+0.21}_{-0.19}(\text{syst.})$, which is compatible with the SM [88].

6.2 Procedure for evaluating the uncertainties

As mentioned, MC simulation of the signal and background played a key role in the likelihood fit used to extract the $V(H \to b\bar{b})$ signal strength, therefore the evaluation of uncertainties relating to this modelling was important. For the signal, uncertainties relating to the following modelling effects were assessed:

- The residual dependence on the renormalisation scale, μ_R, due to missing higher order correc-

tions in the fixed-order differential cross-section and dependence on the factorisation scale, μ_F;

- The effect of varying the PDF and the $\alpha_s(m_Z)$ values;
- The modelling of the parton-shower.

The uncertainties were evaluated using dedicated MC samples, to be described in Section 6.4. These samples were available only at particle-level, therefore the uncertainties were derived via particle-level comparisons using the RIVET analysis framework [89]. A dedicated selection was written to match the detector-level selection as closely as possible and used to perform the studies. This selection is described in Section 6.3.

To mirror the categorisation of nuisance parameters required for the likelihood fit, the effect of each systematic uncertainty was split into two components: acceptance variations affecting event yields in the signal regions, and shape variations reflecting shape differences in the distributions of p_{T}^V and $m_{b\bar{b}}$. Only distributions of p_{T}^V and $m_{b\bar{b}}$ were evaluated as these had the most discriminating power of the list of variables used as input to the BDT. The shape variations represent alternative shape templates which are controlled by nuisance parameters in the fit. To assess the acceptance uncertainties, the samples were normalised to the same cross-section. To assess shape uncertainties, the distributions being compared were normalised to the same area to avoid double-counting the acceptance effects. For both the shape templates and the acceptance, the uncertainties derived were symmetrised such that they represented both the $+1\sigma$ and -1σ variation.

Uncertainties on the total production cross-section for each process and uncertainties relating to NLO electroweak (EW) corrections were also considered in the analysis. Whilst I did not derive these particular uncertainties, they are described briefly in Section 6.5.4 for completeness.

6.3 Event selection

The analysis used three main selections targeting the leptonic decay modes of the two VH associated-production channels: 0-lepton ($ZH \to \nu\bar{\nu}b\bar{b}$), 1-lepton ($WH \to \ell\nu b\bar{b}$) and 2-lepton ($ZH \to \ell^+\ell^- b\bar{b}$), where $\ell = e, \mu$ (contributions from leptonically-decaying τ-leptons are included if the electron or muon pass the kinematic requirements). In all cases the uncertainties for $ZH \to \nu\bar{\nu}b\bar{b}$ were derived using the 0-lepton selection, the uncertainties for $WH \to \ell\nu b\bar{b}$ using the 1-lepton selection, and for $ZH \to \ell^+\ell^- b\bar{b}$ using the 2-lepton selection. The 0- and 1-lepton channels were split further into events with exactly two jets and events with exactly three jets, whilst the 2-lepton channel is split into events with exactly two jets and events with at least three jets. This ≥ 3 jet region will be referred to as the 3-jet region henceforth. A ≥ 4 jet veto in the 0- and 1-lepton

channels was implemented to reduce contamination from large $t\bar{t}$ background in these channels. In the 2-lepton channel, where the $t\bar{t}$ background is relatively smaller, the absence of this veto brings extra sensitivity. In all cases, at least two of the selected jets were required to be b-tagged.

To target regions with high signal-to-background ratio, the events were further categorised into ranges of p_{T}^{V}. In the 0-lepton channel this corresponds to $E_{\mathrm{T}}^{\mathrm{miss}}$; in the 1-lepton channel it is the vector sum of the charged lepton p_{T} and $E_{\mathrm{T}}^{\mathrm{miss}}$; and in the 2-lepton channel it is the p_{T} of the 2-lepton system. In all of the leptonic channels there was a $p_{\mathrm{T}}^{V} > 150\,\mathrm{GeV}$ region, and in the 2-lepton channel there was an additional $75\ \mathrm{GeV} < p_{\mathrm{T}}^{V} < 150\ \mathrm{GeV}$ region. This region was not explored for the 0- and 1-lepton channel as the increase in background outweighed any increased signal sensitivity. No distinction was made between these two p_{T}^{V} regions in the 2-lepton channel when assessing the acceptance uncertainties – they were derived inclusively in p_{T}^{V} for each analysis region.

The selection described above is summarised in Table 6.1. This table also details the kinematic cuts imposed on the leptons and jets and describes some additional selection cuts. In particular, a number of angular selections were made in the 0-lepton channel. These cuts are categorised into multijet rejection cuts, and signal-enhancing cuts. The 0-lepton channel suffered from larger background contamination with respect to the other channels, therefore the extra cuts helped to ensure a maximum signal-to-background ratio. In particular, the multijet rejection cuts reduced the multijet contamination to a negligible level.

Selection	$ZH \to \nu\bar{\nu}b\bar{b}$	$WH \to \ell\nu b\bar{b}$		$ZH \to \ell^+\ell^- b\bar{b}$
		μ sub-channel	e sub-channel	
Leptons	0 loose leptons	1 tight electron	1 medium muon	2 loose leptons $p_T > 7$ GeV, same flavour
	$p_T > 7$ GeV	$p_T > 27$ GeV	$p_T > 25$ GeV	≥ 1 lepton with $p_T > 27$ GeV
E_T^{miss}	> 150 GeV	> 30GeV	—	—
$m_{\ell\ell}$	—	—		81 GeV $< m_{\ell\ell} < 101$ GeV
Jets	Exactly 2 or 3 jets, $p_T > 20$ GeV			Exactly 2 or ≥ 3 jets, $p_T > 20$ GeV
b-jets	Exactly 2 b-tagged jets, leading b-jet $p_T > 45$ GeV			
p_T^V regions	> 150 GeV			$75 < p_T^V < 150$ GeV, $p_T^V > 150$ GeV
$\sum p_T^{jets}$	> 120 GeV (2-jets), > 150 GeV (3-jets)	—		
Multijet rejection:				
$\Delta\phi(E_T^{miss}, E_{T,trk}^{miss})$	$< 90°$	—		
$\min[\Delta\phi(E_T^{miss}, \text{jet})]$	$> 20°$ (2-jets), $> 30°$ (3-jets)	—		
Signal-enhancing:				
$\Delta\phi(E_T^{miss}, bb)$	$> 120°$	—		
$\Delta\phi(b_1, b_2)$	$< 140°$	—		

Table 6.1: Summary of the signal event-selection, adapted from Ref [88]. The angular cuts in the 0-lepton channel have been categorised into multijet rejection cuts, and signal enhancing cuts. The 0-lepton channel suffers from larger background contamination, therefore these extra cuts are required.

6.4 MC samples

As previously mentioned, the VH signal is comprised of three production modes: $ZH \to \nu\bar{\nu}b\bar{b}$, $ZH \to \ell^+\ell^- b\bar{b}$ and $WH \to \ell\nu b\bar{b}$. These processes were simulated using the POWHEG generator with the MINLO (multiscale improved NLO) procedure applied [90], interfaced to PYTHIA8 [91] for the parton shower and applying the AZNLO tune with the NNPDF3.0 PDF [92] set. These samples were used as the nominal prescription.

The POWHEG MINLO +PYTHIA8 samples include systematic variations stored as alternative event weights allowing the effects described in Section 6.2 to be studied. The alternative event weights correspond to:

- Variations of the μ_R and μ_F scales. Both are varied by a factor of 0.5 or 2 in a correlated and independent way, leading to six variations.
- 30 PDF and two α_s variations from the PDF4LHC15_30 set [93, 92, 84, 83, 94, 95, 96].

To investigate the effects of varying the parton shower and underlying event tune, MADGRAPH5-_AMC@NLO +PYTHIA8 samples were used. These samples were produced using MADGRAPH5-_AMC@NLO [97] for the hard scattering generation and PYTHIA8 for the parton shower, hadronisation, underlying event and multiple-parton interaction simulation. The NNPDF2.3 5f FFN [98] PDF sets with A14 tune [99] were used. In addition to this baseline prescription, additional samples with the five variations of the A14 parton shower tune were used [99]. The variations on this tune account for the effects of changing the level of underlying-event activity, changing the colour-reconnection range, and altering the levels of initial-(ISR) and final-state radiation (FSR).

Finally, POWHEG MINLO +HERWIG7 samples were used to assess the effect of using a different parton shower model. This sample was largely the same as the nominal POWHEG MINLO sample with the difference being that it was interfaced with the HERWIG7 parton shower model rather than PYTHIA8, and used the H7-UE-MMHT tune.

The samples were normalised to the best theoretical prediction of the cross-section for the different processes at the time. The cross-sections for qq-initiated WH and ZH were calculated at NNLO in QCD [100] [101] and NLO in EW [102]. The cross-section for gg-initiated ZH was calculated at NLO [103]. These cross-sections are summarised in Table 6.2. The given uncertainties take into account QCD scale, PDF and α_s uncertainties which were added in quadrature and are described in Section 6.5.4.

Process	order	cross-section (pb)
WH	NNLO(QCD)+NLO(EW)	1.37 ± 0.04
W^+H	NNLO(QCD)+NLO(EW)	0.84
W^-H	NNLO(QCD)+NLO(EW)	0.53
ZH	NNLO(QCD)+NLO(EW)	$0.88^{+0.04}_{-0.03}$
$gg \to ZH$	NLO(QCD)	0.12
$qq \to ZH$		0.76

Table 6.2: Inclusive cross-section for the signal processes.

6.5 Results

6.5.1 Parton shower and underlying event variations

To estimate the effect of parton shower modelling on the signal, two different strategies were used: variation of the parton shower tune and the use of a different parton shower model, HERWIG7. Ideally, the former would have been assessed using POWHEG MINLO +PYTHIA8 samples with variations of the AZNLO tune, however these samples were not available. Instead, the baseline MADGRAPH5_AMC@NLO +PYTHIA8 samples were compared to those generated with varied PYTHIA8 A14 tunes. The effect of using an alternative parton shower model was assessed by comparing the nominal POWHEG MINLO +PYTHIA8 sample to POWHEG MINLO +HERWIG7.

Acceptance

Separate uncertainties were derived for the tune variations and for the model comparison. The acceptance prediction from a given variation is defined as a^{var} and the acceptance prediction from the nominal is defined as a^{nom}. There were five tune variations in total which each had an up and down component, with their respective acceptances defined as $a^{\text{var}}_{\text{up}}$ and $a^{\text{var}}_{\text{down}}$. The fractional uncertainty arising from each tune variation was calculated as

$$\frac{\max(|a^{\text{var}}_{\text{up}} - a^{\text{nom}}|, |a^{\text{nom}} - a^{\text{var}}_{\text{down}}|)}{a^{\text{nom}}}. \tag{6.1}$$

These uncertainties were summed in quadrature to get the total uncertainty resulting from tune variations. For the model comparison, the uncertainty was calculated as the percentage difference between the HERWIG7 acceptance prediction and the nominal PYTHIA8 prediction. The final uncertainty was taken as the maximum of these, which was the PYTHIA8-HERWIG7 model comparison in all cases.

Process	Uncertainty	
	2j	3j / 2j
$ZH \to \nu\bar{\nu}b\bar{b}$	10.0%	13.0%
$WH \to \ell\nu b\bar{b}$	12.1%	12.9%
$ZH \to \ell^+\ell^- b\bar{b}$	13.9%	13.4%

Table 6.3: Summary of the uncertainties assigned for the effect of parton shower modelling on the VH acceptance in each analysis region.

This procedure was carried out to derive acceptance uncertainties for the two-jet and three-jet categories of each VH channel. The uncertainties for the 2-jet and 3-jet regions were found to be consistent. As a result, only the 2-jet acceptance uncertainty was used and an additional uncertainty was derived for the ratio between the acceptance in the 3-jet and 2-jet categories in each VH channel, following the same procedure described above. The final values of these acceptance uncertainties are shown in Table 6.3.

Shape

To assess the shape differences arising from the tune variations and the alternative parton shower model, ratios between these variations and the nominal were taken for p_{T}^{V} and $m_{b\bar{b}}$. In each lepton channel, shape differences were considered separately for the 2-jet and 3-jet channels. For p_{T}^{V}, each ratio was parametrised using a linear fit whilst a second-order polynomial was used for $m_{b\bar{b}}$.

The p_{T}^{V} shape differences with respect to the nominal for each tune variation are shown in Figure 6.2. The variation yielding the maximum shape difference in each region is highlighted by a cyan line and represents the shape uncertainty used in each region. The shape difference resulting from the comparison of the models was significantly smaller than for the tune variations, therefore no additional uncertainty was assigned.

The resulting $m_{b\bar{b}}$ shape difference with respect to the nominal for each tune variation in each selection is shown in Figure 6.3. Again, the maximum shape difference is highlighted with a cyan line in each region and represents the shape uncertainty used for this region. Shape deviations were also observed in the model comparison, which are shown in Figure 6.4. These shapes were very similar for each selection and due to their complicated nature, were difficult to fit with a continuous distribution. As a result, the ratio histogram representing the largest deviation was used as an additional shape template for each region.

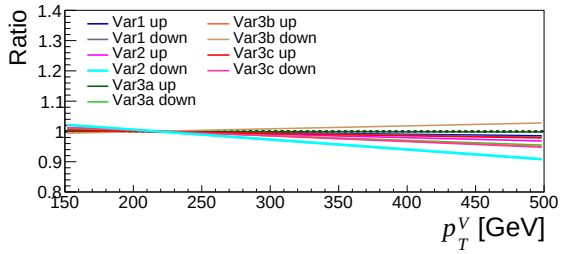

(a) $ZH \to \nu\bar{\nu}b\bar{b}$, 0 lepton, 2 jets

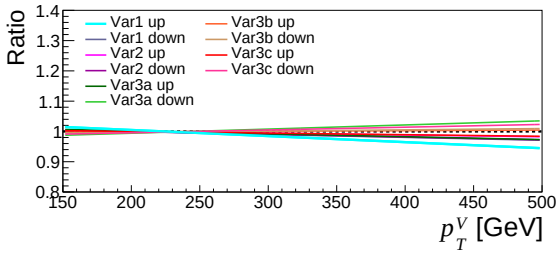

(b) $ZH \to \nu\bar{\nu}b\bar{b}$, 0 lepton, 3 jets

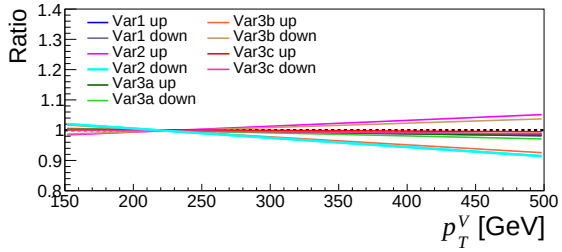

(c) $WH \to \ell\nu b\bar{b}$, 1 lepton, 2 jets

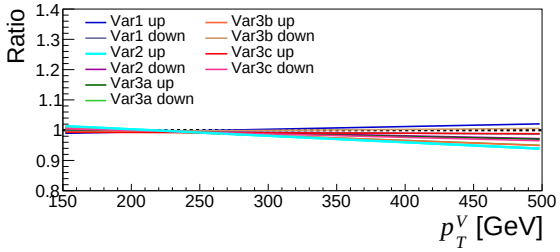

(d) $WH \to \ell\nu b\bar{b}$, 1 lepton, 3 jets

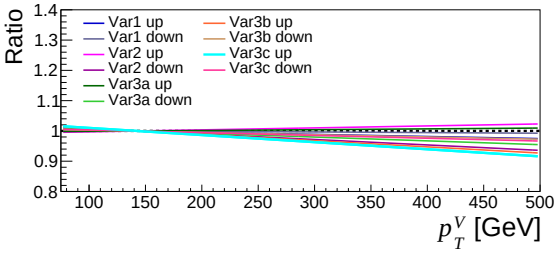

(e) $ZH \to \ell^+\ell^- b\bar{b}$, 2 lepton, 2 jets

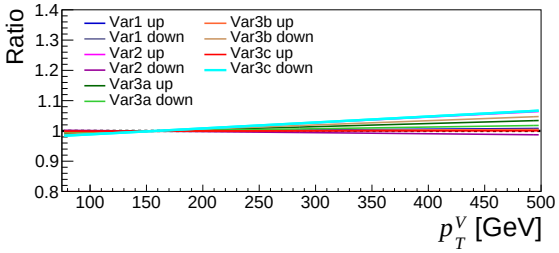

(f) $ZH \to \ell^+\ell^- b\bar{b}$, 2 lepton, ≥ 3 jets

Figure 6.2: Shape comparison of the p_{T}^V distributions for each VH process, i.e. lepton channel, and each number of jets category. The fit through the up and down variation of each tune is shown, where the maximum fit is highlighted by the cyan line. The latter was used as a shape uncertainty.

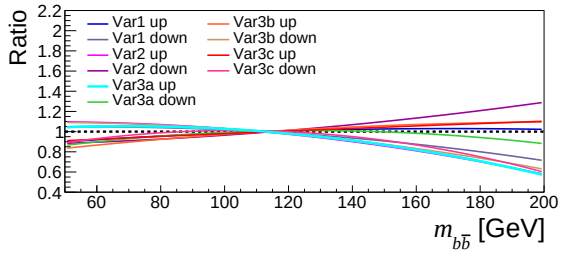

(a) $ZH \to \nu\bar{\nu}b\bar{b}$, 0 lepton, 2 jets

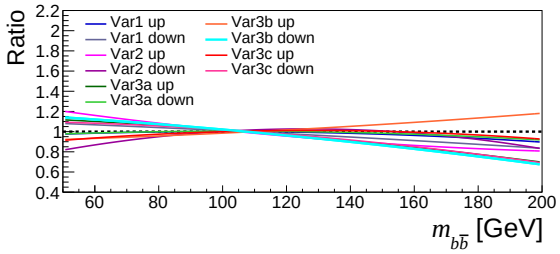

(b) $ZH \to \nu\bar{\nu}b\bar{b}$, 0 lepton, 3 jets

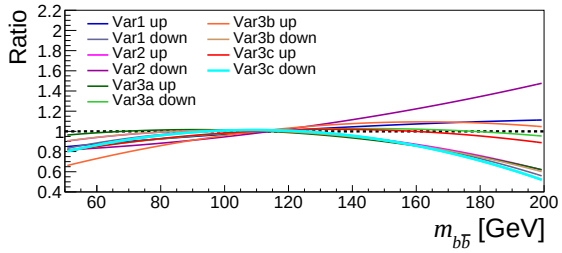

(c) $WH \to \ell\nu b\bar{b}$, 1 lepton, 2 jets

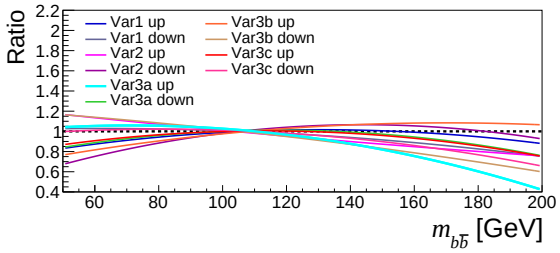

(d) $WH \to \ell\nu b\bar{b}$, 1 lepton, 3 jets

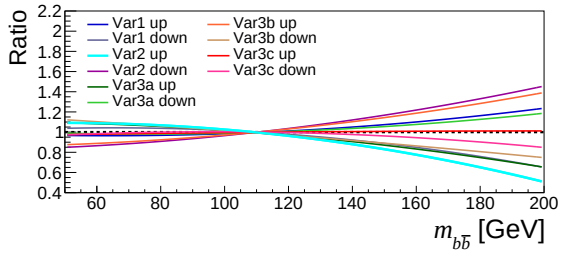

(e) $ZH \to \ell^+\ell^- b\bar{b}$, 2 lepton, 2 jets

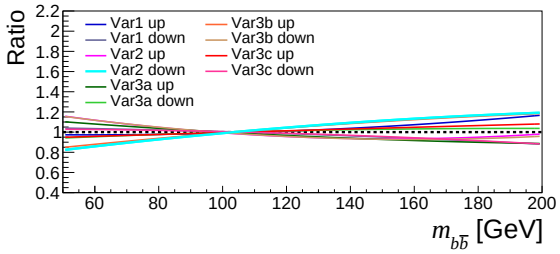

(f) $ZH \to \ell^+\ell^- b\bar{b}$, 2 lepton, $\geq$ 3 jets

Figure 6.3: Shape comparison of the $m_{b\bar{b}}$ distributions for each VH process, i.e. lepton channel, and each number of jets category. The fit through the up and down variation of each tune is shown, where the maximum fit is highlighted by the cyan line. The latter was used as a shape uncertainty.

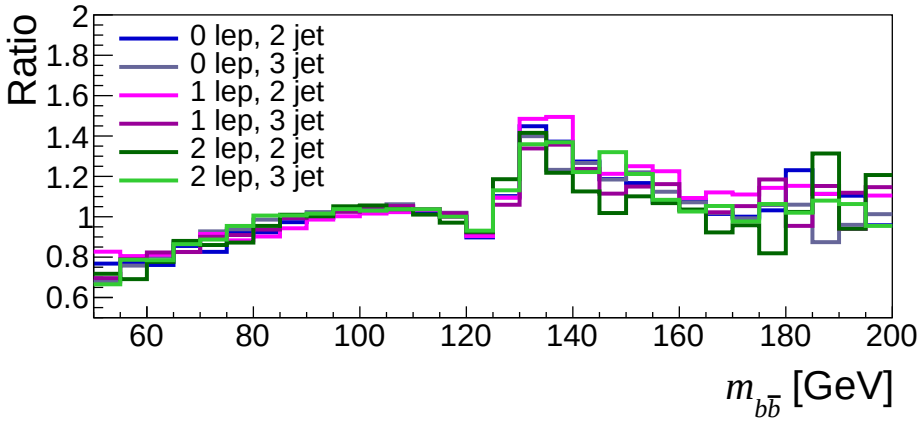

(a)

Figure 6.4: Ratios of the $m_{b\bar{b}}$ distributions for each VH process, i.e. lepton channel, and each number of jets category from the POWHEG MINLO +PYTHIA8 vs POWHEG MINLO +HERWIG7 comparison.

6.5.2 PDF and α_s

These uncertainties were derived from comparisons between the nominal POWHEG MINLO +PYTHIA8 samples and those generated with the PDF and the $\alpha_s(m_Z)\pm0.001$ variations from the PDF4LHC15_30 PDF set.

Acceptance

Acceptance uncertainties were calculated inclusively as the 2-jet and 3-jet uncertainties were found to be consistent. The percentage difference between each varied sample and the nominal was calculated and summed in quadrature to derive the PDF component of the uncertainty. The percentage differences between the varied α_s samples and the nominal were derived, and their average was taken as the α_s component of the uncertainty. These components were added in quadrature to get the final uncertainty. The values of these acceptance uncertainties are summarised in Table 6.4.

Shape

The ratio of $m_{b\bar{b}}$ and p_T^V between each varied sample and the nominal was taken. The shapes were considered separately between the 2-jet and 3-jet categories. The ratios were parametrised by a linear fit for p_T^V and a second-order polynomial for $m_{b\bar{b}}$. It was found that the PDF and α_s variations had a negligible effect on the $m_{b\bar{b}}$ shape and therefore no shape uncertainty was assigned to this distribution. Figure 6.5 shows the fitted ratios for each PDF and α_s variation in each region, where

Process	Uncertainty (inclusive)
$ZH \to \nu\bar{\nu}b\bar{b}$	1.1%
$WH \to \ell\nu b\bar{b}$	1.3%
$ZH \to \ell^+\ell^- b\bar{b}$	0.5%

Table 6.4: Summary of the systematic uncertainties on the VH acceptance originating from altering the PDF and α_s uncertainties.

the envelope is highlighted by the green line. The shape deviations are small and similar across all of these regions, therefore the largest shape variation was taken as the final shape uncertainty for all channels, which was the envelope shown in the 0-lepton 2-jet region.

6.5.3 Scale variations

The nominal POWHEG MINLO +PYTHIA8 samples were compared to those generated with weights corresponding to varied factorisation and renormalisation scales, in order to derive uncertainties based on these variations.

Acceptance

The acceptance uncertainties were derived using the Stewart-Tackmann-method (ST method) to ensure that correlations between the perturbative uncertainties in the exclusive jet bins were correctly taken into account, as well as additional uncertainties induced by imposing a jet boundary [104]. This method translates uncertainties on inclusive jet selections into a set of uncertainties on the exclusive jet selections used in the analysis. The inclusive jet categories were defined as ≥ 2 jets, ≥ 3 jets, and ≥ 4 jets. For each of these categories, the envelope of the percentage differences between the nominal and each scale variation was taken. These, along with the nominal inclusive acceptances, were the ingredients for the method. The application of the ST method, which involves solving a covariance matrix defined in Reference [104], results in a correlated and uncorrelated uncertainty in each two-jet bin, an uncertainty for each three-jet bin, and an additional uncertainty accounting for the > 4 jet veto in the 0- and 1-lepton channels, shown in Table 6.5.

Shape

To derive the shape uncertainties for $m_{b\bar{b}}$ and p_{T}^V, the ratio between each variation and the nominal description was parametrised by a linear fit for p_{T}^V and a second-order polynomial for $m_{b\bar{b}}$, shown in Figures 6.6 and 6.7 respectively. For both variables, the shapes were considered separately for the

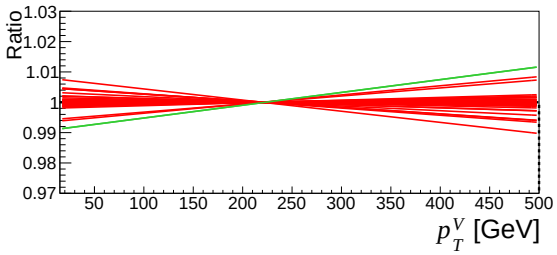

(a) $ZH \to \nu\bar{\nu}b\bar{b}$, 0 lepton, 2 jets

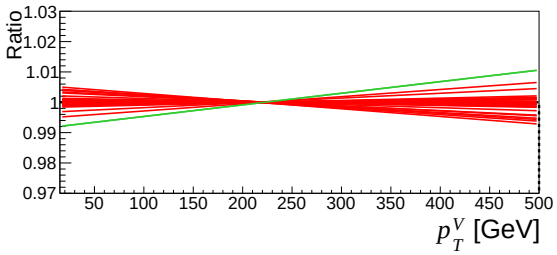

(b) $ZH \to \nu\bar{\nu}b\bar{b}$, 0 lepton, 3 jets

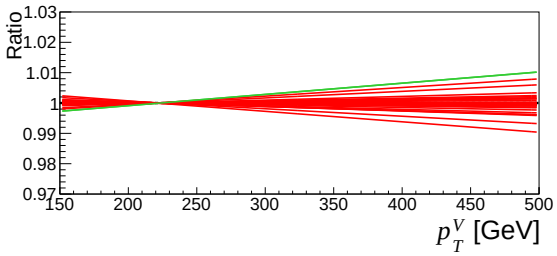

(c) $WH \to \ell\nu b\bar{b}$, 1 lepton, 2 jets

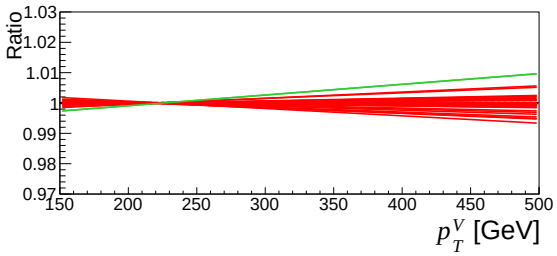

(d) $WH \to \ell\nu b\bar{b}$, 1 lepton, 3 jets

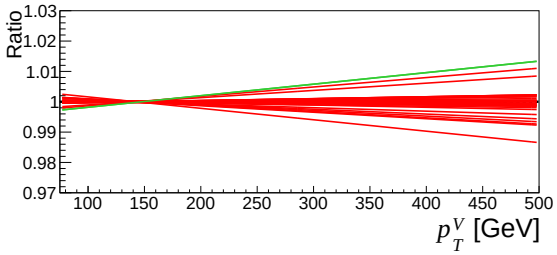

(e) $ZH \to \ell^+\ell^- b\bar{b}$, 2 lepton, 2 jets

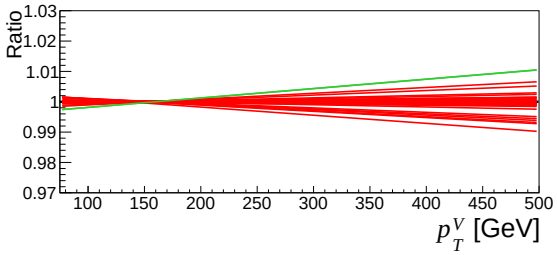

(f) $ZH \to \ell^+\ell^- b\bar{b}$, 2 lepton, $\geq$3 jets

Figure 6.5: p_{T}^V: Fits through shape differences arising from each PDF and α_{s} variation, for each VH process, i.e. lepton channel, split into the 2-jet and 3-jet category. The green line shows the envelope of those variations in each region. These shapes are consistent, therefore the maximum of these envelopes was used as the systematic uncertainty in all regions which was the envelope shown for the 0-lepton 2-jet region.

Process	Uncertainty			
	2-jet	2-jet (correlated with 3-jet)	3-jet	4-jet veto
$ZH \to \nu\nu b\bar{b}$	6.9%	−7.0%	5.0%	−2.5%
$ZH \to llb\bar{b}$	3.3%	−3.2%	3.9%	-
$WH \to \ell\nu b\bar{b}$	8.8%	−8.6%	6.8%	3.8%

Table 6.5: Summary of the acceptance uncertainties resulting from scale variations, computed using the Stewart Tackman method.

2-jet and 3-jet categories. In each region and for each variable, the envelope of these variations is highlighted by a cyan line; this envelope was used as the shape uncertainty in each of these regions.

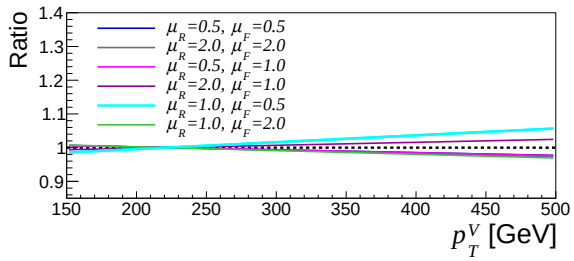

(a) $ZH \to \nu\bar{\nu}b\bar{b}$, 0 lepton, 2 jets

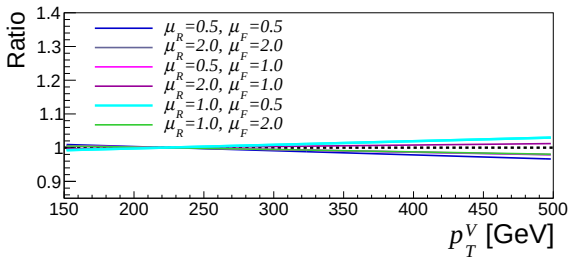

(b) $ZH \to \nu\bar{\nu}b\bar{b}$, 0 lepton, 3 jets

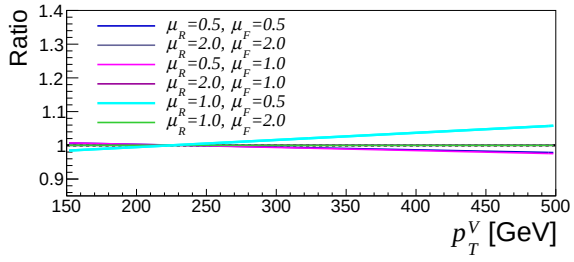

(c) $WH \to \ell\nu b\bar{b}$, 1 lepton, 2 jets

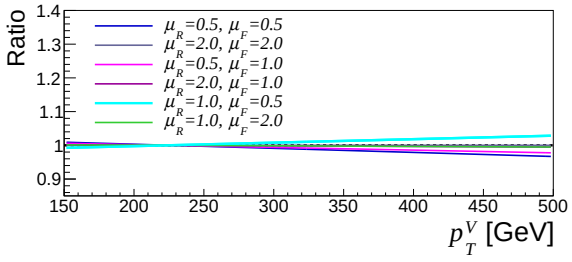

(d) $WH \to \ell\nu b\bar{b}$, 1 lepton, 3 jets

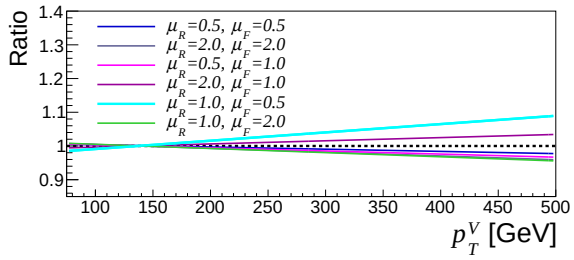

(e) $ZH \to \ell^+\ell^- b\bar{b}$, 2 lepton, 2 jets

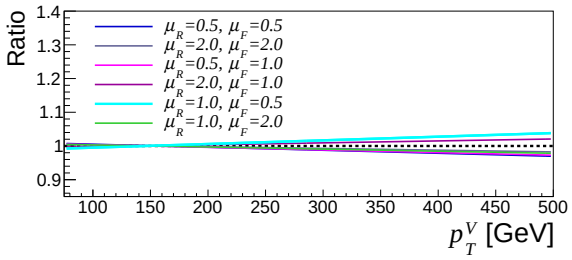

(f) $ZH \to \ell^+\ell^- b\bar{b}$, 2 lepton, $\geq$3 jets

Figure 6.6: p_{T}^V: Fits through the deviations originating from each scale variation for each VH process, i.e. lepton channel, split into the 2-jet and 3-jet category. The cyan line shows the envelope of those variations and was chosen as a systematic uncertainty for the p_{T}^V shape in each respective region.

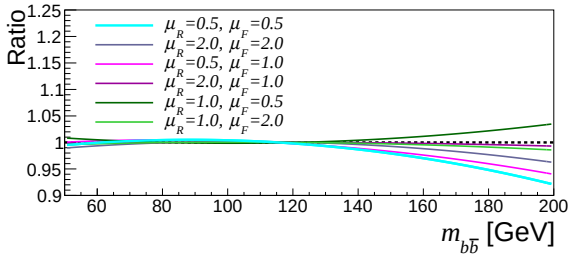

(a) $ZH \to \nu\bar{\nu}b\bar{b}$, 0 lepton, 2 jets

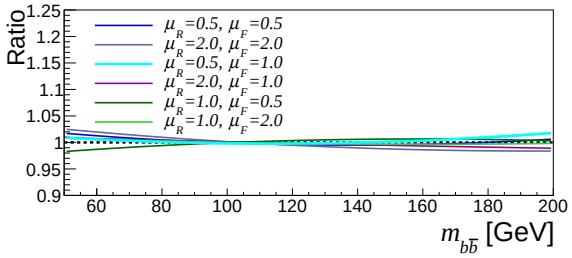

(b) $ZH \to \nu\bar{\nu}b\bar{b}$, 0 lepton, 3 jets

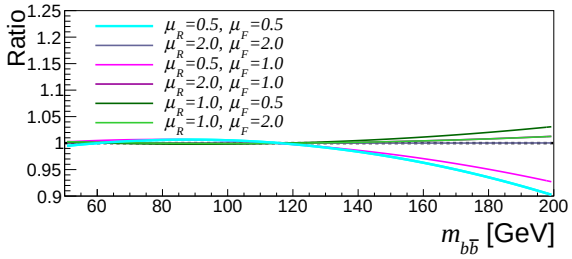

(c) $WH \to \ell\nu b\bar{b}$, 1 lepton, 2 jets

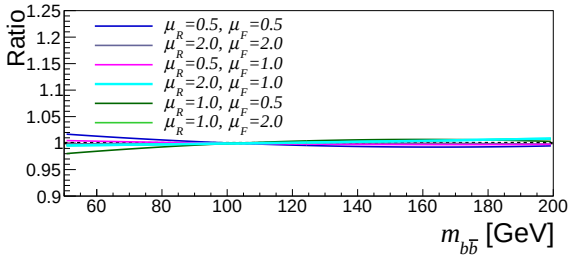

(d) $WH \to \ell\nu b\bar{b}$, 1 lepton, 3 jets

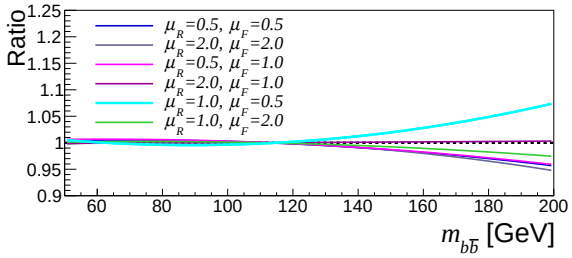

(e) $ZH \to \ell^+\ell^- b\bar{b}$, 2 lepton, 2 jets

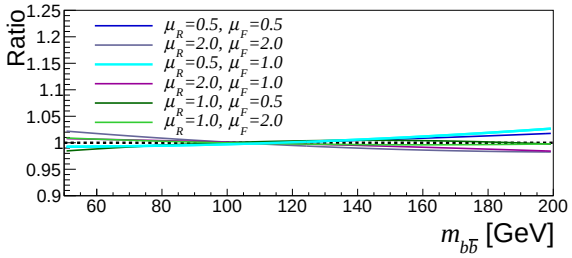

(f) $ZH \to \ell^+\ell^- b\bar{b}$, 2 lepton, $\geq$3 jets

Figure 6.7: $m_{b\bar{b}}$: Fits through the deviations originating from each scale variation for each VH process, i.e. lepton channel, split into the 2-jet and 3-jet category. The cyan line shows the envelope of those variations and was chosen as a systematic uncertainty for the $m_{b\bar{b}}$ shape in each respective region.

6.5.4 Additional uncertainties

In addition to the analysis-specific uncertainties described in the previous sections, additional uncertainties relating to the calculation of the total production cross-sections, the $H \to b\bar{b}$ branching ratio, and the effect of NLO EW corrections on differential distributions were also included in the analysis. I did not derive these uncertainties, however a brief description is given here for completeness.

The uncertainties on the calculated total cross-sections reported in Table 6.2 arise due to the effects of varying the scales μ_F and μ_R, as well as variation of the PDF and α_s value. These uncertainties were treated as normalisation nuisance parameters in the fit. An uncertainty was also considered for the $H \to b\bar{b}$ branching ratio, which was also treated as a normalisation nuisance parameter. This uncertainty took into account missing higher-order effects in the calculation of the branching ratio and uncertainties on the mass of the b-quark and α_s, Whilst the effect of NLO EW corrections was included in the calculated total cross-sections, their effect on the differential distributions was not. Since they were expected to have a significant effect on the p_T^V distributions, corresponding corrections were derived as a function p_T^V. The signal samples were then reweighted such that they included these corrections.

6.5.5 Impact of uncertainties

The acceptance and shape uncertainties derived were assigned as normalisation and shape nuisance parameters in the fit, respectively. To estimate the contribution of the signal-modelling uncertainties as a whole to the total systematic uncertainty, their nuisance parameters were fixed to their best-fit value. The fit was then repeated and a new total uncertainty was extracted. The difference in quadrature between the new uncertainty and the original gave an estimate of the signal-modelling uncertainties' impact to the total uncertainty. This was done for each category of uncertainty considered in the analysis as shown in Figure 6.8. From these results it can be seen that the signal-modelling uncertainties were the leading contributor to the total systematic uncertainty. In particular, it was the parton shower acceptance uncertainties, which as a whole, were the single leading source of systematic uncertainty in the analysis at 10–13.9%.

6.6 Summary

Systematic uncertainties relating to the modelling of the $V(H \to b\bar{b})$ signal were assessed. They were found to be the largest contributor to the total systematic uncertainty on the final result, with

Source of uncertainty		σ_μ
Total		0.39
Statistical		0.24
Systematic		0.31
Experimental uncertainties		
Jets		0.03
$E_{\mathrm{T}}^{\mathrm{miss}}$		0.03
Leptons		0.01
b-tagging	b-jets	0.09
	c-jets	0.04
	light jets	0.04
	extrapolation	0.01
Pile-up		0.01
Luminosity		0.04
Theoretical and modelling uncertainties		
Signal		0.17
Floating normalisations		0.07
Z + jets		0.07
W + jets		0.07
$t\bar{t}$		0.07
Single top quark		0.08
Diboson		0.02
Multijet		0.02
MC statistical		0.13

Figure 6.8: A summary of the impact of each source of uncertainty on the resulting signal strength with respect to the SM [88].

the leading uncertainty coming from the parton shower acceptance effects.

The analysis techniques described in Section 6.1 formed the basis for an updated search using 79.8 fb^{-1} of Run-2 data, where a 4.9σ excess of $V(H \to b\bar{b})$ signal events was observed [105]. This result was included in two combinations: firstly with 7 TeV and 8 TeV Run-1 data; secondly with the results of other $H \to b\bar{b}$ searches via the $t\bar{t}H$ and vector-boson fusion production modes which also combined Run-1 and Run-2 results. These combinations resulted in observation of the $H \to b\bar{b}$ decay mode with a significance of 5.4σ. Another combination of the result with other searches for VH production, where the Higgs decayed to two photons or two Z bosons, resulted in an excess of VH signal events with a observed significance of 5.3σ. The resulting signal strengths with respect to the SM from the combinations described are shown in Figure 6.9.

Whilst I didn't actively work on this iteration of the analysis, the uncertainties derived as described in this chapter were mostly re-used in this analysis as the signal MC samples remained the same for the most part. The exception to this was the parton shower acceptance uncertainties. Updated POWHEG MINLO +PYTHIA8 samples with AZNLO tune variations became available as well as an updated POWHEG MINLO +HERWIG7 sample which offered improved MC statistics. Following re-evaluation of the parton shower uncertainties with the inclusion of these new samples, the acceptance uncertainties decreased from being in the range of 10–13.9% to 2.9–11.9%. Despite this, whilst their contribution to the total uncertainty as a whole decreased, the signal-modelling uncertainties remained the largest contributor to the total systematic uncertainty with respect to other categories of uncertainty. The parton shower acceptance uncertainty was still one of the largest, however in this analysis it was no longer the single largest source of systematic uncertainty.

For future iterations of the analysis there are certainly improvements to be made in how the signal-modelling uncertainties are evaluated. So far the signal-modelling uncertainties have always been derived at particle-level and with a particle-level framework, however this means that truth-to-reconstruction resolution effects in $m_{b\bar{b}}$ and p_{T}^{V} are not assessed or accounted for. In addition, if the uncertainties were evaluated at detector-level their effect on the BDT discriminant directly could be assessed rather than using $m_{b\bar{b}}$ and p_{T}^{V} as a proxy. Progress has been made in this area where a new framework has been developed which allows for truth-to-reconstruction matching between physics objects used to evaluate the uncertainties. Studies are also beginning on the feasibility of using the BDT discriminant to derive uncertainties rather than $m_{b\bar{b}}$ and p_{T}^{V}. Finally, due to the lack of available samples, dedicated uncertainties were not assessed for gg-initiated ZH production. In the future it would be interesting to see what the size of these uncertainties would be and if they are indeed compatible with those derived for qq-initiated ZH production.

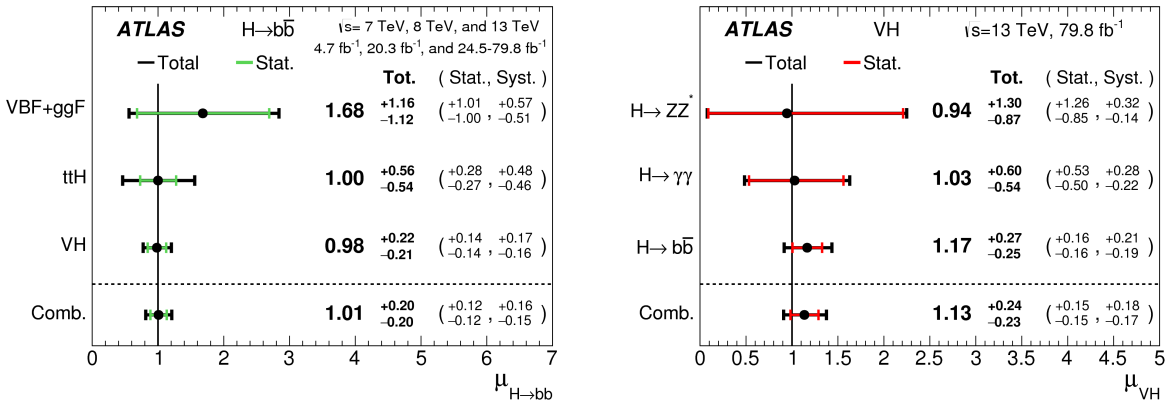

(a) (b)

Figure 6.9: The fitted values of a) the $H \to b\bar{b}$ signal strength for the separate production channels and their combination, and b) the VH signal strength for the different Higgs decay channels and their combination, both taken from Reference [105].

Chapter 7

Conclusion

In 2017, the first evidence for the $H \to b\bar{b}$ decay was obtained in a search for $V(H \to b\bar{b})$. A dominant background for this search is $Z + b\bar{b}$, the mis-modelling of which was one of the leading systematic errors in the analysis. Improving the understanding of this background is therefore a key part of improving the $V(H \to b\bar{b})$ search in the future, as well as being an interesting process in its own right. $Z + b\bar{b}$ is sensitive to uncertainties relating to the predictions of perturbative QCD; in particular uncertainties regarding the treatment of the kinematics and amplitude of b-quarks in the initial and final state. Measuring this process can therefore help to constrain these uncertainties. The identification of b-quarks is a crucial aspect of both the $V(H \to b\bar{b})$ search and $Z + b\bar{b}$ measurement, hence it is important that the performance of b-tagging algorithms is well-understood.

In this thesis a calibration of the b-tagging efficiency of the MV2c10 algorithm in track-jets was performed in data collected at a centre of mass energy of $\sqrt{s} = 13$ TeV. The calibration was performed using the tag-and-probe method and the resulting scale-factors were an important validation of the scale-factors obtained using the likelihood calibration method, which are used by analyses in ATLAS. This calibration is important for ensuring that the MC simulation correctly describes the performance of the MV2c10 b-tagging algorithm in data.

With the performance of the b-tagging algorithm understood, a measurement of the kinematic variables of a high p_{T} b-tagged large-R jet produced in association with a Z-boson was then presented. The measurement was performed on a dataset corresponding to 36 fb^{-1} collected at a centre of mass energy of $\sqrt{s} = 13$ TeV. This is the first measurement of this process in the boosted phase-space. The cross-sections were measured as a function of the large-R jet p_{T} & mass in both the inclusive region and the 2-tag region, the separation between the tagged sub-jets, $\Delta R(b, \bar{b})$, and the p_{T} of the vector-sum of the Z-boson and the large-R jet as well as their separation in ϕ in the inclusive region. The shape of the variables tended to be mismodelled by the MC predictions in

the inclusive region, whilst the predictions were more compatible with the data within 1σ for variables in the 2-tag region. The total fiducial cross-sections for the inclusive and 2-tag region were also measured. The data was found to agree with the SHERPA prediction within 1σ in the inclusive region and consistent with the MADGRAPH5_AMC@NLO+PYTHIA8 prediction within 1σ in the 2-tag region.

The $Z+$jets process is a dominant and important background for many Higgs analyses, a particular example being the $V(H\to b\bar{b})$ search, which is also presented in this thesis. The studies performed to assess the signal-modelling uncertainties in the 2017 analysis, where the first evidence for this process was seen, have been presented. It was found that the dominant signal-modelling uncertainty arose from the parton-shower modelling, which in fact turned out to be the leading systematic uncertainty in the analysis. Since this process is sensitive to the modelling of the parton shower, the understanding regarding $g \to b\bar{b}$ splitting gained from the $Z + b\bar{b}$ measurement will be crucial for future searches.

In parallel to the boosted $Z+$jets measurement described in this thesis, a resolved measurement was performed by another ATLAS group of analysers, where a lower momentum phase space was targeted. The produced b-quarks are less collimated in this phase-space, meaning small-radius $R = 0.4$ calorimeter jets can be used to resolve them – hence the term "resolved". The results from both this analysis and the boosted analysis presented in this thesis are very important for future $V(H\to b\bar{b})$ searches. The results from these $Z+$jets analyses will be invaluable for constraining the modelling uncertainties associated with this background process in the search, which as mentioned earlier are currently one of the leading sources of systematic uncertainty. Along with the inclusion of the full Run-2 dataset, this could be a key contribution towards achieving a single-channel observation of the $V(H\to b\bar{b})$ process.

In addition to the analyses presented in this thesis, I was also involved in a Run-2 measurement of observables sensitive to the b-quark fragmentation function, which is the function governing the transition of a b-quark into a b-hadron. Thus far, the treatment of b-quark fragmentation functions in MC generators has been based on measurements made at LEP [106, 107, 108], hence it is important to check whether the modelling still holds true at a hadron collider. The results of this measurement along with the results of the $Z + b\bar{b}$ measurement can be used for future Monte Carlo development and tuning, which will in turn help the many analyses for which b-quarks play an important role.

Bibliography

[1] The ATLAS Collaboration. "Observation of a new particle in the search for the Standard Model Higgs boson with the ATLAS detector at the LHC". In: *Phys. Lett.* B716 (2012), pp. 1–29. DOI: 10.1016/j.physletb.2012.08.020. arXiv: 1207.7214 [hep-ex].

[2] The CMS collaboration. "Observation of a new boson at a mass of 125 GeV with the CMS experiment at the LHC". In: *Phys. Lett.* B716 (2012), pp. 30–61. DOI: 10.1016/j.physletb.2012.08.021. arXiv: 1207.7235 [hep-ex].

[3] Chanda J. Jog. "Large scale asymmetry of rotation curves in lopsided spiral galaxies". In: *Astron. Astrophys.* 391 (2002), p. 471. DOI: 10.1051/0004-6361:20020832. arXiv: astro-ph/0207055 [astro-ph].

[4] J. H. Christenson et al. "Evidence for the 2π Decay of the K_2^0 Meson". In: *Phys. Rev. Lett.* 13 (4 July 1964), pp. 138–140. DOI: 10.1103/PhysRevLett.13.138. URL: https://link.aps.org/doi/10.1103/PhysRevLett.13.138.

[5] Makoto Kobayashi and Toshihide Maskawa. "CP Violation in the Renormalizable Theory of Weak Interaction". In: *Prog. Theor. Phys.* 49 (1973), pp. 652–657. DOI: 10.1143/PTP.49.652.

[6] Michael E. Peskin and Daniel V. Schroeder. *An Introduction to quantum field theory*. Reading, USA: Addison-Wesley, 1995. ISBN: 9780201503975, 0201503972. URL: http://www.slac.stanford.edu/~mpeskin/QFT.html.

[7] Matthew D. Schwartz. *Quantum Field Theory and the Standard Model*. Cambridge University Press, 2014. ISBN: 1107034736, 9781107034730. URL: http://www.cambridge.org/us/academic/subjects/physics/theoretical-physics-and-mathematical-physics/quantum-field-theory-and-standard-model.

[8] R. Keith Ellis, W. James Stirling, and B. R. Webber. "QCD and collider physics". In: *Camb. Monogr. Part. Phys. Nucl. Phys. Cosmol.* 8 (1996), pp. 1–435.

[9] C.Englert A.Banfi. *Lecture notes for the 2016 HEP School for Experimental High Energy Physics Students*. Sept. 2016.

[10] F. Halzen and Alan D. Martin. *Quarks and Leptons: An introductory course in modern particle physics*. 1984. ISBN: 0471887412, 9780471887416.

[11] C. Patrignani et al. "Review of Particle Physics". In: *Chin. Phys.* C40.10 (2016), p. 100001. DOI: 10.1088/1674-1137/40/10/100001.

[12] M. Aker et al. "An improved upper limit on the neutrino mass from a direct kinematic method by KATRIN". In: (2019). arXiv: 1909.06048 [hep-ex].

[13] David J. Gross and Frank Wilczek. "Ultraviolet Behavior of Non-Abelian Gauge Theories". In: *Phys. Rev. Lett.* 30 (26 June 1973), pp. 1343–1346. DOI: 10.1103/PhysRevLett.30.1343. URL: https://link.aps.org/doi/10.1103/PhysRevLett.30.1343.

[14] H. David Politzer. "Reliable Perturbative Results for Strong Interactions?" In: *Phys. Rev. Lett.* 30 (26 June 1973), pp. 1346–1349. DOI: 10.1103/PhysRevLett.30.1346. URL: https://link.aps.org/doi/10.1103/PhysRevLett.30.1346.

[15] Steven Weinberg. "A Model of Leptons". In: *Phys. Rev. Lett.* 19 (21 Nov. 1967), pp. 1264–1266. DOI: 10.1103/PhysRevLett.19.1264. URL: https://link.aps.org/doi/10.1103/PhysRevLett.19.1264.

[16] Sheldon L. Glashow. "The renormalizability of vector meson interactions". In: *Nucl. Phys.* 10 (1959), pp. 107–117. DOI: 10.1016/0029-5582(59)90196-8.

[17] Abdus Salam and J. C. Ward. "Weak and electromagnetic interactions". In: *Il Nuovo Cimento (1955-1965)* 11.4 (Feb. 1, 1959), pp. 568–577. ISSN: 1827-6121. DOI: 10.1007/BF02726525. URL: https://doi.org/10.1007/BF02726525.

[18] Peter W. Higgs. "Broken Symmetries and the Masses of Gauge Bosons". In: *Phys. Rev. Lett.* 13 (16 Oct. 1964), pp. 508–509. DOI: 10.1103/PhysRevLett.13.508. URL: https://link.aps.org/doi/10.1103/PhysRevLett.13.508.

[19] F. Englert and R. Brout. "Broken Symmetry and the Mass of Gauge Vector Mesons". In: *Phys. Rev. Lett.* 13 (9 Aug. 1964), pp. 321–323. DOI: 10.1103/PhysRevLett.13.321. URL: https://link.aps.org/doi/10.1103/PhysRevLett.13.321.

[20] Nicola Cabibbo. "Unitary Symmetry and Leptonic Decays". In: *Phys. Rev. Lett.* 10 (12 June 1963), pp. 531–533. DOI: 10.1103/PhysRevLett.10.531. URL: https://link.aps.org/doi/10.1103/PhysRevLett.10.531.

[21] Makoto Kobayashi and Toshihide Maskawa. “CP-Violation in the Renormalizable Theory of Weak Interaction”. In: *Progress of Theoretical Physics* 49.2 (Feb. 1973), pp. 652–657. ISSN: 0033-068X. DOI: 10.1143/PTP.49.652. eprint: http://oup.prod.sis.lan/ptp/article-pdf/49/2/652/5257692/49-2-652.pdf. URL: https://doi.org/10.1143/PTP.49.652.

[22] John Ellis. “Higgs Physics”. In: arXiv:1312.5672. (Dec. 2013). Lectures presented at the ESHEP 2013 School of High-Energy Physics, 117–168. 52 p. DOI: 10.5170/CERN-2015-004.117. URL: https://cds.cern.ch/record/1638469.

[23] R. P. Feynman. “The Theory of Positrons”. In: *Phys. Rev.* 76 (6 Sept. 1949), pp. 749–759. DOI: 10.1103/PhysRev.76.749. URL: https://link.aps.org/doi/10.1103/PhysRev.76.749.

[24] Peter Skands. “Introduction to QCD”. In: *Proceedings, 2nd Asia-Europe-Pacific School of High-Energy Physics (AEPSHEP 2014)*. 2013, pp. 341–420. DOI: 10.1142/9789814525220_0008,10.23730/CYRSP-2017-002.63. arXiv: 1207.2389 [hep-ph].

[25] G. Altarelli and G. Parisi. “Asymptotic freedom in parton language”. In: *Nuclear Physics B* 126.2 (1977), pp. 298–318. ISSN: 0550-3213. DOI: https://doi.org/10.1016/0550-3213(77)90384-4. URL: http://www.sciencedirect.com/science/article/pii/0550321377903844.

[26] Yuri L. Dokshitzer. “Calculation of the Structure Functions for Deep Inelastic Scattering and e+ e- Annihilation by Perturbation Theory in Quantum Chromodynamics.” In: *Sov. Phys. JETP* 46 (1977). [Zh. Eksp. Teor. Fiz.73,1216(1977)], pp. 641–653.

[27] V. N. Gribov and L. N. Lipatov. “Deep inelastic e p scattering in perturbation theory”. In: *Sov. J. Nucl. Phys.* 15 (1972). [Yad. Fiz.15,781(1972)], pp. 438–450.

[28] Fabio Maltoni, Giovanni Ridolfi, and Maria Ubiali. “b-initiated processes at the LHC: a reappraisal”. In: *JHEP* 07 (2012). [Erratum: JHEP04,095(2013)], p. 022. DOI: 10.1007/JHEP04(2013)095,10.1007/JHEP07(2012)022. arXiv: 1203.6393 [hep-ph].

[29] Andy Buckley et al. “General-purpose event generators for LHC physics”. In: *Phys. Rept.* 504 (2011), pp. 145–233. DOI: 10.1016/j.physrep.2011.03.005. arXiv: 1101.2599 [hep-ph].

[30] Rene Brun et al. *GEANT: Detector Description and Simulation Tool; Oct 1994*. CERN Program Library. Long Writeup W5013. Geneva: CERN, 1993. DOI: 10.17181/CERN.MUHF.DMJ1. URL: https://cds.cern.ch/record/1082634.

[31] Stefan Hoche. "Introduction to parton-shower event generators". In: *Proceedings, Theoretical Advanced Study Institute in Elementary Particle Physics: Journeys Through the Precision Frontier: Amplitudes for Colliders (TASI 2014): Boulder, Colorado, June 2-27, 2014*. 2015, pp. 235–295. DOI: 10.1142/9789814678766_0005. arXiv: 1411.4085 [hep-ph].

[32] V. V. Sudakov. "Vertex parts at very high-energies in quantum electrodynamics". In: *Sov. Phys. JETP* 3 (1956). [Zh. Eksp. Teor. Fiz.30,87(1956)], pp. 65–71.

[33] Stefano Catani et al. "The Dipole formalism for next-to-leading order QCD calculations with massive partons". In: *Nucl. Phys.* B627 (2002), pp. 189–265. DOI: 10.1016/S0550-3213(02)00098-6. arXiv: hep-ph/0201036 [hep-ph].

[34] T. Sjöstrand. *On the $g \to Q\bar{Q}$ rate*. 2014. URL: http://home.thep.lu.se/~torbjorn/pdfdoc/g2qqbarsplit.pdf (visited on 06/19/2019).

[35] Bo Andersson et al. "Parton Fragmentation and String Dynamics". In: *Phys. Rept.* 97 (1983), pp. 31–145. DOI: 10.1016/0370-1573(83)90080-7.

[36] B.R. Webber. "A QCD model for jet fragmentation including soft gluon interference". In: *Nuclear Physics B* 238.3 (1984), pp. 492–528. ISSN: 0550-3213. DOI: https://doi.org/10.1016/0550-3213(84)90333-X. URL: http://www.sciencedirect.com/science/article/pii/055032138490333X.

[37] Lyndon Evans and Philip Bryant. "LHC Machine". In: *JINST* 3 (2008), S08001. DOI: 10.1088/1748-0221/3/08/S08001.

[38] *LEP design report*. Copies shelved as reports in LEP, PS and SPS libraries. Geneva: CERN, 1984. URL: https://cds.cern.ch/record/102083.

[39] Fabienne Marcastel. "CERN's Accelerator Complex". In: (Oct. 2013). General Photo. URL: http://cds.cern.ch/record/1621583.

[40] The ATLAS Collaboration. "The ATLAS Experiment at the CERN Large Hadron Collider". In: *Journal of Instrumentation* 3.08 (Aug. 2008), S08003–S08003. DOI: 10.1088/1748-0221/3/08/s08003. URL: https://doi.org/10.1088/1748-0221/3/08/s08003.

[41] The CMS Collaboration. "The CMS experiment at the CERN LHC". In: *Journal of Instrumentation* 3.08 (Aug. 2008), S08004–S08004. DOI: 10.1088/1748-0221/3/08/s08004. URL: https://doi.org/10.1088/1748-0221/3/08/s08004.

[42] The LHCb Collaboration. "The LHCb Detector at the LHC". In: *Journal of Instrumentation* 3.08 (Aug. 2008), S08005–S08005. DOI: 10.1088/1748-0221/3/08/s08005. URL: https://doi.org/10.1088/1748-0221/3/08/s08005.

[43] The ALICE Collaboration. "The ALICE experiment at the CERN LHC". In: *Journal of Instrumentation* 3.08 (Aug. 2008), S08002–S08002. DOI: 10.1088/1748-0221/3/08/s08002. URL: https://doi.org/10.1088/1748-0221/3/08/s08002.

[44] S Van der Meer. *Calibration of the effective beam height in the ISR*. Tech. rep. CERN-ISR-PO-68-31. ISR-PO-68-31. Geneva: CERN, 1968. URL: https://cds.cern.ch/record/296752.

[45] The ATLAS collaboration. "Luminosity determination in pp collisions at $\sqrt{s} = 8$ TeV using the ATLAS detector at the LHC". In: *The European Physical Journal C* 76.12 (Nov. 28, 2016), p. 653. ISSN: 1434-6052. DOI: 10.1140/epjc/s10052-016-4466-1. URL: https://doi.org/10.1140/epjc/s10052-016-4466-1.

[46] The ATLAS collaboration. *Luminosity Public Results Run 2*. 2019. URL: https://twiki.cern.ch/twiki/bin/view/AtlasPublic/LuminosityPublicResultsRun2 (visited on 05/16/2019).

[47] The ATLAS Collaboration. *ATLAS inner detector: Technical Design Report, 1*. Technical Design Report ATLAS. Geneva: CERN, 1997. URL: https://cds.cern.ch/record/331063.

[48] The ATLAS Collaboration. *ATLAS Insertable B-Layer Technical Design Report*. Tech. rep. CERN-LHCC-2010-013. ATLAS-TDR-19. Sept. 2010. URL: https://cds.cern.ch/record/1291633.

[49] The ATLAS collaboration. "Performance of the ATLAS track reconstruction algorithms in dense environments in LHC Run 2". In: *The European Physical Journal C* 77.10 (Oct. 11, 2017), p. 673. ISSN: 1434-6052. DOI: 10.1140/epjc/s10052-017-5225-7. URL: https://doi.org/10.1140/epjc/s10052-017-5225-7.

[50] ATLAS Collaboration. *Technical Design Report for the Phase-II Upgrade of the ATLAS LAr Calorimeter*. Tech. rep. CERN-LHCC-2017-018. ATLAS-TDR-027. Geneva: CERN, Sept. 2017. URL: http://cds.cern.ch/record/2285582.

[51] The ATLAS collaboration. *ATLAS muon spectrometer: Technical Design Report*. Technical Design Report ATLAS. Geneva: CERN, 1997. URL: https://cds.cern.ch/record/331068.

[52] The ATLAS Collaboration. "The ATLAS Data Acquisition and High Level Trigger system". In: *Journal of Instrumentation* 11.06 (June 2016), P06008–P06008. DOI: 10.1088/1748-0221/11/06/p06008. URL: https://doi.org/10.1088/1748-0221/11/06/p06008.

[53] The ATLAS collaboration. "Performance of the ATLAS trigger system in 2015". In: *The European Physical Journal C* 77.5 (May 18, 2017), p. 317. ISSN: 1434-6052. DOI: 10.1140/epjc/s10052-017-4852-3. URL: https://doi.org/10.1140/epjc/s10052-017-4852-3.

[54] T Cornelissen et al. "The new ATLAS track reconstruction (NEWT)". In: *Journal of Physics: Conference Series* 119.3 (July 2008), p. 032014. DOI: 10.1088/1742-6596/119/3/032014. URL: https://doi.org/10.1088/1742-6596/119/3/032014.

[55] The ATLAS collaboration. "Reconstruction of primary vertices at the ATLAS experiment in Run 1 proton-proton collisions at the LHC". In: *Eur. Phys. J.* C77.5 (2017), p. 332. DOI: 10.1140/epjc/s10052-017-4887-5. arXiv: 1611.10235 [physics.ins-det].

[56] The ATLAS Collaboration. *Electron efficiency measurements with the ATLAS detector using the 2015 LHC proton-proton collision data*. Tech. rep. ATLAS-CONF-2016-024. Geneva: CERN, June 2016. URL: https://cds.cern.ch/record/2157687.

[57] W Lampl et al. *Calorimeter Clustering Algorithms: Description and Performance*. Tech. rep. ATL-LARG-PUB-2008-002. ATL-COM-LARG-2008-003. Geneva: CERN, Apr. 2008. URL: https://cds.cern.ch/record/1099735.

[58] T G Cornelissen et al. "The global χ^2track fitter in ATLAS". In: *Journal of Physics: Conference Series* 119.3 (July 2008), p. 032013. DOI: 10.1088/1742-6596/119/3/032013. URL: https://doi.org/10.1088/1742-6596/119/3/032013.

[59] The ATLAS Collaboration. *Improved electron reconstruction in ATLAS using the Gaussian Sum Filter-based model for bremsstrahlung*. Tech. rep. ATLAS-CONF-2012-047. Geneva: CERN, May 2012. URL: https://cds.cern.ch/record/1449796.

[60] The ATLAS collaboration. "Electron and photon energy calibration with the ATLAS detector using 2015–2016 LHC proton-proton collision data". In: *Journal of Instrumentation* 14.03 (Mar. 2019), P03017–P03017. DOI: 10.1088/1748-0221/14/03/p03017. URL: https://doi.org/10.1088/1748-0221/14/03/p03017.

[61] The ATLAS Collaboration. "Muon reconstruction performance of the ATLAS detector in proton–proton collision data at $\sqrt{s} = 13$ TeV". In: *The European Physical Journal C* 76.5 (May 23, 2016), p. 292. ISSN: 1434-6052. DOI: 10.1140/epjc/s10052-016-4120-y. URL: https://doi.org/10.1140/epjc/s10052-016-4120-y.

[62] The ATLAS Collaboration. "Topological cell clustering in the ATLAS calorimeters and its performance in LHC Run 1". In: *The European Physical Journal C* 77.7 (July 24, 2017), p. 490. ISSN: 1434-6052. DOI: 10.1140/epjc/s10052-017-5004-5. URL: https://doi.org/10.1140/epjc/s10052-017-5004-5.

[63] Matteo Cacciari, Gavin P. Salam, and Gregory Soyez. "The anti-k_t jet clustering algorithm". In: *JHEP* 04 (2008), p. 063. DOI: 10.1088/1126-6708/2008/04/063. arXiv: 0802.1189 [hep-ph].

[64] Gavin P. Salam. "Towards Jetography". In: *Eur. Phys. J.* C67 (2010), pp. 637–686. DOI: 10.1140/epjc/s10052-010-1314-6. arXiv: 0906.1833 [hep-ph].

[65] David Krohn, Jesse Thaler, and Lian-Tao Wang. "Jet trimming". In: *Journal of High Energy Physics* 2010.2 (Feb. 24, 2010), p. 84. ISSN: 1029-8479. DOI: 10.1007/JHEP02(2010)084. URL: https://doi.org/10.1007/JHEP02(2010)084.

[66] The ATLAS Collaboration. *Monte Carlo Calibration and Combination of In-situ Measurements of Jet Energy Scale, Jet Energy Resolution and Jet Mass in ATLAS*. Tech. rep. ATLAS-CONF-2015-037. Geneva: CERN, Aug. 2015. URL: https://cds.cern.ch/record/2044941.

[67] *Jet Calibration and Systematic Uncertainties for Jets Reconstructed in the ATLAS Detector at $\sqrt{s} = 13$ TeV*. Tech. rep. ATL-PHYS-PUB-2015-015. Geneva: CERN, July 2015. URL: https://cds.cern.ch/record/2037613.

[68] The ATLAS collaboration. "Performance of jet substructure techniques for large-R jets in proton-proton collisions at $\sqrt{s} = 7$ TeV using the ATLAS detector". In: *Journal of High Energy Physics* 2013.9 (Sept. 13, 2013), p. 76. DOI: 10.1007/JHEP09(2013)076. URL: https://doi.org/10.1007/JHEP09(2013)076.

[69] The ATLAS Collaboration. *Recommendations for 2015+2016 data analysis aiming for 2017 winter conferences*. 2016. URL: https://twiki.cern.ch/twiki/bin/view/AtlasProtected/JetUncertainties2016Moriond2017#ResolutionUncertainties (visited on 10/25/2019).

[70] The ATLAS Collaboration. *Expected performance of the ATLAS b-tagging algorithms in Run-2*. Tech. rep. ATL-PHYS-PUB-2015-022. Geneva: CERN, July 2015. URL: https://cds.cern.ch/record/2037697.

[71] "Performance of b-jet identification in the ATLAS experiment". In: *Journal of Instrumentation* 11.04 (Apr. 2016), P04008–P04008. DOI: 10.1088/1748-0221/11/04/p04008. URL: https://iopscience.iop.org/article/10.1088/1748-0221/11/04/P04008.

[72] The ATLAS Collaboration. "Measurements of b-jet tagging efficiency with the ATLAS detector using $t\bar{t}$ events at $\sqrt{s} = 13$ TeV". In: *JHEP* 08 (2018), p. 089. DOI: 10.1007/JHEP08(2018)089. arXiv: 1805.01845 [hep-ex].

[73] The ATLAS Collaboration. *Expected flavour tagging performance in release 20.7*. 2016. URL: https://twiki.cern.ch/twiki/bin/view/AtlasProtected/BTaggingBenchmarksRelease2 (visited on 10/25/2019).

[74] D. J. Lange. "The EvtGen particle decay simulation package". In: *Nucl. Instrum. Meth. A* 462 (2001), p. 152. DOI: 10.1016/S0168-9002(01)00089-4.

[75] S. Agostinelli. "Geant4: a simulation toolkit". In: *Nuclear Instruments and Methods in Physics Research Section A: Accelerators, Spectrometers, Detectors and Associated Equipment* 506.3 (2003), pp. 250–303. ISSN: 0168-9002. DOI: https://doi.org/10.1016/S0168-9002(03)01368-8. URL: http://www.sciencedirect.com/science/article/pii/S0168900203013688.

[76] The ATLAS collaboration. "Luminosity determination in pp collisions at $\sqrt{s} = 8$ TeV using the ATLAS detector at the LHC". In: *Eur. Phys. J.* C76.12 (2016), p. 653. DOI: 10.1140/epjc/s10052-016-4466-1. arXiv: 1608.03953 [hep-ex].

[77] R. Keith Ellis, G. Marchesini, and B. R. Webber. "Soft Radiation in Parton Parton Scattering". In: *Nucl. Phys.* B286 (1987). [Erratum: Nucl. Phys.B294,1180(1987)], p. 643. DOI: 10.1016/0550-3213(87)90456-1,10.1016/0550-3213(87)90628-6.

[78] The ATLAS Collaboration. "Measurement of differential production cross-sections for a Z boson in association with b-jets in 7 TeV proton-proton collisions with the ATLAS detector". In: *JHEP* 10 (2014), p. 141. DOI: 10.1007/JHEP10(2014)141. arXiv: 1407.3643 [hep-ex].

[79] The CMS collaboration. "Measurement of the cross section and angular correlations for associated production of a Z boson with b hadrons in pp collisions at $\sqrt{s} = 7$ TeV". In: *JHEP* 12 (2013), p. 039. DOI: 10.1007/JHEP12(2013)039. arXiv: 1310.1349 [hep-ex].

[80] Matteo Cacciari, Gavin P. Salam, and Gregory Soyez. "The Catchment Area of Jets". In: *JHEP* 04 (2008), p. 005. DOI: 10.1088/1126-6708/2008/04/005. arXiv: 0802.1188 [hep-ph].

[81] Georgios Choudalakis. "Fully Bayesian Unfolding". In: (2012). arXiv: 1201.4612 [physics.data-an].

[82] R. Fletcher. *Practical methods of optimization*. Wiley-Interscience publication v. 1. Wiley, 1987. ISBN: 9780471915478. URL: https://books.google.co.uk/books?id=W0zvAAAAMAAJ.

[83] Sayipjamal Dulat et al. "New parton distribution functions from a global analysis of quantum chromodynamics". In: *Phys. Rev. D* 93.3 (2016), p. 033006. DOI: 10.1103/PhysRevD.93.033006. arXiv: 1506.07443 [hep-ph].

[84] L.A. Harland-Lang et al. "Parton distributions in the LHC era: MMHT 2014 PDFs". In: *Eur. Phys. J. C* 75.5 (2015), p. 204. DOI: 10.1140/epjc/s10052-015-3397-6. arXiv: 1412.3989 [hep-ph].

[85] The ATLAS and CMS collaborations. "Measurements of the Higgs boson production and decay rates and constraints on its couplings from a combined ATLAS and CMS analysis of the LHC pp collision data at $\sqrt{s} = 7$ and 8 TeV". In: *JHEP* 08 (2016), p. 045. DOI: 10.1007/JHEP08(2016)045. arXiv: 1606.02266 [hep-ex].

[86] D. de Florian et al. "Handbook of LHC Higgs Cross Sections: 4. Deciphering the Nature of the Higgs Sector". In: (2016). DOI: 10.23731/CYRM-2017-002. arXiv: 1610.07922 [hep-ph].

[87] Nicolo Cartiglia. "Measurement of the proton-proton total, elastic, inelastic and diffractive cross sections at 2, 7, 8 and 57 TeV". In: (2013). arXiv: 1305.6131 [hep-ex].

[88] The ATLAS Collaboration. "Evidence for the $H \to b\bar{b}$ decay with the ATLAS detector". In: *JHEP* 12 (2017), p. 024. DOI: 10.1007/JHEP12(2017)024. arXiv: 1708.03299 [hep-ex].

[89] Andy Buckley et al. "Rivet user manual". In: *Comput. Phys. Commun.* 184 (2013), pp. 2803–2819. DOI: 10.1016/j.cpc.2013.05.021. arXiv: 1003.0694 [hep-ph].

[90] Gionata Luisoni et al. "HW ±/HZ + 0 and 1 jet at NLO with the POWHEG BOX interfaced to GoSam and their merging within MiNLO". In: *Journal of High Energy Physics* 2013.10 (2013), p. 83. ISSN: 1029-8479. DOI: 10.1007/JHEP10(2013)083. URL: http://dx.doi.org/10.1007/JHEP10(2013)083.

[91] Torbjorn Sjostrand, Stephen Mrenna, and Peter Skands. "A brief introduction to {PYTHIA} 8.1". In: *Computer Physics Communications* 178.11 (2008), pp. 852–867. ISSN: 0010-4655. DOI: http://dx.doi.org/10.1016/j.cpc.2008.01.036. URL: http://www.sciencedirect.com/science/article/pii/S0010465508000441.

[92] Richard D. Ball et al. "Parton distributions for the LHC Run II". In: *JHEP* 04 (2015), p. 040. DOI: 10.1007/JHEP04(2015)040. arXiv: 1410.8849 [hep-ph].

[93] Jon Butterworth et al. "PDF4LHC recommendations for LHC Run II". In: *J. Phys.* G43 (2016), p. 023001. DOI: 10.1088/0954-3899/43/2/023001. arXiv: 1510.03865 [hep-ph].

[94] Jun Gao and Pavel Nadolsky. "A meta-analysis of parton distribution functions". In: *JHEP* 07 (2014), p. 035. DOI: 10.1007/JHEP07(2014)035. arXiv: 1401.0013 [hep-ph].

[95] Stefano Carrazza et al. "An Unbiased Hessian Representation for Monte Carlo PDFs". In: *Eur. Phys. J.* C75.8 (2015), p. 369. DOI: 10.1140/epjc/s10052-015-3590-7. arXiv: 1505.06736 [hep-ph].

[96] G. Watt and R. S. Thorne. "Study of Monte Carlo approach to experimental uncertainty propagation with MSTW 2008 PDFs". In: *JHEP* 08 (2012), p. 052. DOI: 10.1007/JHEP08(2012)052. arXiv: 1205.4024 [hep-ph].

[97] J. Alwall et al. "The automated computation of tree-level and next-to-leading order differential cross sections, and their matching to parton shower simulations". In: *JHEP* 07 (2014), p. 079. DOI: 10.1007/JHEP07(2014)079. arXiv: 1405.0301 [hep-ph].

[98] Richard D. Ball et al. "Parton distributions with LHC data". In: *Nucl. Phys.* B867 (2013), pp. 244–289. DOI: 10.1016/j.nuclphysb.2012.10.003. arXiv: 1207.1303 [hep-ph].

[99] The ATLAS Collaboration. *ATLAS Run 1 Pythia8 tunes*. Tech. rep. ATL-PHYS-PUB-2014-021. Geneva: CERN, Nov. 2014. URL: https://cds.cern.ch/record/1966419.

[100] Oliver Brein, Abdelhak Djouadi, and Robert Harlander. "NNLO QCD corrections to the Higgs-strahlung processes at hadron colliders". In: *Phys. Lett.* B579 (2004), pp. 149–156. DOI: 10.1016/j.physletb.2003.10.112. arXiv: hep-ph/0307206 [hep-ph].

[101] Oliver Brein et al. "Top-Quark Mediated Effects in Hadronic Higgs-Strahlung". In: *Eur. Phys. J.* C72 (2012), p. 1868. DOI: 10.1140/epjc/s10052-012-1868-6. arXiv: 1111.0761 [hep-ph].

[102] Ansgar Denner et al. “Electroweak corrections to Higgs-strahlung off W/Z bosons at the Tevatron and LHC with HAWK”. In: *JHEP* 03 (2012), p. 075. DOI: 10.1007/JHEP03(2012)075. arXiv: 1211.5142 [hep-ph].

[103] Lukas Altenkamp et al. “Gluon-induced Higgs-strahlung at next-to-leading order QCD”. In: *JHEP* 02 (2013), p. 078. DOI: 10.1007/JHEP02(2013)078. arXiv: 1211.5015 [hep-ph].

[104] Iain W. Stewart and Frank J. Tackmann. “Theory uncertainties for Higgs mass and other searches using jet bins”. In: *Phys. Rev. D* 85 (3 Feb. 2012), p. 034011. DOI: 10.1103/PhysRevD.85.034011. URL: https://link.aps.org/doi/10.1103/PhysRevD.85.034011.

[105] The ATLAS Collaboration. “Observation of $H \to b\bar{b}$ decays and VH production with the ATLAS detector”. In: *Phys. Lett.* B786 (2018), pp. 59–86. DOI: 10.1016/j.physletb.2018.09.013. arXiv: 1808.08238 [hep-ex].

[106] J. Abdallah et al. “A study of the b-quark fragmentation function with the DELPHI detector at LEP I and an averaged distribution obtained at the Z Pole”. In: *Eur. Phys. J.* C71 (2011), p. 1557. DOI: 10.1140/epjc/s10052-011-1557-x. arXiv: 1102.4748 [hep-ex].

[107] A. Heister et al. “Study of the fragmentation of b quarks into B mesons at the Z peak”. In: *Phys. Lett.* B512 (2001), pp. 30–48. DOI: 10.1016/S0370-2693(01)00690-6. arXiv: hep-ex/0106051 [hep-ex].

[108] G. Abbiendi et al. “Inclusive analysis of the b quark fragmentation function in Z decays at LEP”. In: *Eur. Phys. J.* C29 (2003), pp. 463–478. DOI: 10.1140/epjc/s2003-01229-x. arXiv: hep-ex/0210031 [hep-ex].